

https://dspace.org/

The design and development of a light-weight aluminium semi-trailer

Elston, Malcolm John Mac Gregor

1991

http://hdl.handle.net/10539/22707

Elston, Malcolm John Mac Gregor (1991) The design and development of a light-weight aluminium semi-trailer, University of Witwatersrand, Johannesburg, <http://wiredspace.wits.ac.za/handle/10539/22707>

Downloaded from a DSpace repository. https://dspace.org/

THE DESIGN AND DEVELOPMENT OF A LIGHT-WEIGHT ALUMINIUM SEMI-TRAILER

Malcolm John Mac Gregor Elston

VOLUME 1

A dissertation submitted to the Faculty of Engineering, University of the Witwatersrand, Johannesburg, in fulfilment of the requirements for the degree of Master of Science in Engineering.

Johannesburg, 1991

DECLARATION

I declare that this dissertation is my own, unaided work. It is being submitted for the degree of Master of Science in Engineering in the University of the Witwatersrand, Johannesburg. It has not been submitted before for any degree or examination in any other University.



MALCOLM JOHN ELSTON

12th day of December 1991

ABSTRACT

With increasing competition in the commercial vehicle industry, future vehicle designs need to be able to carry greater payloads within the bounds of existing legislation. Increasing the payload efficiency of transport vehicles involves two main areas:

a. Optimizing the size and mass distribution of the vehicle for the purpose intended.

b. Keeping the tare mass as low as possible through efficient design and the use of lighter and stronger materials.

The use of aluminium for light-weight trailer design is investigated through the design and construction of a 13,7 metre long, aluminium chassied, wide spaced tridem, platform semi-trailer capable of carrying a payload of thirty tonnes. A brief historical perspective is also given, describing the use of aluminium trailers in South Africa and overseas, followed by a discussion on vehicle structural and endurance testing techniques.

The tare mass saving achieved in comparison to a similar size conventional steel chassied semi-trailer with a tare mass of 7 800 kilograms, is 1 220 kilograms. In spite of the higher initial cost of the aluminium semi-trailer, this additional payload is shown to translate into a payback period of approximately twenty four months.

To my wife,

Catherine

and to my parents,

Isabel and Laurence

for without their continual support,

this work would not have been possible

ACKNOWLEDGEMENTS

I would like to express my sincere appreciation to the following persons for their valuable comments and guidance throughout the duration of this project:

Professor R D Marcus
Professor A Nurick
Mr M Bailey

Furthermore, I record my gratitude to the management and staff of the following organizations for their kind contributions and assistance:

The University of the Witwatersrand Technology Centre
School of Mechanical Engineering, University of the Witwatersrand
Henred Fruehauf Trailers (Pty) Ltd
Huletts Aluminium Limited
Alusuisse (S.A.) (Pty) Ltd
Diesel Electric S.A. (Pty) Ltd
John Simms and Associates (Pty) Ltd
Motolek (Pty) Ltd
Sigma Power Corporation (Pty) Ltd
MAG Brakes (Pty) Ltd

CONTENTS

		Page
VOLUME I:		
DECLARATION		i
ABSTRACT		ii
DEDICATION		iii
ACKNOWLEDGEMENTS		iv
CONTENTS		v
LIST OF FIGURES		xii
LIST OF TABLES		xviii
LIST OF GRAPHS		xxi
LIST OF PHOTOGRAPHS		xxvi
LIST OF SYMBOLS		xxxii
1.	**INTRODUCTION**	1
1.1	**General**	1
1.2	**Aluminium semi-trailers – Historical perspective and current status**	8
2.	**DESIGN SPECIFICATIONS**	12
2.1	**General**	12
2.2	**Semi-trailer specification**	12
2.2.1	Chassis and ancillary structure	12
2.2.2	Suspension, axles and wheels	14
2.2.3	Braking system	15
2.2.4	Electrical system and lights	15
2.3	**Semi-trailer weight distribution**	15

3. INITIAL TRAILER TESTS AND PROPOSED TESTING TECHNIQUES 17

3.1 [illegible] 17
3.2 [illegible] vibration frequency tests 19
3.3 [illegible] data acquisition system 25
3.4 [illegible] testing techniques 30

4. DESIGN EVALUATION 42

4.1 Introduction 42
4.2 General 42
4.2.1 General vehicle concept, legal considerations and overall dimensions 42
4.2.2 Design payload and chassis mass 47
4.2.3 Pseudo-dynamic loading design approach and stress analysis 48
4.3 Main chassis I-beams 51
4.3.1 Loading analysis of main I-beams 51
4.3.2 Stress distributions in main chassis I-beams 54
4.3.3 Failure critical stress areas in main chassis I-beams 92
4.3.4 Buckling of main chassis I-beams 94
4.3.5 Fatigue analysis of main chassis I-beams 96
4.4 Chassis sub-structure 102
4.4.1 Side rails and outriggers 102
4.4.2 Deck planks 108
4.4.3 Torsion tubes 109
4.4.4 Upper coupler structure 110

4.5 [illegible] 112
4.5.1 [illegible] 113
4.5.2 [illegible] 115
4.5.3 [illegible] 116
4.5.4 [illegible] jack-knife device 118
4.6 [illegible] and wheels 121
4.6.1 [illegible] 121
4.6.2 [illegible] 129
4.6.3 [illegible] and tyres 131
4.7 [illegible] system 132
4.7.1 [illegible] system operation 133
4.7.2 Service braking performance 137
4.7.3 Braking compatibility of the truck-tractor and semi-trailer combination 138
4.8 Lights, retro-reflectors and electrical system 139

5. SEMI-TRAILER CONSTRUCTION 141

5.1 General 141
5.2 Aluminium welding 141
5.3 Construction of the aluminium chassis structure and associated sub-structure 144
5.4 Assembly of landing legs 171
5.5 Assembly of axles and suspension 172
5.6 Mounting of Hope anti-jack-knife king-pin 184
5.7 Assembly of brake system and pneumatic circuitry 188
5.8 Assembly of lights, retro-reflectors and electrical system 196

6. CONCLUSION 202

6.1 Lightweight aluminium chassis 202
6.2 Wide spread tridem axle concept 206
6.3 Pseudo-dynamic based acceleration based design model 208
6.4 Final conclusions and recommendations 210

VOLUME II:

APPENDICES 211

APPENDIX A STRESS ANALYSIS OF MAIN CHASSIS I-BEAMS 211

A.1 Introduction 211
A.2 Loading analysis of main chassis I-beams 211
A.2.1 General 211
A.2.2 Pseudo-dynamic fully distributed load analysis (Case 1) 212
A.2.3 Static fully distributed load analyses (Case 2 and (Case 3) 222
A.2.4 Static load analyses for various axles lifted (Case 4 to Case 7) 223
A.2.5 Longitudinal loading analysis 226
A.3 Stress analysis of main chassis I-beams 230
A.3.1 Stress distributions 230
A.3.2 Failure critical stress areas 237
A.4 Buckling of main chassis I-beams 256
A.4.1 Construction of buckling diagram 257
A.4.2 Buckling strength distribution 258

A.5 Fatigue analysis of main chassis I-beams 264
A.5.1 Fatigue stress levels 264
A.5.2 Frequency distribution of fatigue stress spectrum 267
A.5.3 Cumulative fatigue damage 270

APPENDIX B GENESYS 'FRAME-ANALYSIS/2' SUB-PROGRAM 279

B.1 Introduction 279
B.2 General 279
B.3 GENESYS 'FRAME-ANALYSIS/2' input data and results tables 287

APPENDIX C STRESS ANALYSIS OF CHASSIS SUB-STRUCTURE 311

C.1 Introduction 311
C.2 Side rails and outriggers 311
C.2.1 Calculation of outrigger flexibility 313
C.2.2 Calculation of deck plank flexibility 319
C.2.3 Continuous beam analysis of side rail/outrigger structure 320
C.2.4 Maximum stress in side rail 327
C.2.5 Maximum stress in outriggers 328
C.3 Deck planks 330
C.3.1 Stress in the deck plank for a single point load midway between the main chassis beams 332
C.3.2 Stress in the deck plank for loading at the side rail 334
C.4 Torsion tubes 336
C.5 Upper coupler 344
C.5.1 Upper coupler structure – horizontal load analysis 345
C.5.2 Upper couple structure – vertical load analysis 349
C.5.3 Rubbing plate mounting bolts 352
C.5.4 Hope king-pin foundation plate bolts 353

APPENDIX D STRESS ANALYSIS OF ANCILLARY STRUCTURE 355

D.1 Introduction 355
D.2 Rear under-ride bumper 355
D.2.1 Stresses due to load at P_1 357
D.2.2 Stresses due to load at P_2 359
D.2.3 Stresses due to load at P_3 363
D.3 Headboard 365
D.4 Landing legs 370
D.4.1 Landing leg mounting bracket welds 372
D.4.2 Landing leg mounting bracket bolts and bolt holes 375
D.4.3 Rearward brace 376
D.4.4 Cross brace 380
D.4.5 Landing leg brace ends 382
D.4.6 Landing leg cross-member 384
D.5 Hope king-pin foundation plate 391
D.5.1 Bearing stresses 392
D.5.2 Thread stresses 393

APPENDIX E MATERIAL SPECIFICATIONS AND MECHANICAL PROPERTIES 396

E.1 Aluminium alloys 396
E.1.1 Anticorodal-112 aluminium alloy 396
E.1.2 Anticorodal-100 aluminium alloy 397
E.1.3 D65S aluminium alloy 399
E.1.4 B51S aluminium alloy 400
E.1.5 D54S aluminium alloy 401
E.2 Filler alloys – aluminium welds 402
E.3 ROC-tuf AD690 steel 403
E.4 BS4360 – Gd 43A steel 404
E.5 Nuts, bolts and washers 405

APPENDIX F SEMI-TRAILER BRAKE SYSTEM 406

F.1 General 406
F.2 Available braking forces 406
F.3 Compatibility curves 408
F.4 Load-sensing valve settings 410
F.5 Parking brake 419
F.6 Required brake reservoir capacity 422

APPENDIX G SELECTION OF OVERALL VEHICLE PARAMETERS 427

G.1 General 427
G.2 Sample calculation 430
G.2.1 Case A - Full use of payload capacity of truck-tractor 430
G.2.2 Case B - Maximum load on trailer tri-axle bogie and front axle of truck-tractor 432
G.2.3 Case C - Maximum load on front axle of truck-tractor and centre of gravity of payload at centre of trailer deck 433
G.3 Results 435

APPENDIX H ENGINEERING DRAWINGS 441

REFERENCES 443

LIST OF FIGURES

Figure		Page
2.1	Semi-trailer weight distribution and general dimensions	16
3.1	A typical block of strain gauge data from the initial vibration frequency tests	20
3.2	High speed computer controlled data acquisition system	28
3.3	A typical block of strain time data	31
3.4	The effect of rainflow counting using full and segmented load histories	33
3.5	Methods that improve the failure prediction reliability of the Palmgren-Miner hypothesis	37
3.6	A typical stress-strain hysteresis loop for a ductile metal	38
3.7	A typical strain-life curve	41
4.1	Semi-trailer design weight distribution and general dimensions	45
4.2	Hope anti-jack-knife device	119
4.3	Semi-trailer tri-axle bogie self-steering configuration for trailer as built	122

5.1 Relevant dimensions for the alignment of the semi-trailer axles 183

5.2 Minimum clearances for Hope anti-jack-knife installation 187

5.3 The correct brake chamber push rod length and slack adjuster position for the brakes fully released 190

A1 Free body diagram for pseudo-dynamic fully distributed load analysis 214

A2 Load transfer within the suspension during braking 217

A3 Suspension hanger moments 220

A4 Skewed load distribution 221

A5 Longitudinal loading on chassis I-beams during braking 228

A6 Bolt holes nearest to position of maximum bending moment 238

A7 Main chassis I-beam cross-section at the king pin 243

A8 Torsion tube bolt pattern at 2000 mm from the king pin 246

A9 Chassis I-beam cross section at foremost landing leg mounting bracket weld 251

A10 Chassis I-beam cross-section at the rearmost upper coupler cross-member 254

A11 Unsupported flange and web heights 260

A12	Values of m to give slenderness ratios for local buckling of shapes	262
A13	Fatigue stress parameters	265
A14	Classification of structural members	271
A15	Fatigue curves relating cycles to failure to mean and alternating stresses	272
A16	Curves relating maximum stress, stress ratio and number of cycles for class 1 members	273
A17	Curves relating maximum stress, stress ratio and number of cycles for class 3 members	274
A18	Curves relating maximum stress, stress ratio and number of cycles for class 4 members	275
B1	Main chassis I-beam nodes ('MEMBERS')	280
B2	Three axle suspension model ('LINKS/3')	282
B3	Suspension model for supports at foremost axle ('LINKS/F')	283
B4	Suspension model for supports at centre axle ('LINKS/C')	283
B5	Suspension model for supports at rearmost axle ('LINKS/R')	284
B6	Suspension model for supports at foremost and centre axle ('LINKS/FC')	284

C1	Typical loading configuration on portion of the side rail	312
C2	Outrigger/torsion tube structure	313
C3	Loading and deflection diagrams for a torsion tube loaded via an outrigger	314
C4	Deflected outrigger/torsion tube structure	315
C5	Combined cross-member/rubbing plate section	318
C6	Loading diagram for deck plank loaded at side rail	319
C7	Support node positions for the analysis of the outrigger/side rail structure	321
C8	Bending moment sign convention for continuous beam program	322
C9	Approximated deck plank section	331
C10	FBD of deck plank loaded at centre	332
C11	Torsionally deflected semi-trailer chassis viewed from rear	337
C12	Main chassis I-beams in deflected position (exaggerated) as viewed from side	338
C13	Bending moments and shear forces on the ends of the torsion tubes resulting from the torsional twisting of the chassis	340
C14	Chassis I-beams approximated as stepped beams	341

C15	Section through upper coupler support structure at king-pin	346
C16	Free body diagram of upper coupler structure for horizontal loading	347
C17	Contact area between 5th wheel and rubbing plate	350
C18	Plastic hinges at edge of upper coupler structure	351
D1	Resistance points P_1, P_2 and P_3	356
D2	General dimensions of bumper showing position of point P_1	357
D3	Free body diagram of bumper bar for 100 kN load at point P_2	359
D4	Free body diagram of bumper bar for 25 kN load at point P_3	364
D5	Load distribution on headboard	365
D6	Shear force and bending moment diagrams for headboard inner members	366
D7	Shear force and bending moment diagrams for horizontal headboard member	369
D8	Headboard channel welds	370
D9	2-g support slam condition	371
D10	Landing leg mounting bracket	373
D11	Landing leg rearward brace	376

D12	Landing leg cross braces	381
D13	Free body diagram of landing leg cross member	385
D14	Free and fixing moment diagrams of landing leg cross member	386
D15	Total bending moment diagram of landing leg cross member	387
D16	Weld cross section at landing leg cross member flanges	389
E1	Strength of fillet welds for AA 5356 filler alloy	403
F1	Load-sensing valve ratio as a function of tri-axle bogie load	413
F2	Design curves for 'Firestone' IT15-9 air bag used on 'Fruehauf T' air suspension	414
F3	'Wabco' automatic load-sensing valve (model 475 700 220 0)	415
F4	Nomogram I for 'Wabco' load-sensing valve	417
F5	Nomogram II for 'Wabco' load-sensing valve	418
F6	Spring force curve for Type 24/30 spring brake	420
F7	Maximum gradient for trailer park brake	421
F8	Simplified schematic representation of semi-trailer service brake system	423
G1	Relevant dimensions for truck-tractor/semi-trailer load distribution analysis	429

LIST OF TABLES

Table		Page
3.1	Average vibration frequency test results	21
4.1	Typical dynamic acceleration factors for highway vehicles	49
A1	Longitudinal loading distribution for main chassis I-beams	229
A2	Longitudinal direct stress distribution (Case 1 loading)	231
A3	Maximum transverse shear stress distribution (neutral axis - Case 1 loading)	232
A4	Extreme fibre bending stress distribution (Upper flange - Case 1 loading)	233
A5	Distributions of principal stresses, principal shear stress and Von Mises stress at the extremne fibres of the upper flange (Case 1 loading)	234
A6	Distributions of principal stresses, principal shear stress and Von Mises stress at the web/flange joint above the neutral axis (Case 1 loading)	235
A7	Distributions of principal stresses, principal shear stress and Von Mises stress at the main I-beam welds above the neutral axis (Case 1 loading)	236
A8	Web buckling strength distribution	263

A9	Fatigue stresses at extreme fibres of tension flange at node 9	266
A10	Fatigue stresses at lower beam welds at node 9	266
A11	Fatigue stresses at lower torsion tube bolt hole at 2 109 mm from king-pin	267
A12	Normal distribution of fatigue stress cycles	268
A13	Constant amplitude cycles to failure at extreme fibres of tension flange at node 9	276
A14	Constant amplitude cycles to failure at main beam welds at node 9	276
A15	Constant amplitude cycles to failure at bolt hole 2 109 mm from king-pin	277
C1	Support node flexibilities for the outrigger/side rail analysis	323
C2	Bending moment, reaction and deflection results for the side rail for load case 1	324
C3	Bending moment, reaction and deflection results for the side rail for load case 2	325
C4	Bending moment, reaction and deflection results for the side rail for load case 3	326
C5	Bending moment distribution for deck plank loaded at centre	333

E1 Weld parent alloy combinations and filler alloys 402

E2 Nut and bolt proof loads 405

E3 Bolt tightening torques 405

F1 Suspension air-bag pressures for laden and unladen conditions 415

G1 Truck-tractor data 436

G2 Maximum GCM and payload 437

G3 Results for Case A weight distributions 438

G4 Results for Case B weight distributions 439

G5 Results for Case C weight distributions 440

H1 Permissibile deviation for non-toleranced machined dimensions 442

H2 Permissible deviation for non-toleranced fabrication dimensions 442

LIST OF GRAPHS

Graph		Page
3.1	Mean dynamic axle loads recorded during the suspension equalization testing of the Henred Fruehauf PET trailer (Freeway at approx. 75 km/h)	23
3.2	Average maximum percentage load variation recorded during the suspension equalization testing of the Henred Fruehauf PET trailer (Freeway at approx. 75 km/h)	24
3.3	Data logging at ten points per cycle for a vibration cycle represented by a sine wave	27
4.1	Shear force distribution on main chassis I-beam (Case 1 loading)	55
4.2	Bending moment distribution on main chassis I-beam (Case 1 loading)	56
4.3	Deflection diagram for main chassis I-beam (Case 1 loading)	57
4.4	Longitudinal loading distribution on main chassis I-beam (Case 1 loading)	58
4.5	Shear force distribution on main chassis I-beam (Case 2 loading)	59
4.6	Bending moment distribution on main chassis I-beam (Case 2 loading)	60
4.7	Deflection diagram for main chassis I-beam (Case 2 loading)	61

4.8 Shear force distribution on main chassis I-beam (Case 3 loading) 62

4.9 Bending moment distribution on main chassis I-beam (Case 3 loading) 63

4.10 Deflection diagram for main chassis I-beam (Case 3 loading) 64

4.11 Shear force distribution on main chassis I-beam (Case 4 loading) 65

4.12 Bending moment distribution on main chassis I-beam (Case 4 loading) 66

4.13 Deflection diagram for main chassis I-beam (Case 4 loading) 67

4.14 Shear force distribution on main chassis I-beam (Case 5 loading) 68

4.15 Bending moment distribution on main chassis I-beam (Case 5 loading) 69

4.16 Deflection diagram for main chassis I-beam (Case 5 loading) 70

4.17 Shear force distribution on main chassis I-beam (Case 6 loading) 71

4.18 Bending moment distribution on main chassis I-beam (Case 6 loading) 72

4.19 Deflection diagram for main chassis I-beam (Case 6 loading) 73

4.20 Shear force distribution on main chassis I-beam (Case 7 loading) 74

4.21 Bending moment distribution on main chassis I-beam (Case 7 loading) 75

4.22 Deflection diagram for main chassis I-beam (Case 7 loading) 76

4.23 Longitudinal direct stress distribution (Case 1 loading) 77

4.24 Maximum transverse shear stress distribution (Neutral axis - Case 1 loading) 78

4.25 Extreme fibre bending stress distribution (Upper flange - Case 1 loading) 79

4.26 Principal stress distribution at the extreme fibres (Upper flange - Case 1 loading) 80

4.27 Principal shear stress distribution at the extreme fibres (Upper flange - Case 1 loading) 81

4.28 Von Mises stress distribution at the extreme fibres (Upper flange - Case 1 loading) 82

4.29 Principal stress distribution at the web/flange joint above the neutral axis (Case 1 loading) 83

4.30 Principal shear stress distribution at the web/flange joint above the neutral axis (Case 1 loading) 84

4.31 Von Mises stress distribution at the web/flange joint above the neutral axis (Case 1 loading) 85

4.32	Principal stress distribution in the main I-beam welds above the neutral axis (Case 1 loading)	86
4.33	Principal shear stress distribution in the main I-beam welds above the neutral axis (Case 1 loading)	87
4.34	Von Mises stress distribution in the main I-beam welds above the neutral axis (Case 1 loading)	88
4.35	Buckling strength distribution for main chassis I-beams	95
4.36	Bending moment distribution on semi-trailer side rail (Loadcase 1)	105
4.37	Support reaction distribution on semi-trailer side rail (Loadcase 1)	106
4.38	Nodal deflection diagram for semi-trailer side rail (Loadcase 1)	107
4.39	Turning radius versus maximum required tracking angle for various semi-trailer steering configurations	125
4.40	Turning radius versus articulation angle for various semi-trailer steering configurations	126
4.41	Turning radius versus off-tracking dimension for various semi-trailer steering configurations	127
A1	Buckling diagram for Anticorodal - 112 aluminium alloy	259
A2	Normal distribution of fatigue stress cycles	269
D1	Buckling diagram for D55S-TF aluminium alloy	378

F1 Braking compatibility curve - Laden 411

F2 Braking compatibility curve - Unladen 412

LIST OF PHOTOGRAPHS

Photograph		Page
1.1	Light-weight aluminium platform semi-trailer	3
1.2	Aluminium semi-trailer viewed from front	4
1.3	Aluminium semi-trailer viewed from rear	4
5.1	'Cloos' shielded arc automatic MIG welding machine (Type GLC 353 PA)	142
5.2	'Messer Griesheim' motor hand welding torch and 'Cloos' wire feeding device	143
5.3	Chamfer at front of chassis I-beams for rubbing plate lead-in	144
5.4	Drilling of torsion tube and suspension mounting bolt holes	145
5.5	Magnetic base pillar drill on drilling platform	146
5.6	Landing leg mounting bracket	146
5.7	Landing leg rearward brace bracket	147
5.8	Assembly of torsion tubes onto first chassis I-beam	148
5.9	Torsion tube tacked to flange	148
5.10	Second chassis I-beam assembled onto torsion tubes	149
5.11	Landing leg cross-member tacked to flange	150

5.12	Torsion tube cleaned and ready for welding to flange	150
5.13	Foremost axle suspension hanger mounting outer bracket components assembled onto welding jig	152
5.14	Foremost axle suspension hanger mounting outer bracket components tacked into position	152
5.15	Pre-heating of suspension mounting components before welding	153
5.16	Rearmost axle suspension air bag mounting cross-member components assembled onto welding jig	153
5.17	Rearmost axle suspension hanger and air bag mounting cross-members	154
5.18	Suspension hanger mounting cross-member assembly after cleaning and grinding of welds	154
5.19	Suspension air bag mounting outer bracket after cleaning and grinding of welds	155
5.20	Upper coupler cross-member welded to chassis I-beam	156
5.21	Chassis turned over to complete welding on underside of upper coupler assembly	157
5.22	Chassis turned over to complete welding on underside of suspension mounts, etc.	157
5.23	Assembly and welding jig for outriggers	159
5.24	Four degree tapered section outriggers assembled onto chassis I-beams	159

5.25	Upper coupler outrigger tacked to chassis I-beam	160
5.26	Side rail being assembled onto outriggers	161
5.27	Side rail positioned and tacked to outriggers	161
5.28	Outer portions of rear end rails positioned and tacked to side rails	162
5.29	A hydraulic jack used to assist with levelling of the side rail and end rail structure	163
5.30	Welding and grinding of side rail and end rail structure	164
5.31	Deck planks being mounted from the foremost deck plank rearward	165
5.32	Deck planks being mounted towards the rear of the chassis	166
5.33	Deck planks clamped to the top flange of chassis I-beam by means of deck clamp brackets	166
5.34	Deck planks bolted to side rail	167
5.35	Completed deck mounting viewed from underneath	167
5.36	Front deck cover angles being welded to foremost deck plank and front rail	168
5.37	Mounting of wooden rubbing strake	168
5.38	Rear under-ride bumper	169
5.39	Loading of the completed chassis onto a semi-trailer	170

5.40	Completed aluminium trailer chassis leaving I.R. & D. for UWtec	170
5.41	Landing legs mounted to chassis	171
5.42	Landing leg crank bracket	172
5.43	Clamp plate assembly for FIA steering axle	173
5.44	Clamp plate assembly and shock absorber bracket welded to FIA steering axle	174
5.45	Clamp plate assembly and shock absorber bracket welded to Propar fixed axle	174
5.46	Rubber gasket inserted between suspension mount and hanger assembly	176
5.47	Z-pressing cross brace welded to inner face of suspension hanger	176
5.48	View of suspension hanger showing trailing arm and pivot pin assembly	177
5.49	Suspension air bag assembled onto air bag mounting plate	178
5.50	Air bag and mounting plate bolted to suspension air bag mounting cross-member	178
5.51	Propar axle mounted onto suspension trailing arm	179
5.52	FIA steering axle mounted onto suspension trailing arm	180
5.53	FIA steering axle and suspension assembly	180

5.54	Michelin 16.5 R 22.R super single tyres on steel single piece rims	181
5.55	Suspension levelling valve mounted onto chassis	182
5.56	Shock absorber fitted between brackets on axle clamp plate and suspension hanger	184
5.57	First eight deck planks removed to reveal upper coupler assembly	185
5.58	Hope anti-jack-knife device bolted to rubbing plate	186
5.59	Hope anti-jack-knife control valve mounted in close proximity to Hope device	187
5.60	Type 24/30 spring brake chamber fitted to Propar fixed axle	188
5.61	Type 24/30 spring brake chamber fitted to FIA steering axle	189
5.62	Wabco automatic load sensing valve mounted to underside of deck	191
5.63	Relay valve and brake system reservoir mounted to underside of deck	192
5.64	Auxiliary pneumatic circuit pressure control valves mounted to underside of deck	192
5.65	Emergency and service line filters mounted to underside of deck above rear of rubbing plate	193
5.66	Emergency and service line suzies mounted through front plate	174

5.67	Dummy fittings on headboard for stowage of brake suzies	194
5.68	Rubber pneumatic hoses used on axles	195
5.69	View of rear of semi-trailer showing lights and retro-reflectors	197
5.70	Reversing buzzer mounted on inside of rear end rail	197
5.71	Retro-reflector and side marker and direction indicator light mounted below side rail	198
5.72	Retro-reflector and side marker and direction indicator light mounted at rear of trailer	199
5.73	Two core electrical supply cable clipped to underside of deck next to side rail	200
5.74	Electrical supply cable clipped to rear of side marker light bracket	201

LIST OF SYMBOLS

Symbol	Description
a	Width of unsupported flange.
A	Area; cross-sectional area; distance.
b	Fatigue strength exponent; height of I-section measured to medians of flanges; distance.
B	The number of blocks of test data required to cause fatigue failure; distance.
$B; D$	Buckling constants.
c	Fatigue ductility exponent.
C	Distance
CA	Available swing clearance behind truck-tractor cab.
d	Length; length of thin rectangular strip.
d_0	Nominal diameter.
d_{ax}	Axle spread on semi-trailer.
d_m	Major diameter.
d_r	Minor diameter.
D	Cumulative damage ratio.
D_x	Truck-tractor 5th wheel position.
e	Base of natural logarithms.
E	Young's modulus of elasticity.
f_D	Flexibility of deck plant structure.
f_i	Support flexibility at node i.
f_{OR}	Flexibility of outrigger/torsion tube structure.

f_t	Total braking force per unit pressure at the road surface for the full semi-trailer.
F	Force; preload.
F_{max}	Maximum value of force F.
F_k	Braking force at the road surface for the tyres on a semi-trailer axle.
F'_k	Braking force on the suspension hangers of a semi-trailer axle at the trailing arm pivot positions.
F_l	Longitudinal force on semi-trailer chassis I-beams.
$F_{p,r}$	Brake chamber push rod force.
F_s	Brake chamber spring force.
F_t	Total braking force at the road surface for the full semi-trailer.
$F(x)$	Function of variable x.
g	Gravitational acceleration (9,81 m/s^2).
G	Modulus of rigidity.
h	Height.
h_1	Height of centre of gravity of semi-trailer payload and tare mass above the ground level.
h_2	Height of centre of gravity of semi-trailer payload and tare mass above the rubbing plate.
i	Periodic interest rate expressed as a fraction.
I	Second moment of area.
I_c	Second moment of area of the combined upper coupler cross-member/rubbing plate structure.
I_D	Second moment of area of deck plank cross-section.
I_0	Second moment of area of outrigger cross-section.

I_t	Second moment of area of torsion tube cross-section.
I_y	Second moment of area about the y-axis.
J	Polar moment of area.
k	Radius of gyration.
k_c	Braking compatibility curve correction factor for the laden semi-trailer.
k_D	Stiffness of deck plank structure.
k_i	Support stiffness at node i.
k_{OR}	Stiffness of outrigger/torsion tube structure.
k_v	Braking compatibility curve correction factor for the unladen semi-trailer.
ℓ	Length.
ℓ_1	Length 1.
ℓ_2	Length 2.
ℓ_b	Length of semi-trailer chassis I-beams.
ℓ_t	Overall length of semi-trailer.
L_1	Adjustment length for load sensing valve spring.
L_2	Adjustment length for load sensing valve hex screw.
L_3	Adjustment length for load sensing valve hex screw.
m	Buckling coefficient.
M	Bending moment.
M'	Fixing moment.
M_H	Suspension hanger moment.
M_{max}	Maximum bending moment.

M_p	Plastic moment.
$M(x)$	Bending moment distribution function.
M_y	Bending moment about the y-axis.
n	Number of compounding periods.
n_i	Number of fatigue cycles at a particular stress amplitude and mean stress for the ith count group.
(n_i/N_i)	Damage ratio for the ith set of conditions.
N	Number of fatigue cycles
N_1	Dynamic reaction at semi-trailer king-pin.
N_2	Total dynamic reaction at semi-trailer tyres.
$N_2{}'$	Total dynamic reaction at semi-trailer suspension mounting.
N_A	Dynamic reaction at the suspension air bag mountings of a semi-trailer axle.
N_{AX}	Dynamic reaction at the tyres of a semi-trailer axle.
$N_{AX}{}'$	Dynamic reacton at the suspension mountings of a semi-trailer axle.
N_f	The number of cycles to fatigue failure.
N_H	Dynamic reaction at the suspension hanger mountings of a semi-trailer axle.
N_i	Number of fatigue cycles to crack initiation at the ith set of conditions.
OT	Off-tracking dimension.
p	Thread pitch.
p_0	Maximum operating pressure of service brake system.
p_i	Pressure in brake system after the ith application of the service brakes.

P	Force.
P_c	Buckling load.
P_e	Euler buckling load.
P_{OR}	Applied load on end of outrigger.
P_t	Gross weight of the semi-trailer.
P_v	Weight of the semi-trailer chassis plus payload
PMT	Periodic payment.
PV	Present value.
r	Radius; rolling radius of semi-trailer tyre.
r_b	Turning radius of the truck-tractor rear axle bogie measured to the longitudinal centre line of the truck-tractor.
r_f	Turning radius of the truck-tractor steering axle measured to the longitudinal centre line of the truck-tractor
r_{fr}	Turning radius of the outboard steering axle tyre on the truck-tractor; Turning radius of truck-trailer combination.
r_k	Turning radius of the semi-trailer king-pin.
r_{max}	Maximum radius.
r_t	Turning radius of the semi-trailer axle bogie measured to the longitudinal centre line of the semi-trailer.
R	Stress ratio.
R_1	Static reaction at semi-trailer king-pin.
R_2	Total normal static reaction of the road surface on the wheels of the semi-trailer.
$(R_2)_{max}$	Value of R_2 at the maximum weight of the semi-trailer.

P	Force.
P_c	Buckling load.
P_e	Euler buckling load.
P_{OR}	Applied load on end of outrigger.
P_t	Gross weight of the semi-trailer.
P_t'	Weight of the semi-trailer chassis plus payload
PMT	Periodic payment.
PV	Present value.
r	Radius; rolling radius of semi-trailer tyre.
r_b	Turning radius of the truck-tractor rear axle bogie measured to the longitudinal centre line of the truck-tractor.
r_f	Turning radius of the truck-tractor steering axle measured to the longitudinal centre line of the truck-tractor
r_{fr}	Turning radius of the outboard steering axle tyre on the truck-tractor; Turning radius of truck-trailer combination.
r_k	Turning radius of the semi-trailer king-pin.
r_{max}	Maximum radius.
r_t	Turning radius of the semi-trailer axle bogie measured to the longitudinal centre line of the semi-trailer.
R	Stress ratio.
R_1	Static reaction at semi-trailer king-pin.
R_2	Total normal static reaction of the road surface on the wheels of the semi-trailer.
[illegible]	the maximum weight of

$(R_2)_s$	Value of R_2 corresponding to a load-sensing ratio of unity.
R_2'	Total static reaction at the semi-trailer suspension mounting.
R_s	Support reaction.
R_A	Static reaction at the suspension air bag mountings of a semi-trailer axle.
R_{AX}	Static reaction at the tyres of a semi-trailer axle.
R_{AX}'	Total static reaction at the suspension mountings of a semi-trailer axle.
R_s	Support reaction.
R_H	Static reaction at the suspension hanger mountings of a semi-trailer axle.
R_i	Support reaction at node i.
R_L	Static reaction at the semi-trailer landing legs.
R_s	Static reaction at the truck-tractor steering axle.
R_t	Static reaction at the truck-tractor tandem bogie.
$\%RA$	Percentage reduction in area that results from a simple tensile test.
s	Standard deviation.
S	Swing clearance between semi-trailer headboard and truck-tractor cab.
t	Thickness.
t_1	Flange thickness.
t_2	Web thickness.
T	Torque.

T_1	Torque on length 1.
T_2	Torque on length 2.
T_b	Braking torque on a semi-trailer axle.
T_f	Truck-tractor steering axle track.
T_s	Torque on semi-trailer foundation brake s-cam shaft.
T_t	Semi-trailer axle track.
v	Distribution variable.
V	Shear force.
V_c	Total volume of air in service brake chambers.
V_r	Total volume of service brake system reservoirs.
$(V_r)_{min}$	Minimum value for V_r.
V_s	Total volume of air in service brake system air lines.
V_t	Total volume of air in service brake system.
$V(x)$	Shear force distribution function.
W_{AX}	Weight of running gear for one axle.
WB	Truck-tractor wheelbase.
WS	Semi-trailer wheelbase.
x	Co-ordinate; distance; general function variable.
$\bar{x}$	Centroidal distance.
y	Co-ordinate; deflection.
y'	Deflection due to rotation.
y''	Deflection due to bending.
$\bar{y}$	Centroidal distance.
y_i	Vertical deflection of node i.

y_{max}	Maximum distance to extreme fibres measured from the neutral axis.
$y(x)$	Deflection distribution function.
x	Co-ordinate; braking ratio.
α	Articulation angle of truck-tractor/semi-trailer combination.
β	Angle.
γ	Inclination.
δ	Vertical distance between tangential intercepts.
ϵ	Strain.
$\Delta\epsilon$	Total strain range.
ϵ_1	Maximum principal strain.
ϵ_2	Minimum principal strain.
ϵ_e	Elastic strain.
$\Delta\epsilon_e$	Elastic strain range.
ϵ'_f	Fatigue ductility coefficient.
ϵ_p	Plastic strain.
$\Delta\epsilon_p$	Plastic strain range.
θ	Tracking angle of semi-trailer steering axles; angle.
Θ	Angle of twist.
λ	Slenderness ratio.
μ	Mean.
ν	Poisson's ratio.
σ	Stress.
$\Delta\sigma$	Total stress range.

$\sigma_{0,2}$	0,2% Proof stress.
σ_1	Principal stress; Maximum principal stress for plane stress.
σ_2	Principal stress; Minimum principal stress for plane stress.
σ_3	Principal stress.
σ_{alt}	Alternating stress.
σ_b	Bending stress.
$(\sigma_b)_{max}$	Maximum bending stress.
σ_B	Bearing stress.
σ_c	Buckling strength.
σ_d	Direct stress.
σ_e	Endurance limit.
σ_f'	Fatigue strength coefficient.
σ_l	Longitudinal direct stress.
σ_m	Von Mises equivalent stress.
σ_{max}	Maximum stress.
σ_{mean}	Mean stress.
σ_{min}	Minimum stress.
σ_{UTS}	Ultimate tensile strength.
σ_x	x-direction stress.
σ_y	y-direction stress.
σ_{yc}	Compressive yield strength.
σ_{yi}	Yield strength.
σ_{yt}	Tensile yield strength.

τ	Shear stress.
τ_{max}	Maximum shear stress.
τ_p	Principal shear stress.
τ_{ULT}	Ultimate shear strength.
τ_{yi}	Shear yield strength.
ϕ	Angle, angle of twist.
ϕ_1	Angle of twist for length 1.
ϕ_2	Angle of twist for length 2.
ϕ_{total}	Total angle of twist.
Ψ	Change in slope angle of elastic curve.
ω_m	Maximum value of distributed load for pseudo-dynamic load distribution.
ω_n	Minimum value of distributed load for pseudo-dynamic load distribution.
ω_s	Uniformly distributed load for the static load distributions.
∞	Infinity.

CHAPTER 1

INTRODUCTION

1.1 General

Rising fuel prices over the past decade have led to substantial increases, both internationally and locally, in general transport operating costs. In the industrialised nations of Europe and America this has resulted in increased interest in light-weight vehicle designs in order to increase payloads within the bounds of strictly applied legislation.[1-3]

In South Africa considerable increases in wage costs in recent years, in addition to fuel price rises, have further exacerbated escalating transport costs, yet interest in light-weight vehicles has been rather slower to develop. This is mainly due to widespread overloading.[1,4] However, as overloading penalties become more severe and more stringently applied, interest in mass saving vehicle designs has begun to grow.

In response to these trends a semi-trailer research and development programme was initiated at the University of the Witwatersrand's Technology Centre (UWTec) at Frankenwald during 1982, with the aim of working together with industry in the development of trailer design technology. More specifically, the initial programme objectives were:

- the development of appropriate design models for different types of trailer (eg. platform trailers, van trailers).
- the recording of road loading data and component stresses in actual and simulated field usage.
- the assessment of different trailer construction methods and alternative construction materials.

As a pilot project, the design, construction, and development of a light-weight, all aluminium platform semi-trailer was begun during 1983. This project was to follow two distinct phases, viz:

Phase I : The development of a design model, structured in such a way as to interface with the procedures of Phase II, in conjunction with certain initial testing on similar trailers. The detailed design and construction of the semi-trailer.

Phase II: The recording of load and stress histories at various points on the semi-trailer, resulting from road-induced vibrations during simulated and actual field service. These results would then be compared with the inputs to the design model and the original assumptions refined.

This dissertation covers all aspects of phase I of the project and presents a high speed data acquisition system which was developed for use in phase II. In addition, a methodology for endurance testing of the semi-trailer is proposed and discussed together with the theoretical foundation upon which it is based.

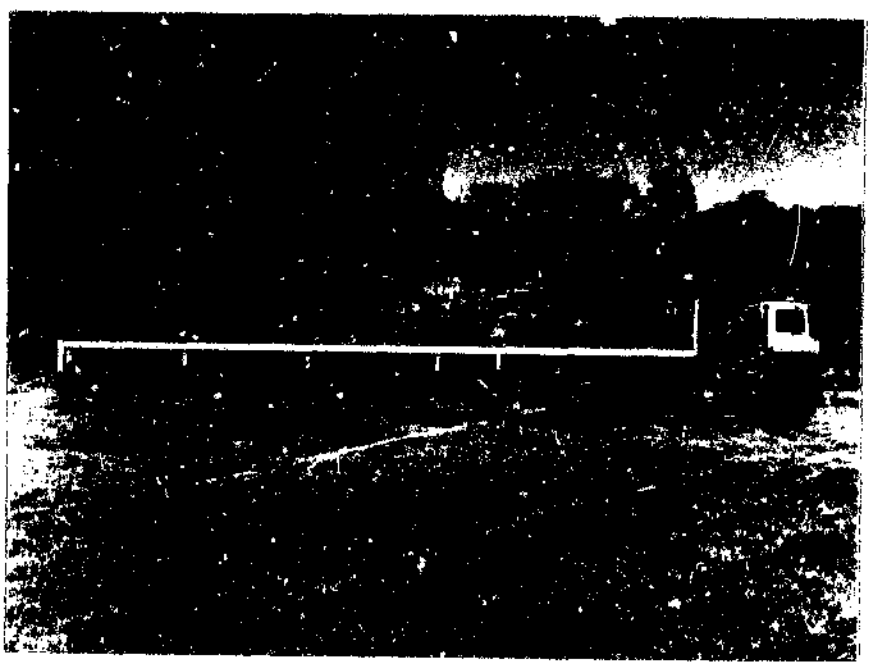
The three main objectives of this study are thus:

- To contribute to the setting up of a semi-trailer research and development programme at UWTec through the completion of this pilot project.
- To propose a methodology for platform semi-trailer design and for subsequent endurance testing, and to use this design model to design a light-weight platform semi-trailer, and to construct the semi-trailer.
- To demonstrate the practicality and suitability of aluminium for light-weight semi-trailer design.

The all aluminium platform semi-trailer designed and constructed in this

project is shown in Photographs 1.1 to 1.3. The basic chassis structure is of a 'ladder' type construction comprising two longitudinal beams running the full length of the trailer and spaced apart at intervals by torsion tube cross-members. Much of the chassis structure and sub-structure was constructed as a series of sub-assemblies and then bolted together. This was done mainly to limit the need for large size assembly jigs and to minimise joint stresses.

The two main chassis I-beams, as well as the floor planks, were manufactured in Switzerland by Schweizerische Aluminium AG (Alusuisse), Zűrich, and then shipped to South Africa. This was because no suitable extrusion dies were available in South Africa for either the I-beam T-section flanges or the deck planks, and because of certain limitations locally in extruding the T-flanges to the necessary lengths. The remainder of the aluminium construction material was supplied by Huletts Aluminium Ltd, South Africa.



Photograph 1.1 Light-weight aluminium platform semi-trailer



Photograph 1.2 Aluminium semi-trailer viewed from front



Photograph 1.3 Aluminium semi-trailer viewed from rear

The overall dimensions of the semi-trailer were selected so as to achieve the maximum payload and maximum practical deck area within the bounds of current legislation (refer Figure 2.1, Chapter 2). Bridge formula restrictions[8] necessitated the use of a wide spread tridem axle configuration, with the foremost and rearmost axles being self-tracking axles, in order to prevent severe tyre scuff. The self-tracking axles were manufactured by FIA of Verona, Italy and supplied by Henred Fruehauf Trailers (Pty) Ltd, together with the Henred Fruehauf Propar 11000 fixed axle and the Fruehauf T air suspension.

Super single tyres mounted on single piece rims were fitted in order to further reduce tare mass and to enhance the roll stability of the semi-trailer. These were supplied by Michelin Tyres. The braking equipment and lights were supplied by Diesel Electric SA (Pty) Ltd and Motolek (Pty) Ltd, respectively.

All component parts for the construction of the semi-trailer were manufactured by the University's School of Mechanical Engineering Laboratory. The construction of the aluminium chassis itself, as well as all aluminium ancillary structures (eg. headboard, under-ride bumper, etc.) took place at Industrial Research and Development (Pty) Ltd in Boksburg North, under the supervision of the author. All aluminium welding was contracted to I R and D. Once completed the chassis was transported to UWTec where the running gear (ie. suspension, axles, and wheels), the landing legs and the king-pin were mounted, and the braking system and lights installed.

The design methodology proposed in this study is based on dynamic accelerations in the longitudinal, vertical, and transverse directions, and is referred to throughout this dissertation as a pseudo-dynamic loading design approach. This approach is adopted since it allows for direct comparison between design loading data and loading data recorded during testing stages. In this way experience gained through testing and through field service is easily incorpo-

rated in future design stages and the accuracy of the original design model improved. Although this study concentrates mainly on the structural design of the trailer chassis and associated structure, a number of aspects relating to the running gear and the braking and electrical systems are also discussed. Particular attention has been paid to safety related features, especially in the areas of lights, braking, and jack-knife prevention.

Aluminium, or more specifically aluminium alloy, was chosen as the principal chassis construction material rather than the more usual steel, mainly because of its superior strength-to-weight ratio. The use of high strength steels (ie. higher yield strength than those typically used in trailer construction at present) in order to reduce tare mass, was not considered since, taking into account the welding configuration typical in trailer chassis construction, the high strength steel grades offer no advantage because once welded they have the same fatigue life expectancy as welded mild steel.[6–8] Furthermore, the high strength steel grades are not generally available in suitable sections (eg. flat bar) for semi-trailer construction.

The principal advantages of aluminium for vehicle construction are:

- High strength-to-weight ratio – aluminium alloys are approximately 2,9 times lighter than steel and, after heat treatment, have proof stresses typically of 240 MPa to 350 MPa.[7,9,10] Aluminium chassis tare masses are thus lighter and allow greater payloads to be carried. For loads below the vehicle's maximum payload (and hence GVM), reduced tare mass contributes to savings in operating costs, particularly in the area of fuel and tyres.
- Excellent corrosion resistance – This results in reduced maintenance, especially when operating in coastal areas. Care must, however, be taken when mixing materials, for example in the use of steel bolts, to prevent

electrolytic corrosion.

- Extrudability – By using extruded T-sections in conjunction with plate material to form the main chassis I-beams, the fatigue sensitive weld region can be operated at a lower stress level than the main flanges. This means that the maximum design stress may be 20 to 40 percent more than the fatigue design stress at the weld. Furthermore, intricate shapes for particular applications can be extruded in one piece since cross-section design possibilities are almost unlimited.

- Good impact resistance – The ability to absorb impact (ie. shock) loads is the function of the strain energy resulting from deformation of the structure which, in turn, is inversely proportional to the elastic modulus. For a given impact load, and provided no stress exceeds the elastic limit, aluminium will be stressed to a value of 60 percent of that created in a similar steel component.[9,11]

- Superior vibration characteristics – The modulus of elasticity of aluminium alloy is about one third of steel and, although the beam section required for an aluminium chassis will be larger, it is likely that the product EI will be less. An aluminium chassis will thus deflect more and have lower frequencies of vibration than a steel one of equivalent strength. Provided none of these frequencies coincide with suspension natural frequencies, the slightly softer ride will tend to reduce the amplitudes of peak stresses and the lower vibration frequencies will contribute to fatigue life. Excessive chassis deflection under load may be counteracted by building a positive camber into the chassis beams.

- Ease of fabrication – Aluminium can be formed, pierced, machined, sawn, and sheared at high operating speeds using conventional equipment. The weldability of aluminium is good and with the gas shielded electric arc process, welding speeds are high and distortion is low. Stress relieving

after welding is not necessary.

- High scrap value – Because aluminium can always be recycled it has traditionally commanded a high scrap value. Recycling involves only one melting and refining process, in contrast to steel which requires resmelting.

In Chapter 2, a detailed specification of all aspects of the light-weight aluminium semi-trailer design is presented together with a weight distribution based on the actual semi-trailer tare.

Chapter 3 begins with a general discussion of vehicle structural and endurance testing and then goes on to describe certain initial trailer testing undertaken by the author, as well as a high speed computer data acquisition system developed for recording vibration data. Finally, a methodology for endurance testing and fatigue life prediction is proposed and discussed, together with the theoretical foundation upon which it is based.

An evaluation of the design of the semi-trailer follows in Chapter 4, whilst Chapter 5 discusses the construction phase. Finally, Chapter 6 draws certain conclusions with regard to the initial project objectives and makes recommendations for future work. All design analyses, material specifications, and engineering drawings are contained in the appendices at the end of the dissertation.

1.2 Aluminium semi-trailers – Historical perspective and current status

In Europe the use of aluminium for trailer chassis construction and in particular semi-trailers, is most widely practised in France, Germany, and Switzerland.[7,12–14] Since the first vehicles of this type were built in the

mid-1960s, more than 5 000 trailers and semi-trailers have been produced with aluminium chassis frames.[12] The majority of these were fitted with tipping bodies while the rest were used with platform or van body-work, or as low loaders and timber carriers. The longitudinal members of the first aluminium chassis were fabricated using flat bar sections for the flange and aluminium plate for the web. Towards the end of the seventies large T-section flange extrusions were developed, in order to achieve better utilisation of the admissible bending stresses of the non-welded material within the fatigue resistance limits.

Many of these second generation vehicles have proved themselves in operating practice, as confirmed by some very high vehicle mileages, and have yielded considerable cost benefits for their owners. Ut.[2] presents an aluminium to steel cost comparison for a Swiss designed and operated, aluminium chassied semi-trailer, travelling 100 000 km a year, where a 750 kg saving in tare mass resulted in an amortization period of 22 months.

In the United Kingdom aluminium is used to a lesser extent as a chassis construction material[7] but there are a few companies who are producing aluminium trailers, and this trend is on the increase. A typical tare mass for a United Kingdom or European 12,5 metre tri-axle aluminium platform semi-trailer is in the region of 6 000 kg.[12,15]

Aluminium has also become reasonably popular in the trailer construction industry in the United States. This is mainly due to stringently enforced load legislation and rising fuel and general operating costs.[16] Consequently, a large number of the major trailer manufacturers in the USA offer a range of all aluminium or aluminium chassied trailers. Tare masses are in general lighter than Europe, with 4 500 kg being a typical tare of a 13,0 metre tandem

axle aluminium platform semi-trailer.[16–18]

In South Africa aluminium has not made much of a mark in the trailer construction industry, except possibly for trailer van body construction and, to a somewhat lesser extent, for tanker shells. To date only a small number of aluminium chassied trailers have been designed and built in this country, and most of these have been on a trial one-off basis. One such example is an all aluminium platform semi-trailer, built on the Reef in 1979 by T.F.M. (Pty) Ltd to a European design, and operated by Huletts Aluminium Ltd between Pietermaritzburg and the Reef.[19,20] The semi-trailer has the following specifications:

Length	9,150 m
Tare	3 300 kg
Mass saving over steel	1 750 kg
Gross vehicle mass	11 300 kg
Payload (max.)	8 000 kg
Truck-tractor tare	5 500 kg
Net cost (1979)	*R*12 500 – 00
Net cost steel equivalent	*R*7 500 – 00
Aluminium price premium	*R*5 000 – 00

In the first two years of service this vehicle travelled approximately 700 000 km and for some 75 percent of this time it was running at full capacity. It was always operated with the same mechanical horse, and hence, accurate comparative operating costs could be kept. Subsequent analysis[19] showed that, even after accounting for the initial aluminium price premium, the reduced trailer tare, and hence increased payload, resulted in a net saving in operating costs of over R5 500-00. A 12,5 metre tandem axle semi-trailer of similar construction has subsequently been built by T.F.M. (Pty) Ltd for Huletts Aluminium Ltd and has also demonstrated encouraging results.

More recently an all aluminium tandem axle platform semi-trailer has been developed by Trailite (Pty) Ltd of Pietermaritzburg, in association with Hulett Aluminium Ltd.[21,22] The prototype trailer was launched in August 1984 and had the following specifications:

Length	12,5 m
Tare	5 124 kg
Tare of steel equivalent	7 094 kg
Gross vehicle mass	25 876 kg
Payload (max.)	31 000 kg
Net cost (1984)	R38 000 – 00
Net cost steel equivalent	R23 000 – 00
Aluminium premium	R15 000 – 00

At that time a cost comparison between the prototype semi-trailer and its steel equivalent was undertaken based on the following assumptions:[22]

- When additional payload is carried it amounts to 60 percent of the 1 970 kg tare mass saving.
- Any additional payload is carried only on 75 percent of all trips.
- The route is Pietermaritzburg to Alrode and back, 514 km each way.
- Ten trips are made each week for 50 weeks of the year.
- The additional revenue accrued from carrying additional payload is at the rate of R64-00 per tonne per trip.

This analysis showed the payback period for the initial aluminium price premium under these conditions to be approximately eight and a half months. No account was taken of the additional savings in fuel, and in tyre and brake wear, et cetera, when the trailer is travelling lightly laden.

CHAPTER 2

DESIGN SPECIFICATIONS

2.1 General

Short concise notes presenting the salient details of the various components and structures of the aluminium semi-trailer chassis, as well as the running gear and ancillary equipment, are presented in this chapter in order to provide a detailed specification of the overall semi-trailer design. At the end of the chapter a schematic diagram is presented showing the weight distribution and actual tare mass achieved, as well as the overall dimensions of the trailer.

2.2 Semi-trailer specification

2.2.1 Chassis and ancillary structure

- Main chassis beams:
  Two I-section beams running the full length of the trailer at 1 060 mm centres. Fabricated from aluminium T-section extrusions (Anticorodal–112 alloy) incorporating 200 mm x 20 mm flanges welded to a 10 mm aluminium web plate (Anticorodal–100 alloy). The beam depth is 290 mm in the neck area, increasing to 600 mm from the landing leg position rearward. Transition area profiled so as to minimise reduction of strength whilst allowing sufficient clearance for the truck-tractor.
- Torsion tubes:
  Eight, 160 mm OD x 6 mm wall aluminium torsion tubes, bolted via 16 mm thick aluminium flanges to the main chassis beams. Designed to resist the torsional twisting of the chassis.
- Outriggers:
  Eight pairs of 100 mm square x 6 mm wall aluminium tubes, bolted via

16 mm thick aluminium flanges to the main beams at positions directly opposite each torsion tube position. Welded at the outboard end to the side rails.

- Front and rear rails and side rails:
  177,8 mm x 50,8 mm extruded aluminium channel. Chosen to resist rugged side and rear loading conditions.

- Platform decking:
  Sixty-nine extruded aluminium interlocking floor planks with a ribbed anti-skid load surface. Transversely mounted to provide load carrying capacity across the width of the trailer, thereby reducing the number of outriggers required. Foremost eight planks removable to facilitate servicing of the upper coupler and king-pin.

- Rubbing plate:
  15,9 mm thick aluminium rubbing plate reinforced with extra deep cross-members. Bolted to lower flanges of main chassis I-beams and removable from underneath for servicing.

- King-pin:
  'Hope' anti-jack-knife device incorporating a standard 50,8 mm SAE king-pin. Bolted to the rubbing plate from above by means of a 12,3 mm steel foundation plate.

- Headboard:
  Full width, 1 025 mm high aluminium headboard designed to provide adequate protection from moving loads. Bolted to front end of main chassis beams and side rails.

- Rear bumper:
  Aluminium rear under-run bumper with 2 300 mm long bumper bar. Designed to conform to the requirements of SABS 1055-1983.[23]

– Landing legs:

'Jost' JS60G two-speed, square leg, 50 000 kg static capacity landing legs with heavy duty sand shoes. Braced to withstand loading from any angle. Two side operation.

3.2.3 Suspension, axles and wheels

– Suspension:

Fruehauf T air-suspension incorporating shock absorbers for improved ride. Fabricated suspension hangers modified to suit the chassis beam height and bolted to chassis via 12 mm steel mounting flanges. Suspension ride height sensed relative to the centre axle by means of a suspension levelling valve mounted above that axle. 950 mm spring centres and 2 620 mm axle spacing.

– Self-steering axles:

'FIA' self-steering axles with hinged trailing arms and stub axles which produce a castor action steering effect. Adjustable tie rod connected between the two hinged arms and fitted with pneumatically controlled axle steer locking pin and damping air bellows. 133 mm OD tubular axle beam. 90 mm diameter journal with interchangeable inner and outer bearings.

– Fixed axle:

'Henred Fruehauf' Propar 11 000, 105 mm square axle beam. 90 mm diameter journal with interchangeable inner and outer bearings.

– Wheel rims:

One piece, 22.5 x 13.0, 10 stud, 15 degree drop centre steel rims with 10 mm central nave.

– Tyres:

'Michelin-double X', 16.5 R 22.5, 20 ply, tubeless radial super single tyres.

- **Mudflaps:**

  'Henred Fruehauf' anti-sail rubber mudflaps incorporating vertical grooves to reduce side spray.

2.2.3 Braking system

- **Brakes:**

  'Henred Fruehauf' Propar 420 x 180 'S' cam brake with inboard mounted drum. Conforming to SABS SV 1051 brake regulations.[24]

- **Braking system:**

  Pneumatic, single circuit, dual line, power braking system with load sensing. Spring actuated emergency and parking brake. Conforming to SABS SV 1051 regulations.

2.2.4 Electrical system and lights

- Electrical system:

  Dual DIN 7-pin socket, 12 volt system utilising chassis return.

- Lights:

  Triple combination stop and tail lights with separate direction indicator lights and twin reverse lights at the rear. Seven combination side marker and direction indicator lights down each side of the trailer.

2.3 Semi-trailer weight distribution

The semi-trailer weight distribution presented in Figure 2.1 is based on the measured tare mass and is thus termed the actual semi-trailer weight distribution. This is as opposed to the design weight distribution (refer Figure 4.1) used in all of the design analyses.

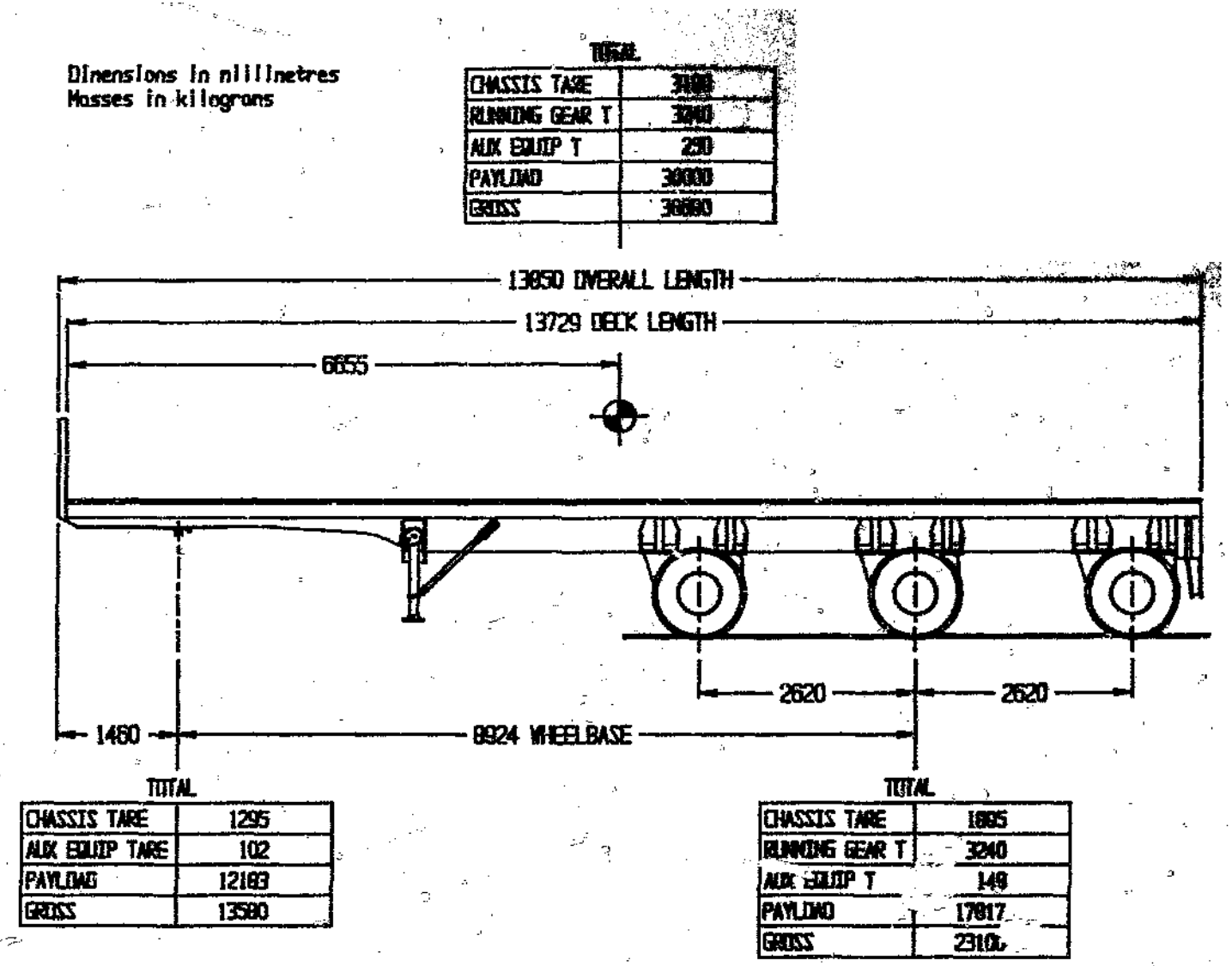


Figure 2.1 **Semi-trailer weight distribution and general dimensions**

CHAPTER 3

INITIAL TRAILER TESTS AND PROPOSED TESTING TECHNIQUES

3.1 General

In general terms, vehicle structural testing is conducted on heavy duty vehicles to assure the maintenance of structural integrity over the projected service life of the vehicle and under the conditions for which it is intended. More specifically, however, such testing is undertaken for a variety of reasons, each of which forms an integral part of the design and development of a new vehicle.

First of all testing is required to provide the designer with information on service loads and load histories, so that the designer can adequqately size and configure initial design components. At this stage this information is often obtained in the form of peak values and frequency distribution spectra of dynamic accelerations in the vertical, longitudinal, and transverse directions. This first step in the design process is at times difficult, since it requires that the initial testing be undertaken on a similar or earlier model to the proposed new vehicle. If the vehicle under consideration embodies previously untried concepts, as in the case of this design project, such background information may not be available or accurate and the best that can be done, especially in the case of loading spectra, is to make certain assumptions with regard to this data (refer Sections 4.2.4 and 4.3.5). The importance of this step cannot be over-emphasised since the accuracy of the design process will depend to a large extent on the definition of the loading on the vehicle structure. Great care must therefore be taken in the measurement and application of such data, and in matching the testing procedures to the projected service conditions of the proposed vehicle.

Static stress calculations are then performed utilising a design model which is structured in such a way as to allow easy interaction between design and testing. In this particular design these are referred to as the pseudo-dynamic stress calculations, to indicate that they refer to the expected peak dynamic loads. Initial fatigue life estimates are also calculated at this stage.

Finally, simulated in-service testing is performed on the prototype vehicle to ensure that peak stresses correlate sufficiently well with design values, and to check that the load spectra used in the initial life predictions are indeed valid. The initial life predictions are also further refined at this stage using the more accurate load histories obtained in these tests.

This last phase is generally known as endurance testing. Here it is extremely important to closely match the test programme to the expected service conditions in terms of the magnitudes and types of load to be carried, the driving cycles the vehicle will experience, and the roadways and surfaces over which it will travel. Certain special occurrences need also to be considered, even for a typical highway operation, and include relatively infrequent load producing actions such as tractor engagement to the trailer, docking manoeuvres, panic brake stops, and tight turns, as well as more frequent occurrences such as hitting a pothole or kerb.

Those aspects of this semi-trailer project which are related to the testing phases of the vehicle's development (refer Section 1.1) are discussed in this chapter. First of all, certain initial trailer testing is described, after which a high frequency data acquisition system, developed by the author for the recording of vibration data during vehicle testing, is presented. Finally, a methodology for endurance testing and fatigue life prediction is proposed and discussed together with the theoretical foundation upon which it is based. This last section is written in the form of a literature survey, and is included

since it relates to the data acquisition instrumentation discussed here and to the fatigue design analysis in Chapter 4, as well as to Phase II of the project as detailed in Chapter 1.

3.2 Initial vibration frequency tests

During 1982 initial testing was conducted on a Henred Fruehauf steel chassied tandem axle platform semi-trailer coupled to a Foden 6 x 4 truck-tractor. The objective of these tests was to gain an initial feel for the nature of the signal that could be expected from a strain gauge or accelerometer during the testing of such a vehicle, and to obtain an estimation of the range of vibration frequencies that could be expected under differing test conditions (eg. type and severity of road surface, speed, payload, etc.).

In these tests two strain gauges were mounted on the upper and lower surfaces respectively, of the lower flange of the pavement side chassis I-beam, a short distance in front of the landing leg position. Two dummy strain gauges were mounted on a small piece of unstressed plate attached to the chassis in close proximity to the two active gauges. All four strain gauges were connected to form a two active arm Wheatstone bridge measuring direct strain in the flange. The bridge was connected to a Kyowa CG-6C Signal Conditioner which both supplied the power to the bridge and received the return signal. After amplification in the signal conditioner, the output signal was recorded on a Kyowa Rapet RMS 11 LPT UV-type chart recorder.

The test procedure adopted was not a rigorous one and consisted mainly of recording a number of short bursts of data (20 to 30 seconds duration) under each given set of test conditions. This was done for the vehicle both unladen and laden (500 x 50 kg pockets of cement, ie. 25 000 kg UDL), on roads ranging from concrete and tar highways at speeds between 60 and 90 km/h,

to secondary tar roads at 40 to 60 km/h, and poor quality dirt roads at low speed (ie. less than 10 km/h). The effect of certain other occurrences was also noted, such as driving over bridge expansion joints and driving through severe potholes on the dirt road.

A typical block of strain gauge data from these tests is shown in Figure 3.1.

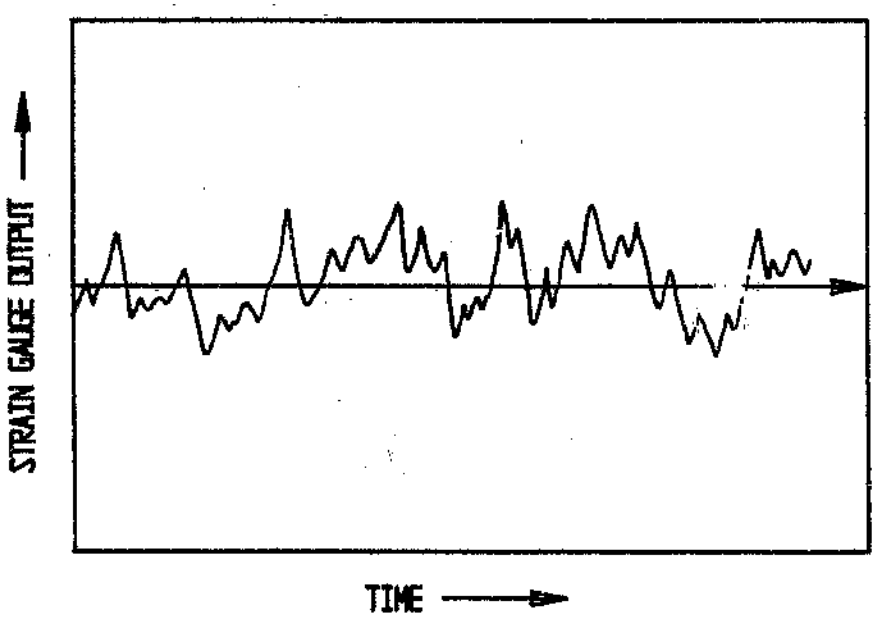


Figure 3.1 A typical block of strain gauge data from the initial vibration frequency tests

In order to analyse the average vibration frequency obtained in each test, the UV-chart recorder traces were magnified and the number of peaks (irrespective of amplitude) occurring over a certain length of the trace were counted. Then, by multiplying by the chart speed selected for each test, the average number of peaks or cycles per second was deduced for each count length. This was done for a few lengths on each test trace. Table 3.1 summarises the

average vibration frequency results obtained for the various test conditions selected.

Table 3.1 Average vibration frequency test results

Type of road surface	Load conditions	Speed (km/h)	Average vibration frequency (Hz)
Concrete highway	laden	70	6,0
Concrete highway (over bridge expansion joints)	laden	70	8,2
Secondary tar road	laden	55	5,0
Dirt road	laden	10 – 15	9,1
Poor quality dirt road (severe potholes)	laden	very slow	4,0
Poor quality dirt road (severe potholes)	unladen	very slow	7,6
Tar highway	unladen	70	17,0

From these results it is seen that the average frequency of vibration of the trailer chassis structure is dependent to a large extent on the load carried by the trailer and only to a lesser extent on the type of road surface (ie. concrete, tar, dirt) or speed. This is to be expected since a heavily laden trailer, being a more massive vibrating system, will have a far lower natural frequency than an empty trailer. A fair increase in frequency was also apparent for the laden trailer travelling on the dirt road, and over the bridge expansion joints on the concrete highway. This was due to the severely rutted nature of the particular stretch of dirt road selected for the tests and due to the closely spaced expansion joints on the highway, forcing the higher vibration frequencies.

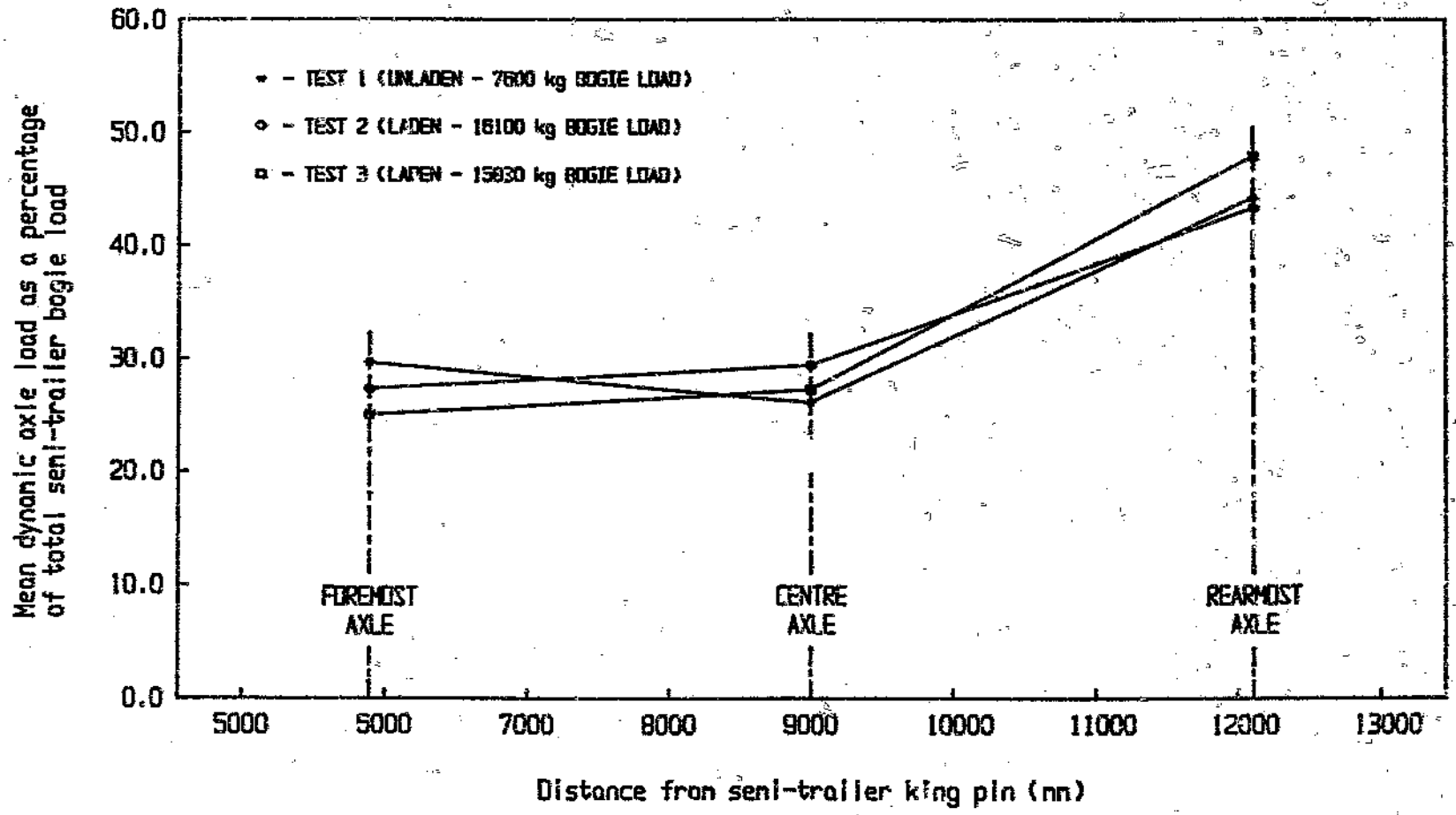
The vibration frequencies of Table 3.1 correspond to between 2,37 and 3,24 metres travelled per vibration cycle for the laden trailer on tar or concrete roads. For the unladen trailer on the tar highway this figure is 1,14 metres travelled per vibration cycle.

At the request of Henred Fruehauf Trailers (Pty) Ltd, testing was also conducted by the author during May 1983 on Henred Fruehauf's 28 tonne PET prototype semi-trailer.[25]. The purpose of this study was to determine the effectiveness, from the point of view of dynamic axle load equalization of the wide spread tri-axle suspension. This suspension was of the conventional leaf spring type but with modified rockers inter-connected via long connecting rods to cater for the 3 110 millimetre spread between axle centres. Testing was undertaken for varying road conditions (ie. freeway, secondary tar roads, and dirt roads) with no load on the trailer and with the tri-axle bogie loaded to approximately 69 percentof the maximum legal bogie load (ie. 24 600 kg).

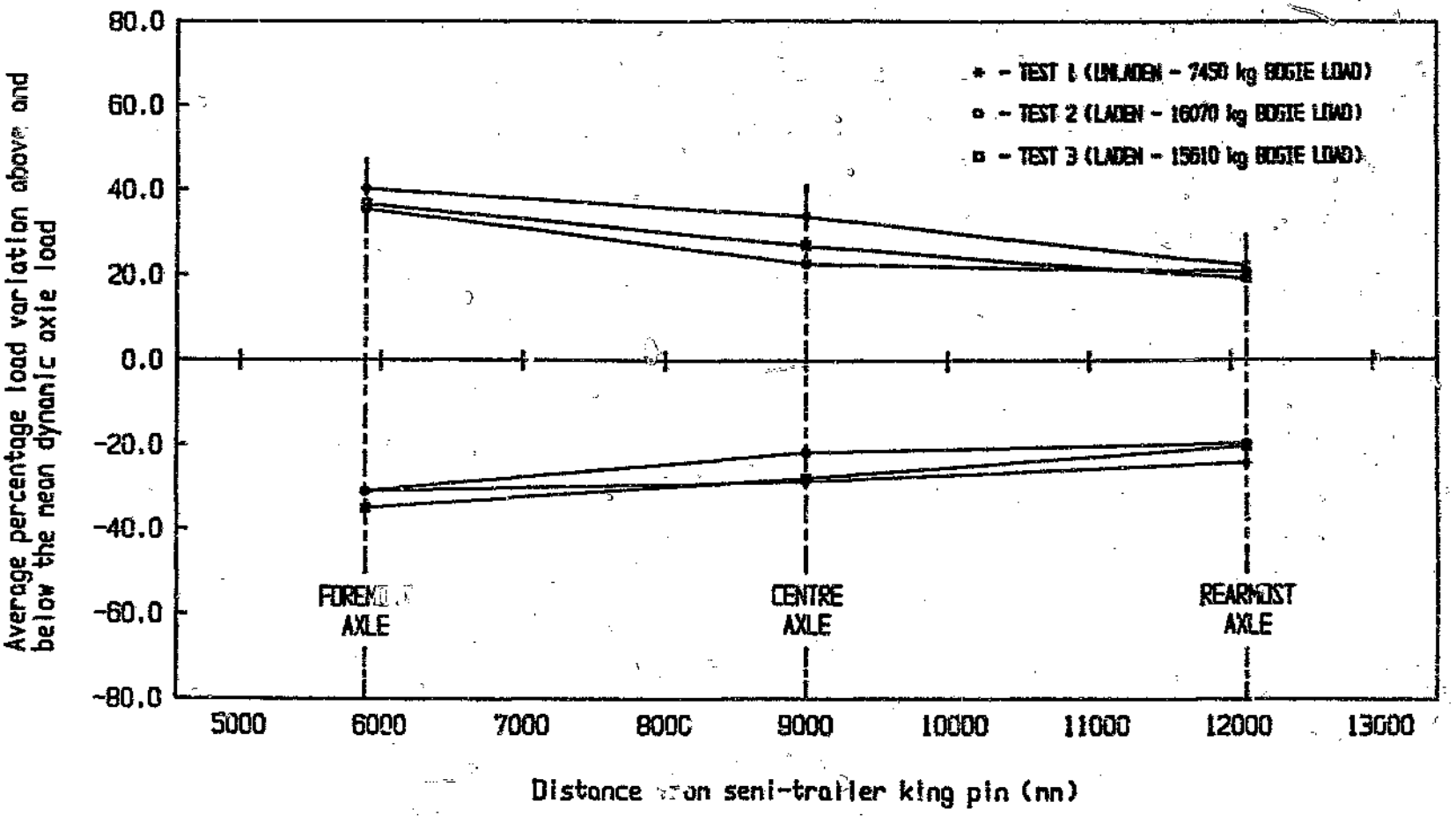
Strain gauges mounted on the upper and lower surfaces of the axle beams, between the spring mounting positions, were used to sense the loads supported by each of the three axles. A Watanabe multi-channel chart recorder was used throughout the tests to record the axle strain gauge bridge output signals. Callibration of each bridge output signal was achieved by comparison to a range of axle loads measured using a set of assayed weigh pads.

Three test runs were undertaken; one unladen and two laden. The mean dynamic axle loads for each axle in each of the three test runs are presented, in Graph 3.1, as a percentage of total triden bodie load for the freeway conditions at approximately 75 km/h. These were calculated for the smoother freeway surface only, since the road conditions varied somewhat on the secondary tar and dirt roads, making the calculation of mean loads under these conditions extremely difficult. From this graph it can be seen that the mean

Graph 3.1 Mean dynamic axle loads recorded during the suspension equalization testing of the Heared Fruehauf PET trailer (Freeway at approx. 75 km/h)



Graph 3.2 Average maximum percentage load variation recorded during the suspension equalization testing of the Henred Fruehauf PET trailer (Freeway at approx. 75 km/h)



axle load for the rearmost axle was considerably higher throughout the tests than for the other two axles. This is obviously a characteristic of that particular suspension geometry. Further, the average maximum percentage load variation from the mean was found to be greater for the foremost and centre axles (refer Graph 3.2) indicating a greater instability or tendency to bounce for these two axles. Here the average maximum load variation was judged by eye from the chart recorder traces and extreme peaks, such as those resulting from driving over bridge expansion joints, were ignored.

When negotiating severely undulating ground, or when turning corners where there was a large difference in relative slope between the two intersecting roads, extremely high axle loads were at times recorded. This was because of the inability of the load equalisation system of the suspension to operate under such extreme conditions, and was mainly due to the very wide axle spacing.

In the above discussion the importance of an efficient load equalisation system for wide spaced tri-axle suspensions is apparent. This is not only to properly distribute forces into the chassis but also to ensure a uniform load distribution at the road surface, thereby minimising pavement damage.

3.3 Computer data acquisition system

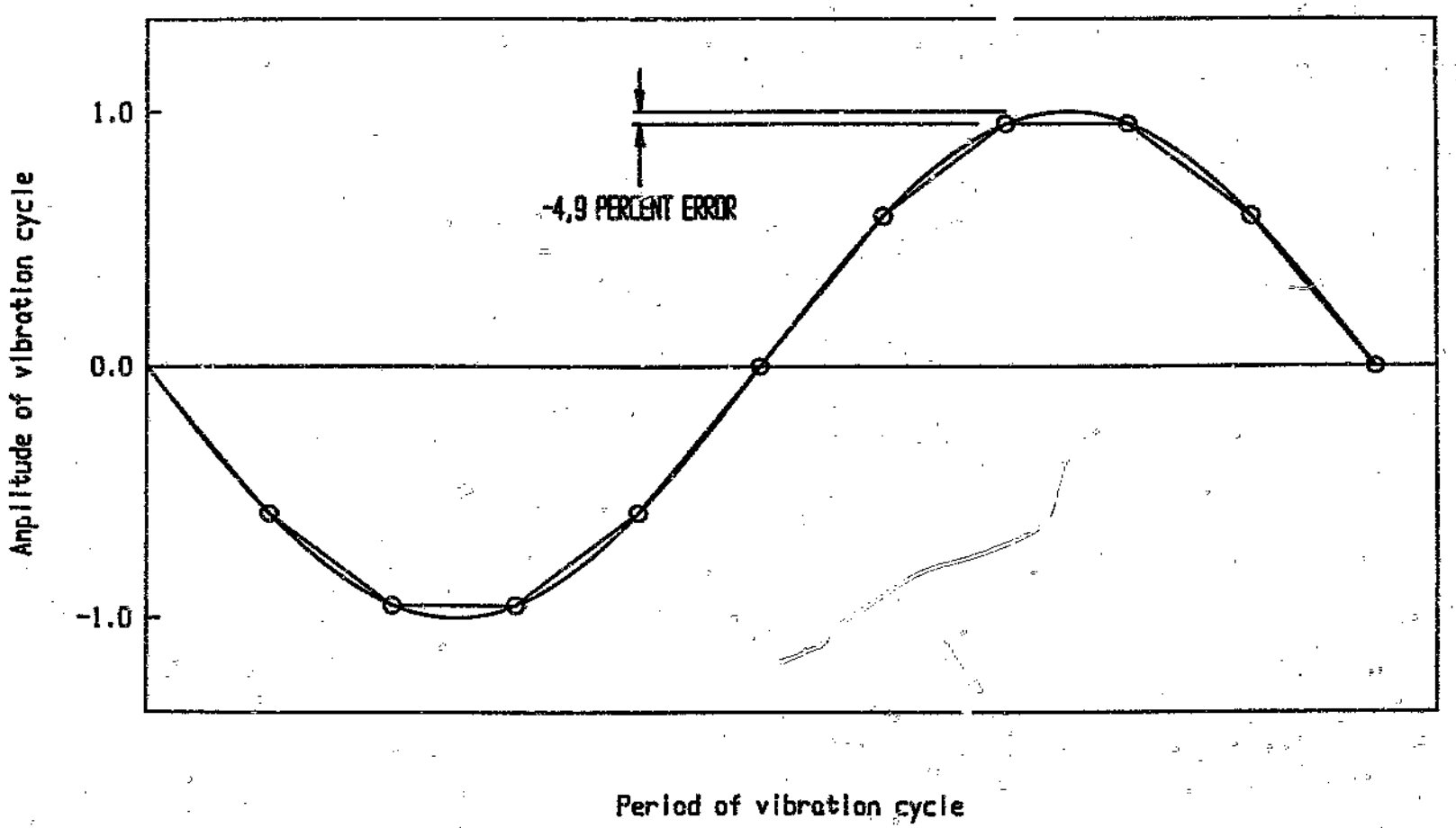
In selecting the appropriate instrumentation for acquiring field service data, provision must be made for the recording of both analog and digital information. Analog data is required in order to give a detailed picture of the stresses or strains experienced by particular vehicle components, while digital data on the other hand, allows the direct computation of peak values and how often the particular components are subjected to the various levels of stress or strain. Although it is possible to record all of the data in analog form (for

example by using an FM tape recorder), and to determine peak values and count levels at a later stage, it is generally necessary to limit analog data gathering to specific combinations of manoeuvres and load conditions which are known to produce high stress levels. Otherwise the task of data reduction and assimilation can be overwhelming. The identification of critical combinations of manoeuvres and loading conditions may at times be difficult and obviously can only be resolved by judicious use of both techniques.

The required digital data logging rate (ie. the number of analog to digital data conversions per unit time) is deduced from the number of data points necessary to properly define, to a predetermined accuracy, one full vibration cycle at the highest expected vibration frequency component. In this project a minimum of ten data points per cycle was selected. This is illustrated in Graph 3.3, where the vibration cycle is represented by a sine wave. The maximum error occurs at the peak and trough for the ten data points as shown, and is equal to -4,9 percent. Obviously the shape of the actual vibration cycles encountered during testing will vary to some degree from this sinusoidal shape, but the maximum possible error is not expected to differ significantly from the above figure.

The maximum average frequency of vibration recorded during the initial vibration frequency tests (refer to Section 3.2) was 17 cycles per second (ie. tar freeway - unladen). Further, the highest vibration frequency component during all of the tests was never more than three times the averge frequency. Hence the required digital data logging rate per channel is 510 data points per second for ten data points logged per cycle. For data acquisition via twenty input channels, this figure rises to an overall total of 10 200 data points per second. At the start of any series of tests, however, data should initially be logged over a few representative channels at a somewhat higher frequency per channel than suggested above (for example, at 2 000 to 3 000 data points

Graph 3.3 Data logging at ten points per cycle for a vibration cycle represented by a sine wave



per second per channel) before any final decision on the required minimum data logging rate is made.

In the data acquisition system developed for this project both the analog and digital data logging functions are catered for in a single data acquisition system controlled by a micro-computer. Figure 3.2 shows a schematic layout of the full system.

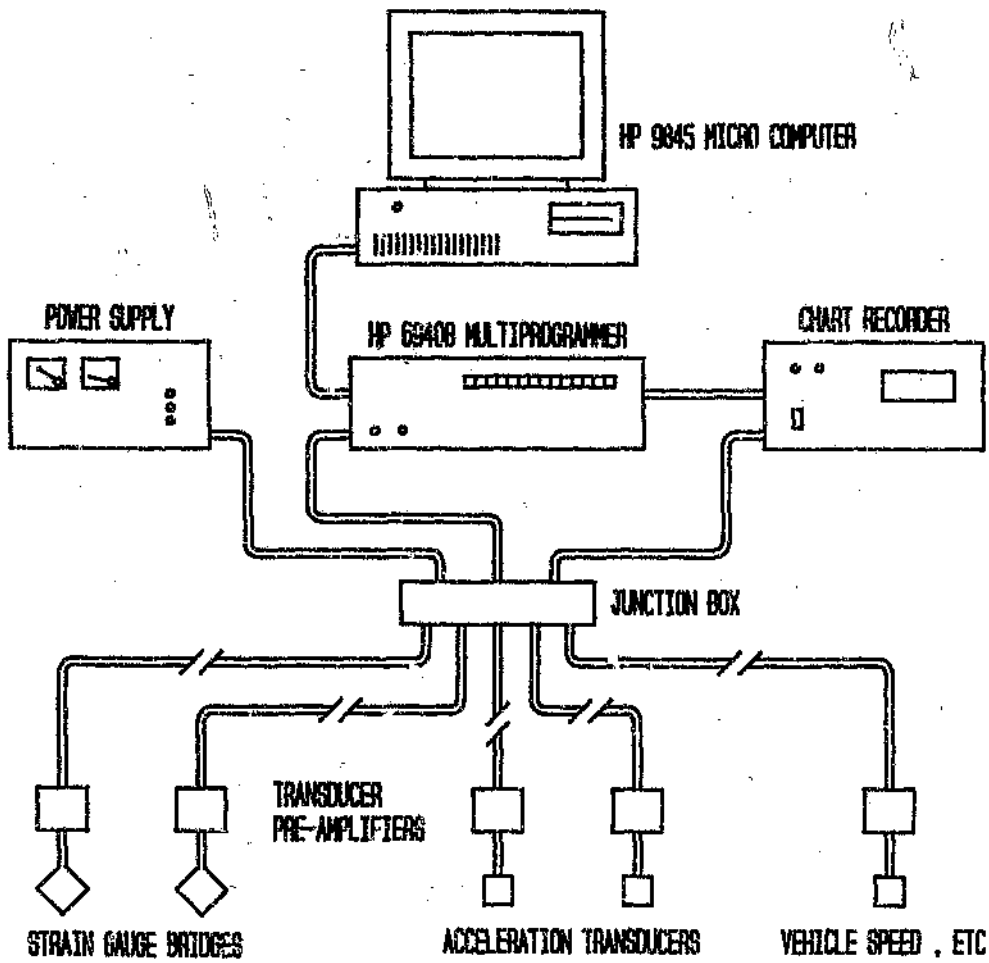


Figure 3.2 High speed computer controlled data acquisition system

A Hewlett Packard 6940B Multiprogrammer is used to multiplex between each of the input channels in use and to perform the analog to digital conversions. The digital data is then transferred to a Hewlett Packard 9845 micro-computer via a series/parallel interface and stored in RAM memory. Together these two devices are capable of performing analog to digital conversions and storing the digital data at a total rate of up to 22 000 conversions per second. This can be via a single input channel or divided equally between any number of the 32 input channels available. As well as storing the digital data, the micro-computer is used to control the overall data acquisition sequence and for data reduction and processing (for example, cycle counting). At low data logging rates direct data processing is possible, whilst at high rates it is necessary to log data into the computer RAM memory in short bursts and process the data inbetween. Although this system was not used for the collection of field service data during this phase of the project, the system was bench tested against a signal generator in order to verify maximum data logging rates.

Analog information is obtained via a chart recorder which is either operated manually or by computer program control via the Multiprogrammer's output channels. In this way it is possible to pre-program those portions of the total test data for which an analog record is required. Furthermore, accurate indexing of the analog and digital data is easily accomplished.

The 3-volt DC input voltage required by the strain gauge bridges and the accelerometers is provided by a transformer/rectifier type power supply. This bridge supply voltage is also connected to one of the Multiprogrammer's input channels which allows the micro-computer to monitor the voltage and to take remedial action should it deviate beyond predetermined limits.

Transducer pre-amplifiers, positioned in close proximity to their respective

transducers, are used in the system to amplify the low level transducer output signals. The amplification lessens the susceptibility of the output signals to interference due to electrostatically and magnetically induced noise, and provides a uniform signal range across all of the input channels, as required by the Multiprogrammer. Due to the high cost of purchasing a large number of instrumentation pre-amplifiers (ie. approximately twenty), two types of differential instrumentation amplifiers were built by the author at UWTec. The first of these is based on a National Semiconductor LM363-H100 precision instrumentation amplifier IC chip and was designed for use with strain gauge bridges. It has a fixed gain of 100. The second pre-amplifier is constructed using a National Semiconductor LH0038 true instrumentation amplifier IC chip and is configured for a closed loop gain of 500, although gains of 100 to 2 000 may be set by jumpering gain setting resistors included on the chip. This amplifier was designed for use with the Kyowa AS-C acceleration transducers and any other transducers where very low level output signals are obtained. During bench tests both amplifiers were shown to exhibit excellent gain linearity and extremely low input offset voltage. The closed loop frequency response was also investigated for an input voltage to the amplifiers of 2,0 mV. The resultant frequency response curves indicated usable frequency ranges for no fall-off in gain, of zero to 10 kHz for the LM363-H100 amplifier, and zero to 20 kHz for the LH0038 amplifier. The bandwidths for the LM363-H100 and LH0038 amplifiers were shown to be 35 kHz and 86 kHz respectively.

3.4 Endurance testing techniques

As previously discussed, vehicle structural testing comprises two main areas of concern. These are the determination of exceptional loading in order to verify stress calculations, and the recording of loading histories in order to assess fatigue life or to validate earlier fatigue life predictions. The latter

of these two is termed endurance testing. In this section a methodology for endurance testing as applied to heavy duty vehicles is proposed and discussed together with the theoretical foundation upon which it is based.

A typical block of strain-time data, as would be expected from a strain gauge attached to a road vehicle, is shown in Figure 3.3 below.

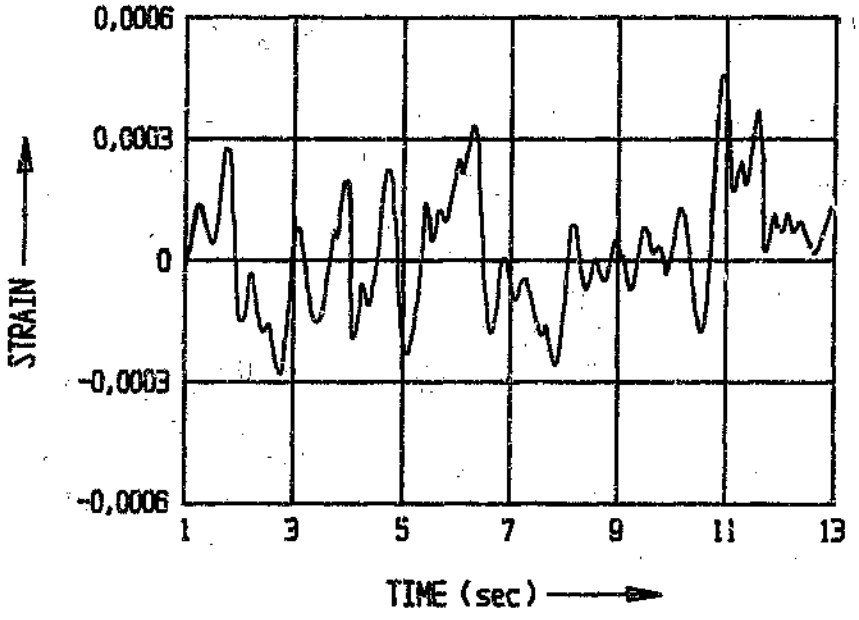


Figure 3.3 A typical block of strain-time data

Once digitised and stored in computer RAM memory, the strain history data is categorised into several groups, each having the same amplitude and mean strain. Several counting techniques are available for counting the number of cycles belonging to each group, the most common being the 'level counting', 'range counting', and 'rainflow counting' algorithms. Rainflow counting is considered to be more accurate in that it defines cycles as closed stress-strain hysteresis loops and hence identifies events in a complex strain

sequence which are compatible with constant amplitude fatigue data.[26–28] A numbe of computer routines are available to perform rainflow counting. Unfortunately, the majority require that the entire load history be known before t. \ counting process starts, because of the limitation that the load history must be rearranged to begin and end with the maximum peak (or minimum valley). As a result they are not suitable for 'on-board' real time data processing. Downing et al[27] have, however, developed a routine to overcome this limitation which can be begun and ended at any point in the stress history, whilst identifying the same hysteresis loop cycles.

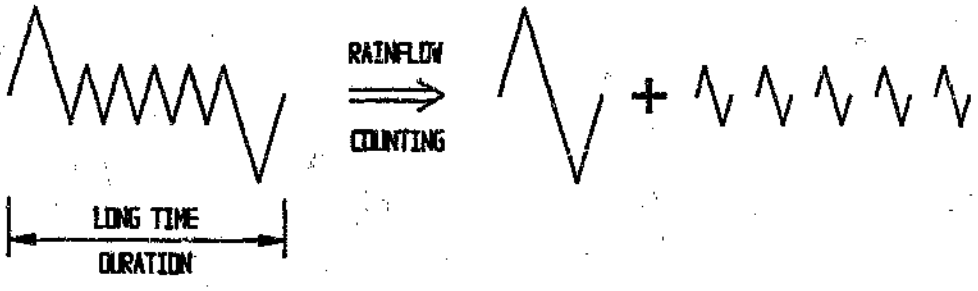
Further, when counting load histories of very long time duration using rainflow counting, partial cycles (ie. partial hysteresis loops) very far removed from each other may be combined during the counting procedure. This is illustrated in Figure 3.4(a). Schultz[29] suggests that the load-time history in such a case be divided into segments which are counted separately before the results are combined (Figure 3.4(b)). The exact duration of these segments must be judged from the particular merits of the test being undertaken.

The strain amplitude and mean strain readings (or maximum and minimum strain) in each count level group are converted to stresses by reference to the stress-strain curve for that material. For a uniaxial stress field below the limit of proportionality, Hookes Law may be used. In a biaxial stress situation fatigue damage is based on the maximum (algebraic) principal stress which is obtained from the stress-strain relationship:[30]

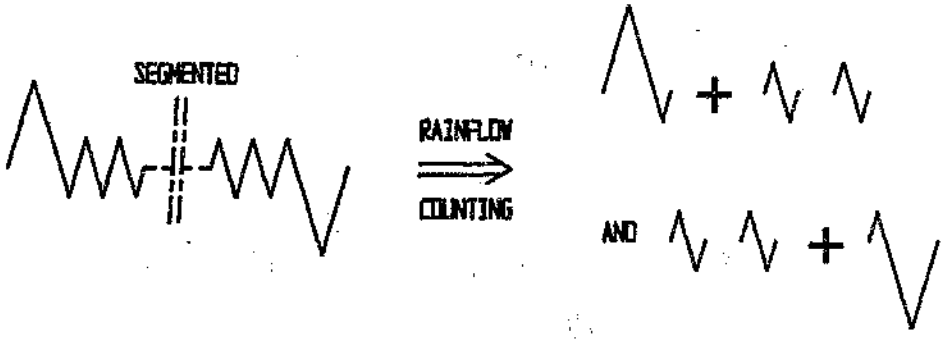
$$\sigma_1 = \frac{E}{1-\nu^2}(\epsilon_1 + \nu\epsilon_2)$$

Here ϵ_1 and ϵ_2 refer to the maximum and minimum principal strains respectively, which are obtained from the three component strain readings from the

three strain gauges making up the strain gauge rosette at the test position. For a detailed discussion of rosette strain computations the reader is referred to a text by Benham and Warnock.[30] This approach assumes that the peak fatigue stresses will always be in the elastic range of the material. From the



(a) Full load history



(b) Segmented load history

Figure 3.4 The effect of rainflow counting using full and segmented load histories

design calculations of Appendix A, this is expected to be valid for all positions on the trailer chassis for dynamic accelerations up to approximately 3-g. Further, should local tensile stresses exceed the limit of proportionality once

or twice during the life of a component, the resulting residual compressive stresses will reduce the magnitude of subsequent tensile fatigue stresses, thus biasing life predictions conservatively.

The resulting cumulative fatigue damage is calculated from the test data using the Palmgren-Miner hypothesis or Linear Damage Rule.[26,30–33] The Palmgren-Miner theory states that:

- each count level group of cycles (ie. same stress amplitude and means stress) contributes an amount of damage given by the linear cycle ratio for the group.
- the damage arising from any group of cycles is not dependent on the group's location in the stress history.
- the total cumulative fatigue damage is the linear sum of the damages contributed by each group. That is:

$$D = \sum \left(\frac{n_i}{N_i} \right) \geq 1 \qquad \text{for failure}$$

where

n_i	=	the number of cycles which occur at a particular stress amplitude and mean stress – i^{th} count level group.
N_i	=	the number of cycles to crack initiation at the i^{th} set of conditions.
(n_i/N_i)	=	damage ratio for the i^{th} set of conditions.
D	=	cumulative damage ratio.

The numbers of cycles N_i are obtained from the materials S-N curve (ie. stress-life curve) for the relevant stress amplitude and mean stress values.

In the above approach, fatigue life is defined as life to crack initiation. This is deemed to be a reasonable measure of the useful life of a component despite the fact that components can often withstand a considerable number

of additional cycles after crack initiation, before fracture occurs.

Miner's Rule states that crack initiation occurs when the cumulative damage ratio equals unity. For a particular block of test data, which represents a portion of the total life stress history of the component, one would expect the cumulative damage ratio for the block to be small. Hence, Miner's Rule is often expressed as:

$$B\left[\sum\left(\frac{n_i}{N_i}\right)\right]_{\text{per block}} = 1 \qquad \text{at failure.}$$

Using this equation the numbers of such blocks of test data B required before crack initiation occurs can be determined.

Although the Palmgren-Miner model provides a mechanism that is relatively easy to use in the analysis of complicated stress histories, it does however have certain shortcomings. Firstly, it does not account for the fact that fatigue life to some degree depends on the order in which the different stress levels are applied. In fact, test results show that the cumulative damage ratio D at failure can differ widely from the value of unity.[29,30,32,33] Wirsching et al[32] suggest that values of D at failure usually fall in the range from 0,7 to 2,2 , whilst Benham et al[30] suggest a usual range of 0,6 to 2,0. Extreme values of D well outside these ranges have also been found to occur in a few cases. The Palmgren-Miner Rule is, however, generally valid when the various amplitudes of stress cycles are fairly evenly distributed throughout the life of the member. In an attempt to allow for the variation in the cumulative damage ratio, a value of D based on previous experimental results on similar structures may be used. This is known as the Relative Miner-Hűck approach[29] and has been shown to yield a significant improvement in fatigue life prediction reliability.

A second important factor in the use of the Palmgren-Miner rule is that cycles at stress levels below the endurance limit for the material do not contribute to the fatigue life calculation since N_i is infinite below the endurance limit. Experience has shown however[29] that these cycles do contribute to some degree, and at high number of cycles (ie. greater than 100 million cycles) their effect can become significant. In order to include the influence of stress cycles below the endurance limit, a number of methods of modifying the basic S-N curve are used. The first of these employs what is known as an elementary S-N curve[29] in which the sloping portion of the basic S-N line above the endurance limit is projected down to meet the zero stress axis (Figure 3.5(c)). This elementary S-N curve may also be used in conjunction with a reduced endurance limit (for example, half σ_e). A second approach, developed by Haibach,[29] uses a line below the endurance limit down to zero stress, which is at half the slope of the portion of the basic S-N curve above the endurance limit. This projected line is known as the Haibach line (Figure 3.5(b)). The relative failure prediction reliability of each of the above mentioned approaches is indicated in Figure 3.5.

The Palmer-Miner Linear Damage Rule, despite the various shortcomings and difficulties discussed above, still provides a useful starting point for the analysis of fatigue under variable loading spectra. It is also most commonly used because of its simplicity and the experimental fact that other much more complex cumulative damage theories do not yield a significant improvement in fatigue life prediction reliability.

By definition, the approach thus far addresses high cycle fatigue in that peak fatigue stresses are within the elastic range and the expected cycle life exceeds 100 000 cycles. Although unlikely in this particular design, low cycle fatigue

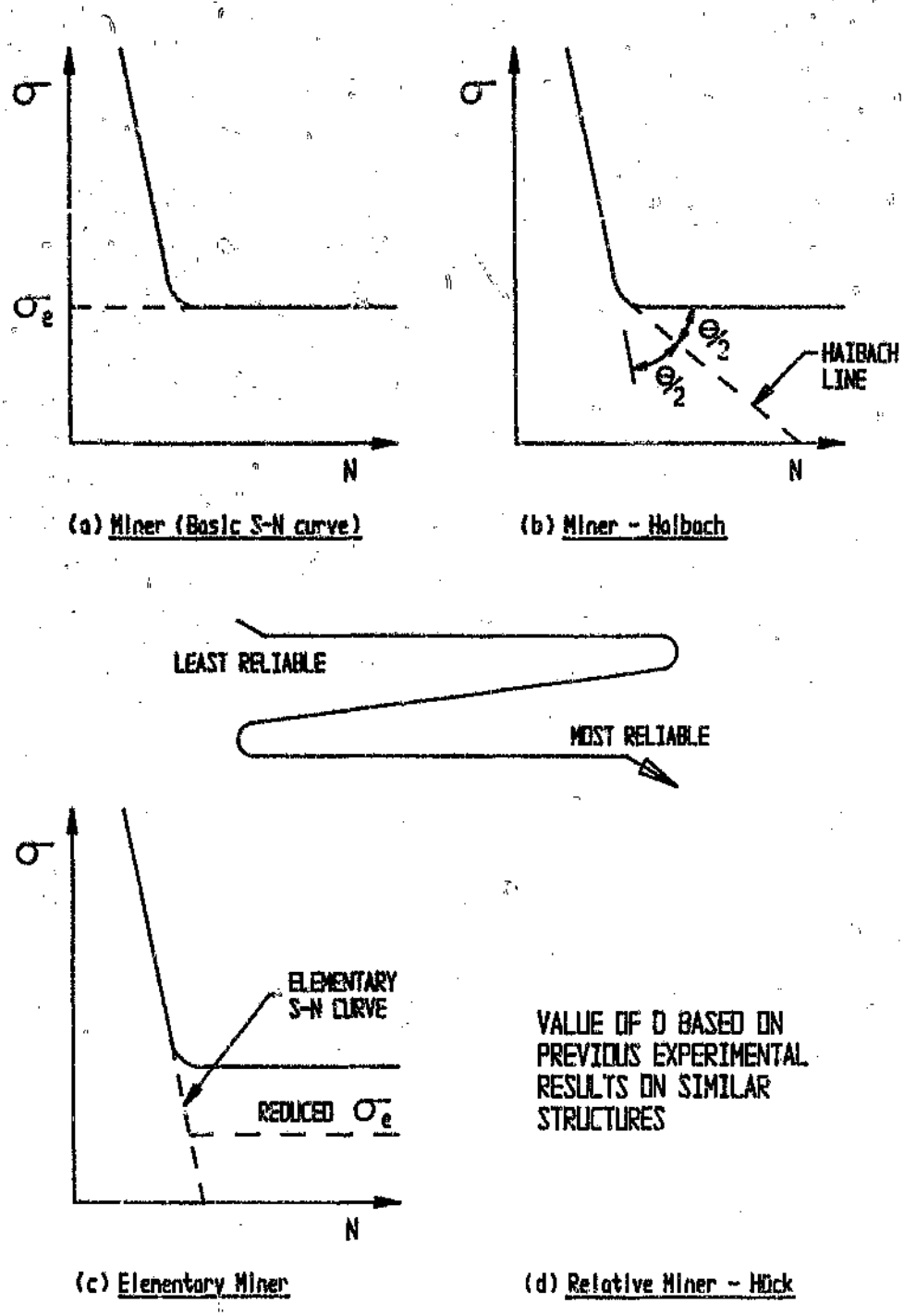


Figure 3.5 **Methods that improve the failure prediction reliability of the Palmgren-Miner hypothesis**

occurs when stresses are high enough to cause plastic deformation, and cycle life as a result of this high loading is usually lower than 100 000 cycles. In the land vehicle industry low cycle fatigue usually occurs during unexpected overload conditions, since few parts are designed to serve under such severe conditions. However, in the interests of completeness, a technique termed the Strain Range approach,[26,34–38] which was developed for use in both the low cycle region and high cycle region, and which has gained considerable acceptance in the automative industry over the past ten years or so, is also discussed here.

The Strain Range fatigue model applies primarily to components that are strain cycled and, as in the stress-life approach discussed above, it predicts life to crack initiation. The model is based on data obtained from the hysteresis curve for metals and yields a modified S-N curve in the low-cycle region.

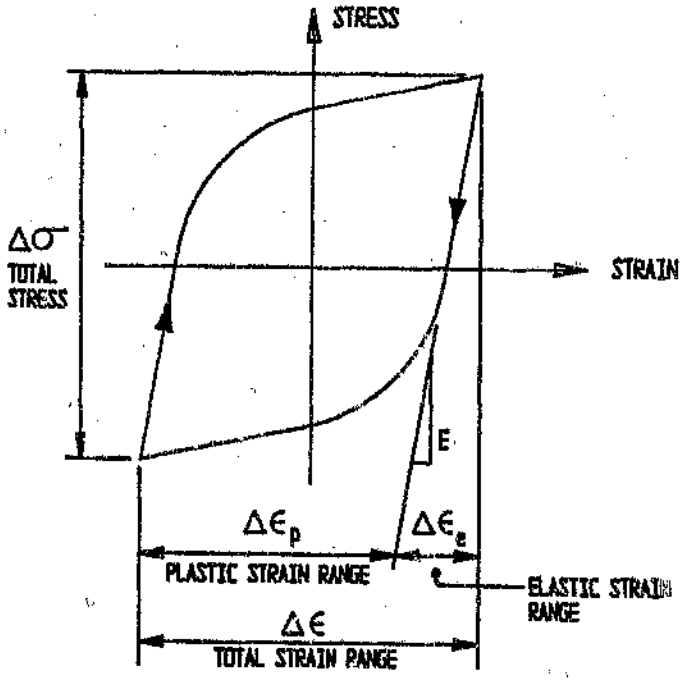


Figure 3.6 A typical stress-strain hysteresis loop for a ductile metal

The steady state hysteresis loop is a plot of the behaviour of a ductile metal under controlled amplitude cyclic loading. As stresses reverse from tensile to compressive, the metal strains as shown in the typical curve of Figure 3.6.

Experiments indicate that, for completely reversed bending, as illustrated above, the amount of plastic strain and cycles to failure are approximately related by:[34]

$$2N_f = \left(\frac{\Delta\epsilon_p}{2\epsilon'_f}\right)^{1/c}$$

where

N_f	=	the number of cycles to failure.
$(\Delta\epsilon_p/2)$	=	plastic strain amplitude.
$\Delta\epsilon_p$	=	full plastic strain range.
ϵ'_f	=	fatigue ductility coefficient. Defined as the true strain required to cause failure on the first reversal. ϵ'_f may be estimated from $\epsilon'_f = \ell n(100/(100 - \%RA))$ where $\%RA$ is the percentage reduction in area that results from a simple tensile test.
c	=	fatigue ductility exponent. A material property approximately equal to -0,6 for many materials including steel and aluminium.

Since these are plastic strains, both strains and stresses within the material are large. This equation then predicts low cycle fatigue.

A similar relationship exists between high cycle life and elastic strain. When strain amplitudes are low enough to remain within the elastic limit of the metal (ie. $\epsilon_p = 0$) fatigue life can be expressed as:[34]

$$2N_f = \left(\frac{E\epsilon_e}{2\sigma'_f}\right)^{1/b}$$

where

N_f	=	the number of cycles to failure.
E	=	modulus of elasticity of the material.
$(\Delta\epsilon_e/2)$	=	elastic strain amplitude.
$\Delta\epsilon_e$	=	elastic strain range.
σ'_f	=	fatigue strength coefficient. Defined as the true stress required to cause fracture on the first reversal. Generally, the relationship $\sigma'_f \cong \sigma_f$ is used, where σ_f is the true fracture strength of the material.
b	=	fatigue strength exponent. For metals in a 'soft' condition $b = -0,1$ and if the metal has been hardened by cold working, b approaches -0,05. $b = -0,085$ may be used as a first estimate or, alternatively, for most metals, $b \cong -(1/6)log(2\sigma'_f/\sigma_{UTS})$

The above two life equations can be combined to provide an expression for the total strain amplitude for a given N_f :[26,34,35]

$$\frac{\Delta\epsilon}{2} = \frac{\sigma'_f}{E}(2N_f)^b + \epsilon'_f(2N_f)^c$$

This equation is plotted on full log co-ordinates and the resultant plot is termed a strain-life curve. A typical example is shown in Figure 3.7.

The effect of mean stress can be accounted for by lowering the elastic component of the strain life curve as follows:[26]

$$\frac{\Delta\epsilon}{2} = \frac{\sigma'_f - \sigma_{\text{mean}}}{E}(2N_f)^b + \epsilon'_f(2N_f)^c$$

where

σ_{mean} = mean stress.

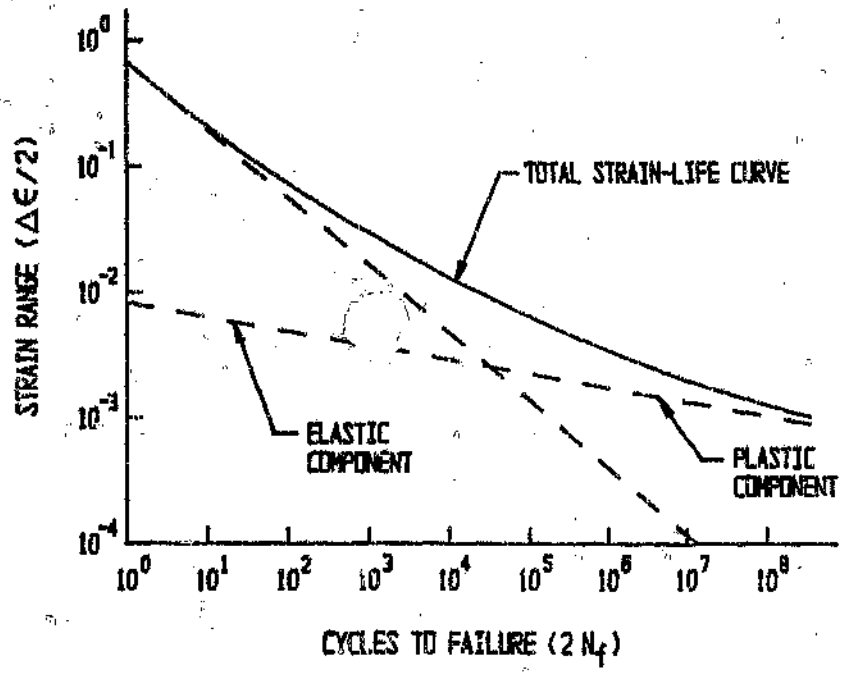


Figure 3.7 A typical strain-life curve

Note that the plastic component is unaffected by the mean stress. Further, a tensile mean stress will reduce total cycle life whilst a compressive mean stress increases total life.

In the case of complex load histories, this fatigue model may be applied in conjunction with the Palmgren-Miner hypothesis, in a similar manner as discussed above, for the stress-life approach. Here the strain data in the various count level groups is converted into strain range and mean stress values by reference to the cyclic (hysteresis loop) stress-strain curve for the material.

CHAPTER 4

DESIGN EVALUATION

4.1 Introduction

This chapter presents a general overview of the approach adopted in the design of all aspects of the semi-trailer and details some of the more important design decisions. For the most part this takes the form of a discussion or evaluation of the design analyses detailed in the appendices to this dissertation.

The first part of the chapter presents a discussion of certain general aspects which include the overall vehicle concept and main dimensions as well as design payload and chassis mass, and the approach adopted in the stress analysis of the vehicle chassis. Thereafter, each different section of the trailer design is evaluated individually in conjunction with the analyses in the appendices. In each case the methodology adopted is discussed and the more important results are presented. Reference is also made to the engineering drawings in Appendix H.

4.2 General

4.2.1 General vehicle concept, legal considerations, and overall dimensions

Although the principal criterion governing the vehicle concept in this project was to obtain a high payload (refer Section 1.1), the semi-trailer has also been designed with a view to obtaining the maximum overall length and width within the bounds of present legislation. The main dimensional and mass restrictions for a truck-tractor and semi-trailer combination are:[5]

(i) Dimensional limitations:

– maximum combination length	17,0 m
– maximum semi-trailer length	No restriction
– maximum semi-trailer wheelbase	9,0 m
– maximum semi-trailer front overhang	1,5 m
– maximum semi-trailer overall width	2,5 m

(ii) Legal pavement loadings:

The regulation stipulates the following shall not be exceeded:

– Maximum axle mass loads of 7 700 kg for an axle with single tyres and 8 200 kg for an axle with dual tyres.

– Tyre rating as specified by SABS ARP 008 - 1989 (Parts I - VII and X)[37]

– Manufacturer's axle rating.

(iii) Limitations imposed by bridges and culverts:

The maximum legal load on a group of axles may not exceed the value obtained from the formula:

$$\text{Load} = 1{,}8(s) + 16\,000 \text{ kg}$$

where s is the distance in millimetres between the centre lines of the extreme axles in that group.

The limiting bridge formula span for the majority of 6 x 4 truck-tractor and semi-trailer combinations on the road at present is usually the extreme axle span (ie. from the steering axle of the truck-tractor to the rearmost axle of the semi-trailer) or the span from the foremost drive axle of the truck to the rearmost axle of the trailer. Maximising these dimensions will thus ensure the highest possible payload, and a wide spaced tridem axle or PET (payload efficiency trailer) type semi-trailer is the most obvious way of satisfying the criterion of maximum payload and deck length.

The semi-trailer configuration selected in this design project is shown in Figure 4.1, together with the projected or design weight distribution used for all design calculations. For the truck-tractor and semi-trailer combination having a legal maximum overall length of 17,0 metres, and with no restriction placed on the length of the semi-trailer itself, the maximum length of the trailer depends on the dimensions of the towing vehicle. In this respect forward control truck tractors have a distinct advantage over their normal control counterparts. By selecting a truck-tractor with a very short driver's cab and no bonnet (eg. 'Mack F700') a semi-trailer of up to 14,5 metres can be obtained (eg. Henred Fruehauf PET trailer[1,35]). In this particular design, however, it was considered prudent to size the overall length of the semi-trailer so that it could be coupled (within the 17,0 metre overall combination length restriction) to the majority of forward control truck-tractors on the South African market. To this end, eighteen representative forward control truck-tractors were considered (refer Appendix G) and a maximum semi-trailer length of 13,85 metres was selected as being suitable for approximately 75 percent of the vehicles analysed. The majority of the remaining 25 percent of the truck-tractors could, however, be coupled to a semi-trailer of this length but only with an associated reduction in allowable payload. This is because the necessary 5th-wheel positions result in an unfavourable weight distribution on the truck-tractor, which necessitates a reduction in king-pin load, and hence payload, so as not to overload the steering axle of the truck-tractor. After allowing for the protrusion of the rear bumper and headboard, etc, the 13,85 metre overall semi-trailer length results in a deck length of 13,73 metres.

The wheelbase measurement (ie. from the king-pin to the centre of the trailer axle bogie or, in this case, the centre axle) has been reduced to marginally below the 9,0 metre legal maximum (ie. 8,924 metres) to allow for changes

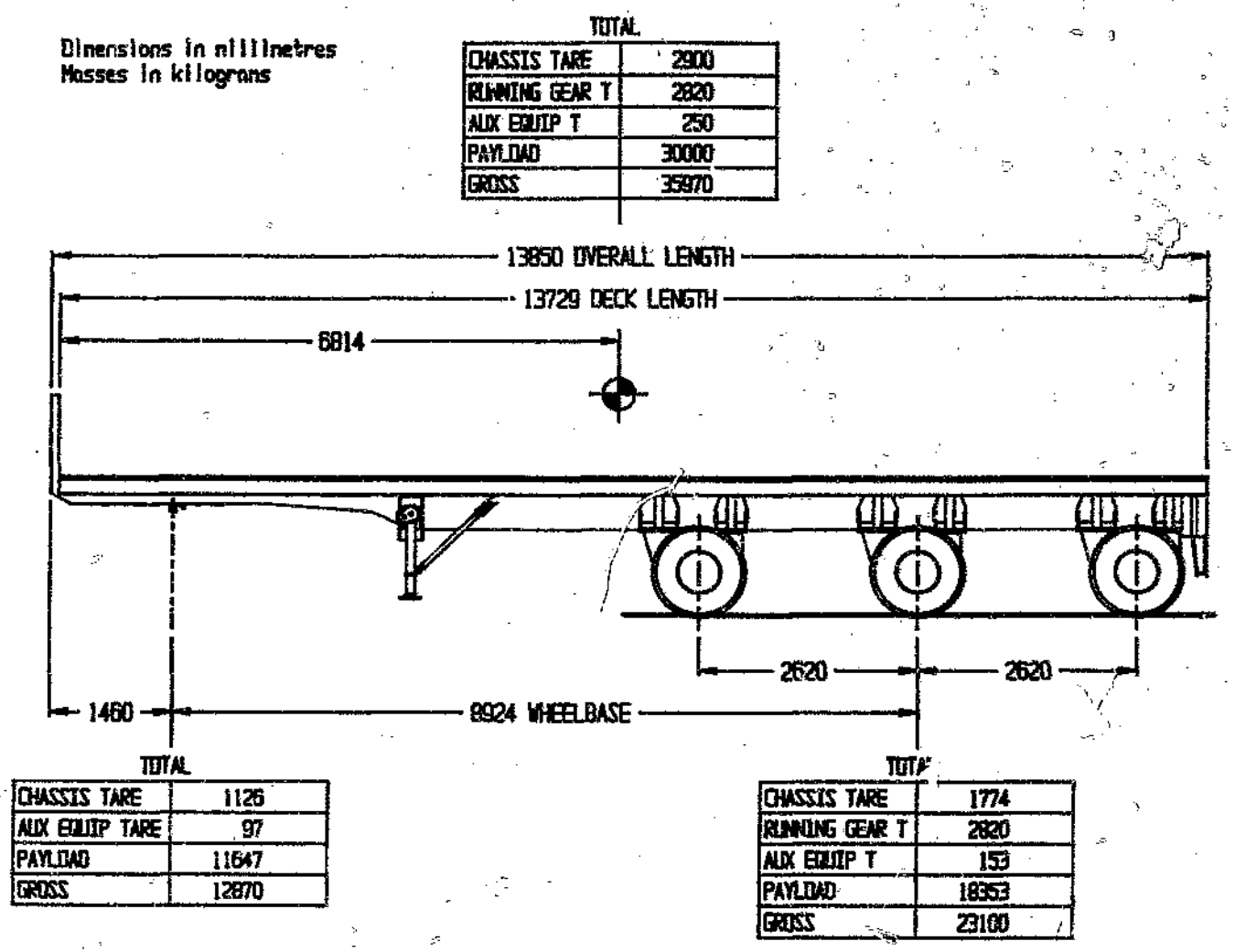


Figure 4.1 Semi-trailer design weight distribution and general dimensions

to the suspension geometry at a later date. For example, the axle mounting position on the suspension trailing arm may be varied at some later date in order to alter the load distribution between the suspension hanger and air bag, or to increase suspension travel. The rearmost axle was then placed as close to the rear of the trailer as possible without fouling the rear bumper or mudflap, when at maximum steer angle. This was done to obtain the maximum extreme axle spacing for the combination and thereby, as discussed above, to achieve maximum payload. The foremost axle was then positioned an equal distance in front of the centre axle to ensure symmetrical steering characteristics and because the wheelbase for a tridem semi-trailer is defined as the distance from the king pin to halfway between the formost and rearmost axles of the tri-axle bogie.

A deck width of 2,40 metres was selected as this allows for the protrusion of drop-sides or side-posts, if fitted. Front overhang, including the headboard, was set at 1,460 metres.

The basic chassis structure is of a ladder type construction comprising two longitudinal beams running the full length of the trailer and spaced apart at intervals by torsion tube cross-members. The longitudinal I-section main beams support the longitudinal and vertical loads, whilst the torsion tubes resist torsional twisting of the frame. The 1,060 metre dimension between the main I-beam centres was chosen since this gives the maximum practical spread between the trailing arms of the suspension for reasons of roll stability, and since it allows for convenient mounting of the suspension air-bag and associated air supply, without interfering with the steering ability of the self-tracking axles.

For the most part the semi-trailer chassis structure was designed as a series of sub-assemblies (eg. torsion tubes, outriggers, suspension mounts) which

are bolted together to form the full trailer chassis. This was done to eliminate the need for large scale assembly jigs during the 'one-off' construction phase and since, in some areas (eg. torsion tube ends), this method results in lower joint stresses than a welded only joint, and removes the possibility of cracks propagating from one component into another. Other advantages are that sub-assemblies may be removed for repair or modification, or during testing of the trailer, in order to fit instrumentation or for laboratory simulated tests on individual components. In order to prevent electrolytic corrosion, all of the bolts, washers and nuts used were cadmium plated, and wherever steel components were bolted to the aluminium structure, a gasket was inserted between the two surfaces and the steel part painted with zinc chromate primer (eg, 'Hope' device foundation plate).

4.2.2 Design payload and chassis mass

The maximum legal payload attainable for a semi-trailer of this type is obviously dependent on the tare mass and dimensions of the towing vehicle as well as the dimensions and tare mass of the trailer itself. From the analyses of Appendix G, the maximum payload was for a Foden S106 - 6×4 truck-tractor and is equal to 29 417 kg. A round figure of 30 000 kg was hence used as the design payload.

The design tare mass for the trailer was approximated to be 5 970 kg (refer Figure 4.1) which was further divided into 2 900 kg chassis mass (including deck, outriggers, side rails, headboard, etc.), 250 kg auxiliary equipment (including 'Hope' anti-jack-knife device, braking equipment, and lights) and 2 820 kg tri-axle bogie mass (including axles and brakes, suspension, wheels, tyres, etc.).

4.2.3 Pseudo-dynamic loading design approach and stress analysis

There are two commonly used approaches to the design analysis of a road vehicle. The first of these involves the application of a load factor to the stresses calculated from the static (1-g) load distribution. The usual value taken for this load factor (sometimes referred to as a safety factor) is of the order of 2,5 , although values as low as 2,2 are at times used.[2,7,39–41] Alternatively, a design model based on dynamic accelerations in the vertical, longitudinal and transverse directions may be applied.

The latter of these two approaches is felt to be more realistic. Firstly, it is a better approximation to the actual situation in that it takes into account such occurrences as load transfer to the front of the vehicle during braking. Also, larger longitudinal g-forces than those resulting from braking deceleration (approximately 0,65-g maximum during braking) may occur as a result of potholes and other severe irregularities in the road surface, or due to king-pin slack. Secondly, dynamic accelerations recorded during testing stages can easily be compared with values used in the design stage (also refer Chapter 3). For these reasons this approach is preferred and was adopted in this project.

Typical dynamic accelerations for highway vehicles are presented in Table 4.1.[2,39,41,42] The acceleration factors listed under 'maximum' are the values adopted in this project in the pseudo-dynamic loading design approach to the main chassis longitudinals and certain other structures. For the static load distribution the vertical acceleration factor is 1,0 and the longitudinal and transverse factors are zero.

Table 4.1 Typical dynamic acceleration factors for highway vehicles

Direction	Acceleration factor	
	Maximum	Normal running
Vertical	2,0	1,1 to 1,3
Longitudinal	1,0	0,1 to 0,2
Transverse	1,0	0,1 to 0,2

In keeping with current design practice,[2,3,40] all of the vertical and longitudinal loads are assumed to be carried by the two main chassis I-beams only (refer Section 4.3). This assumption is deemed valid since the contribution of the side rails and decking is negligible, in that the deck planks are transversely mounted, and the side rails are far removed from the main beams and hence only share the bending loads by virtue of the somewhat flexible connections through the deck planks and outriggers. Transverse loads on the semi-trailer are not included in the analyses of the main chassis I-beams since their effect on the stresses in these beams is negligible due to the relatively large width, and hence, lateral bending stiffness of the ladder frame chassis.

Furt and again in line with current design practice, the 30 000 kg payload and 2 900 kg chassis mass are assumed to be uniformly distributed over the full length of the trailer chassis.

For the most part the Shear Strain Energy Theory or Von Mises Criterion[11,30,43] is used as the failure criterion in the stress analyses of this report. This theory postulates that the shear strain energy in the complex stress system and in simple tension are equal, viz:

$$(\sigma_1 - \sigma_2)^2 + (\sigma_2 - \sigma_3)^2 + (\sigma_3 - \sigma_1)^2 \leq 2\sigma_{yt}^2 \qquad \text{for no failure}$$

where

σ_{yt} = tensile yield strength

$\sigma_{1,2,3}$ = principal stresses

For $\sigma_3 = 0$, the criterion reduces to:

$$\sigma_1^2 + \sigma_2^2 + (\sigma_1 - \sigma_2)^2 \leq 2\sigma_{yt}^2$$

This is the form in which the equation is most often used in this dissertation. In the case of ductile metals the von Mises Failure Criterion correlates well with material behaviour[30] and is thus selected for the aluminium alloys used in the construction of this semi-trailer.

Principal stresses are calculated from Mohr stress circle principles[30,43], viz:

$$\sigma_{1,2} = \left(\frac{\sigma_x + \sigma_y}{2}\right) \pm \sqrt{\left(\frac{\sigma_x - \sigma_y}{2}\right)^2 + \tau^2}$$

where

σ_x = x-direction stress

σ_y = y-direction stress

τ = shear stress

4.3 Main chassis I-beams

4.3.1 Loading analysis of main I-beams

Seven different load cases were analysed in an attempt to cover all possible loading situations on the main chassis I-beams (refer Section A.2, Appendix A). The first of these is the pseudo-dynamic loading situation as discussed in Section 4.2.3 above, whilst the remaining six are static load situations for various support conditions. These are denoted 'Case 1' to 'Case 7' loading in the analyses of Appendix A, and are discussed in detail below.

The analysis of each load case was undertaken using the 'Genesys Frameanalysis/2' structural analysis sub-program on the University of the Witwatersrand's IBM 370 mainframe computer (refer Section A.2 in Appendix A and Appendix B). Due to lateral symmetry of the chassis structure, only one chassis I-beam was analysed in each case, and this was loaded with half of the uniformly distributed payload and chassis mass. The varying depth I-beam was modelled as a series of two node beam elements joining 31 nodes positioned along the neutral axis of the beam (refer Figure B1). The load equalizing characteristics of the tri-axle air suspension were modelled by using a 'fir tree' system of pin jointed links. These links were attached to the I-beam model at the suspension hanger and air bag nodes and were proportioned to correctly distribute the load between axles and between hanger and air bag mounts. The five systems of links used to model the suspension for the various tridem bogie support conditions, are depicted in Figures B2 to B6 in Appendix B. In order to ensure that the deflections of the suspension linkage system were small in comparison with the chassis I-beam deflections, and could thus be neglected, the suspension link members were given high values of cross-sectional area and of second moment of area. Together the

chassis I-beam model and the suspension model form a two dimensional plane frame structure.

Case 1 loading

As already mentioned, this load case corresponds to the pseudo-dynamic loading situation and represents the maximum vertical and longitudinal forces expected to be imposed on the trailer chassis during its working life. Acceleration factors of 1-g for longitudinal and 2-g for vertical loads were used (refer Section 4.2.3 and Sections A.2.2 and A.2.5).

The method of analysis adopted was firstly to calculate the load transfer from the semi-trailer tridem axle bogie to the king-pin resulting from the longitudinal deceleration and for an assumed distribution of retarding forces between the king-pin and bogie. An assumed distribution of retarding forces was necessary because of static indeterminacy, and was estimated to be such that 40 percent of the deceleration was due to retarding forces at the tyres of the semi-trailer and 60 percent due to retarding forces at the king-pin. The overall centre of gravity (chassis mass and payload) of the laden trailer was estimated to be 800 mm above the deck. The load transfer within the suspension itself was then calculated and the pseudo-dynamic reactions at the king-pin and suspension hanger and air bag mounts were obtained.

Working backwards, a skewed load distribution (refer Figure A4) of total magnitude equal to the design payload plus chassis mass multiplied by the 2-g vertical acceleration, was then calculated to produce these pseudo-dynamic support reactions. This skewed load distribution was then approximated by a stepped load distribution, denoted 'LOADING/V2L1' and used for Case 1 loading in the analyses of Appendix B.

Longitudinal loading on the chassis I-beams (refer Section A.2.5) was calcu-

lated by assuming that the friction forces between the uniformly distributed payload and the trailer deck are also uniformly distributed, and adding these forces to the longitudinal retarding forces at the king-pin and suspension hangers.

Shear force, bending moment, deflection and longitudinal load diagrams from the results tabulated in Appendix B are presented for this load case in Graphs 4.1 to 4.4.

Case 2 and Case 3 loading

These two load cases correspond to static loading situations (ie. 1-g vertical acceleration only) for the stationary semi-trailer standing on level ground (refer Section A.2.3). Case 2 represents support at the king-pin and tridem bogie (ie. semi-trailer coupled to truck-tractor) whilst Case 3 is for support at the landing legs and tridem bogie (ie. semi-trailer uncoupled). The static load distribution is denoted in Appendix B by 'LOADING/1'.

Shear force, bending moment, and deflection diagrams are presented in Graphs 4.5 to 4.10 for these two loading situations from the tabulated results of Appendix B.

Case 4 to Case 7 loading

The last four load cases simulate situations where the tyres of one or more of the axles of the semi-trailer tri-axle bogie are lifted completely off the ground. These situations arise, for example, when negotiating large humps or dips in the road surface, when entering or exiting driveways over storm water gulleys, or when turning sharp corners where there is a large difference in relative slope between the two intersecting roads. This phenomenon is characteristic of PET type semi-trailers due to the wide axle spacing of the

tridem bogie and is caused by the load equalization system of the suspension not having sufficient travel to maintain all three sets of tyres firmly in contact with the ground at all times.[25] Due to the extreme nature of the conditions required to produce each of these load cases, they occur at low speed and hence at low dynamic acceleration. For this reason the static load distribution (ie, 'LOADING/1') was used in each of these analyses in Appendix B.

The four load cases are as follows:

Case 4 - support at king-pin and foremost axle only.

Case 5 - support at king-pin and centre axle only.

Case 6 - support at king-pin and rearmost axle only.

Case 7 - support at king-pin and foremost and centre axle.

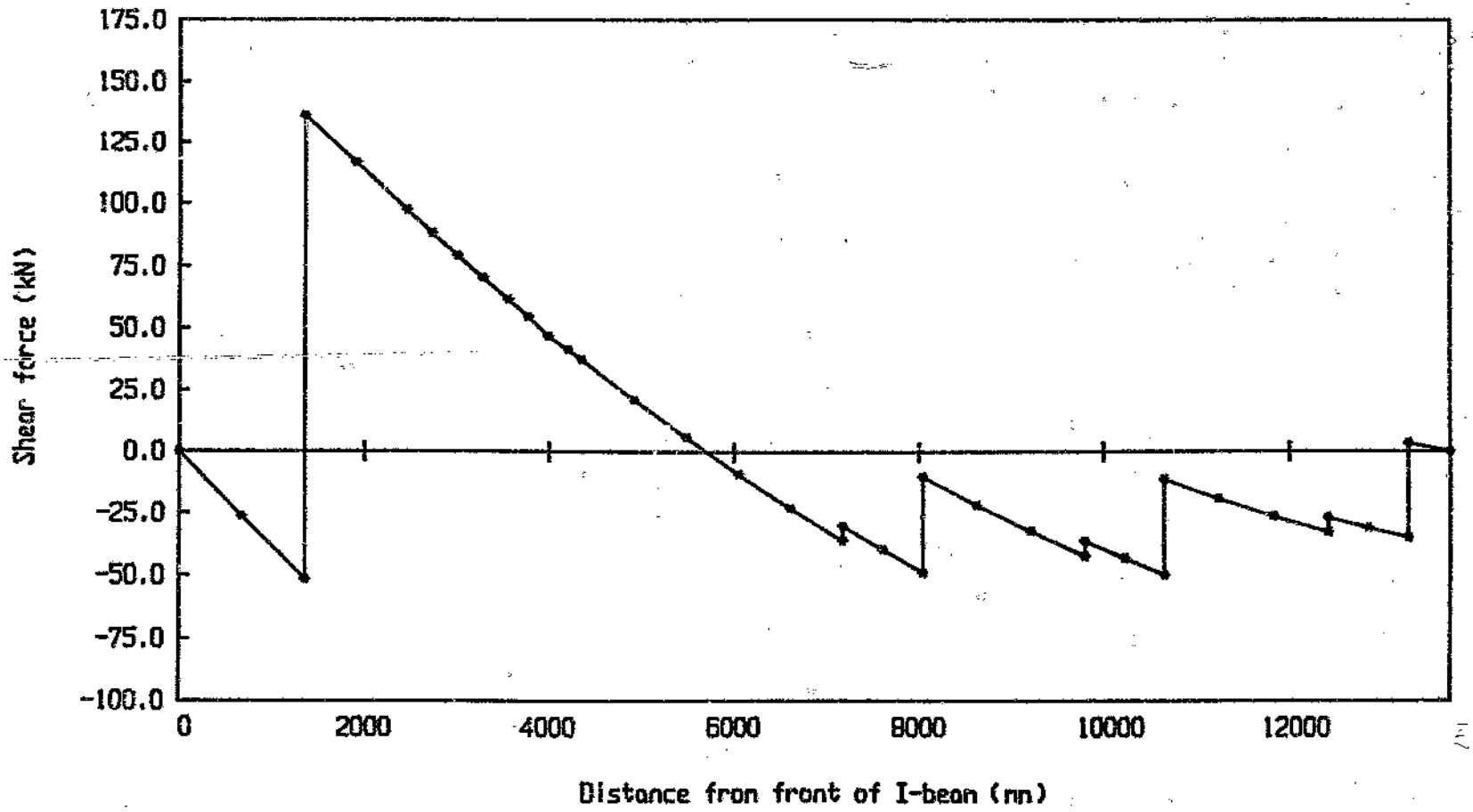
The shear force, bending moment and deflection diagrams for each of these loading situations from the results of Appendix B are presented in Graphs 4.11 to 4.22.

4.3.2 Stress distributions in main chassis I-beams

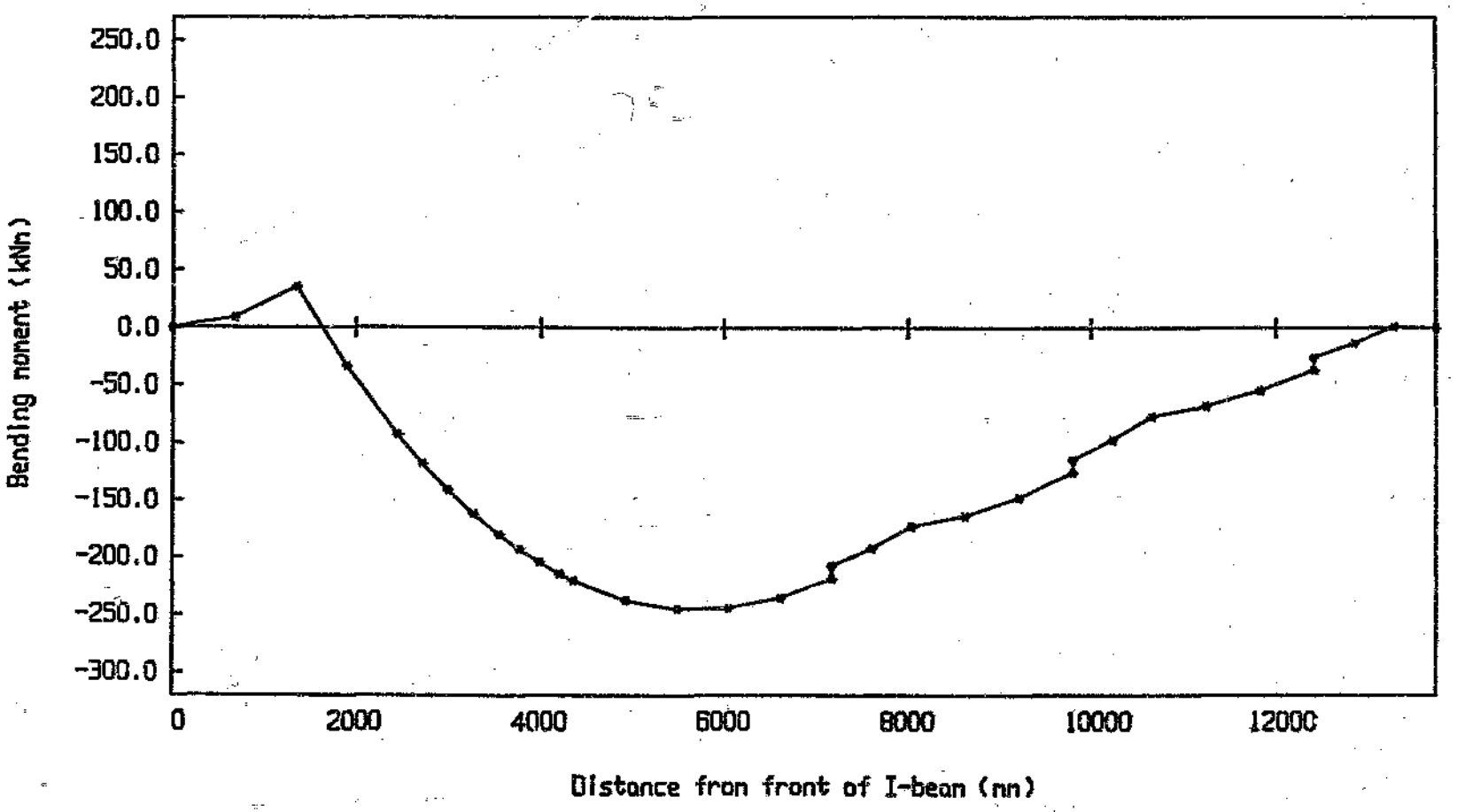
The twelve stress distributions listed below were calculated over the full length of the main chassis I-beams (refer Tables A2 to A7 in Section A.3.1) are presented here in graphical form in Graphs 4.23 to 4.34.

Apart from the distributions of longitudinal direct stress and maximum transverse shear stress (at the neutral axis), three areas of the I-beam cross-section were considered in these analyses. These are the extreme fibres, the web to

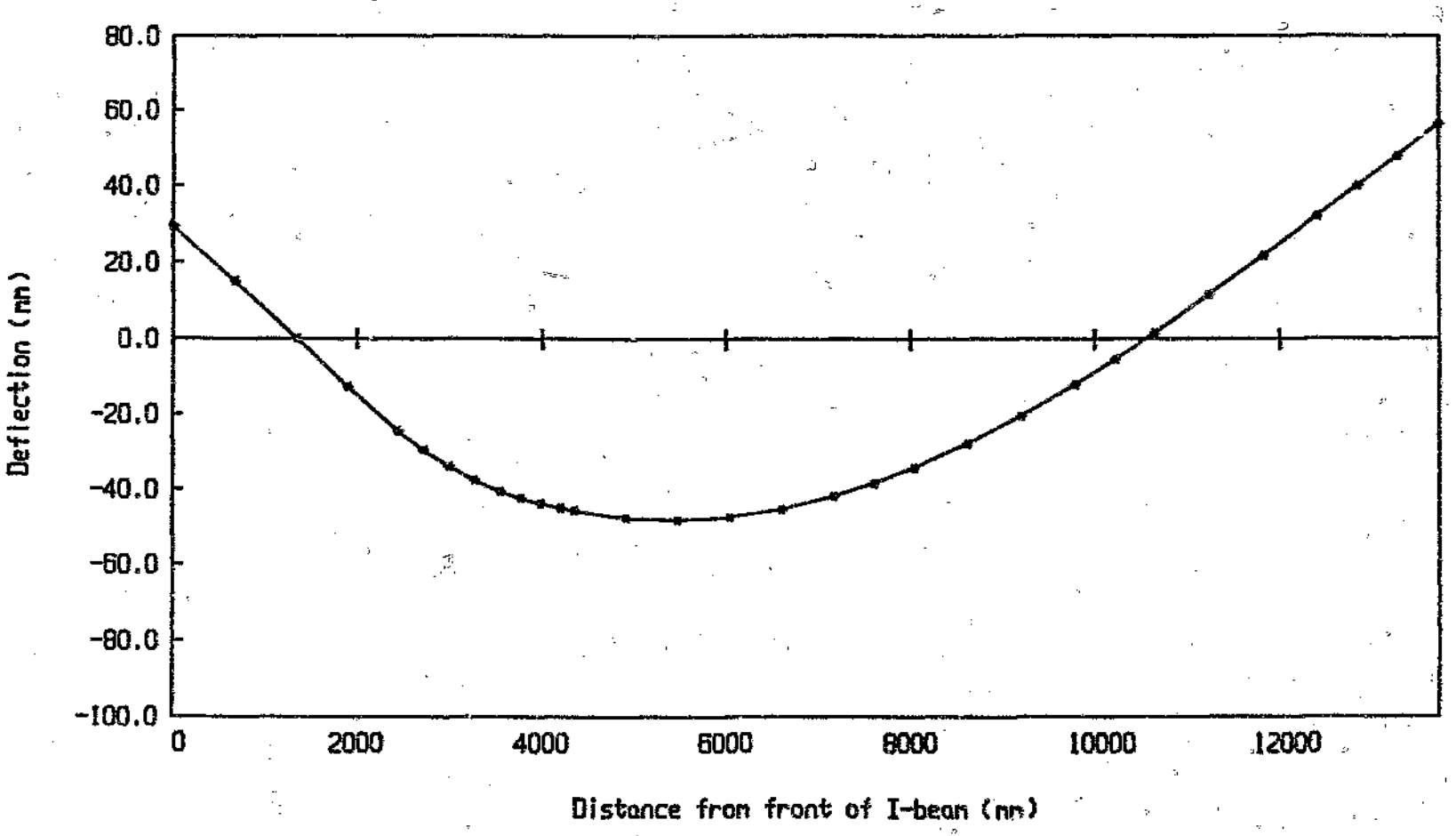
Graph 4.1 Shear force distribution on main chassis I-beam (Case 1 loading)



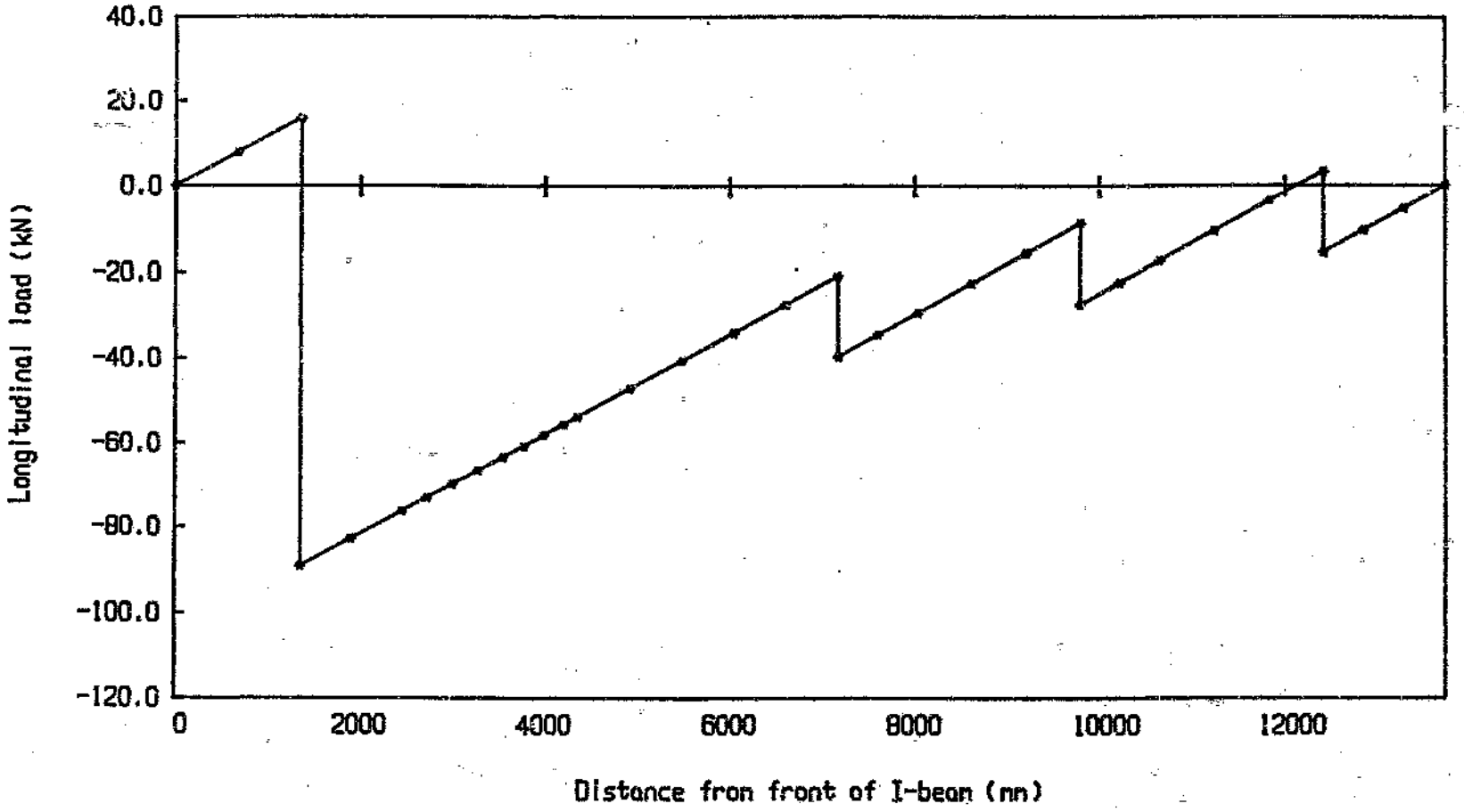
Graph 4.2 Bending moment distribution on main chassis I-beam (Case 1 loading)



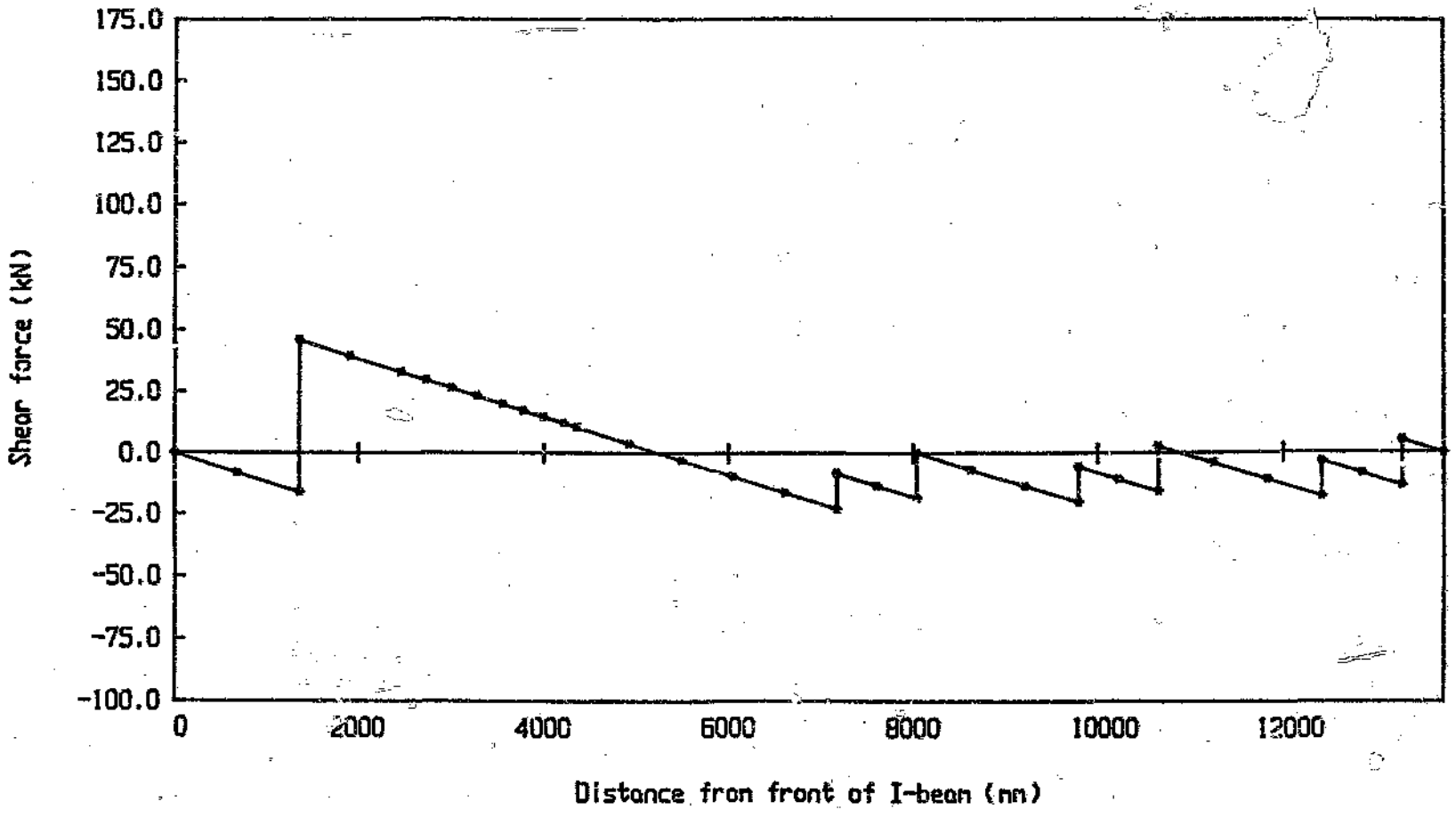
Graph 4.3 Deflection diagram for main chassis I-beam (Case 1 loading)



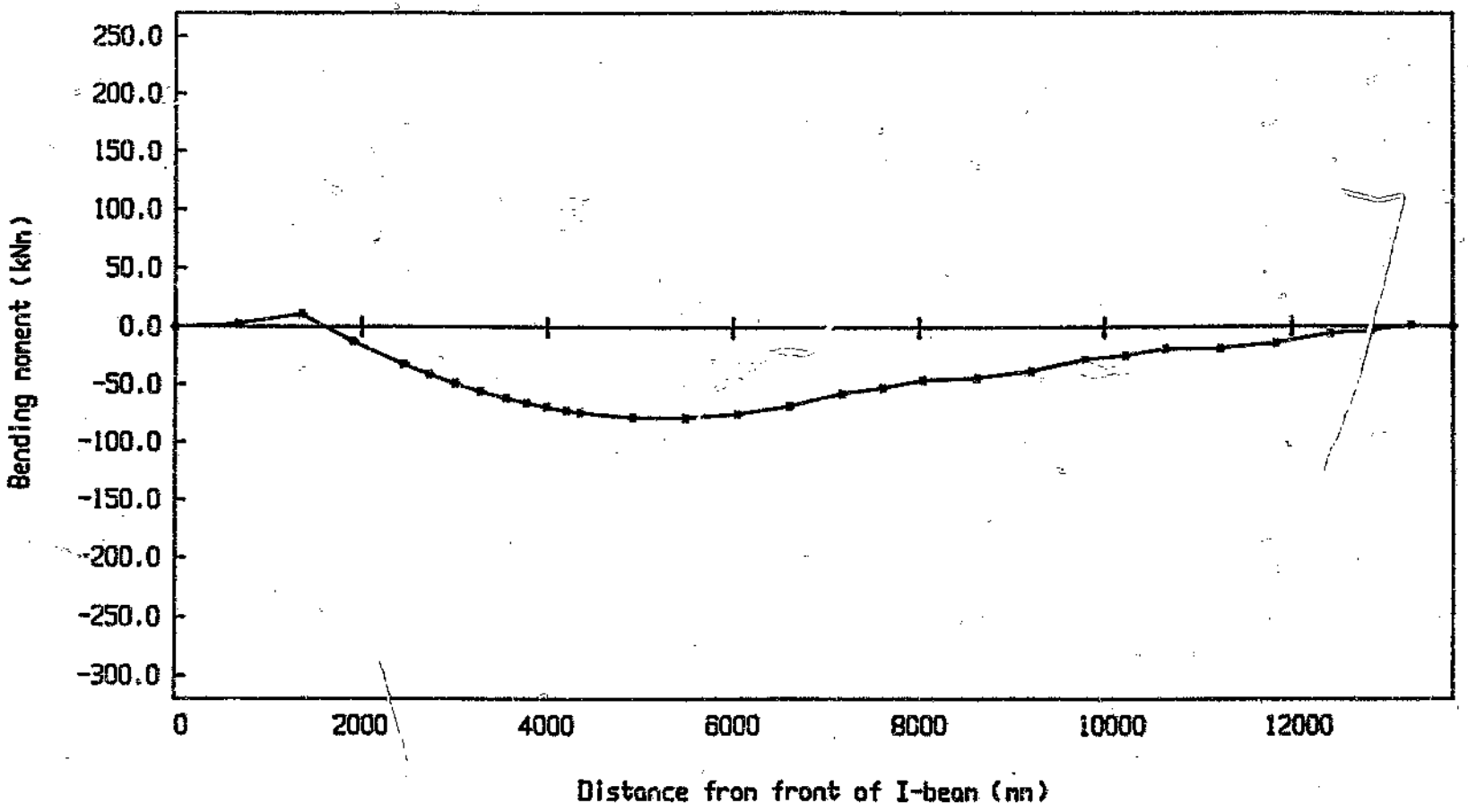
Graph 4.4 Longitudinal loading distribution on main chassis I-beam (Case 1 loading)



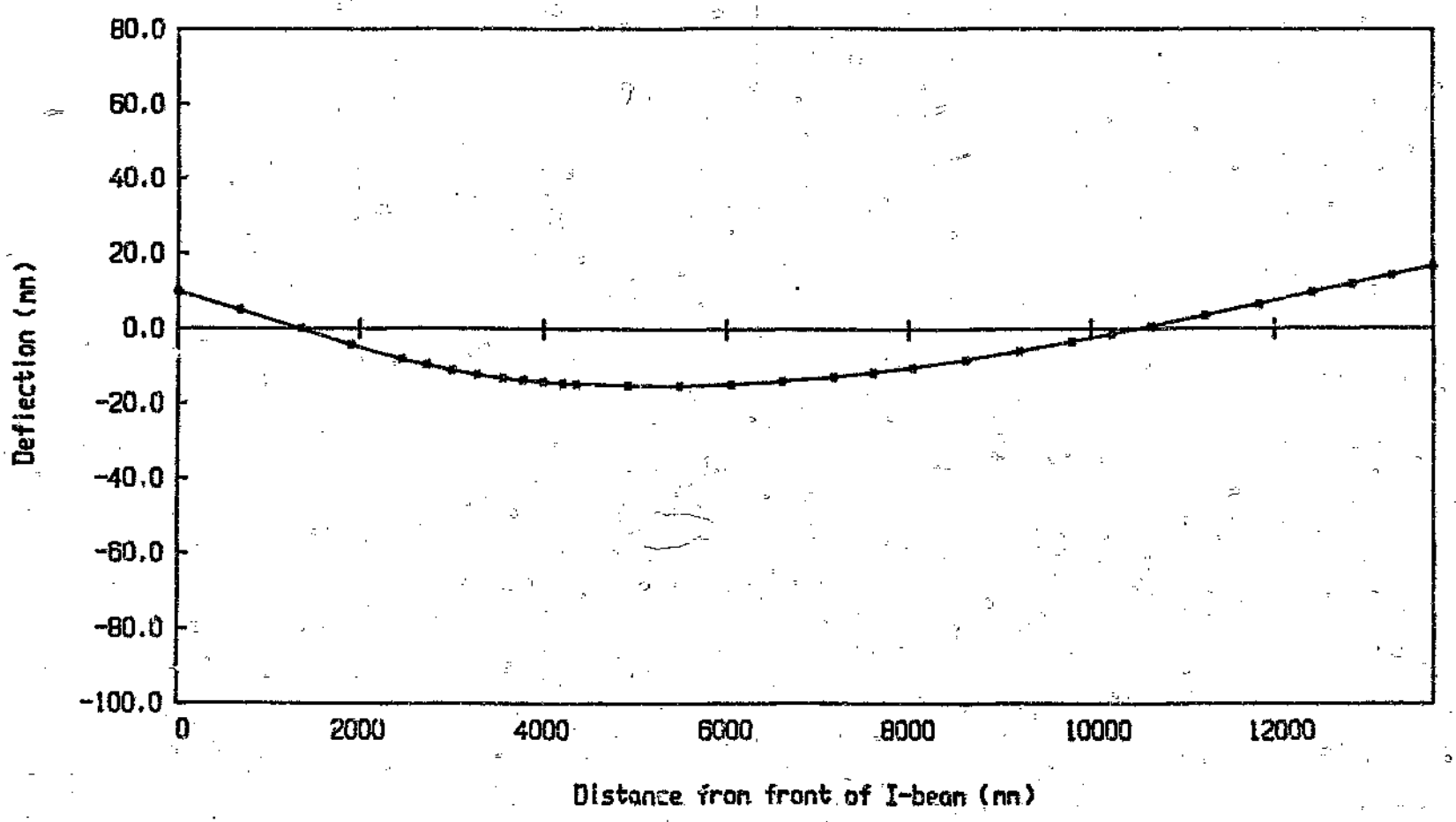
Graph 4.5 Shear force distribution on main chassis I-beam (Case 2 loading)



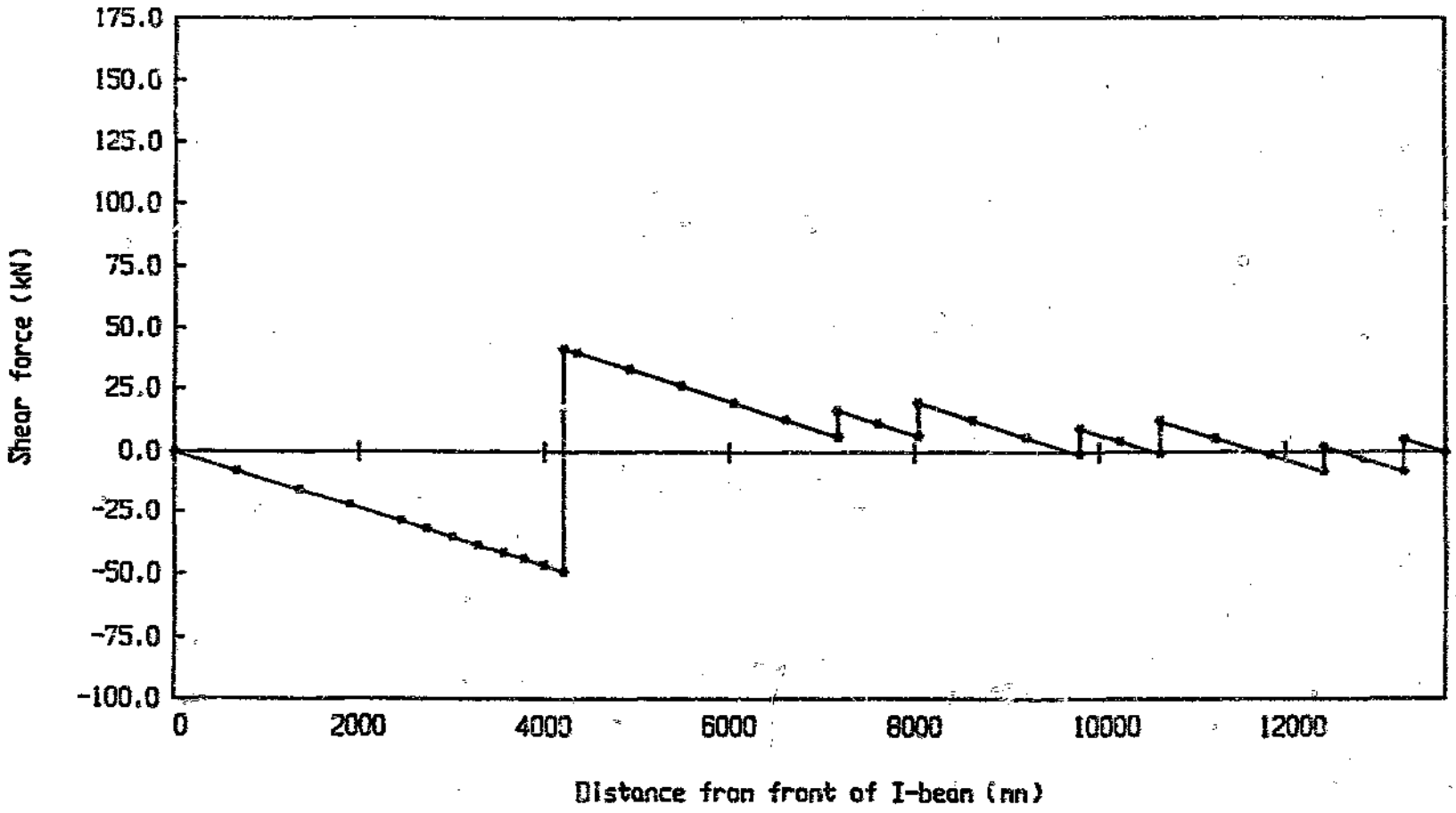
Graph 4.6 Bending moment distribution on main chassis I-beam (Case 2 loading)



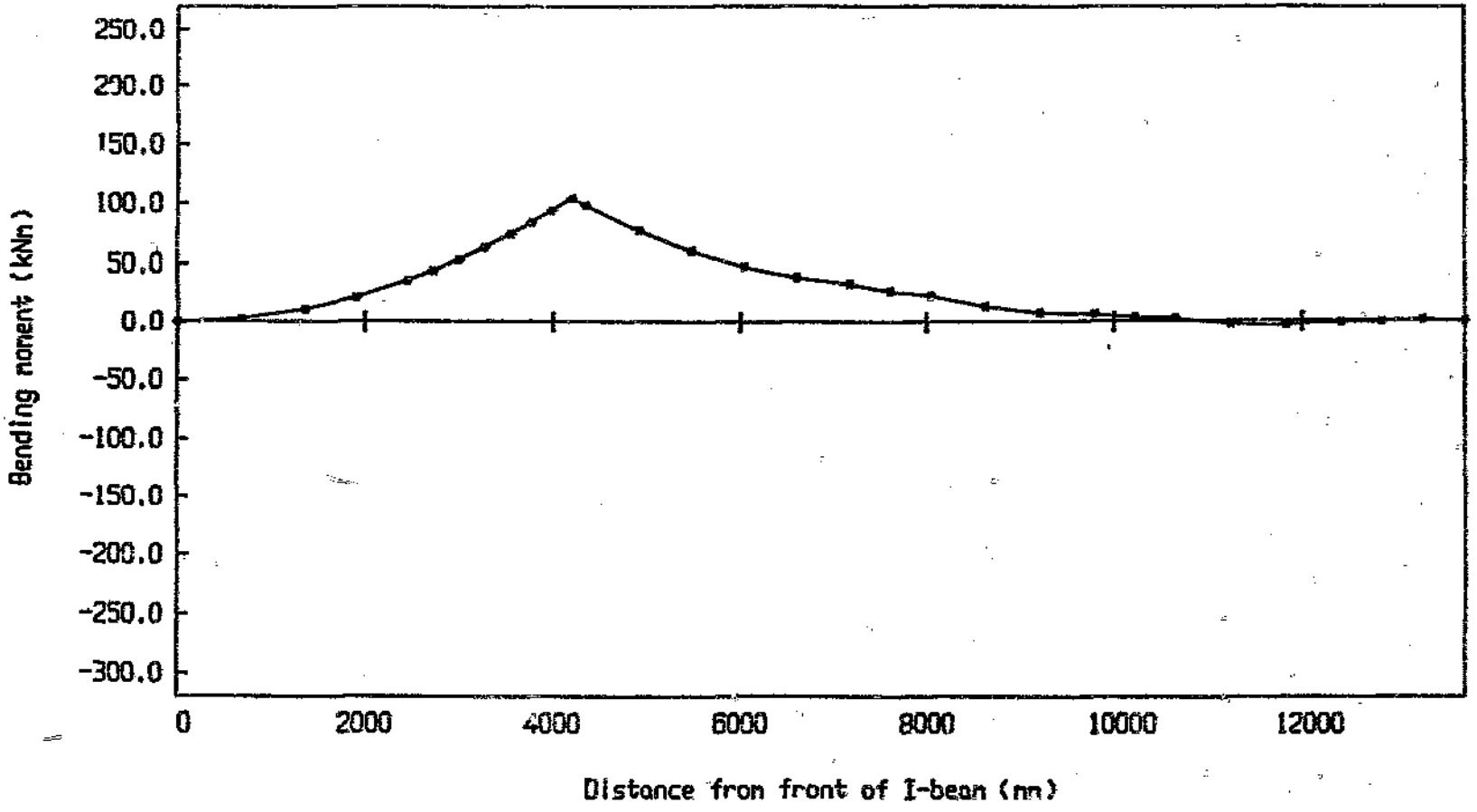
Graph 4.7 Deflection diagram for main chassis I-beam (Case 2 loading)



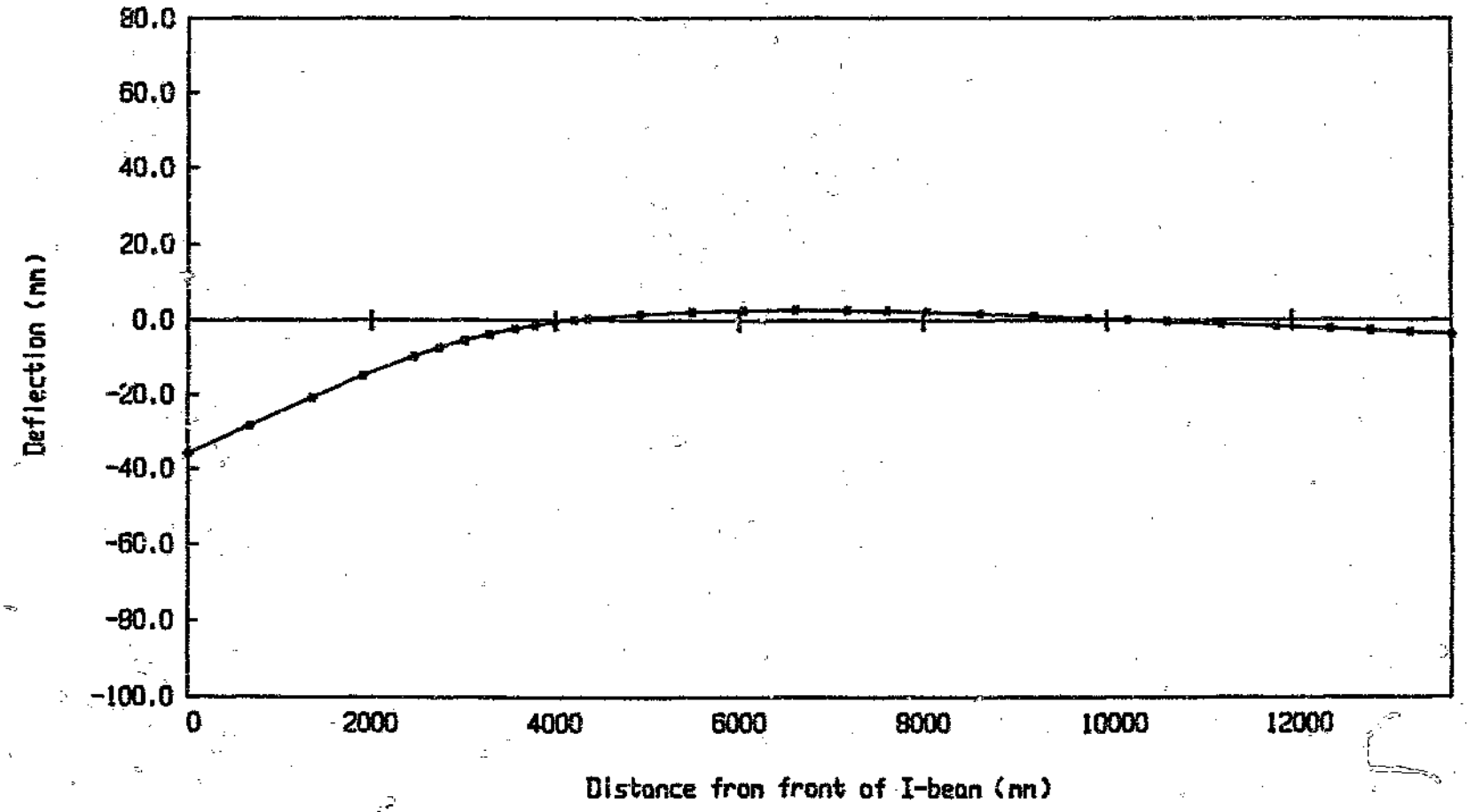
Graph 4.8 Shear force distribution on main chassis I-beam (Case 3 loading)



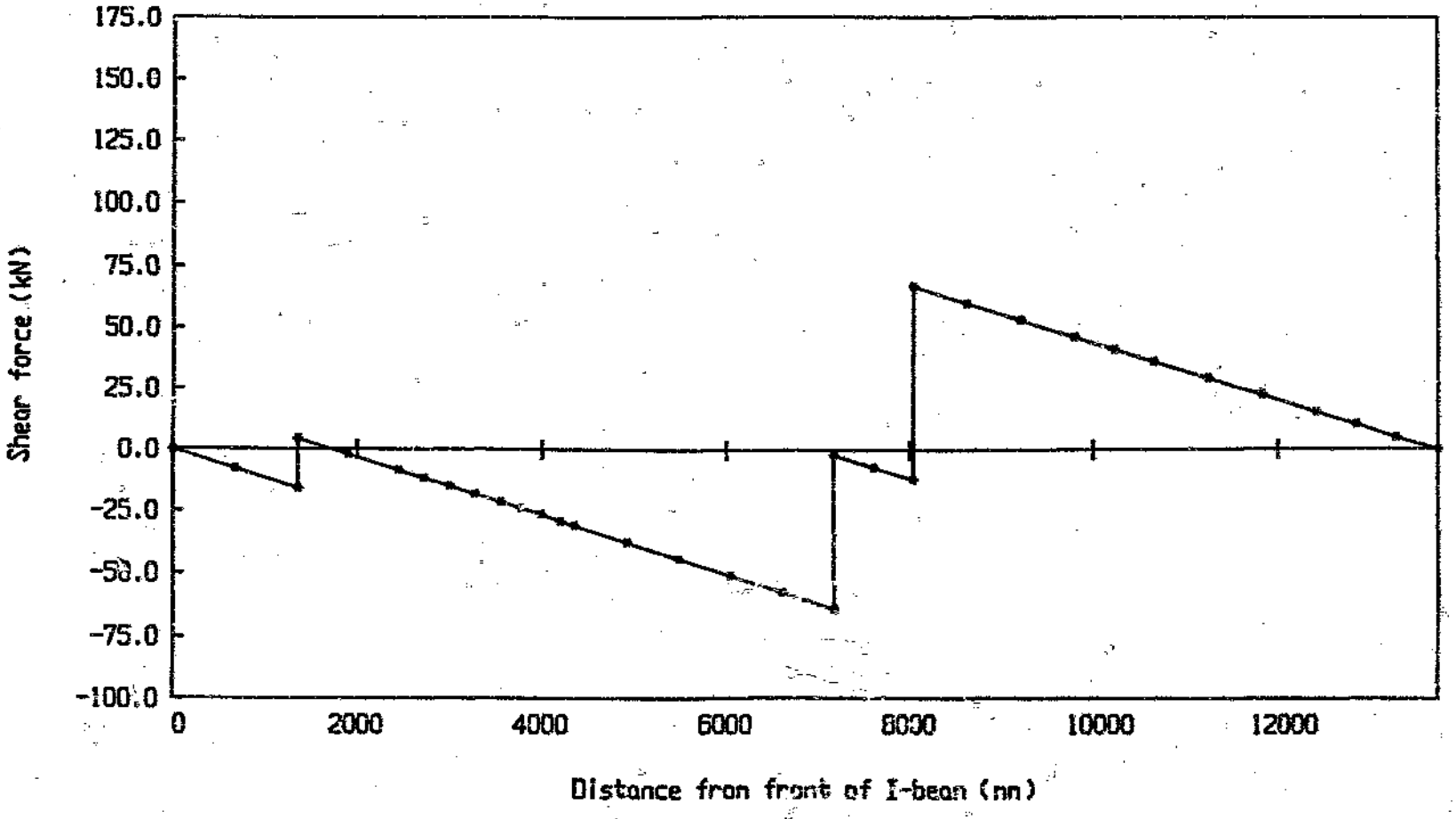
Graph 4.9 Bending moment distribution on main chassis I-beam (Case 3 loading)



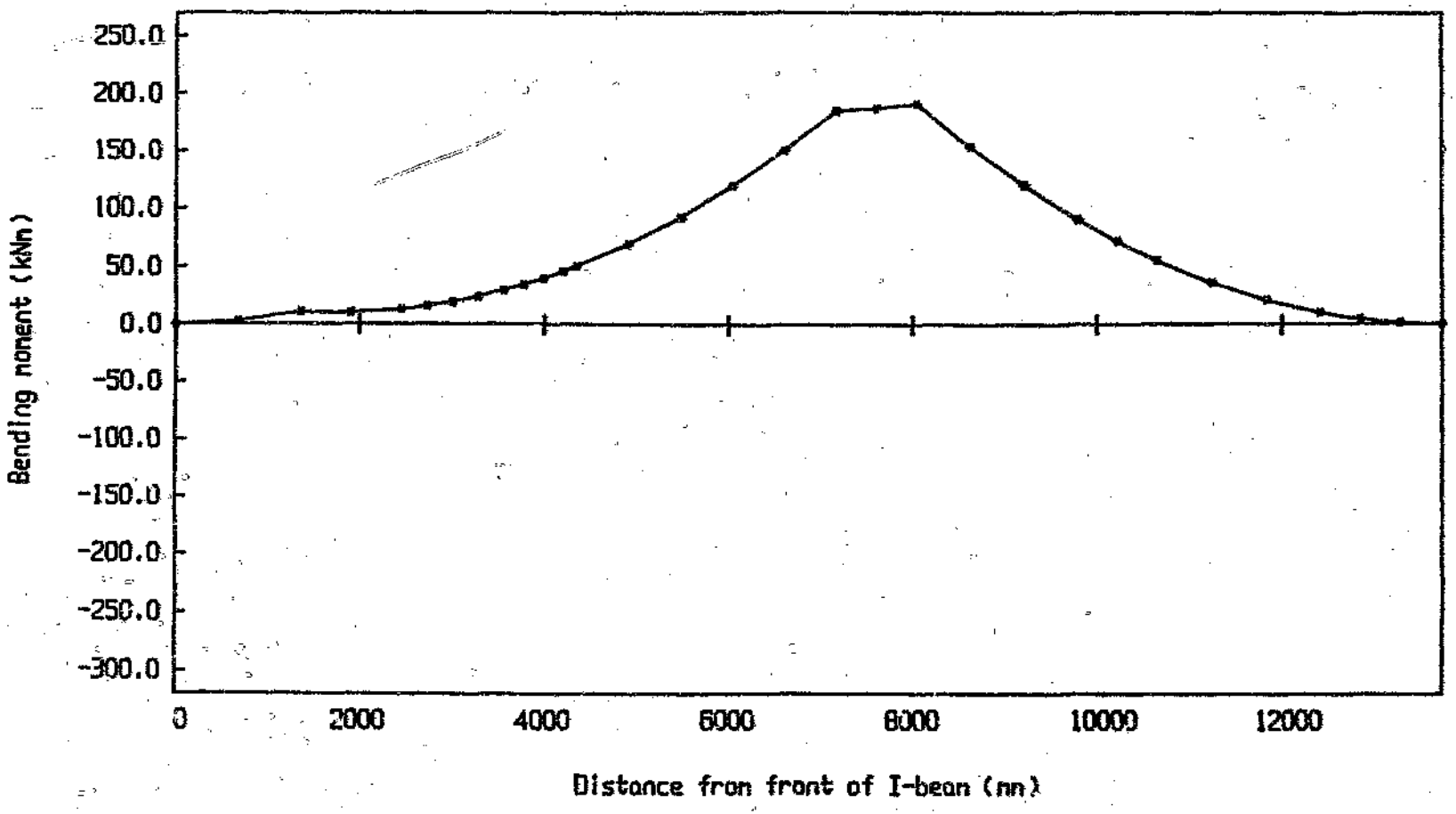
Graph 4.10 Deflection diagram for main chassis I-beam (Case 3 loading)



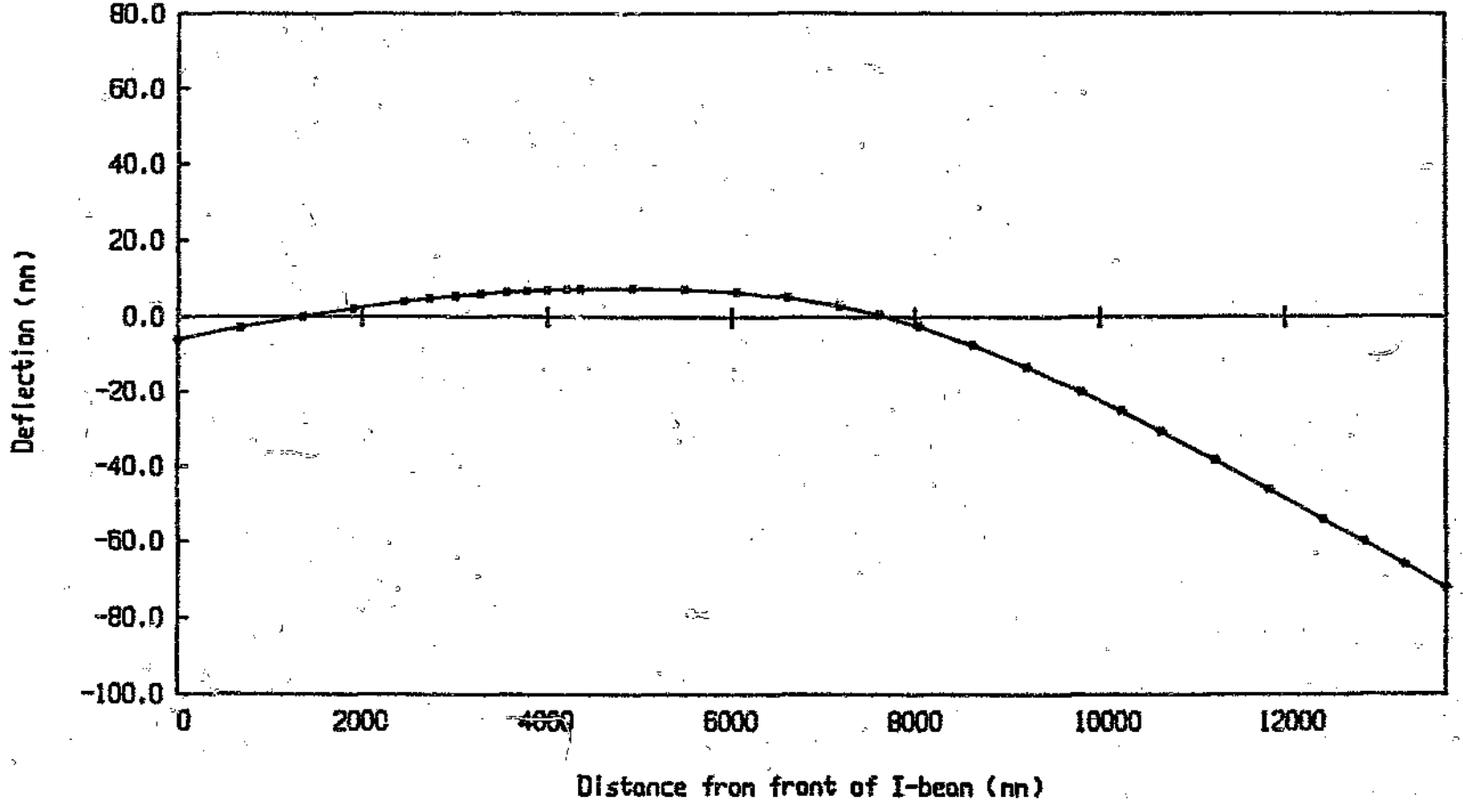
Graph 4.11 Shear force distribution on main chassis I-beam (Case 4 loading)



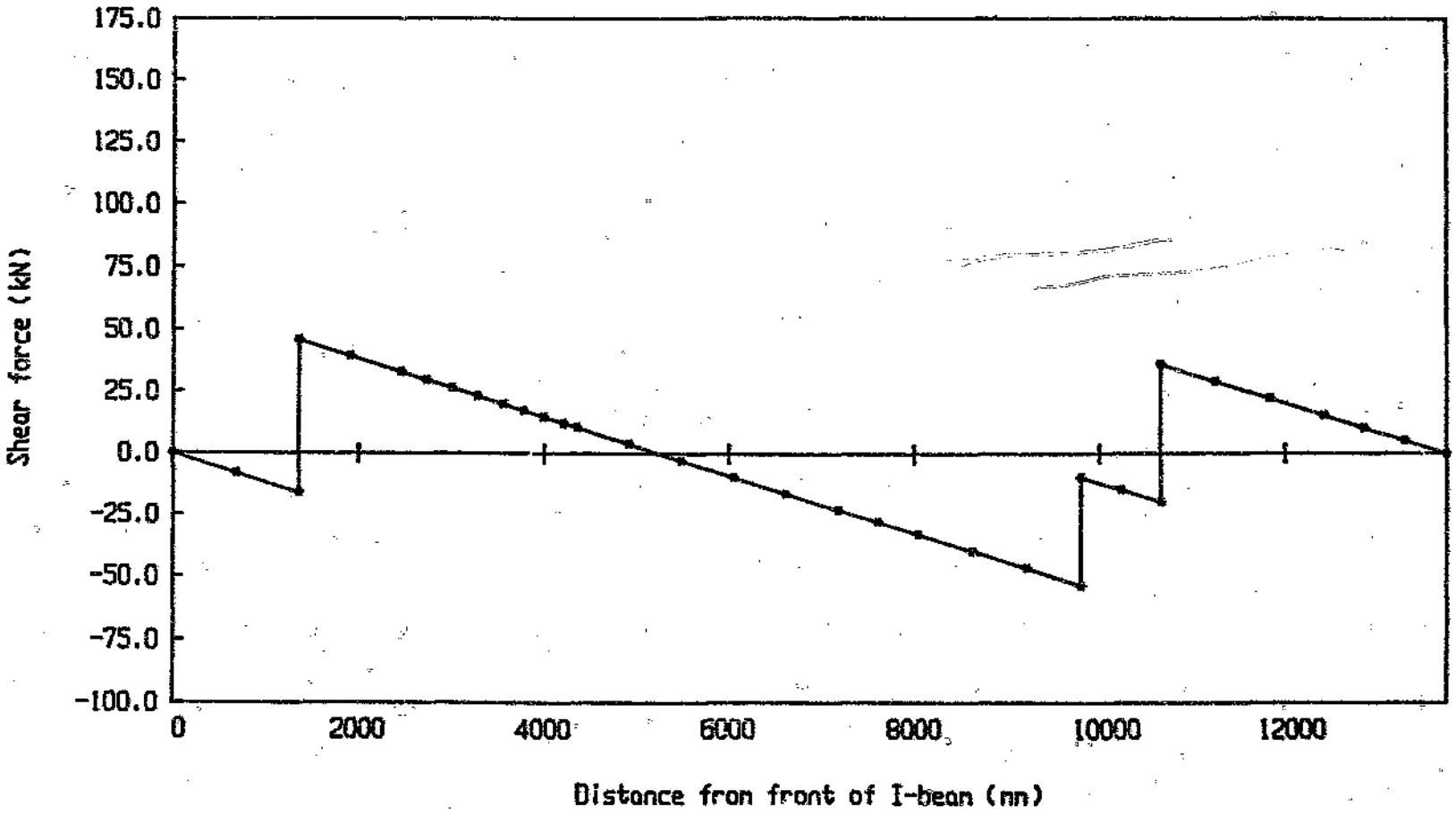
Graph 4.12 Bending moment distribution on main chassis I-beam (Case 4 loading)



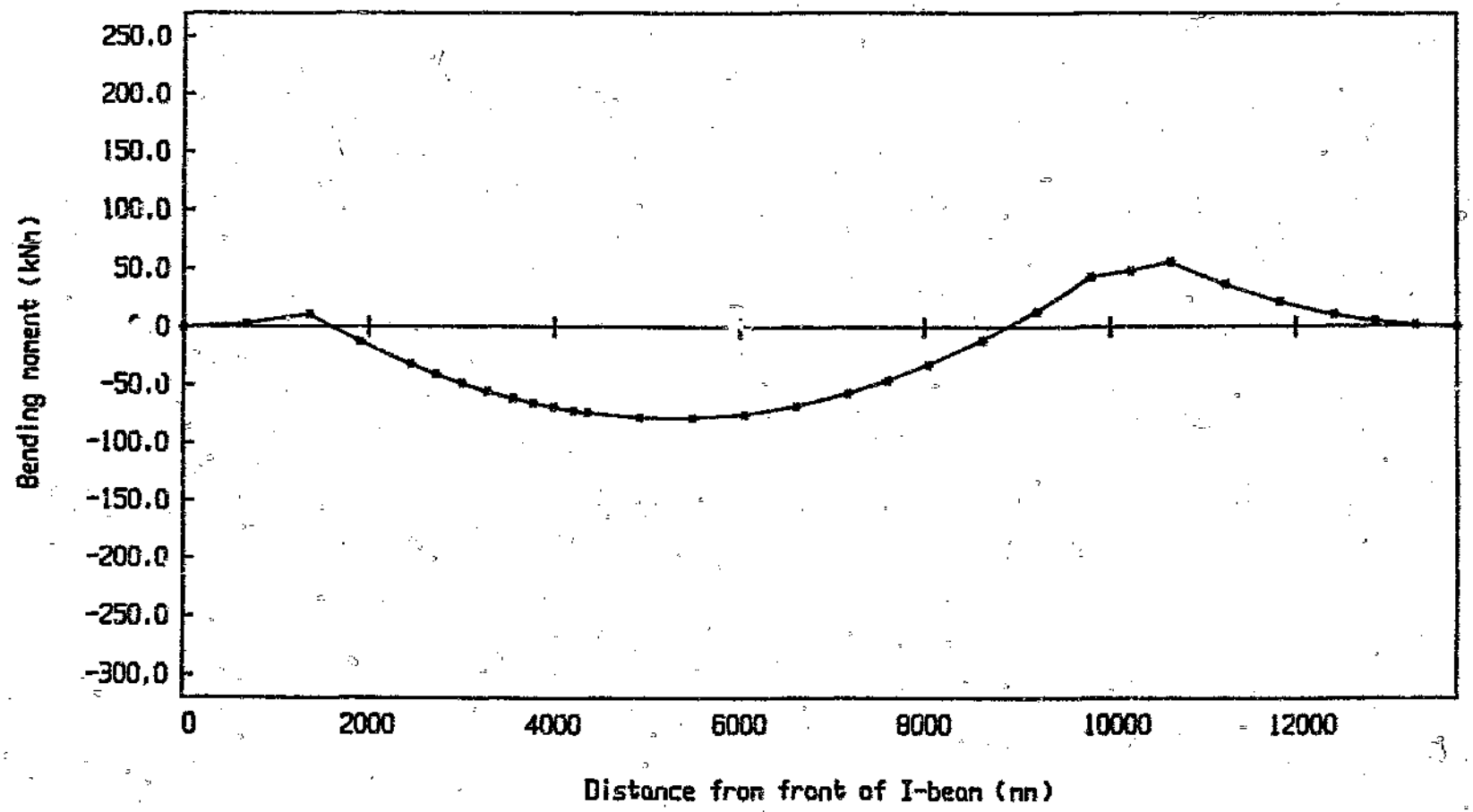
Graph 4.13 Deflection diagram for main chassis I-beam (Case 4 loading)



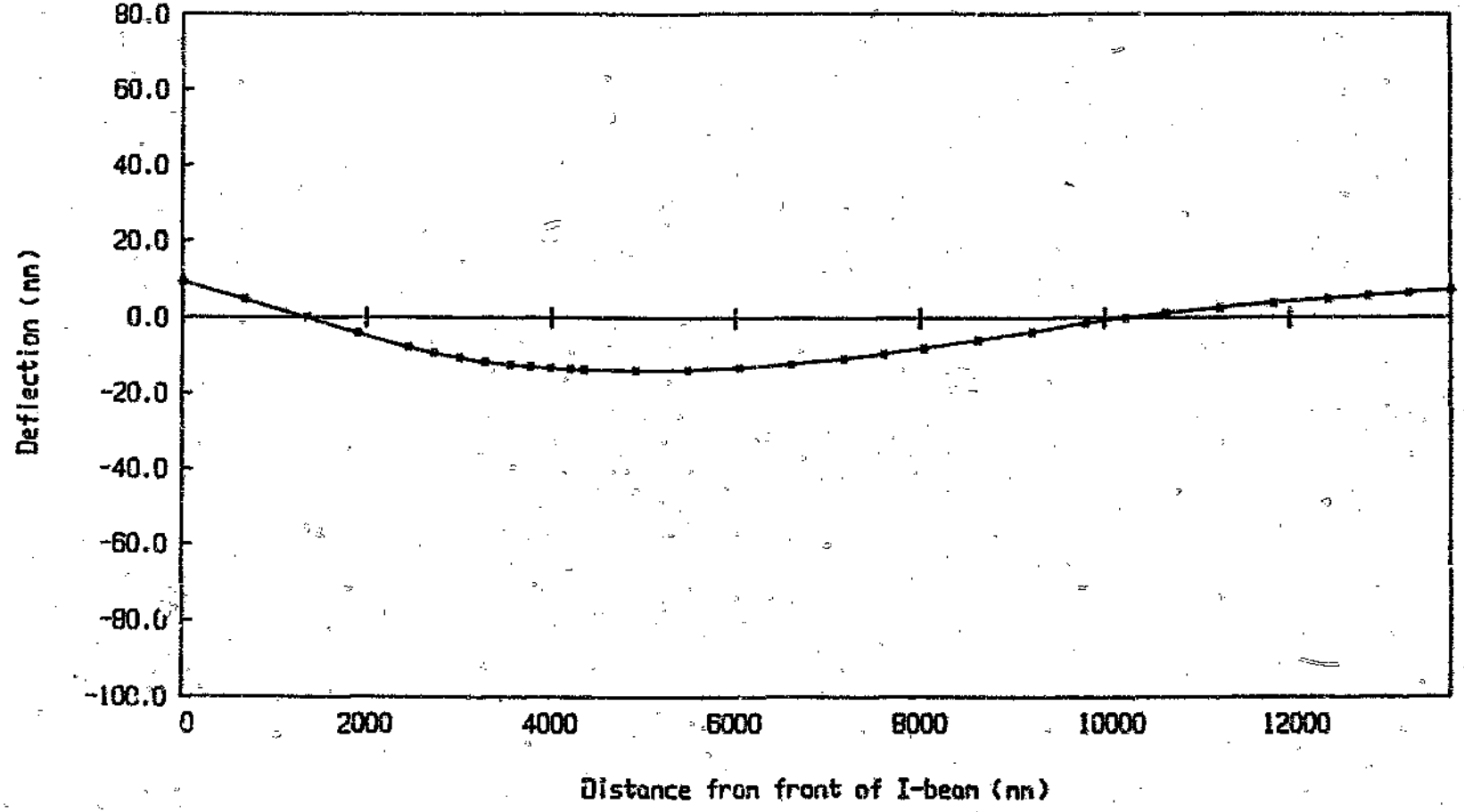
Graph 4.14 Shear force distribution on main chassis I-beam (Case 5 loading)



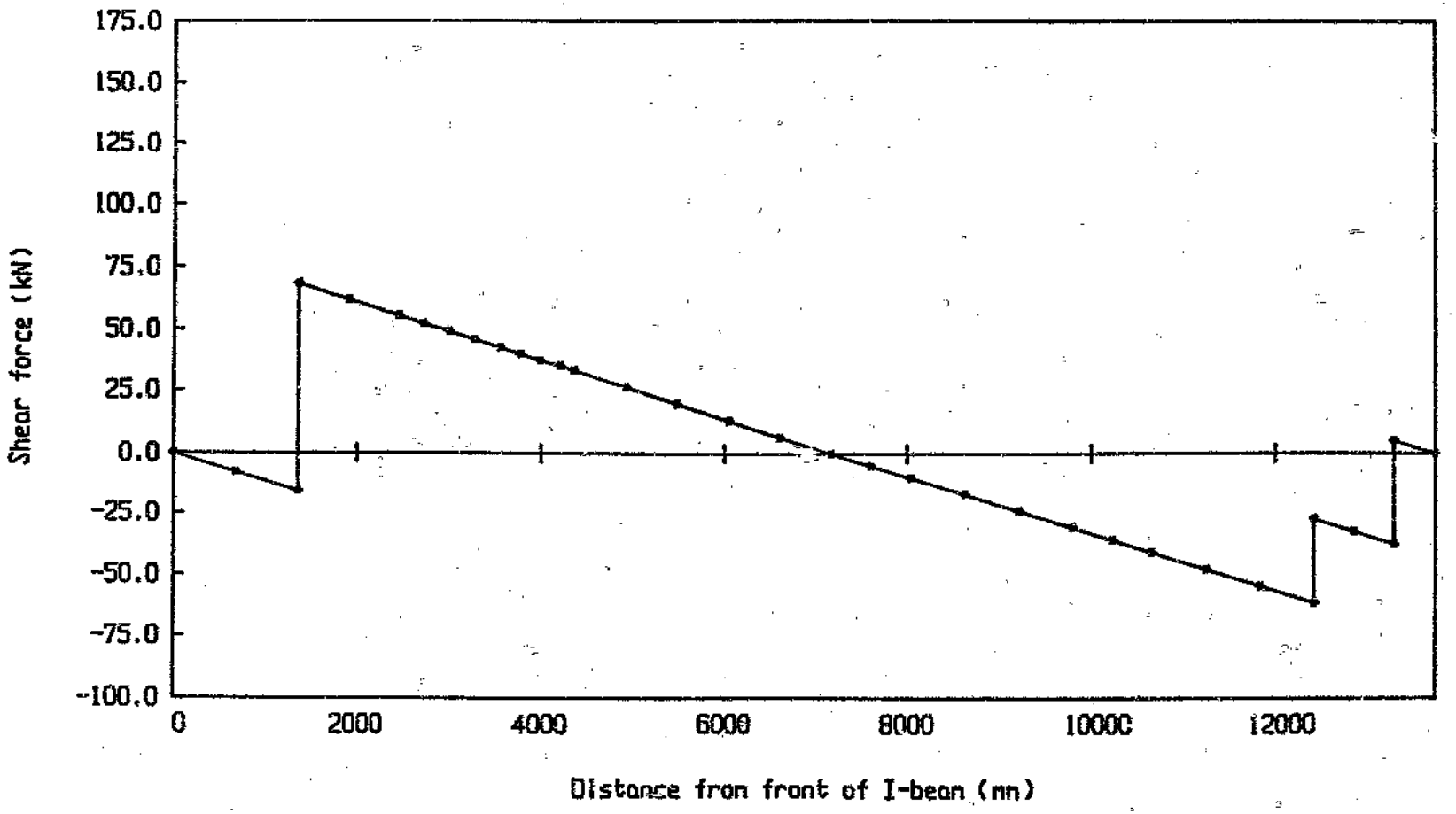
Graph 4.15 Bending moment distribution on main chassis I-beam (Case 5 loading)



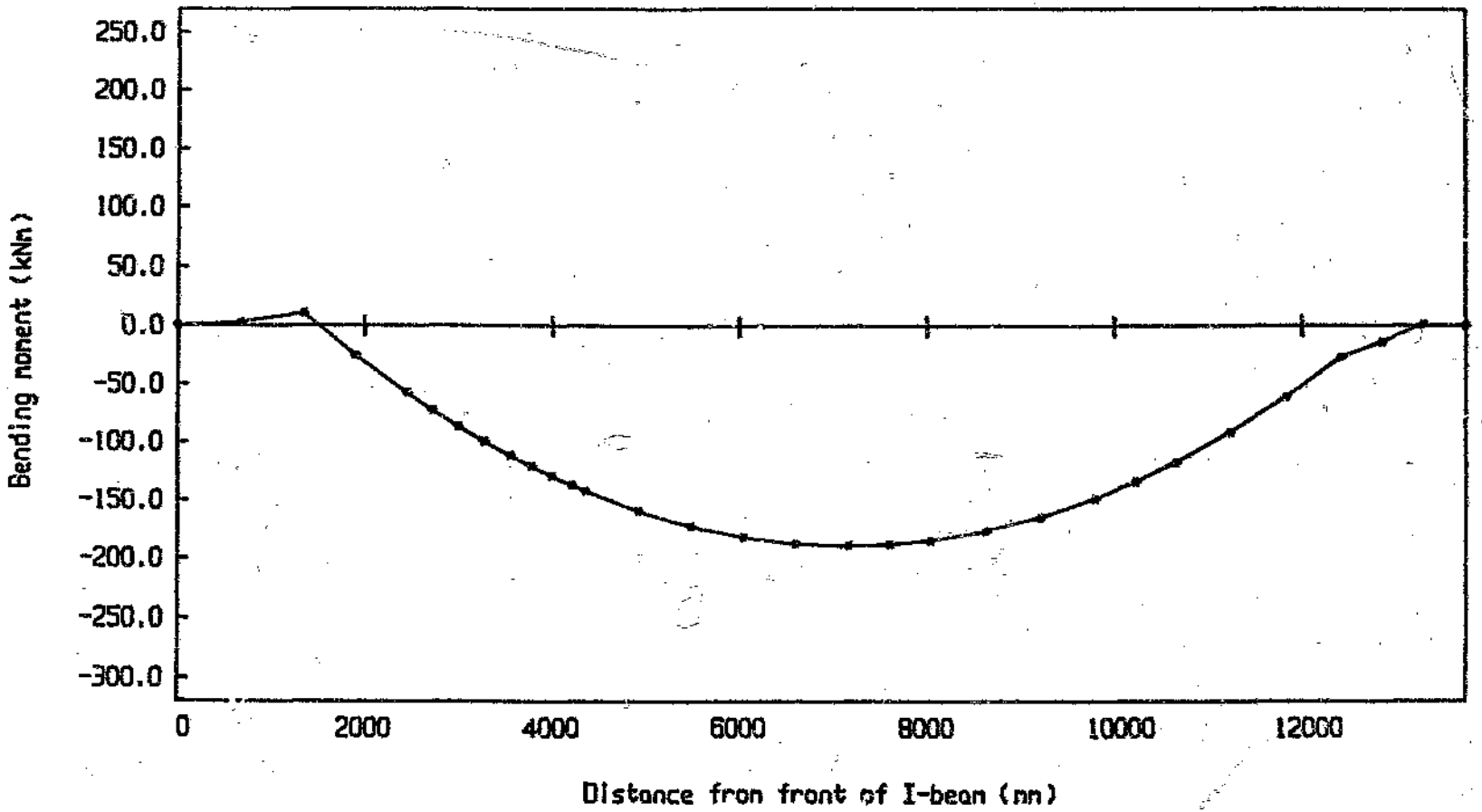
Graph 4.16 Deflection diagram for main chassis I-beam (Case 5 loading)



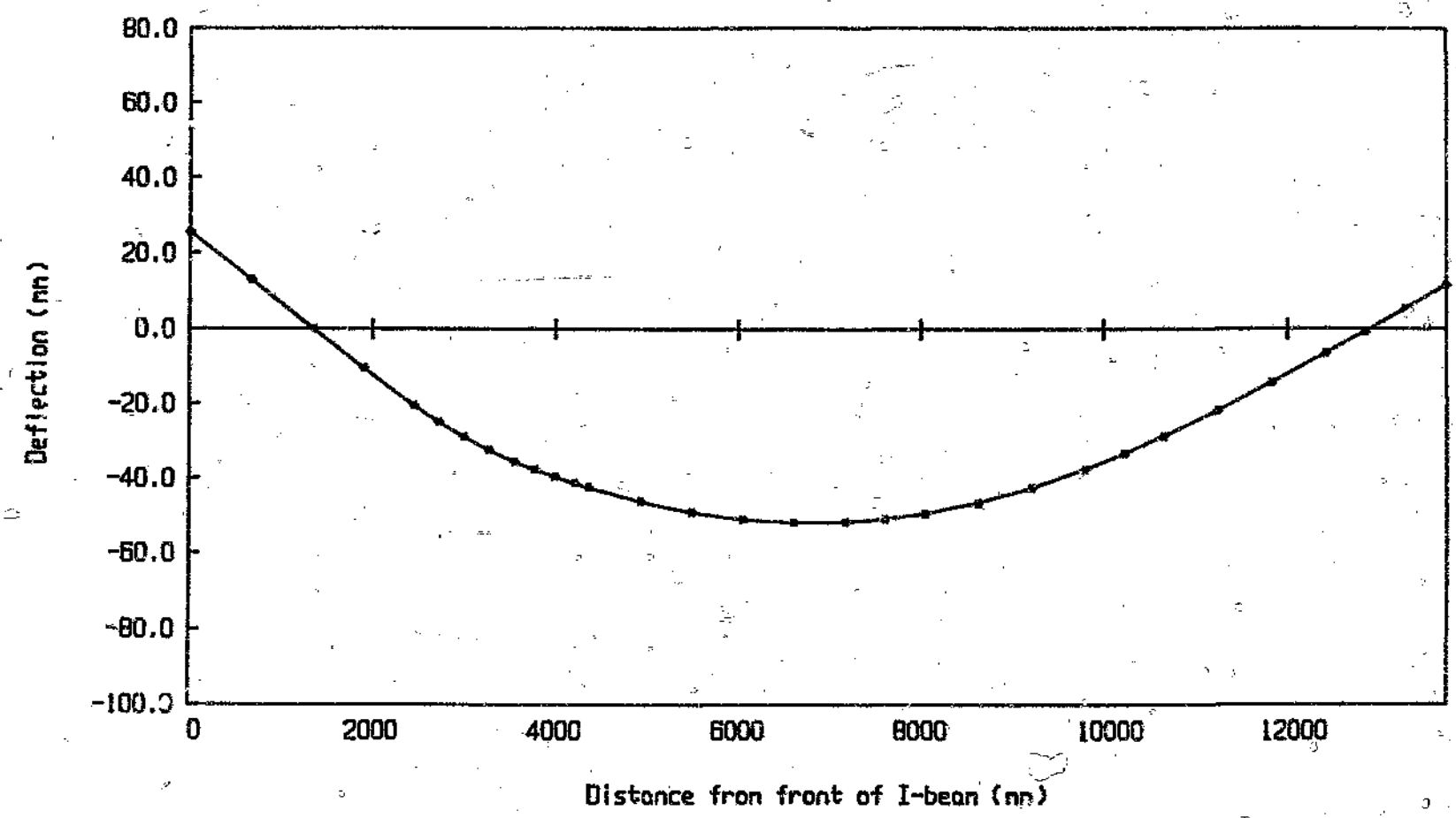
Graph 4.17 Shear force distribution on main chassis I-beam (Case 6 loading)



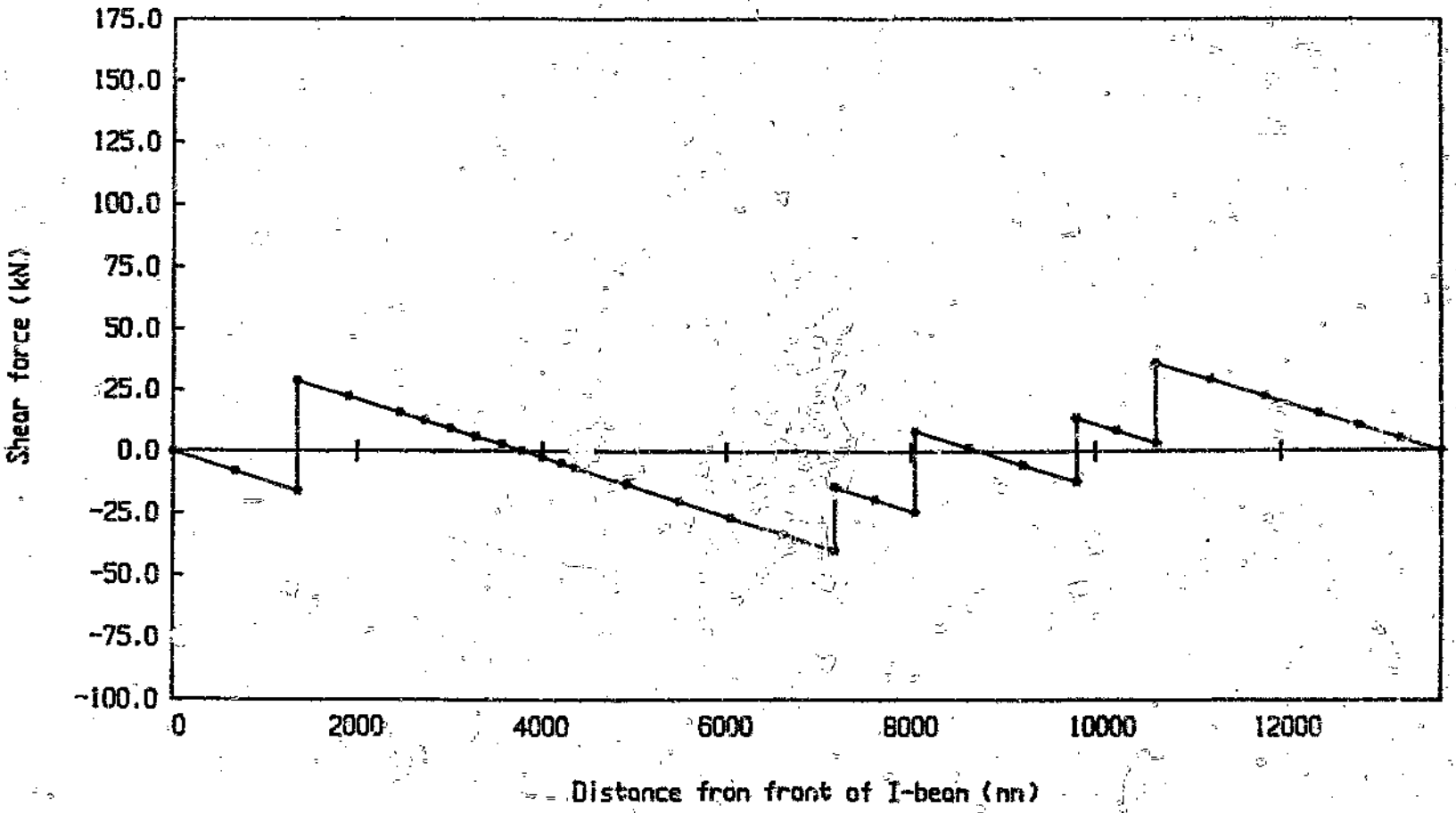
Graph 4.18 Bending moment distribution on main chassis I-beam (Case 6 loading)



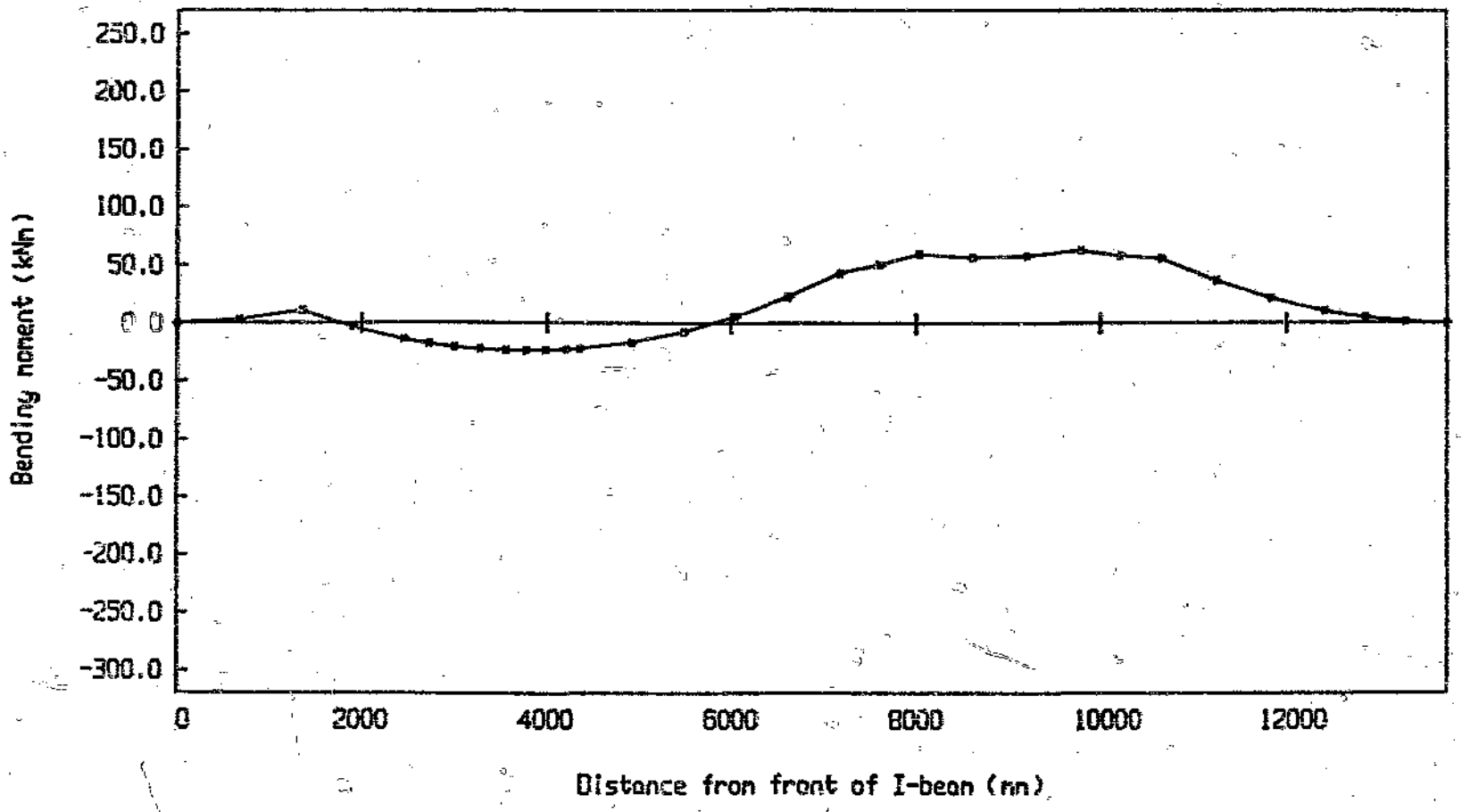
Graph 4.19 Deflection diagram for main chassis I-beam (Case 6 loading)



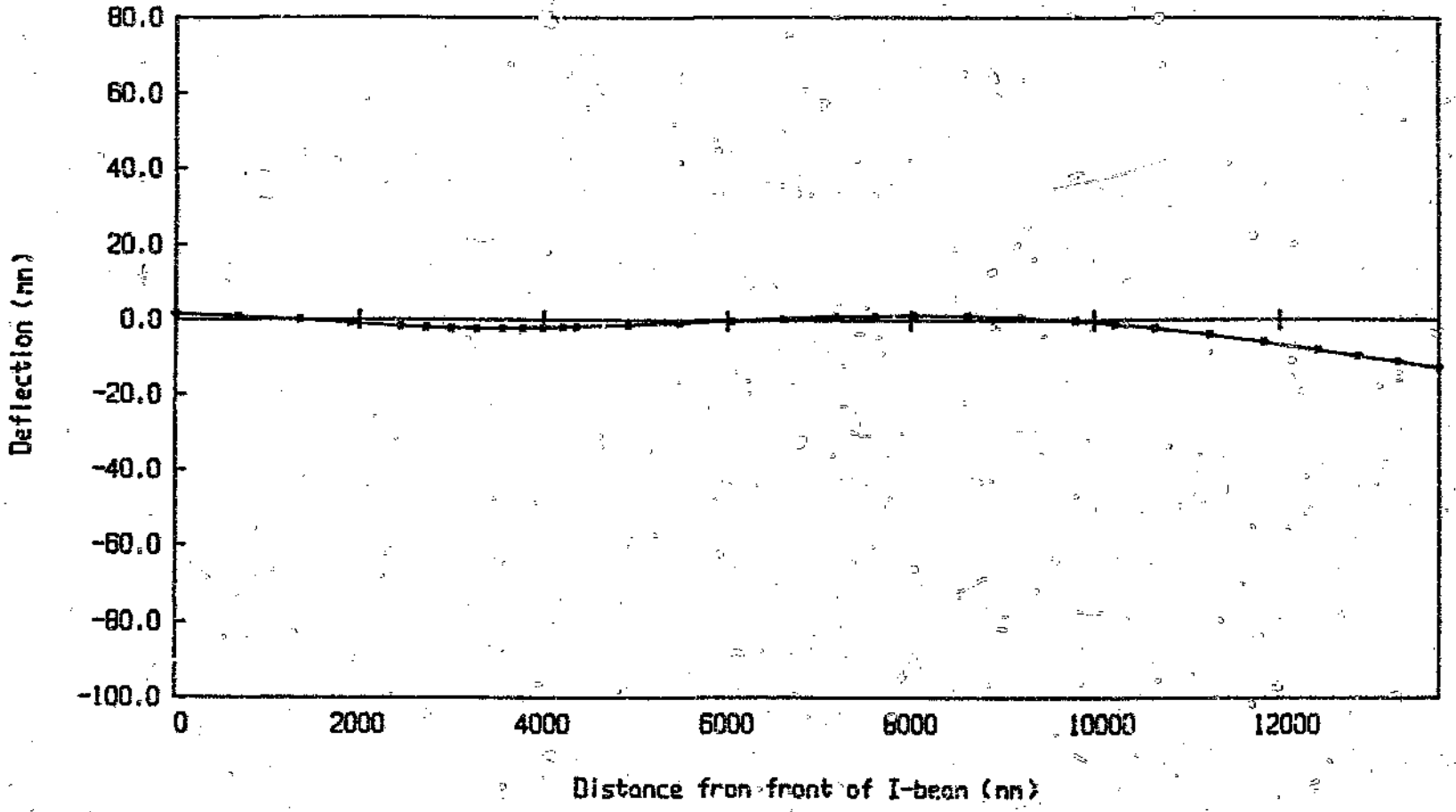
Graph 4.20 Shear force distribution on main chassis I-beam (Case 7 loading)



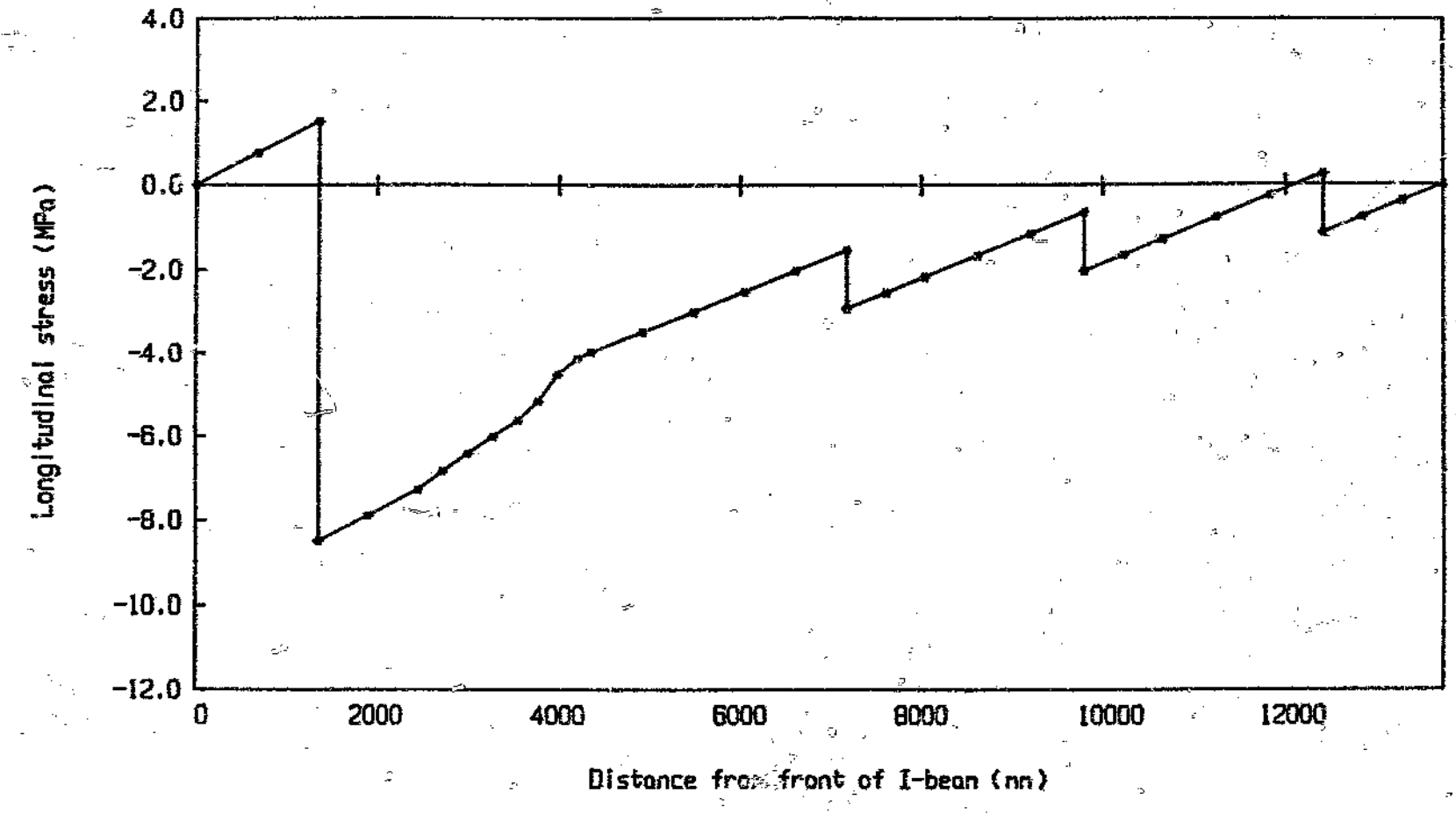
Graph 4.21 Bending moment distribution on main chassis I-beam (Case 7 loading)



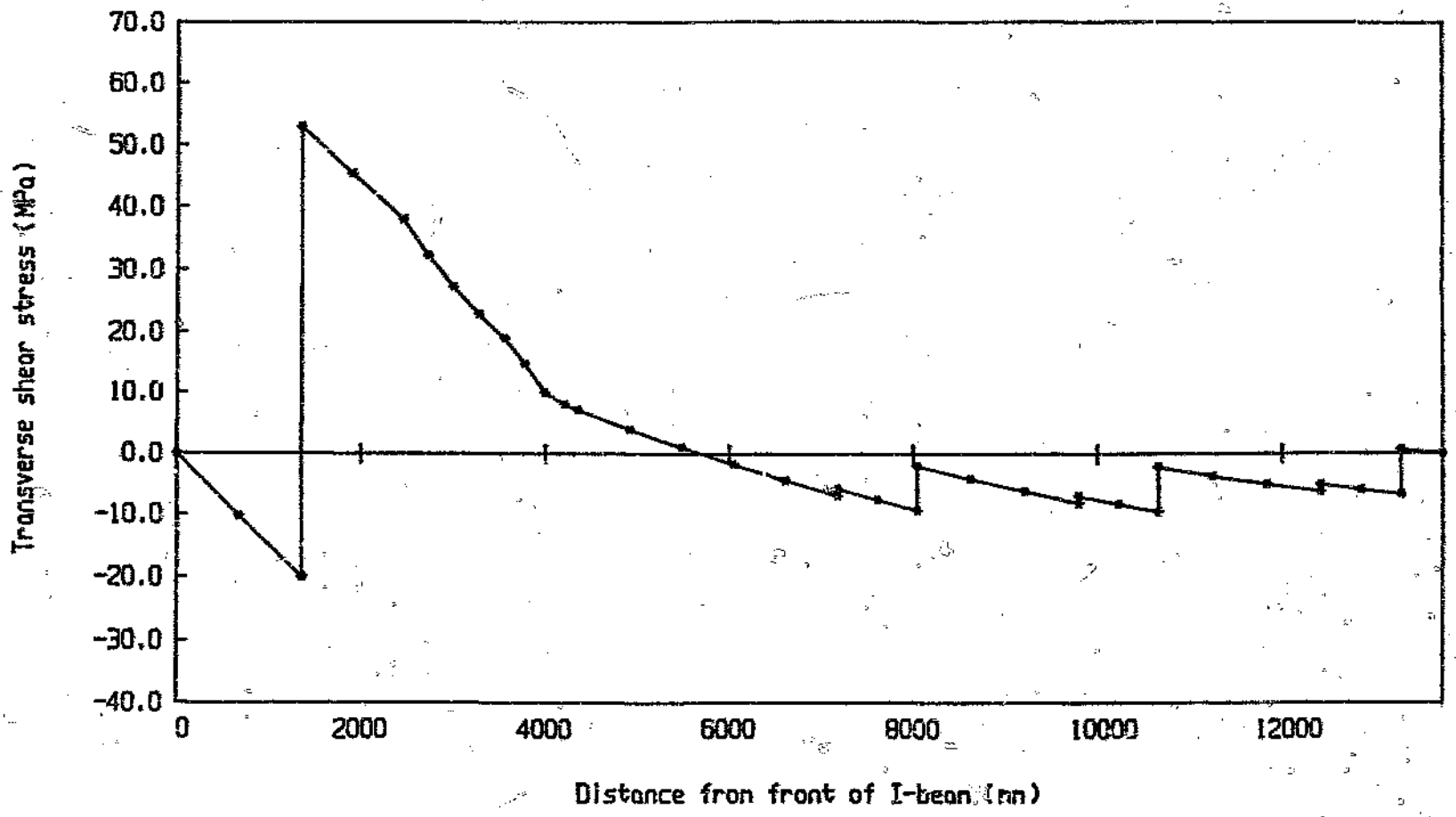
Graph 4.22 Deflection diagram for main chassis I-beam (Case 7 loading)



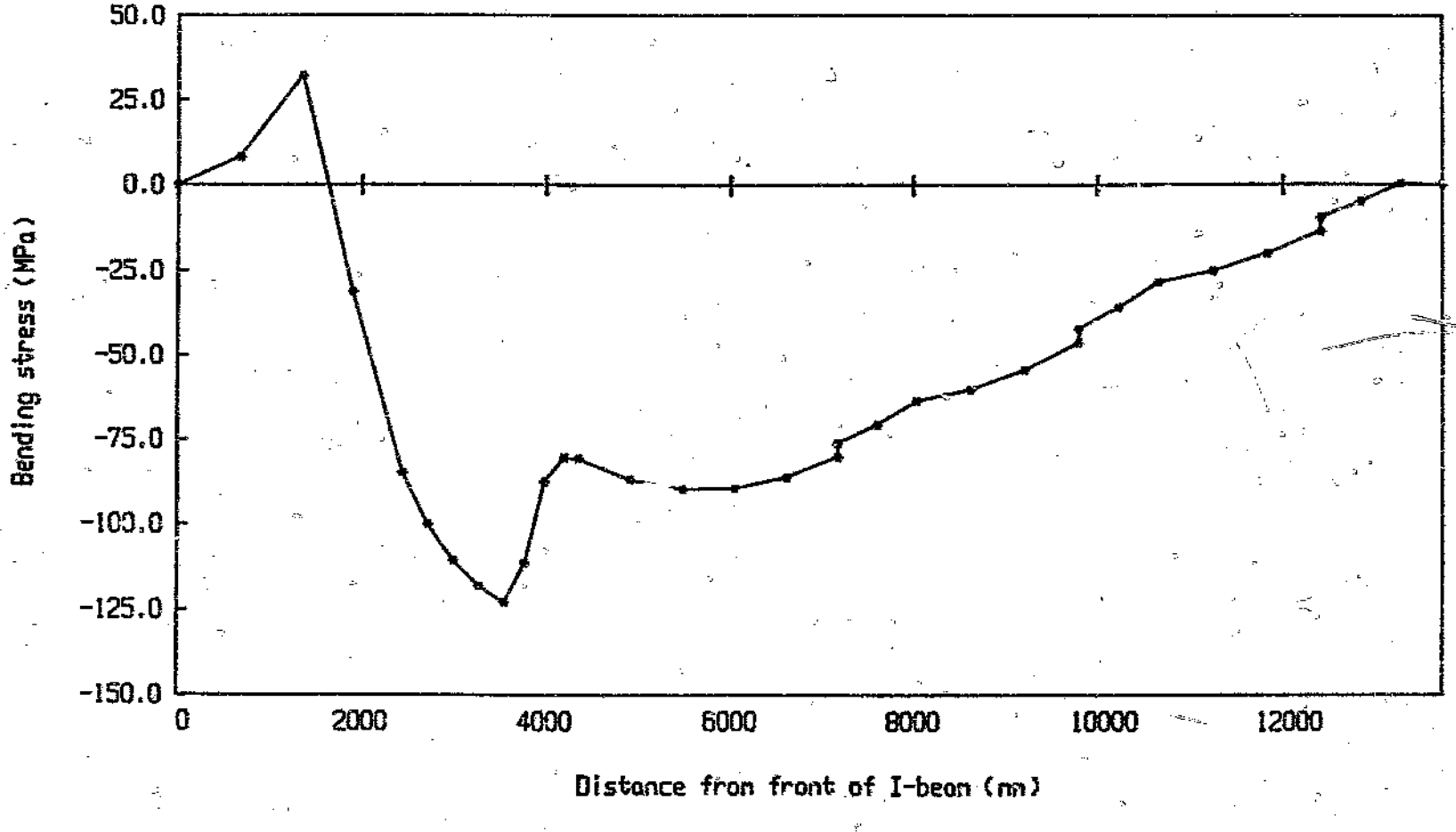
Graph 4.23 Longitudinal direct stress distribution (Case 1 loading)



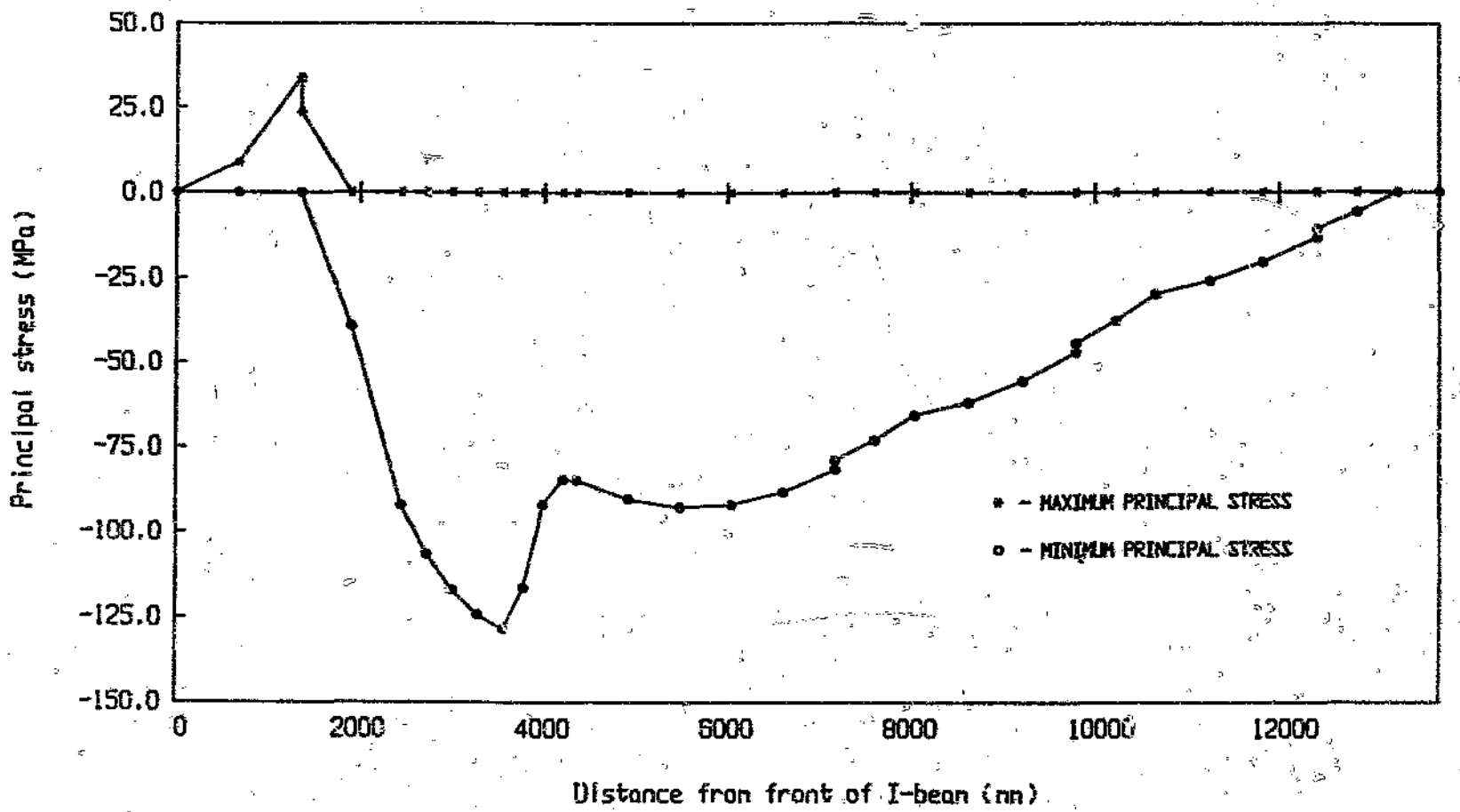
Graph 4.24 Maximum transverse shear stress distribution (Neutral axis - Case 1 loading)



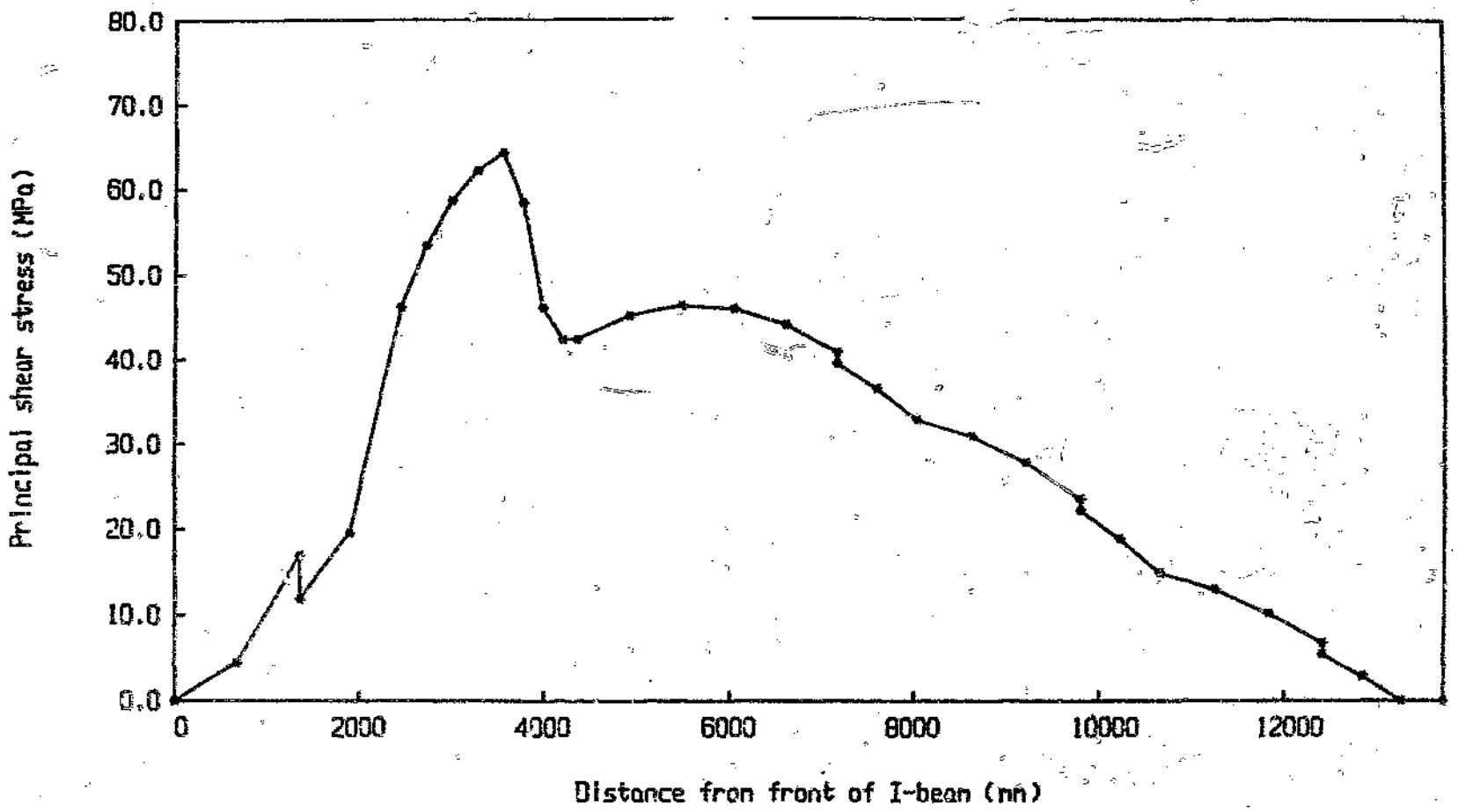
Graph 4.25 Extreme fibre bending stress distribution (Upper flange - Case 1 loading)



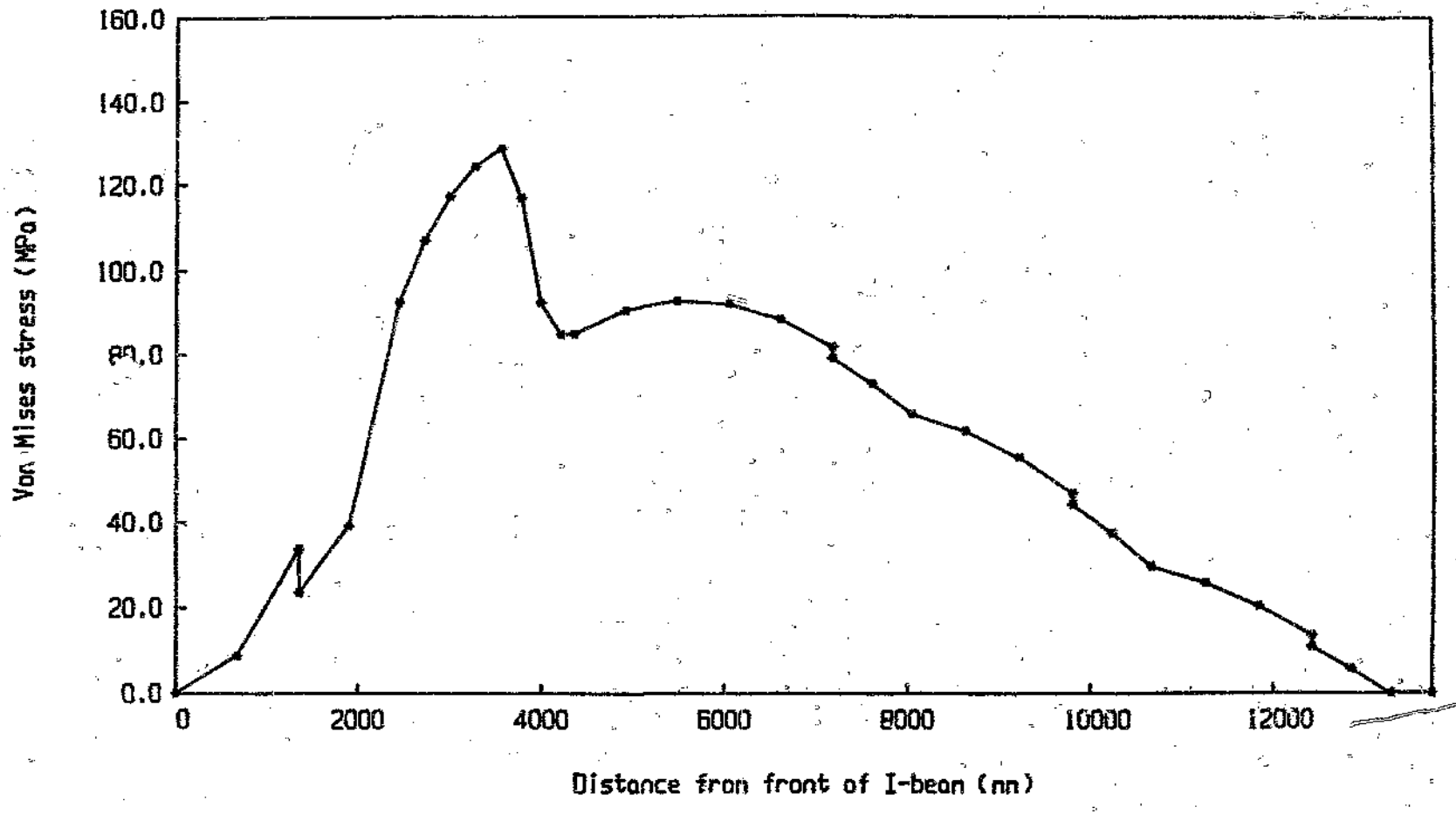
Graph 4.26 Principal stress distribution at the extreme fibres (Upper flange - Case 1 loading)



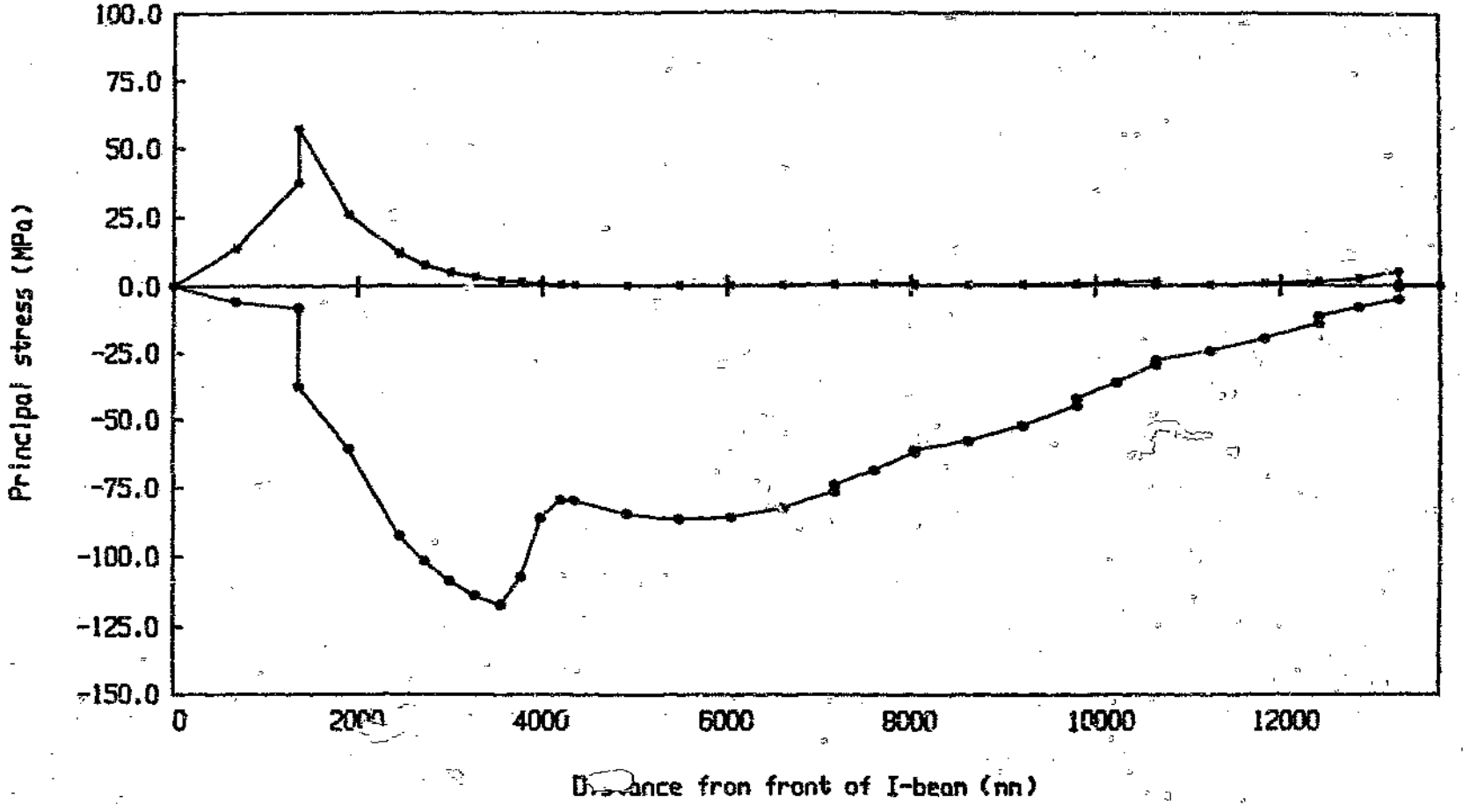
Graph 4.27 Principal shear stress distribution at the extreme fibres (Upper flange - Case 1 loading)



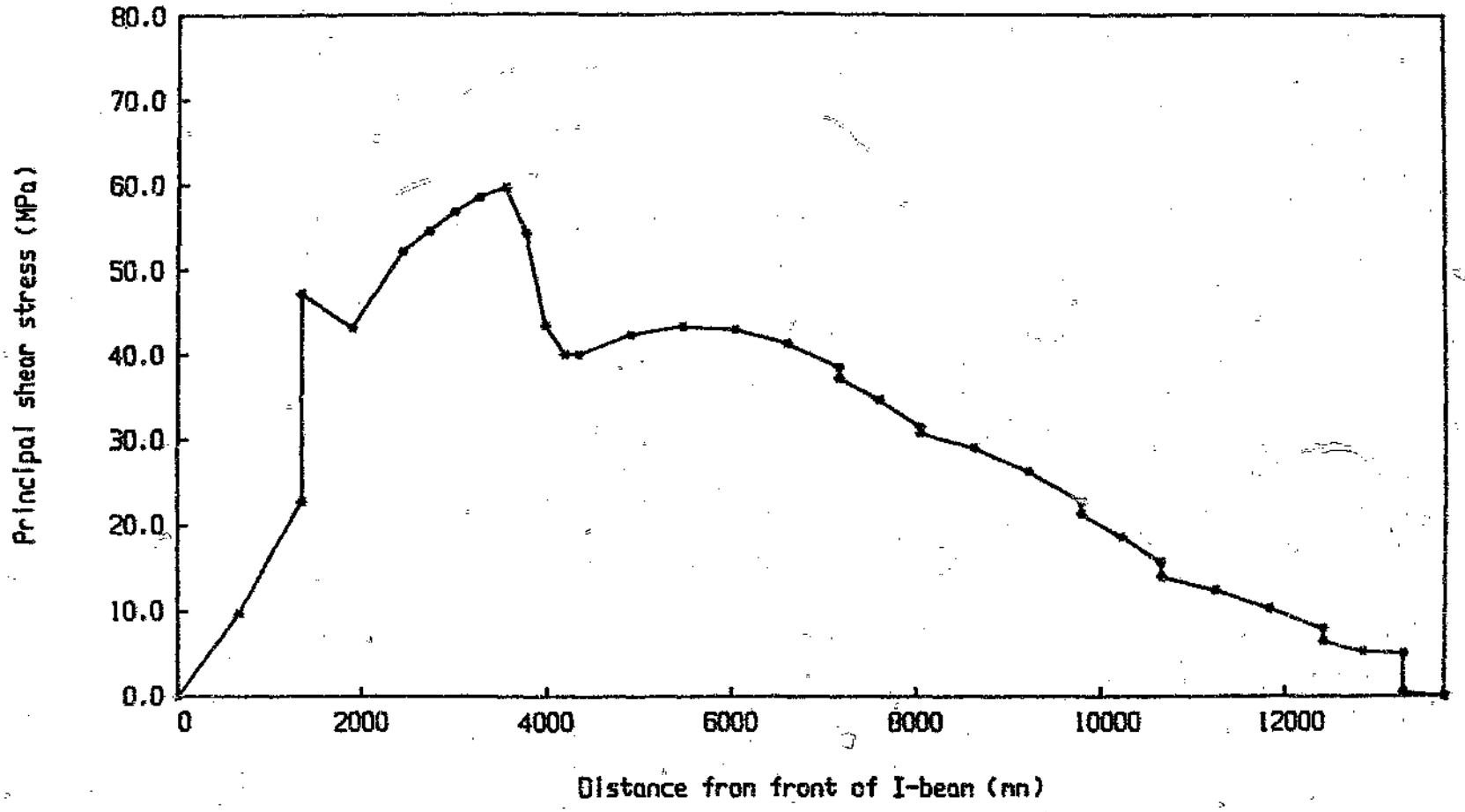
Graph 4.28 Von Mises stress distribution at the extreme fibres (Upper flange - Case 1 loading)



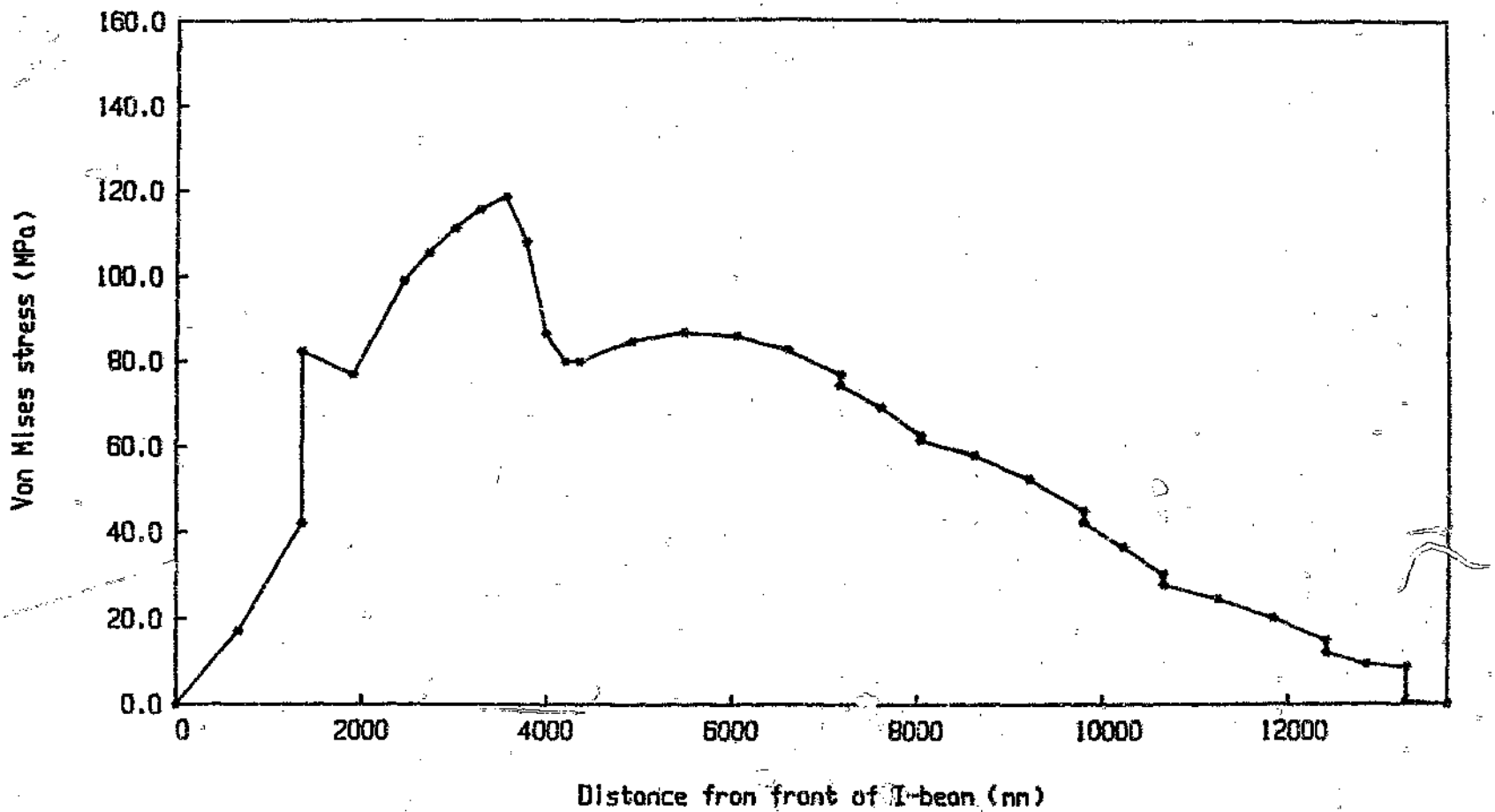
Graph 4.29 Principal stress distribution at the web/flange joint above the neutral axis (Case 1 loading)



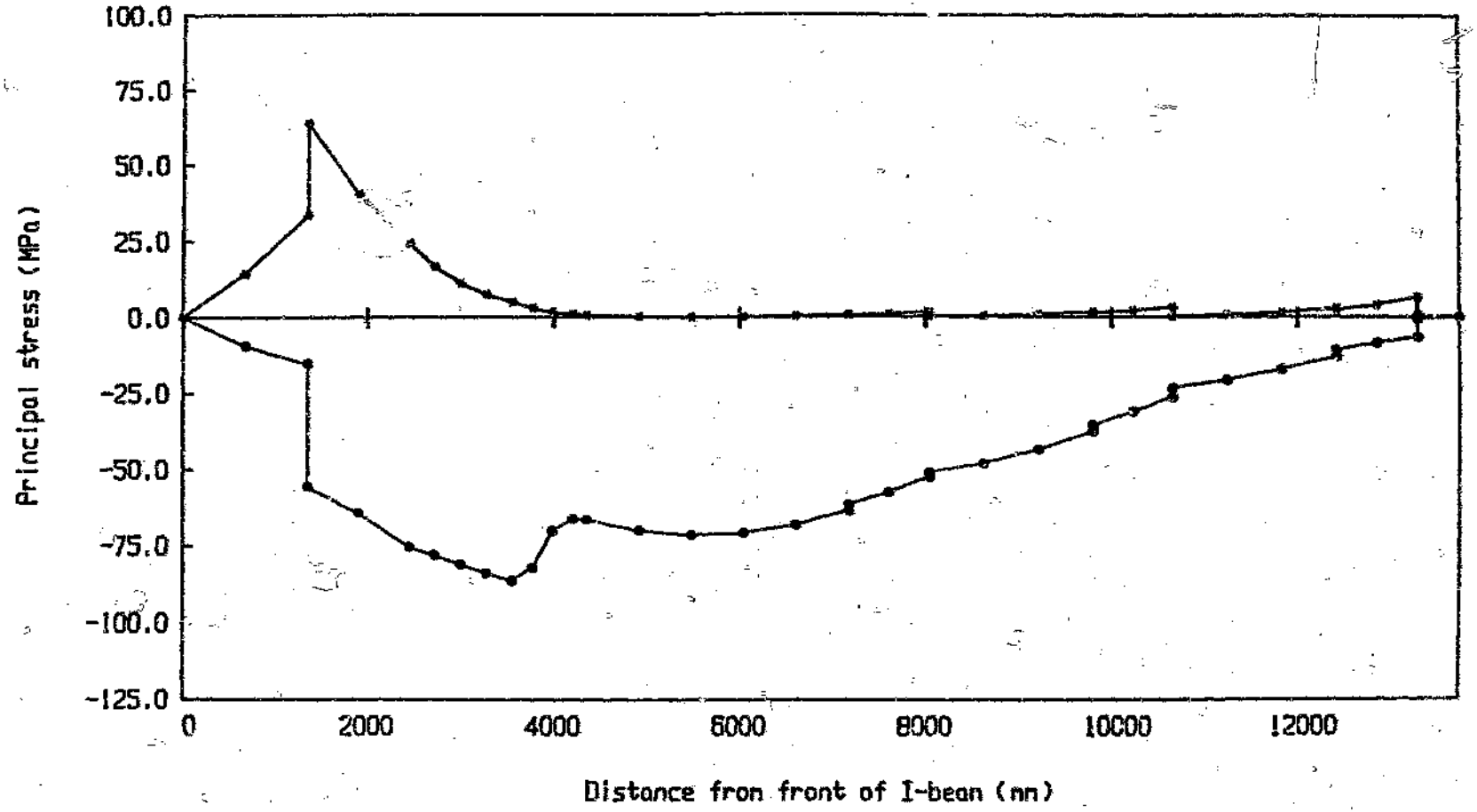
Graph 4.30 Principal shear stress distribution at the web/flange joint above the neutral axis (Case 1 loading)



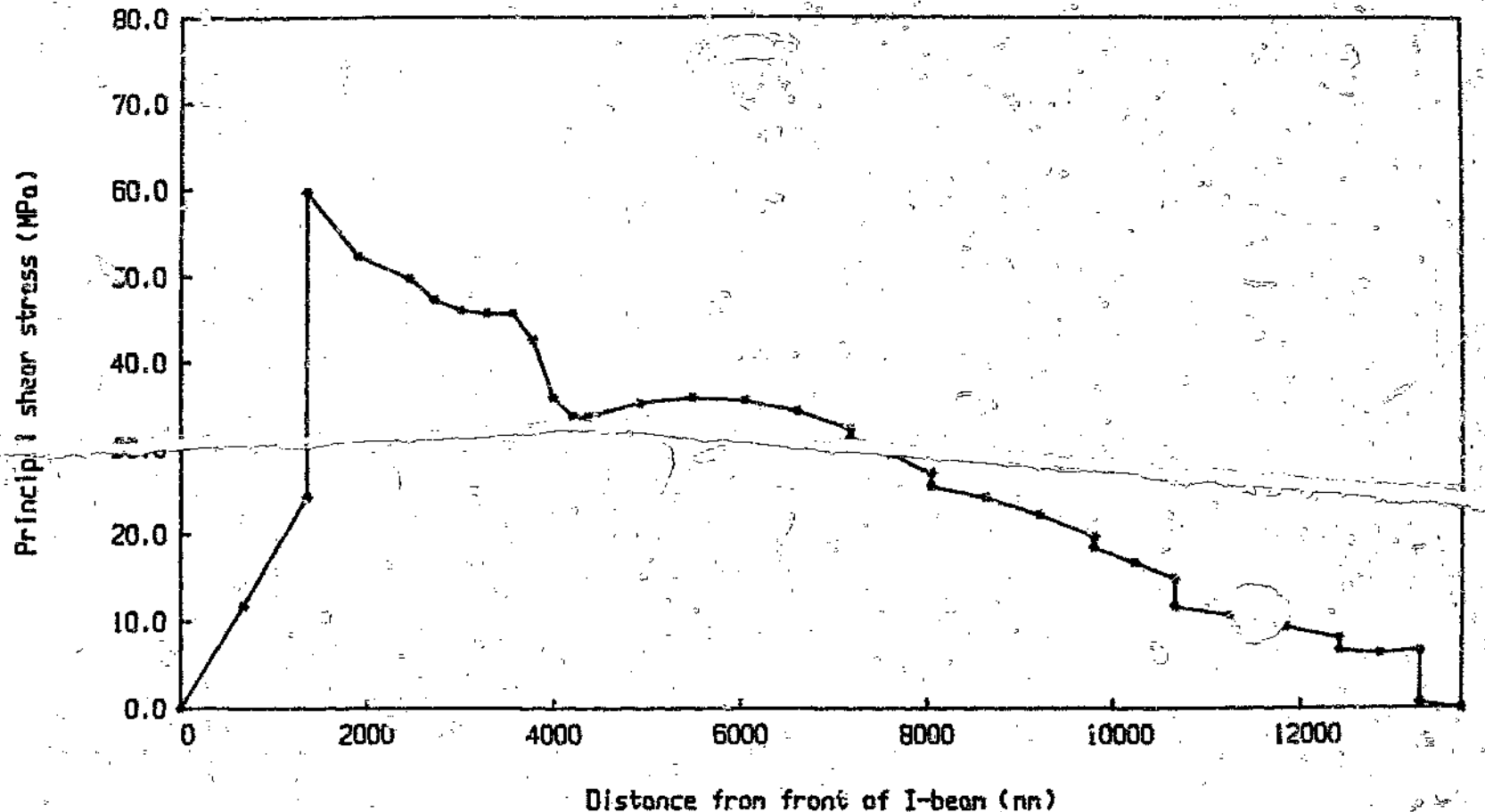
Graph 4.31 Von Mises stress distribution at the web/flange joint above the neutral axis (Case 1 loading)



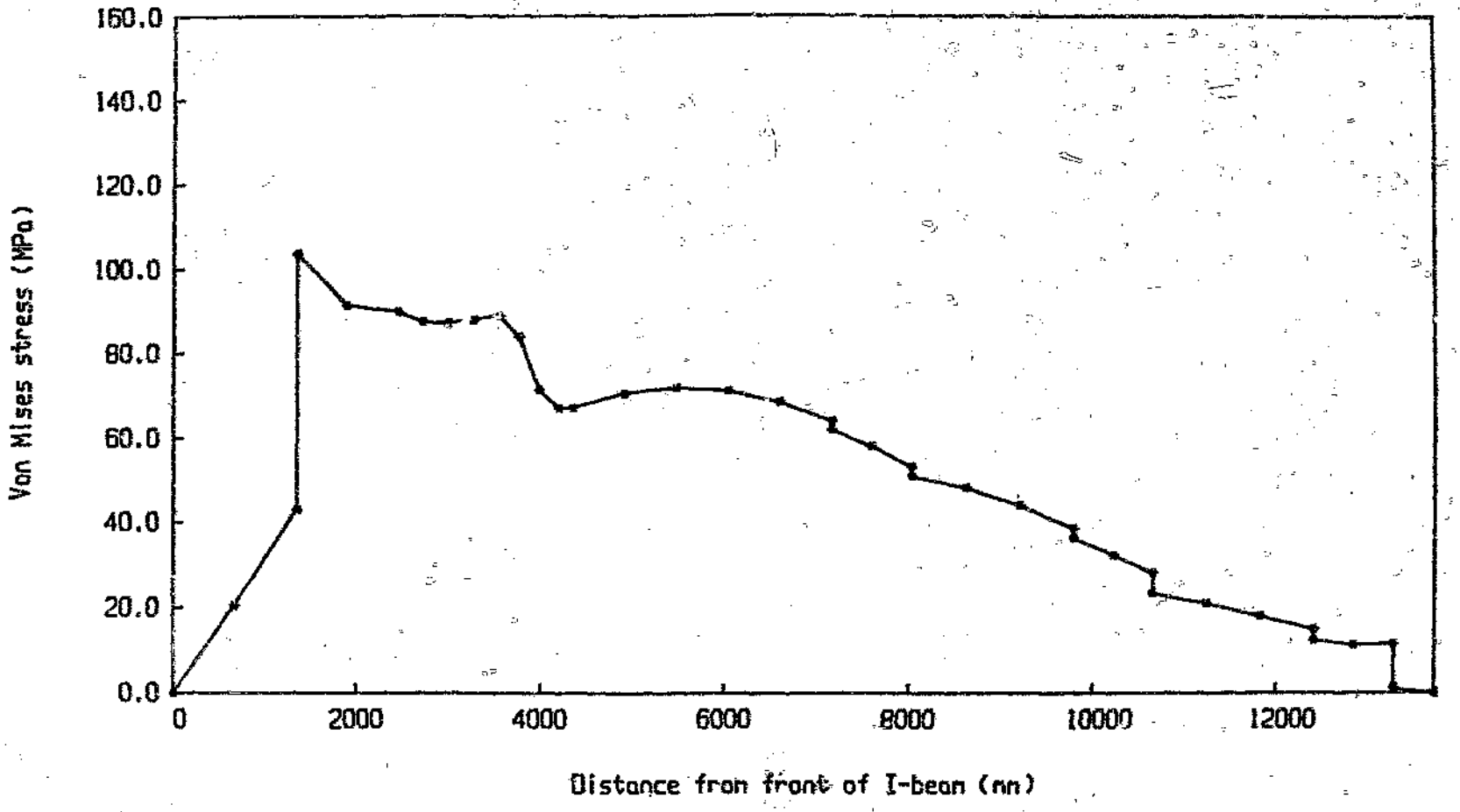
Graph 4.32 Principal stress distribution in the main I-beam welds above the neutral axis (Case 1 loading)



Graph 4.33 Principal shear stress distribution in the main I-beam welds above the neutral axis (Case 1 loading)



Graph 4.34 Von Mises stress distribution in the main I-beam welds above the neutral axis (Case 1 loading)



flange joint (ie. immediately below the flange within the T-section extrusion) and the web to T-section flange welds. In each of the stress distributions discussed, maximum loads occur under pseudo-dynamic loading conditions and hence, all of the stress distributions were calculated for the Case 1 loading analysis (ie. 'LOADING/V2L1').

The twelve stress distributions are:

- Longitudinal direct stress.
- Maximum transverse shear stress (neutral axis).
- Extreme fibre bending stress (upper flange).
- Principal stresses at the extreme fibres (upper flange).
- Principal shear stress at extreme fibres (upper flange).
- Von Mises stress at extreme fibres (upper flange).
- Principal stresses at the web/flange joint (above the neutral axis).
- Principal shear stress at the web/flange joint (above the neutral axis).
- Von Mises stresses at the web/flange joint (above the neutral axis).
- Principal stresses in the main I-beam welds (above the neutral axis).
- Principal shear stress in the main I-beam welds (above the neutral axis).
- Von Mises stresses in the main I-beam welds (above the neutral axis).

The stress distributions at the extreme fibres and at the web-flange joint were considered since, in general, the principal stress of greatest magnitude for an I-section occurs either at the extreme fibres or at the web-flange joint.[43] Comparing Graphs 4.26 and 4.29, the minimum principal stress (ie. σ_2-compressive) is seen to be of greater magnitude at the web-flange joint than at the extreme fibres for the first 2,455 metres from the front of

the beam (ie. node 1 to node 5) and for a short length at the very rear of the beam. The maximum principal stress (ie. σ_1-tensile), on the other hand, is greater at the web-flange joint than at the extreme fibres for the full length of the beam.

The stress distributions at the main I-beam welds (ie. web to T-section flange welds) were deemed important because of reduced material strength, especially in terms of fatigue (refer Section 4.3.5), at that position.

All of the principal stress, principal shear stress, and Von Mises stress distributions were evaluated above the neutral axis since the longitudinal direct stress is of the same sign as the bending stress in this region over most of the length of the beams, and hence results in greater x-direction stresses. This then yields greater principal and Von Mises stresses over these lengths (also refer Section 4.3.3).

The longitudinal direct stress distribution of Graph 4.23 is, for the most part, linear except at discontinuities caused by support reactions and over that length of the beam where the depth of the I-beam section varies. As expected, maximum longitudinal direct stress occurs at the king-pin due to the high retarding forces at that position.

Maximum transverse shear stress at the neutral axis (Graph 4.24) occurs at the king-pin position as a result of the high dynamic forces at the king-pin for Case 1 loading.

Although the maximum bending moment on the I-beams for Case 1 loading occurs at 5,709 metres from the front of the beams (ie. approximately at node 15 - refer Graph 4.2), the greatest value of extreme fibre bending stress is seen in Graph 4.25 to occur at 3,555 metres from the front of the beam

(ie. at node 9). This is because of the considerably reduced I-beam depth at that position. Also, as expected, the minimum principal stress, principal shear stress, and Von Mises stress at the extreme fibres are also greatest at node 9 (refer Graphs 4.26 to 4.28).

At the upper web-flange joint, the peak minimum principal stress (ie. σ_2-compressive) in Graph 4.29 is seen to occur at 3,555 metres from the front of the beams (node 9). This is due to the high bending stress at that position. The maximum principal stress (ie. σ_1-tensile), on the other hand, is greatest at the king-pin (ie. 1,355 metres from the front of the beams - node 3) due to the high shear loads and low bending stress at the king-pin. The principal shear stress and Von Mises stress distributions in Graph 4.30 and 4.31 peak at 3,555 metres (node 9), with lesser peaks occurring at the king-pin.

Similarly, in Graph 4.32, the greatest values of the maximum and minimum principal stress in the I-beam welds are again at the king-pin and at 3,555 metres respectively. The principal shear stress and Von Mises stress distributions (Graphs 4.33 and 4.34), however, both peak at the king-pin in this case as a result of the greater influence of transverse shear stress closer to the neutral axis, coupled with the high shear force at the king-pin. Lesser peaks occur at 3,555 metres from the front of the beams (ie. node 9) due to the high magnitude of the minimum principal stress at that position.

In each of the principal shear stress and Von Mises stress distributions presented in this section, the stresses are at all positions along the length of the main chassis I-beams, below the allowable shear yield stress (τ_{yt}) and tensile yield stress ($\sigma_{yt} = \sigma_{0,2}$) respectively for the Anticorodal–112 aluminium alloy used in the construction of the beams (refer Section E.1.1 in Appendix E).

4.3.3 Failure critical stress areas in main chassis I-beams

Eleven areas along the length of the main chassis I-beams are identified in Section A.3.2 of Appendix A as being possible failure critical areas. That is, those areas or positions where failure is most likely to initiate. These include areas of high basic stress as well as areas where the high stress is due to the presence of stress raisers. The eleven positions along with their associated Von Mises stresses are as listed below. As in Section 4.3.2, these stresses were evaluated for Case 1 loading.

- Stress at extreme fibres of the top flange at maximum bending moment ($\sigma_m = 92{,}60$ MPa).
- Stress in upper main I-beam welds at maximum bending moment ($\sigma_m = 71{,}72$ MPa).
- Stress at extreme fibres of the top flange at maximum bending stress ($\sigma_m = 128{,}4$ MPa).
- Stress in upper main I-beam welds at maximum bending stress ($\sigma_m = 89{,}00$ MPa).
- Stress at torsion tube bolt hole nearest to maximum bending moment ($\sigma_m = 130{,}7$ MPa).
- Stress at maximum transverse shear stress ($\sigma_m = 92{,}10$ MPa).
- Stress in lower main I-beam welds at maximum shear force ($\sigma_m = 106{,}2$ MPa).
- Stress at torsion tube bolt holes 2000 mm rearward of the king-pin ($\sigma_m = 173{,}3$ MPa and $173{,}5$ MPa).
- Stress in main I-beam web at landing leg mounting bracket welds ($\sigma_m = 53{,}23$ MPa).

- Stress at rubbing plate bolt holes in main I-beam flanges (σ_m = 121,9 MPa).
- Stress in main I-beam web at upper coupler cross-member welds (σ_m = 72,08 MPa).

The greatest Von Mises stress for as extruded material is seen to occur at the extreme fibres of the upper flange at maximum bending stress (ie. at 3,555 metres from the front of the beams - node 9).

For areas where high stress is due to the stress concentrating effect of a bolt hole, the maximum Von Mises stress occurs at the torsion tube bolt holes 2 000 millimetres rearward of the king-pin. Although stress concentration factors can, for the most part, be neglected for static loading of ductile materials, since the plastic yielding that occurs on overstressing causes a local redistribution of stress,[43,44] an elastic stress concentration factor has been included in all such stress analysis in Section A.3.2. This is justified since the maximum stress after the application of the stress concentration factor is in every case substantially less than the tensile yield strength, and hence local yielding is extremely unlikely. Furthermore, since the majority of stressing of the trailer chassis frame occurs under dynamic conditions, and since the effect of stress concentration is considerably more pronounced in the fatigue situation,[44] even for ductile materials, the use of a stress concentration factor at this stage of the analysis serves to illumine possible failure critical areas for the fatigue analysis of Section 4.3.5 and Section A.5. Roark and Young[44] suggest a stress concentration factor of 3 for in-plane bending of a finite width flat plate where the ratio of the hole radius to its distance from the edge of the plate is small (ie. less than 0,05). In the absence of more accurate data, this case is used here to approximate the situation of the torsion tube bolt holes in the main I-beam webs. No data was found to

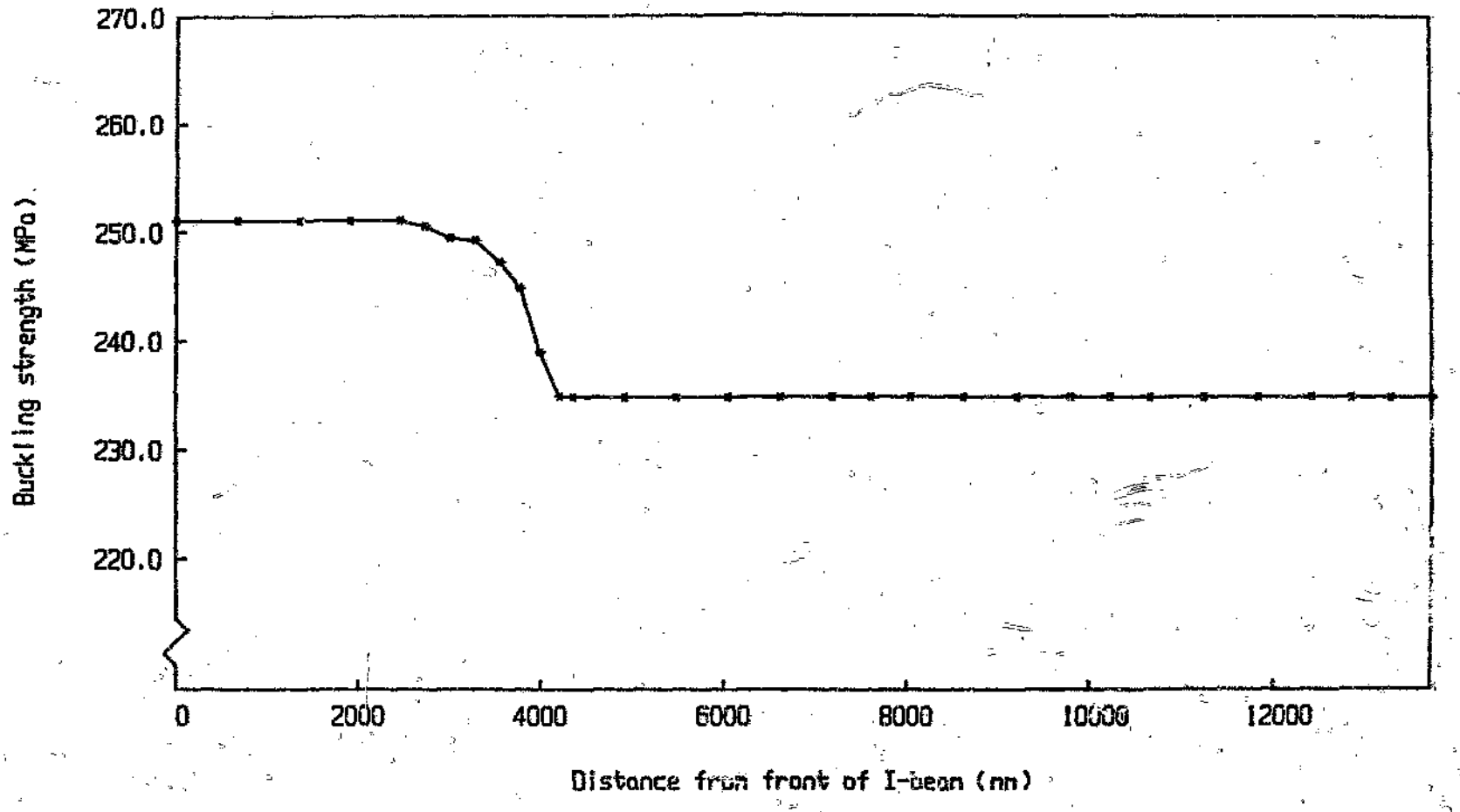
approximate the stress concentration resulting from the rubbing plate bolt holes for the lower I-beam flange in compression and thus a value of 3 was also used. It is expected however, especially for the case of the rubbing plate bolt holes, that these values are, if anything, too high and that concentration factors of between 2,0 and 2,5 are more likely. In all of these calculations the principal stresses are evaluated as if the hole were not present and are then multiplied by the relevant stress concentration factor before the Von Mises failure criterion is applied.

4.3.4 Buckling of main chassis I-beams

Under the application of various types of loading, a beam may fail by either lateral or local buckling. In the case of the two main I-beams of the semi-trailer chassis, lateral buckling is extremely unlikely for the type of loading encountered, and because the beams are restrained laterally by the deck and torsion tubes. Local buckling of the I-beam web or flanges may occur however, if local compressive stresses become excessive. It should be noted that local buckling is not necessarily indicative of imminent collapse and the beams would most likely be capable of carrying loads above those required to cause local instability. This is particularly true for beams in bending where web buckling precedes flange buckling, as is the case for the main chassis I-beams.

In Section A 4 the buckling diagram for the Anticorodal-112 aluminium alloy is presented in Graph A1, whilst the local buckling strength of the web at each of the 31 main I-beam nodes is presented in Table A8. The distribution of the buckling strength data is plotted here in Graph 4.35. As expected, the web buckling strength varies over the length of the beams in a similar manner to the beam depth. Further, by comparison with the stress distributions of Section 4.3.1, and in particular the stress at the web-flange joint, it is seen

Graph 4.35 Buckling strength distribution for main chassis I-beams



that the web buckling strength is considerably greater at all 31 nodes than the actual compressive stresses encountered and hence, buckling failure is improbable.

4.3.5 Fatigue analysis of main chassis I-beams

By far the most common mode of structural failure for the majority of road vehicles, especially heavy duty vehicles, is fatigue cracking. This is due to the fluctuating stresses induced in the chassis frame components as a result of the random vibration of the structure and payload as the vehicle travels over irregular surfaces, and the very high number of such stress cycles experienced over the service life of the vehicle. The analysis of the fatigue life or endurance life of a prototype vehicle is hence of extreme importance, and is best approached by identifying the spectrum of differing stress levels experienced by the vehicle by means of extensive testing, relating them to the appropriate stress-life curves and then using Miner's Cumulative Damage Law.[7,26,30,32,34] These procedures are discussed in greater detail in Chapter 3.

At the design phase some estimation of endurance life is also necessary so that the designer can, as far as possible, adequately size and configure components for the expected service load conditions. At this stage the fatigue loading spectrum is usually provided by previous experience gained from testing similar vehicles. In the design of this particular semi-trailer, however, such background information was not available and the best that could be done was to make certain assumptions as to the loading spectrum that could be expected. For this reason, and for a number of other reasons which will become apparent in later discussions, any assessment at this stage of endurance life will, at best, be inaccurate. Nevertheless, some discussion of fatigue life prediction for this vehicle, in order to outline methodology and

to obtain an estimation of endurance life, is appropriate here.

In Section A.5 of Appendix A, the fatigue life of the main chassis I-beams was evaluated at the following three points:

- At the extreme fibres of the tension (lower) flange at maximum bending stress (ie. at node 9).
- At the main I-beam welds below the neutral axis at maximum bending stress (ie. at node 9).
- At the lower torsion tube bolt hole at 2,109 metres from the king-pin.

These three positions were chosen since they represent the three most failure-critical areas along the length of the beams (refer Section 4.3.3 and Section A.3.2) and since they demonstrate the methodology of the fatigue calculations for a wrought or extruded material as well as for welded and bolted joints. Although greater stresses were obtained above the neutral axis in Sections 4.3.3 and A.3.2 in all three cases, the fatigue stresses have been evaluated below the neutral axis since the tensile mean stress below the neutral axis at these positions results in a greater susceptibility to fatigue cracking than compressive mean stresses.[30,44–46] Further, though a greater Von Mises stress was obtained in the main beam welds at node 3 (ie. at the king-pin) than at node 9 for the pseudo-dynamic loading in Section A.3.2, a greater maximum principal stress was obtained at node 9 for the uniform load distribution used in this fatigue analysis.

The fatigue stresses were evaluated for vertical dynamic accelerations only (ie. no longitudinal acceleration) in the range from 1-g (static loading) up to 2-g (assumed maximum dynamic acceleration) in steps of 0,1-g. The shear force and bending moment data for each stress level was obtained from the static 1-g loading distribution (ie. Case 2 loading of Section 4.3.1 and

Appendix B) by multiplying the static loading values by the vertical g-level factor. In each case the relevant fatigue stresses were taken to be the maximum principal stresses at the point, with the maximum stress equal to the stress corresponding to the particular g-level and the mean stress that stress resulting from static loading. The alternating stress is then the difference between the maximum and mean stresses, and the minimum stress is equal to the mean stress minus the alternating stress. The stress ratio is the ratio of the minimum to maximum stresses. Tables of the maximum, minimum and alternating stresses, as well as the stress ratio at each of the three positions listed above, are presented in Section A.5.1 in Appendix A. In the case of the bolt hole these stresses are presented without the inclusion of any stress concentration factor since such effects are included in the stress-life curves.

A Gaussian or Normal frequency distribution was used to approximate the frequency distribution of stress levels for the fatigue stress spectrum over the projected service life of the vehicle. This particular distribution was chosen since it closely approximates the distribution of random variables (ie. such as encountered during road induced vibration of the semi-trailer chassis). The Gaussian distribution function[47] is given by:

$$F(x) = \frac{1}{s\sqrt{2\pi}} \int_{-\infty} e^{-\frac{1}{2}[(v-\mu)/s]} dv$$

where

s = standard deviation of the distribution

μ = mean of the distribution

v = distribution variable

In applying this equation the following two assumptions were used:

- The 2-g stress level corresponds to six standard deviations from the mean stress.
- The semi-trailer experiences one stress cycle for every metre travelled.

The value of six standard deviations was chosen so as to achieve a frequency of 2-g stress cycles in the order of one in approximately every 10 000 km travelled. The actual value achieved was one in every 15 679 km (refer Section A.5.2). The assumption of one stress cycle per metre travelled was selected for simplicity and results in frequencies of vibration of 16,7 Hz at 60 km/h and 27,8 Hz at 100 km/h. These frequencies are slightly higher than the frequencies obtained during the initial vibration frequency tests undertaken at the beginning of this project (refer Section 3.2). Furthermore, an aluminium chassis will, in general, have lower frequencies of vibration than a steel one of equivalent strength because of the lower EI product for the aluminium chassis beams. For both these reasons the fatigue calculations of Section A.5 are considered to be conservatively biased.

The number of cycles to failure at each stress level (constant amplitude cycles) were determined from two sources of stress-life data for medium strength aluminium alloys. These are Alcan data ('Alcan Canada Products Ltd')[9] and BS CP 118: 1969.[46] The Alcan fatigue curves (Figure A15, Section A.5.3) relate the number of cycles to failure to the mean and alternating stress for nine classes of members. BS CP 118 on the other hand, presents individual curves for each class of structural member in terms of the number of constant amplitude cycles to failure, the maximum stress and the stress ratio (Figures A16 to A18 in Section A.5.3). The nine classes of structural members are depicted in Figure A14 in Section A.5.3. The three classes referred to in this analysis, in the same order as the three critical

positions listed above to which they refer, are as follows:[9,46]

Class 1 – As rolled or ex... ...d surfaces with no other stress raisers.

Class 3 – Members fabricated or connected by close fitting bolts or by cold driven aluminium rivets and so designed so that secondary bending stresses are not introduced; and full penetration butt welds made from both sides and with light bead reinforcement.

Class 4 – Members with continuous longitudinal fillet welds made without interruptions during welding; and butt welds with near maximum bead reinforcement made from both sides.

The number of constant amplitude cycles to failure at each stress level for the three positions are presented in Tables A13 to A14 in Section A.5.3. The number of cycles to failure are in excess of 5×10^8 cycles for the full stress range at the extreme fibres at node 9 and at the bolt hole, and for the stress range up to a g-level factor of 1,6 at the main beam welds at node 9. Such number of cycles exceed the maximum ranges of both sets of stress-life curves and represent distances travelled of greater than 500 000 km for the assumption of one stress cycle per metre travelled. The number of cycles to failure in all such cases was thus taken to be infinite.

In applying Miner's Cumulative Damage Rule then, the total number of cycles to failure for the full spectrum of stress levels is infinite at the extreme fibres at node 9 and at the bolt hole. In the case of the main I-beam welds at node 9, the total cumulative cycles to failure obtained were:

Alcan data : $1,37 \times 10^{11}$ cycles

BS CP 118 data : $4,78 \times 10^{10}$ cycles

For the assumption of one metre travelled per stress cycle these represent total distances travelled of 187 and 47,8 million km respectively, both of

which, to all practical purposes, represent an infinite life.

With regard to the accuracy of this analysis, the following points should be noted. Firstly, it is not sufficient to assume a spectrum of stress levels as has been done here. Notwithstanding the fact that a Gaussian distribution in general closely approximates the frequency function for random variables, relatively small deviations from the true frequency distribution can have a marked effect on the cumulative life calculation. For example, one 2-g stress cycle in every 15 679 km, as discussed above, may seem reasonable. Yet a corresponding frequency of occurrence of one 1,5-g stress cycle every 73,7 metres, or one 1,6-g stress cycle every 425 metres, would seem to be excessive (refer Table A12, Section A.5.2). Further, the semi-trailer is likely to spend a fair proportion of its service life travelling unladen, under which conditions the frequency distribution would be made up of a larger number of smaller magnitude stress cycles and a lesser number of larger magnitude cycles. This suggests a number of different frequency spectra of stress levels to account for various operating conditions (eg. laden on highway, unladen on highway, laden on secondary roads, etc); the total spectrum then being obtained by summing the individual spectra in the correct proportions for the projected service conditions.

Secondly, with reference to the fatigue stress calculations and the stress-life curves, the assumption of the fatigue stresses being equal to the maximum principal stress, albeit necessary in this analysis because of the general nature of the stress-life curves, is in general an over-simplification. Stress-life curves for the particular alloys used in the construction of the semi-trailer, and for stress situations which more precisely model those encountered during the operation of the semi-trailer, need to be derived. Further, for both sets of stress-life data, the accuracy with which the graphs could be read was, at best, poor. In the case of the Alcan data for the welds at node 9, this was

due to the low angle of the curve for class 4 members in the region where the 1,7 to 2,0 g-level stresses intersect the curve and the difficulty in reading the abscissa scale accurately. The main source of inaccuracy for the BS CP 118 stress-life curves may be attributed to the fact that linear interpolation was used for data points between the constant life curves and the difficulty in interpolating accurately between these closely spaced curves.

4.4 Chassis sub-structure

The term 'chassis sub-structure' refers to those portions of the semi-trailer chassis which contribute to the load bearing ability of the complete structure.

This section evaluates and discusses the stress analysis of such sub-structure as detailed in Appendix C.

4.4.1 Side rails and outriggers

Maximum stresses occur in the outrigger and side rail structure during loading and unloading operations (eg. due to forklift truck tyre loads) and not when the laden semi-trailer is travelling. This is due to the fact that the load per square metre for the 30 000 kg design payload uniformly distributed over the full length and width of the semi-trailer is approximately 900 kg per square metre (1 800 kg for a maximum vertical acceleration of 2-g - refer Sections 4.2.2 and 4.2.3), whereas the laden front axle mass of a typical forklift truck, as used on the deck of a trailer, is often in excess of 3 000 kg. The ISO container floor test load[48] is thus used as a representative maximum load in the side rail and outrigger analysis in Section C.2 of Appendix C, since the trailer deck support structure is likely to experience similar loading conditions to those of a shipping container's floor.

ISO 1496/1 - 1978(E)[48] specifies maximum loads as follows:

- 5 460 kg over two tyres
- Tyre centres at 0,76 metres

This load simulates the load imposed by the front axle tyres of a forklift truck and accounts for both the static load and a vertical bump acceleration.

The worst case for loading on the side rails and outriggers occurs when the two tyre loads are applied on the deck directly above the side rail (refer Figure C1 in Section C.2). This situation simulates a forklift truck driving onto or off the trailer deck from a side loading dock (ie. forklift truck travelling perpendicular to the length of the semi-trailer) where the front axle is directly above the side rail. In this situation a portion of the applied load is supported by the transversely mounted deck planks and the remainder by the outrigger structure. The side rail serves to distribute load in either direction from the applied loads to the outriggers and deck planks.

In the analysis of Section C.2 the side rail was considered as a continuous beam supported over its entire length on multiple elastic supports. These elastic supports were placed at each outrigger and end rail position, as well as midway between each pair of outriggers. Each support was then considered as being made up of a combination of the deck planks for the half span on either side of the support position and, if present, an outrigger or end rail. The flexibility or stiffness of the outriggers and cantilevered deck planks was calculated individually and the total stiffness at each elastic support was then taken to be the sum of the individual outrigger (or end rail) and deck stiffnesses at that position. The proportions of a particular support reaction carried by the outrigger structure and the deck planks respectively, were then determined relative to the outrigger and deck stiffnesses at that support position.

The calculations were carried out using a beam analysis computer program, developed by the author at Henred Fruehauf Trailers(Pty)Ltd and based on the 3-Moment equation for continuous beams. This program calculates the bending moments, support reactions and deflections at up to 26 nodes along the length of a continuous beam. Each node may be either a support node or a free node and a support flexibility is required at each node. A finite value is entered for a flexible support, whereas rigid supports have flexibilities of zero. Very high flexibilities (eg. 1 000 000 mm/N) are entered for free nodes. Up to 26 loads may be applied and each of these may either be applied at a point or distributed over a short length.

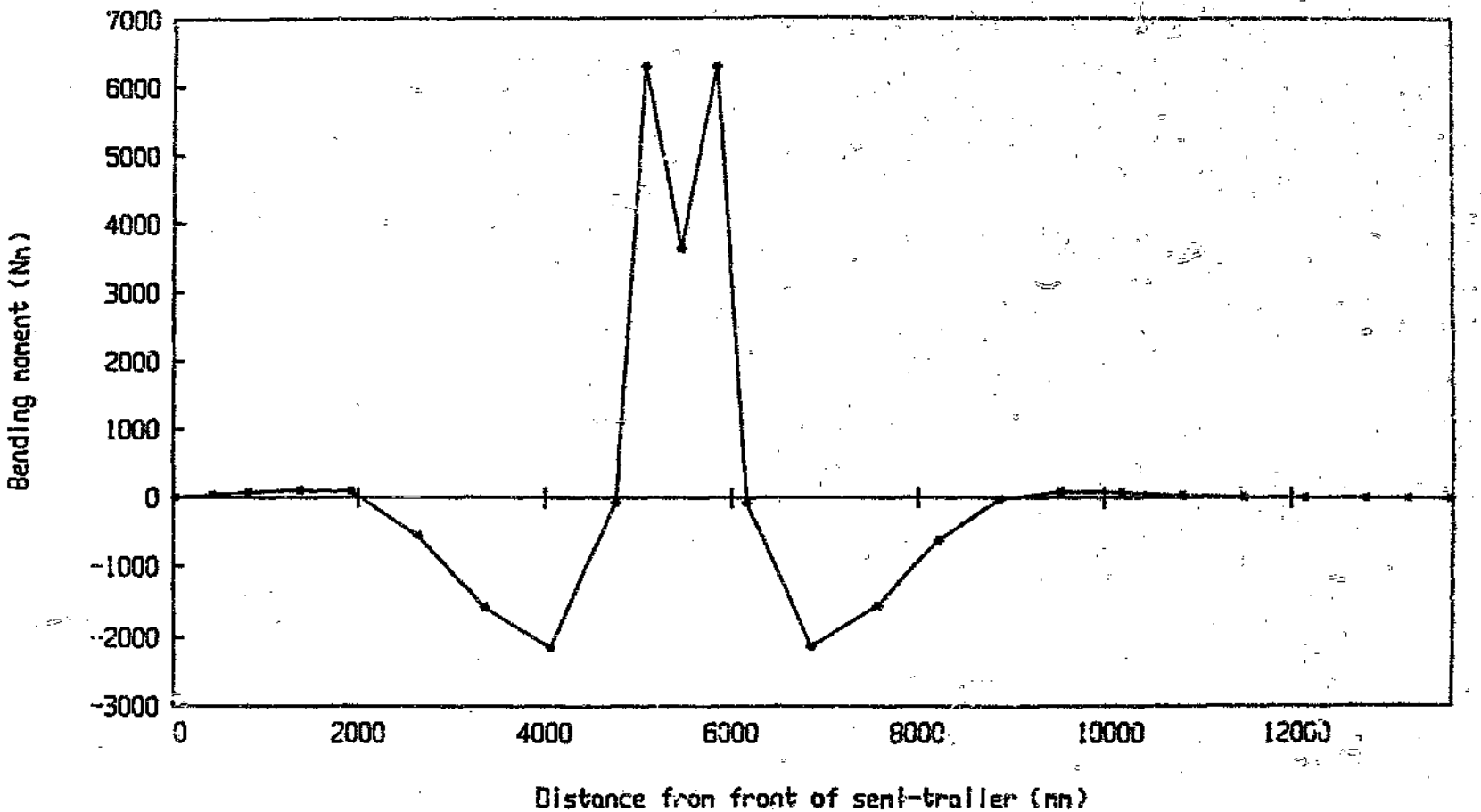
The 23 support node positions for the side rail model are shown in Figure C7, and their respective support flexibilities in Table C1 in Section C.2.3. Three loadcases were considered in the analysis, viz:

Loadcase 1 – Here the two tyre loads were positioned on the side rail symmetrically arranged about the mid-span node between two outrigger nodes. This situation results in maximum stress in the side rail.

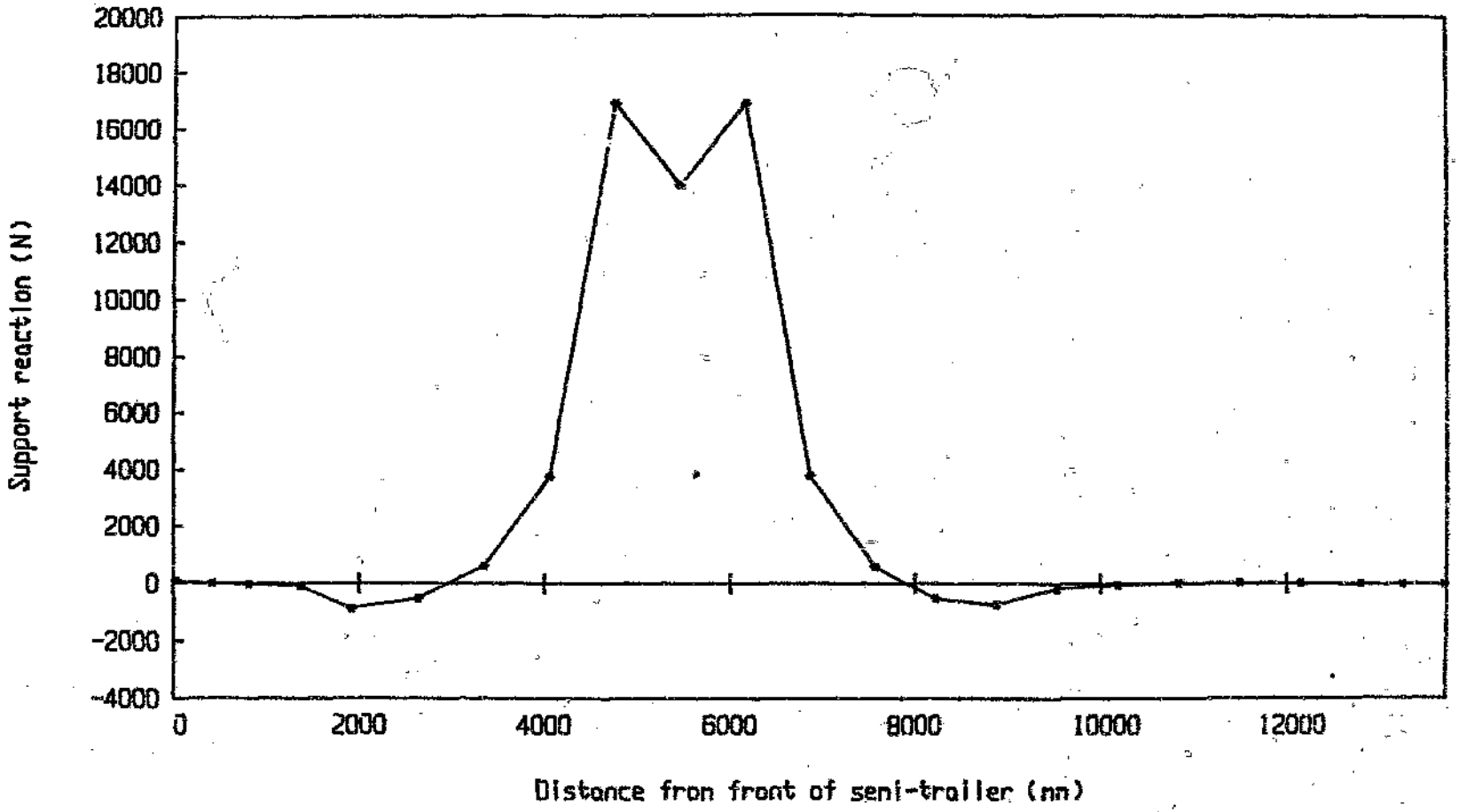
Loadcase 2 and 3 – Here the two tyre loads were positioned on the side rail with each load an equal distance on either side of a square tube or upper coupler outrigger respectively. These two loading conditions result in maximum load (and hence maximum stress) on the outrigger under consideration.

The bending moment, support reaction and deflection results are presented in Tables C2 to C4 in Section C.2.3, and plotted here for loadcase 1 in Graphs 4.36 to 4.38.

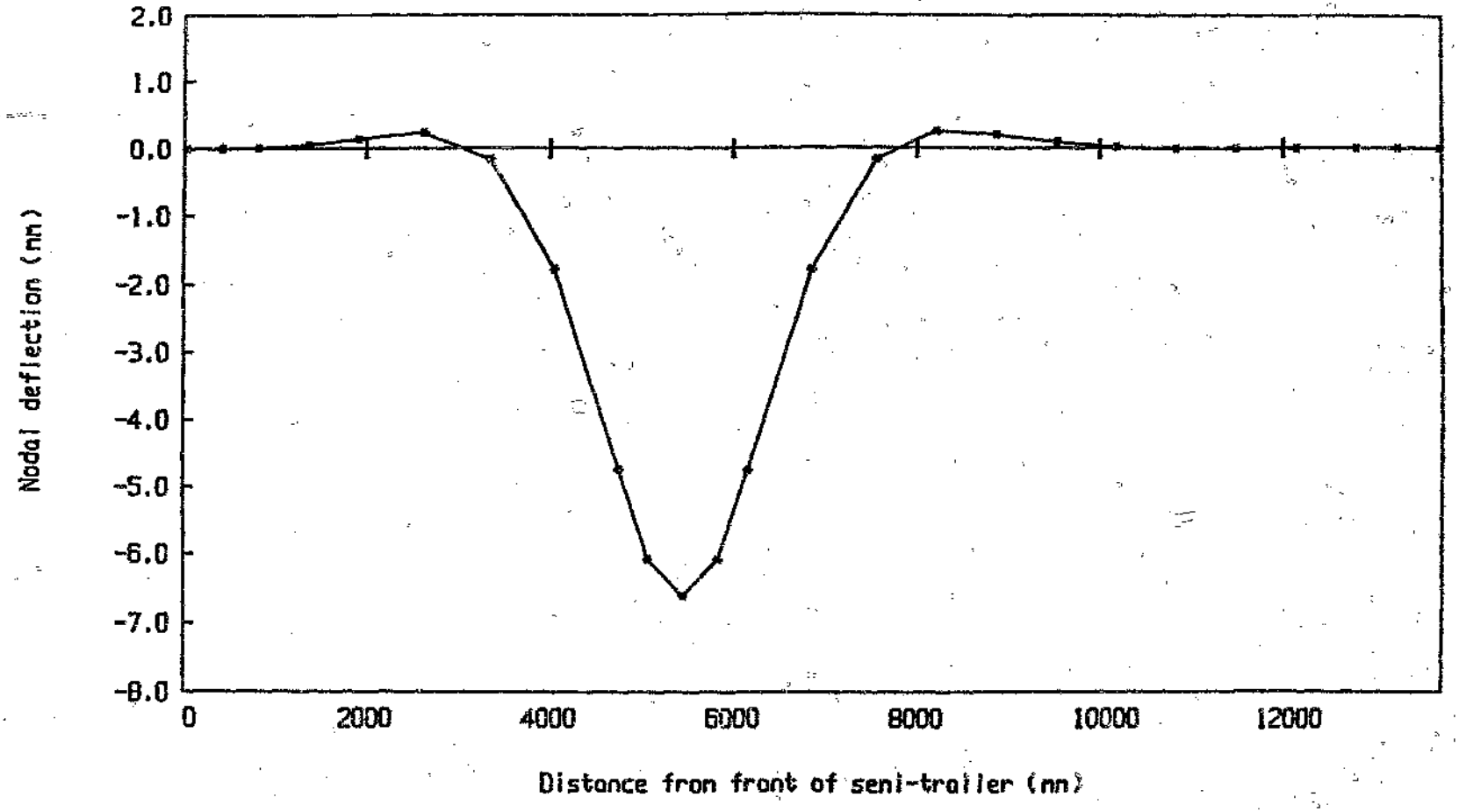
Graph 4.36 Bending moment distribution on semi-trailer side rail (Loadcase 1)



Graph 4.37 Support reaction distribution on semi-trailer side rail (Loadcase 1)



Graph 4.38 Nodal deflection diagram for semi-trailer side rail (Loadcase 1)



Maximum stress in the side rail for loadcase 1 occurs at the positions of the applied loads between nodes 10 and 11 (ie. 5,814 metres from the front). The resultant Von Mises stress at the extreme fibres is 62,32 MPa.

The maximum support loads for the square tube and upper coupler outriggers result for the applied loads positioned above the outriggers at 6,136 metres and 1,892 metres, respectively, from the front of the chassis. The Von Mises stresses at the extreme fibres of the inboard end of the outriggers are 88,89 MPa and 106,7 MPa respectively.

Other than contributing to the support of deck loads the outriggers also stiffen the side rails to allow for the fitment of side posts at a later date and serve to space the side rails, thereby preventing side movement of the deck planks due to slippage at the deck mounting clamps. Further, stiffer outriggers were used in the area adjacent to the upper coupler because of the high impact forces that occur in that region, as a result of stiff rear axle springs on many truck-tractors, and play at the rubbing plate/5th wheel interface.

4.4.2 Deck planks

A transversely mounted extruded aluminium planked deck was chosen in this semi-trailer design since it eliminates the requirement for deck supporting cross-members and is thus simpler to mount. The particular self-supporting deck planks used (refer Drawing No. DE-05) are rated as being able to carry a forklift truck of maximum 3 500 kg gross vehicle mass.[15,49]

In Section C.3, this value was checked for a single point load applied on a deck plank midway between the main chassis I-beams (ie. at maximum span). Section properties for the deck-plank cross-section were evaluated

for the approximated section of Figure C9. The maximum static load (ie. no dynamic acceleration) at the onset of yielding was found to be 5 976 kg, which is far in excess of the front tyre load from a 3 500 kg GVM forklift truck. For the 2 730 kg ISO 1496/1 forklift truck tyre load (refer Section 4.4.1) the maximum Von Mises stress was calculated as 118,8 MPa.

The greatest stress in the deck planks due to loads applied at the side rail, as detailed in Section 4.4.1 and Section C2, was found to occur for the two tyre loads applied symmetrically about node 11 in Figure C7. This corresponds to loadcase 2 of Section C2. The maximum load supported at the outer end of a single deck plank at this position and under these conditions, was found to be 393 kg. The maximum Von Mises stress resulting from this load occurs at the extreme fibres of the plank, at the outer edge of the chassis I-beam flange, and was found to be 76,22 MPa.

4.4.3 Torsion Tubes

Torsional twisting of the chassis 'ladder frame' structure occurs when the truck-trailer combination is negotiating uneven ground or when cornering where there is a difference in slope between the two intersecting roads. A fairly high degree of torsional rigidity contributes to the prevention of roll during cornering, whereas a fairly torsionally flexible chassis serves to reduce the stresses in the frame resulting from any applied twisting action. With this in mind the chassis frame must be so designed as to meet the first of these two requirements without being unduly stiff.

The twisting action of the chassis is resisted to some extent by the torsional rigidity of the main chassis I-beams but mainly by the torsional rigidity of the 'ladder frame' cross-members. In this design a round tubular section was selected for these cross-members (torsion tubes) since it is the most efficient

section in torsion and since torsional stresses predominate.

The torsional and bending stresses developed in the torsion tubes and the torsional stress in the main chassis I-beams due to twisting of the chassis structure, are analysed in Section C.4 in Appendix C. This analysis was undertaken for the chassis subject to a representative angle of twist over the length from the king-pin to the centre of the tridem bogie. This was arrived at by considering the tyres on one side of the trailer to be parked on a 200 mm high kerb, whilst the tyres on the other side and all the tyres on the truck-tractor are resting on level ground. The angle of twist of the torsion tubes was then deduced by viewing the trailer from the side and noting the relative rotation between the I-beams in that plane. The angle of twist of the I-beams on the other hand, was obtained by viewing the trailer from the rear and assuming that the main I-beam webs remain perpendicular to the deck. The bending moment applied to the ends of the torsion tubes was then taken to be equal to the resulting torsional moment induced in the chassis I-beams.

Maximum stress in the torsion tubes was shown to occur at the ends of the tubes, immediately adjacent to the welds, at the upper and lower ends of a vertical major diameter. The magnitude of the resultant Von Mises stress is 42,01 MPa.

4.4.4 Upper coupler structure

The king-pin mounting and associated upper coupler structure (refer Drawing No. UC-01) are safety critical portions of the chassis structure. Furthermore, these components are subjected to high impact loads resulting from coupling and uncoupling operations, and from movement at the king-pin/5th wheel interface as a result of wear. For these reasons the upper coupler structure

was designed to stringent design requirements.

The horizontal load used in the analysis of the upper coupler structure (refer Section C.5 in Appendix C) was obtained from the Fruehauf Design Data Book[41] which specifies a maximum horizontal load applied at the king-pin, once in the life of the semi-trailer, of 3,5 times the laden GVM. Maximum vertical load on the other hand, is equal to the king-pin reaction for the pseudo-dynamic (Case 1) loading condition in Section A.2 in Appendix A. Further, because of the extreme nature of these loads, they were not considered to act simultaneously.

The horizontal load at the king-pin is applied via the wearing ring and lock jaw assembly of the truck-tractor 5th wheel, and is thus applied relatively close to the plane of the rubbing plate. Consequently, this load is resisted largely by the rubbing plate acting as a large shear plate. The upper coupler cross-members and rubbing plate cross-brace channels, especially those in close proximity to the king-pin, also help to stiffen the rubbing plate structure and to transfer the load to the chassis.

In the analysis of the upper coupler support structure in Section C.5, all of the horizontal king-pin load was assumed to be transferred to the chassis longitudinals by the two rubbing plate cross-brace channels immediately adjacent to the king-pin, as well as a 732 millimetre wide portion of the rubbing plate (refer Figure C15). The resultant composite beam was loaded over the width of the 'Hope' king-pin mounting recess, and was considered to extend across the width of the trailer, from the inner row of rubbing plate mounting bolts in the lower flange of one chassis I-beam to the same row of mounting bolts in the opposite chassis I-beam. A worst case of simply supported end fixing conditions was assumed. Furthermore, because the shear centre of this composite beam structure can be shown to be slightly below the under sur-

face of the rubbing plate (ie. roughly in line with the 5th wheel wearing ring and lock jaw assembly), the beam was considered to be loaded in bending and shear only and torsion was excluded. In this situation, the most failure critical position was found to be at the centre of the beam, in the heat affected zone adjacent to the outer set of cross-brace channel to rubbing plate welds, where the Von Mises stress was shown to be 86,28 MPa.

The vertical load on the upper structure, on the other hand, is distributed over the approximately oval contact area between the truck-tractor 5th wheel coupling and the rubbing plate. For a typical 5th wheel,[51] this contact area extends to a total width of 915 millimetres (ie. 72,5 millimetres from the centreline of the chassis I-beam webs). In this case the expected mode of failure is the development of plastic hinges at the lower end of the chassis I-beam webs and in the rubbing plate along each side of the 5th wheel contact area. In Section C.5.2, the vertical load required to cause such failure was shown to be 362280 N, which is 1,93 times greater than the maximum expected vertical load.

Bearing stresses result at the rubbing plate mounting bolt holes and at the 'Hope' anti-jack-knife device mounting bolt holes during horizontal loading at the king-pin. Assuming in each case that only eighty percent of the bolts are bearing at any time, in order to allow for manufacturing inaccuracies, maximum bearing stress was shown to occur in the rubbing plate at the 'Hope' device mounting bolt holes and was equal to 337,5 MPa. Bearing stresses at the bolt holes in the 'Hope' device steel foundation plate are dealt with in Section 4.5.4.

4.5 Ancillary structure

The term 'ancillary structure' is used here to refer to any portion of the

semi-trailer structure that is in general non-load bearing structure, except in special circumstances (eg. rear end collision in the case of the rear bumper), and to minor vehicle components.

This section evaluates and discusses the stress analysis of such ancillary structure as detailed in the analyses of Appendix D.

4.5.1 Rear under-ride bumper

During a rear end collision between a passenger car and a commercial vehicle, the severity of the damage to the vehicles, as well as injury to the occupants of the passenger car, is very often increased by the car under-riding the lead vehicle with consequent intrusion into the passenger compartment. This is particularly true for trucks and trailers having large rear overhangs behind the rearmost axle. In the case of vehicles with shorter rear overhangs the relatively large gap between the chassis members (often in excess of one metre) will still allow considerable under-run to occur, especially in the case of smaller, narrower passenger cars, or those having short bonnets. Further, reliance on the rearmost axle tyres of the truck or trailer to effectively act as a bumper is inadvisable since, in many cases, the front end of the impacting car is drawn into the gap between the rear tyres and the underside of the load platform, as a result of the rotation of the truck tyres.

In his investigative report into rear under-ride protectors for commercial vehicles, Hillman[50] states that, although the incidence of rear under-ride accidents plays a small but significant part in the annual road accident injury cost in South Africa (both in terms of lives and money), this could be considerably reduced by improving the rear end conspicuity of heavy motor vehicles, and by fitting some form of rear under-ride protector to them.

A rear under-run protection bumper, designed to meet the specifications of SABS 1055 - 1983: 'Rear under-run protection devices',[23] was fitted to the rear of this aluminium semi-trailer, the design of which is detailed in Section D.2. The bumper extends over the full width of the trailer with the bumper bar being 2,3 metres long, and is positioned with the centre line of the bumper bar 0,497 metres above the road surface. This height was selected since it was within the maximum and minimum height limitations of SABS 1055 and conforms closely to the recommendations of Hillman's study and to European standards. The question of rear end conspicuity is dealt with in Section 4.8.

With reference to Figure D1 in Appendix D and to SABS 1055, the strength requirements for the under-run bumper are such that the device must offer adequate resistance to forces applied parallel to the longitudinal axis of the vehicle at points P1, P2 and P3, the magnitude of these forces being:

- A horizontal force of 25 kN applied successively to both points P1 and to point P3.
- A horizintal force of 100 kN applied successively to both points P2.

These strength requirements are deemed to be satisfied if it is shown that both during and after the application of these forces, the horizontal distance between the rear of the device and the rearmost extremity of the vehicle does not exceed 400 mm. This suggests that some degree of deformation of the bumper structure on impact is permissible. This would have the effect of absorbing a portion of the impact energy, thus reducing the deceleration forces experienced by the car occupants. This approach is supported by Hillman who states that deformation of the under-ride protector, on impact, up to a maximum of 100 mm, is highly desirable and therefore overdesign should be avoided.

From Section D.2 of Appendix D the maximum Von Mises stress in the I-section bumper bar occurs at the extreme fibres for the forces at P1, and is equal to 111,0 MPa. The maximum Von Mises stress in the bumper uprights is 117,4 MPa and this occurs at the extreme fibres of the cross-section immediately below the attachment plate welds for the 100 kN forces applied at points P2. Both of these stresses occur in the heat affected zone immediately adjacent to welded areas.

As shown on Drawing No. RB-01, the rear under-run bumper was assembled as a sub-assembly and then bolted to the trailer chassis by means of twelve M16 bolts. This was done to allow the bumper to be removed for repair or replacement after a rear impact, and to facilitate easier servicing of the rearmost axle.

4.5.2 Headboard

The headboard serves to prevent the forward movement of the semi-trailer payload during braking and must be capable of sustaining such loads. A wide variety of magnitudes and distributions of load on the headboard are possible depending on the nature of the payload being carried and the degree to which it is strapped down.

In the analysis of Section D.3, a generalized payload made up of a number of separate layers was used. These layers could be taken to represent, for example, boards or boxes. The load was considered to cover the full length and breadth of the deck and to extend to the top of the 4,77 mm cover plate on the headboard (ie. 765 mm above the deck). This yielded an average payload density of 1 200 kg/m^3 for the 30 000 kg design payload. Then, for a maximum average braking deceleration of 0,65-g and for an assumed limiting coefficient of friction of 0,5 between the payload and the deck and between

the individual layers of the payload, the total force exerted on the headboard by the n'th payload layer was deduced. This showed that the vertical load distribution increased linearly from zero at the deck to a maximum at 765 mm above the deck and that the total force exerted on the headboard was 5 000 kg. The two inner upright members were assumed to each support one-third of this total force whilst the outer uprights were assumed to support one sixth of the force.

The most failure-critical section for the upright members is immediately adjacent to the lowest headboard cross-member welds at the deck level due to reduced material strength in the heat affected zone. The resultant Von Mises stress at the extreme fibres for this section was calculated as 108,5 MPa.

The centre of the three rows of horizontal channel sections on the headboard was shown to support the largest force (ie. 2 400 kg uniformly distributed over the full width of the headboard) and was analysed as a continuous beam supported on four rigid supports. The maximum Von Mises stress obtained was 16,16 MPa at the channel to upright welds for the centre channel section. This analysis is to some degree an oversimplification since the supports at the headboard uprights will deflect under load and will most likely result in slightly higher stresses than those calculated. However, since large margins of safety were obtained, the analysis was considered sufficient.

The headboard is secured to the front end of the main beams and the front end rail by means of twelve M16 bolts, and thus may be removed if required.

4.5.3 Landing legs

The stresses in the landing leg mountings and support structure are analysed in Section D.4 for various loading conditions. The first of these is referred to

as a 2-g support slam[41] and models a vertical impact load at the foot of the landing legs resulting from an uncoupling operation where the landing legs were not fully extended to ground level. In the analysis this was depicted mathematically by superimposing onto the 1-g uniform load distribution, for the semi-trailer supported at the landing legs and all three axles (refer Section 4.3.1 - Case 3 loading), an additional skewed load distribution of such magnitude as to double the static landing leg reaction. In order to accomplish this, the centroid of the additional load was positioned directly above the landing leg location (refer Figure D9). The resultant 2-g slam load per leg was shown to be 181448 N (ie. 18 496 kg). This is somewhat less that the allowable maximum static load of 25 000 kg per leg specified for the Josef E240G landing legs[51] (refer Section 2.2.1). The stresses generated in the main chassis beams for the 2-g support slam load are less than the stresses resulting from the pseudo-dynamic load analysis (refer Section 4.3).

The maximum stresses in the welds of the landing leg mounting bracket, resulting from the 2-g slam load, occur in the welds attaching the bracket to the main chassis I-beam web (refer Drawing No. CH-04), due to the shorter total weld length on that side of the bracket and the additional effect of the bending moment. The maximum Von Mises stress calculated was 84,24 MPa at the lower end of the weld pattern.

Each landing leg is bolted to its respective mounting bracket by means of ten M14, 8.8 grade bolts. For the 2-g slam load the average bearing stress and bolt shear stress were 81,00 MPa and 117,9 MPa, respectively.

In the analysis, maximum transverse and longitudinal loads on the landing legs were limited to 5 000 kg per leg in each direction applied at the underside of the foot (refer Figure D11 and Figure D12). Depending on the direction of application, these forces result in direct tensile or compressive loads being

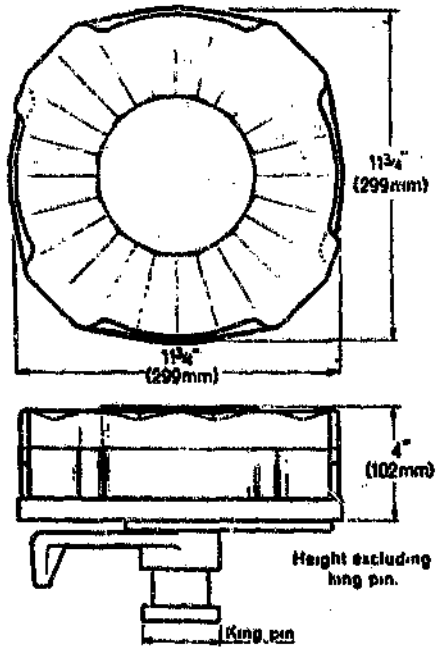
applied to the braces. The resultant maximum loads in the braces were calculated for the landing legs at half extension and were shown to be ± 11 341 kg for the rearward brace and ± 9 549 kg for the cross brace. Any restraining effect at the landing leg mounting bracket was neglected. For the braces under compression, failure is by column buckling. The allowable buckling loads for the rearward and cross braces were shown to be –21 144 kg and –25 364 kg respectively. The tensile mode of failure is by overstressing of the brace end welds. Maximum tensile stress in these welds occurs for the rearward brace and was shown to be 100,7 MPa. The maximum Von Mises stress at the brace end bolt holes was calculated as 434,6 MPa.

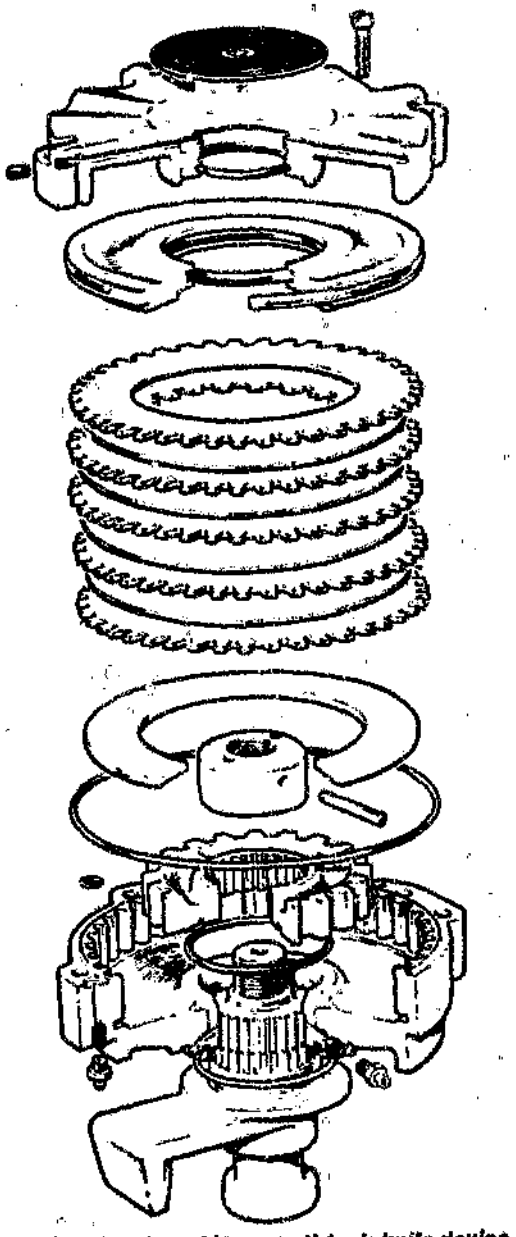
Side loading at the lower ends of the landing legs also causes bending of the landing leg cross-member as a result of the tensile and compressive forces generated at the cross-brace bracket. The maximum Von Mises stress in this case was shown to be 97,7 MPa.

Two side operation landing legs were selected as opposed to single side operation with a cross tube, since they afford better support on uneven ground, as each leg may be extended by a different amount.

4.5.4 Hope anti-jack-knife device

In keeping with the criterion of safety adopted in this design, a Hope anti-jack-knife device (refer Figure 4.2) was fitted to the semi-trailer. The brake layout Drawing No. PM-01 in Appendix H shows how the device and its control valve are connected into the trailer brake circuit. The Hope device is brought into operation every time the trailer brakes are operated, by a control valve which senses the increase in service line pressure, and passes a proportional amount of air from the emergency line into the device to squeeze the clutch discs together. This provides torsional damping at the king-pin,





Exploded drawing of Hope anti-jack-knife device.

Figure 4.2 Hope anti-jack-knife device

related to the degree of brake application, slightly before braking takes place through the road wheels.

The concept of the device is not to arrest a jack-knife or trailer swing once it has started, but rather to prevent the initiation of such an occurrence.[52] This is achieved by providing restraint at the king-pin during braking, thereby damping out any would-be tendency of the truck-tractor and semi-trailer combination to move out of alignment in an uncontrolled manner.

The standard weld on type foundation plate supplied with the Hope device could obviously not be used in this design and there was insufficient space on the foundation plate to drill the necessary bolt holes for a bolted type mounting. Furthermore, the device is so designed that the combined thickness of rubbing plate and foundation plate must be 28,5 mm ± 0,2 mm. The minimum standard foundation plate thickness available is 15,9 mm, which is too thick for use with the 15,88 mm rubbing plate. Hence, a larger and thinner (ie. 12,3 mm thick) bolt on type foundation plate, as detailed in Drawing No. UC-13, was machined for this project. A higher grade of steel than the En3A steel normally used by Hope for foundation plates (ie. Iscor steel ROQ-tuf AD 690 steel - refer Appendix E) was used in order to compensate for the higher than average GVM of the trailer and the fact that thread stresses resulting from the device mounting bolts are higher because of the reduced foundation plate thickness.

In Section D.5 of Appendix D, the stresses in the foundation plate are checked for the same horizontal design load and dynamic loading factor, applied at the king-pin, as used for the upper coupler analysis of Section 4.4.4 and Section C.5. No vertical loads are imposed on the 'Hope' device as all such loads at the king-pin are supported directly by the upper coupler structure. Bearing stresses at the eighteen foundation plate mounting bolt holes were

shown to be 435,8 MPa. The thread stresses in the foundation plate at the $8 \times \frac{1}{2}$ inch UNF device mounting bolts were calculated for a factor of safety of 2. The thread shear stress was 348,9 MPa, whilst the thread bearing stress was –378,6 MPa.

4.6 Axles, suspension and wheels

For the most part the various components of the semi-trailer running gear were supplied ready to be fitted to the trailer by the sponsoring companies. As a result, except for a small amount of work in the design of the suspension mountings, the majority of the design work in this area is concerned with the selection of the various components and configuration design.

4.6.1 Axles

As previously discussed in Section 4.2.1, because of the maximum payload criteria in this design, the axles of the tri-axle bogie are of necessity widely spaced. The use of self-steering or tracking axles for either one or two of the axles in order to prevent severe tyre scuff, is therefore imperative. For the axle positions as defined in Figure 4.1 in Section 4.2.1, various self-steering bogie configurations are possible, viz.

- Foremost and rearmost semi-trailer axles self-steering. Centre axle fixed.
- Foremost and centre semi-trailer axles self-steering. Rearmost axle fixed.
- Centre and rearmost semi-trailer axles self-steering. Foremost axle fixed.
- Foremost semi-trailer axle self-steering. Centre and rearmost axles fixed.
- Rearmost semi-trailer axle self-steering. Foremost and centre axles fixed.

Each of the configurations will exhibit different steering characteristics. In order to select the most suitable configuration and to optimise steering charac-

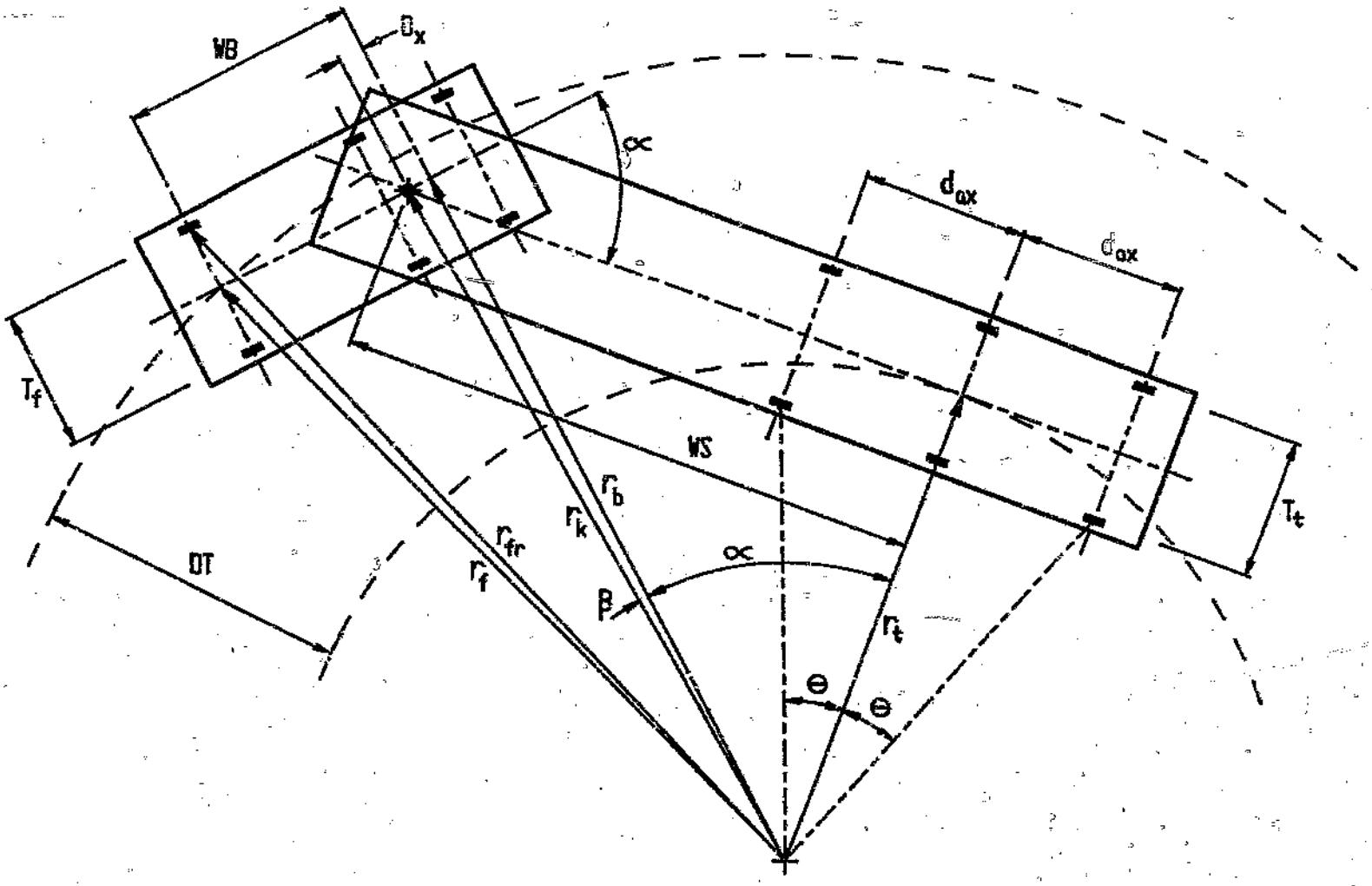


Figure 4.3 Semi-trailer tri-axle bogie self-steering configuration for trailer as built

teristic for the trailer, the steady state zero-speed tracking response of each configuration was analysed. The various radii associated with the steady, zero-speed turning of the steering configuration for the trailer as built are shown in Figure 4.3.

The six axles of the truck-tractor and semi-trailer combination are designated axles one to six, starting at the steering axle of the truck tractor. The truck-tractor wheelbase (WB), front axle track (T_f) and fifth wheel position (D_x) are average values for the truck-tractors analysed in Appendix G.

For the truck-tractor, by Pythagoras:

$$r_b = \sqrt{r_{fr}^2 - WB^2} - T_f/2$$

where r_{fr} is defined as the turning radius for the combination. The turning radius is measured to the centre of the footprint of the outboard steering axle tyre of the truck tractor.

Similarly:

$$r_f = \sqrt{r_b^2 + WB^2}$$

For the trailer, considering the triangles $(WS : r_t : r_k)$ and $(D_x : r_b : r_k)$:

$$r_t^2 = r_b^2 + D_x^2 - WS^2$$

The maximum off-tracking dimension of the combination for this steering configuration is then defined as:

$$OT = r_f - r_t$$

The articulation angle, which is the angle between the longitudinal centre-lines of the truck-tractor and the semi-trailer, is then determined from:

$$\beta) = \left(\frac{WS}{r_t}\right)$$

and

$$tan\ \beta = \left(\frac{D_x}{r_b}\right)$$

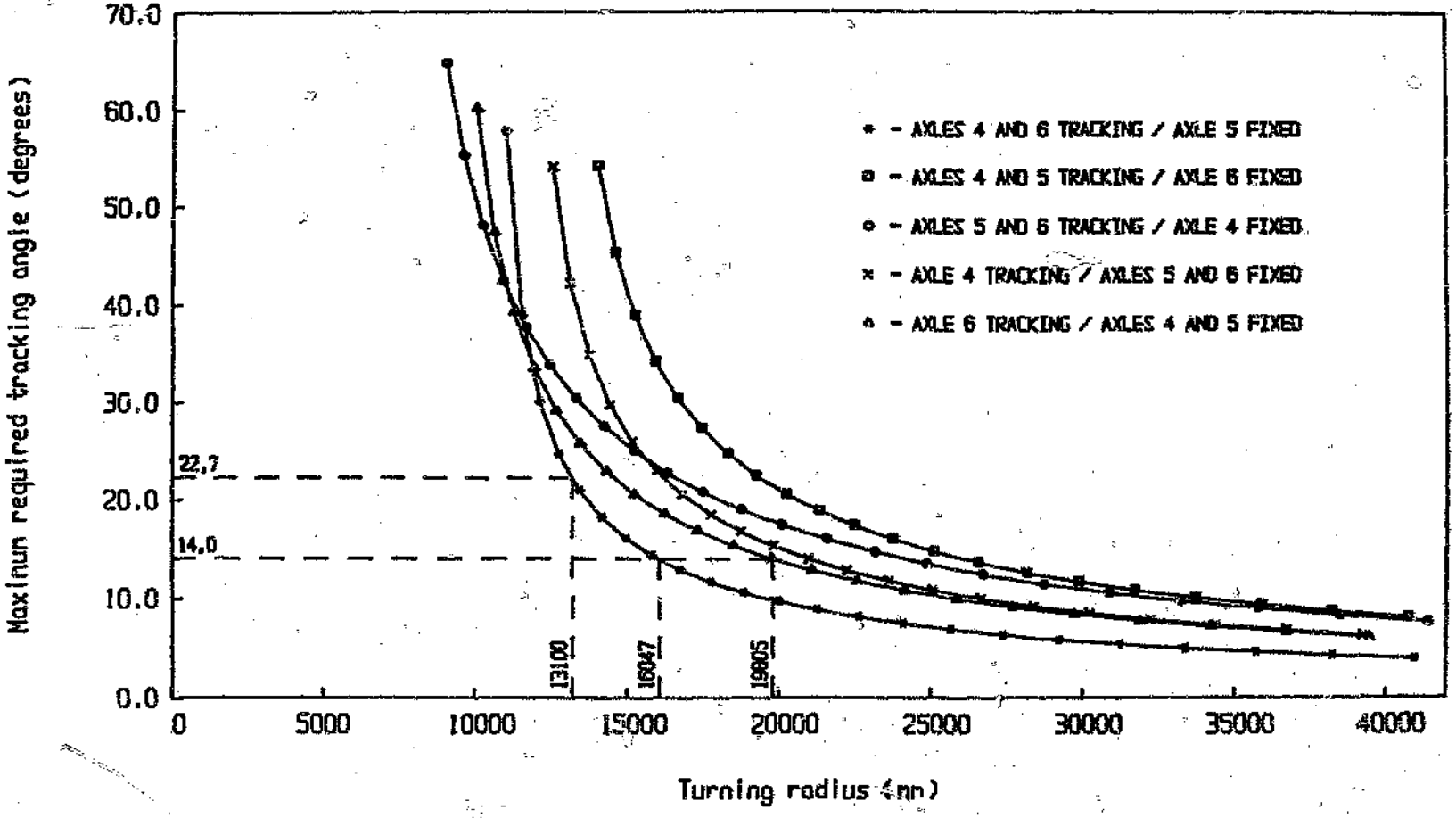
The maximum required tracking angle at the semi-trailer self-steering axles, will be at the inboard tyre of both axles four and six and is determined from the equation:

$$tan\ \theta = \frac{d_{ax}}{(r_t - T_t/2)}$$

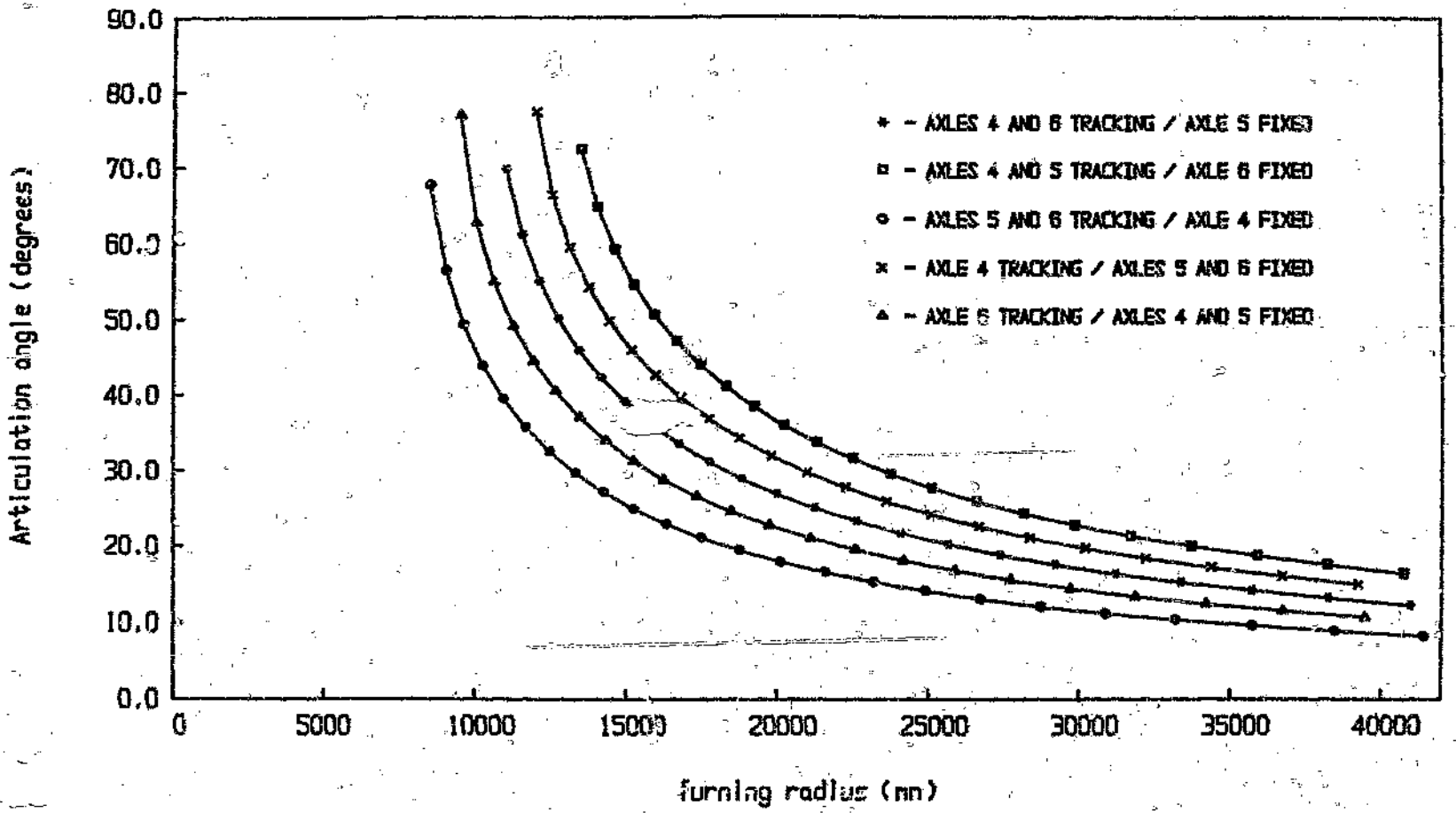
Similar analyses were also completed for the remaining four steering configurations cited above. The relationships between the turning radius and the maximum required tracking angle, the articulation angle and the off-tracking dimension for each of these steering configurations are shown in Graph 4.39 to Graph 4.41.

The maximum tracking angle that can be achieved with the FIA self-steering axles as fitted to the trailer, is 14 degrees. From Graph 4.39, the minimum turning circle for this tracking angle is attained with axles four and six tracking, and is equal to 16,047 metres. Furthermore, Regulation 92 of the Transvaal Road Traffic Regulations[5] requires that the full combination be able to turn with a turning radius of 13,1 metres. For axles four and six tracking, this requires a maximum tracking angle at the inboard self-steering tyres of 22,7 degrees. A certain amount of tyre scuff when cornering

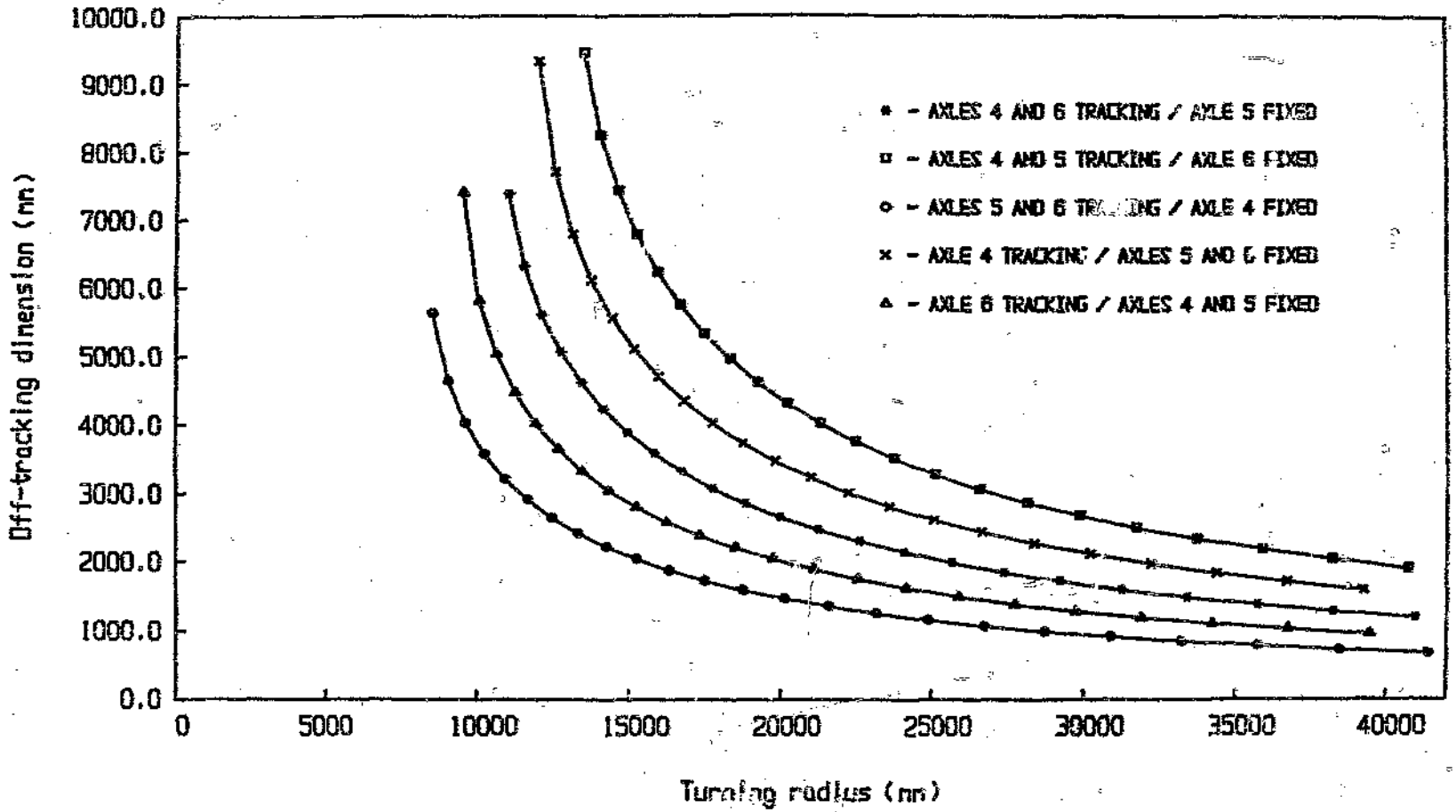
Graph 4.39 Turning radius versus maximum required tracking angle for various semi-trailer steering configurations



Graph 4.40 Turning radius versus articulation angle for various semi-trailer steering configurations



Graph 4.41 Turning radius versus off-tracking dimension for various semi-trailer steering configurations



severely is thus unavoidable, but is however, less for this configuration than the amount of tyre scuff that results at the foremost and rearmost axles of a standard closely spaced triden bogie with fixed axles (typically 1 360 mm axle spacing) at the same wheelbase and in a similar turn. For these reasons the trailer steering configuration as presented in Figure 4.3 was adopted in this design. The articulation angle and the degree of off-tracking are greater for this configuration at all turning radii than for axles five and six, or axle six only, tracking (refer Graphs 4.40 and 4.41), but are no worse than the generally accepted values obtained for semi-trailers with fixed bogies at approximately 9 metre wheelbase.

The steering configuration in which only axle six is tracking, was also considered since only one self-steering axle is required and consequently costs would be lowered. Also, as already mentioned, the off-tracking dimension is reduced due to the slightly shorter effective steering wheelbase. However, the turning radius for the maximum allowable tracking angle of 14 degrees at axle six (no scuff) is 19,805 metres, which is 23,4 percent more than for axles four and six tracking. As well as this, the degree of tyre scuff that results for a turning radius of 13,1 metres is greater than for a closely spaced fixed axle triden bogie at the same wheelbase.

When the semi-trailer is travelling forward, the FIA self-steering axles steer by means of a castor action. Consequently, when the trailer is being reversed it is necessary to lock the trailing arms of the steering axles in the central position. This is accomplished by means of a pneumatically operated locking pin which is activated from the cab of the truck-tractor. The locking pin cylinder is mounted on the axle beam and engages in a hole in a plate welded to the tie bar which connects the two trailing arms (Photo. 5.68).

At speed, and especially on rough road surfaces, there is a tendency for the

trailing arms of the self-steering axles to oscillate from side to side. In order to prevent this from happening an air spring damper is mounted between the axle beam and the tie bar (Photo. 5.68). The air pressure in the damper can be switched between two pressure settings, in order to cater for lightly (25 psi/1,72 bar) and heavily (50 psi/3,45 bar) loaded conditions.

The auxiliary pneumatic circuit which supplies the compressed air for and controls the axle locking pin and restraining bellows, is presented in Drawing No. PM-03 in Appendix H. Supply air is received from the suspension circuit through a non-return protection valve into a 15 ℓ reservoir. When energized the solenoid valve on the locking pin cylinder line opens and allows the compressed air to engage the locking pin. Upon removal of the air pressure, the locking pin is disengaged by the cylinder return spring. In this way failure of either the electrical system or the supply of compressed air to the circuit will ensure that the locking pin remains disengaged. On the air spring damper side of the circuit, with the solenoid valve closed (non-energized), the compressed air flows through the 25 psi regulator to the restraining dampers. When the solenoid valve is energized, compressed air is allowed to flow through the 50 psi regulator to the restraining dampers, and the higher back pressure against the 25 psi regulator causes that regulator to remain closed.

Green polyamide plastic tubing is used throughout on the auxillary pneumatic circuit for easy identification.

4.6.2 Suspension

An air suspension was selected in this design project because of its superior load equalisation characteristics in comparison with conventional leaf-spring suspensions. As discussed in Section 3.2, the efficiency of the suspension

load equalisation system is particularly important for a wide spaced tri-axle suspension. A further reason for selecting an air suspension is that it is more easily applied to the wide spaced tri-axle configuration. This is because the only connection between adjacent axles is a pneumatic air line, whereas in the case of a wide spaced leaf-spring suspension, long tie bars are required between the load equalisation rockers of adjacent axles.

The Fruehauf T air suspension, as fitted to the trailer, employs a single levelling valve which is mounted on the chassis above the centre axle. The suspension ride height is sensed relative to the centre axle by means of a short tie bar connected between the lever arm of the valve and the centre axle. The length of the tie bar can be adjusted to vary the suspension ride height. In this case the ride height was set at 514 millimetres (refer Drawing No. SS-01 in Appendix H).

The levelling valve supplies air to all six air bags, and hence, only vertical springing is undertaken by the air springs. Roll stiffness is provided by the torsional rigidity of the suspension trailing arms. This system is superior to using two levelling valves (ie. one for each side of the trailer) since a punctured air bag will cause the trailer to settle on the rubber back-up buffers, rather than tip to one side.

The pneumatic circuitry for the air suspension is supplied with compressed air from the semi-trailer emergency line via a dual circuit charging valve (refer Drawing Nos. PM-01 and PM-02 in Appendix H). This valve distributes the compressed air to the suspension and brake circuits and ensures that if one of these circuits fails, the air supply to the other intact circuit is maintained (also refer Section 4.7.1).

Black polyamide plastic tubing is used throughout for the suspension pneu-

matic circuitry to facilitate easy identification and servicing.

4.6.3 Wheels and tyres

Michelin 16.5 R 22.5 'Double X' (PR 20) tubeless radial super single tyres mounted on one piece 22.5 x 13.0 inch, 15 degree drop centre rims, were selected for all three trailer axles. These tyres are capable of axle loads of up to 10 300 kg at 8,5 bar inflation pressure,[53] but are limited to a maximum axle load of 7 700 kg by road regulation restrictions.[5] This is however sufficient for the design axle loads as shown in Figure 4.1, Section 4.2.1, albeit with the load centre 50 mm forward of the centre of the trailer deck. The recommended inflation pressure for the 7 700 kg axle load is 6,2 bar.[53]

The primary reasons for selecting super single tyres in this design were, firstly that super single tyres with single piece rims are lighter than conventional dual tyre fitments (often in excess of 100 kg per axle). Secondly, the wider axle track and spring centres achievable with super single tyres significantly increases the roll stability of the trailer.

Other advantages of super single tyre fitments are less rolling resistance and therefore reduced fuel consumption, better ventilation of brake drums and the fact that the safety of other road users is enhanced since the danger of stones becoming trapped between dual tyres is eliminated.

Finally, to further ensure the safety of the occupants of vehicles travelling behind the semi-trailer, two heavy duty anti-spray rubber mudflaps were fitted immediately behind the rearmost set of tyres.

4.7 Braking system

The semi-trailer braking system adopted in this design project acts on all three axles and is classified as a single-circuit, dual-line, compressed-air trailer power brake system. The classification of single-circuit refers to the fact that the braking energy is transmitted to all the brakes on the trailer through one single transmission or circuit, and hence, should a defect occur at any point within that circuit, the entire trailer brake system will be affected. Dual-line indicates that the semi-trailer is connected to the truck-tractor by two lines; one supply line (emergency line) and one brake line (service line). Compressed air is supplied to the trailer at a maximum operating pressure of 6,5 bar which results in the system being classified as low pressure (ie. less than 10 bar). The term power brake system indicates that the vehicle is braked exclusively by an external force (ie. compressed air) and that the muscle power of the driver serves only to control the system and cannot generate any braking force should there be a total energy failure.

The pneumatic circuit diagrams for the brake system and associated systems (ie. Hope anit-jack-knife device, suspension and auxiliary circuits) are presented in Drawing Series PM-01 to PM-03 in Appendix H. Section 4.7.1 discusses the operation of the trailer braking system, whilst the operation of the Hope device circuit and the operation of the suspension and auxiliary circuits are discussed in Sections 4.5.4 and 4.6, respectively.

The semi-trailer braking system is designed to meet the requirements of the specification SABS SV 1051-1980, 'Motor vehicle safety specification for braking'.[24] This specification covers the mandatory requirements for the performance of the braking devices and systems of motor vehicles and their trailers or semi-trailers designed for use on public roads. In this report only those requirements pertaining directly to semi-trailers having a maximum

mass exceeding 10 tonnes (ie. category 04 vehicles) are addressed. Sections 4.7.2 to 4.7.3 discuss each requirement individually, whilst the actual design and compatibility calculations are presented in Appendix F.

4.7.1 Brake system operation

The semi-trailer brake system (refer Drawing No. PM-01 in Appendix H) is comprised of three equipment groups. The compressed air supply stores compressed air received from the truck-tractor and supplies it to the brake system. The service brake system regulates the transmission of compressed air to the wheel brake cylinders of all axles in accordance with the pressure applied to the service brake line from the truck-tractor. The parking brake system controls the supply of compressed air to apply or release the spring brake cylinder actuated parking brake.

All of the 12 mm OD x 1,5 mm wall non-reinforced polyamide tube used in the brake system is colour coded for easy identification. The air supply and parking brake systems (also called the emergency system) are constructed using red tubing whilst the tubing of the service brake system is yellow. White, black, and green tubing is used for the Hope device, suspension and auxiliary circuits respectively (refer Sections 4.5.4 and 4.6). Where a fairly high degree of flexibility is required (ie. between the chassis and the axles), 11 mm bore rubber brake hose is used.

Schäfer plug type connections together with Schäfer adaptors, elbows and tees are used to connect the polyamide tubing to the various circuit components in all of the pneumatic circuits.

Compressed air supply

With the semi-trailer hitched up, compressed air (at approximately 650 KPa

gauge) flows from the truck-tractor through the emergency coupling head and through the line filter into the compressed air supply system. The line filter, which cleans the supply air, is mounted in the circuit in such a way (fitting 2 inlet) that it will open in the event of clogging, thus ensuring that the brake system will remain operational at all times.

The dual circuit charging valve distributes the compressed air between the brake system reservoirs and the suspension system, and ensures that if one of these circuits should fail, the air supply to the other undamaged circuit is maintained. The charging valve also safeguards the pressure in both circuits and allows a limited return flow of air (ie. down to a set closing pressure) from the suspension circuit to the brake circuit, should the air supply to the semi-trailer fail. No return flow is allowed from the brake circuit to the suspension circuit. In this way the suspension system reservoir is able to assist with the supply of air to the brake circuit under such emergency conditions, whilst still maintaining sufficient pressure in the suspension circuit for the air springs to support the load.

From the charging valve the compressed air flows to the two brake reservoirs, where it is stored. A manually operated drain valve is fitted to each reservoir for draining condensation water, and the rearmost reservoir is also fitted with a tyre inflator connection. This connection can also be used to charge the trailer brake system from an external source of compressed air in order to save diesel costs at the truck-tractor.

Under normal driving conditions the supply air also flows through the parking brake valve and the double check valve into the spring brake cylinders, whilst the air line between the double check valve and the manoeuvring valve is exhausted. In the spring brake cylinder the compressed air acts against a diaphragm to compress the parking brake spring, thereby maintaining the

wheel brakes in the released position. If the supply line is exhausted as a result of the trailer breaking away, or if the pressure in the supply line drops drastically as a result of a leak, then the springs in the spring brake cylinders will apply the wheel brakes on all three axles, thus automatically causing the trailer to brake.

Service brake system

When the driver in the truck-tractor actuates the service brake, a braking signal in the form of a pressure rise proportional to the degree of brake pedal depression, is transmitted through the service coupling and line filter into the semi-trailer service brake system.

The automatic load sensing valve regulates the brake pressure transmitted to the service brake chambers as a function of suspension air bag pressure, and consequently as a function of the loading condition of the trailer. This considerably lessens the possibility of wheel lock-up under emergency braking, especially when the trailer is unladen or lightly laden. The valve is adjusted to yield the required pressure ratios for the unladen and legal loaded conditions relative to the corresponding suspension air bag pressures, by means of adjusting screws (refer Section 4.7.3).

A relay valve positioned above each axle accelerates the admission to and removal of air from the brake cylinders. Upon receiving the braking pressure signal from the load sensing valve, the first relay valve directs large quantities of compressed air from the adjacent reservoir to the brake chambers of the first axle, as well as accelerating the transmission of the braking signal towards the rear of the trailer. The second and third relay valves, in turn, receive the braking signal and direct large quantities of compressed air to the second and third axle brake chambers respectively from the second brake system reservoir. The two reservoirs are positioned as close as possible to

the relay valves in order to ensure the rapid admission of air to the brake chambers, and hence, the minimum time delay between the initiation of the service brake signal by the driver and the application of the wheel brakes. When the brake signal is removed the compressed air in the service brake cylinders is exhausted through the relay valves.

Test points are provided at various points in the circuit in order to facilitate time response testing of the system.

Parking brake system

With the trailer coupled, operation of the parking brake valve in the truck-tractor causes compressed air at the maximum operating pressure (ie. approximately 650 KPa) to be directed to the service coupling of the semi-trailer. The trailer service brake system is hence triggered both when the service brake as well as the parking brake of the truck-tractor are operated. When the vehicle is stationary, the spring brake operated parking brakes of the semi-trailer can be applied on their own or in addition to the service brake parking brakes by operating the trailer park brake valve. This exhausts the supply line between the park brake valve and the spring brake chambers, thus releasing the parking brake springs to apply the wheel brakes.

When the trailer is uncoupled, the resultant drop in pressure in the supply line, and hence in the spring brake chambers, automatically causes the spring brake parking brakes to be applied. If required, and providing there is sufficient compressed air remaining in the brake system reservoirs, the spring brakes can be released by operating the manoeuvring valve and allowing compressed air to flow via the double check valve to the spring brake chambers.

4.7.2 Service braking performance

The total available braking force at the road wheels of the semi-trailer is calculated in Section F.2 of Appendix F, in order to assess the performance of the braking system.

The braking force is calculated for a maximum service line pressure, measured at the trailer coupling head, of 650 KPa (gauge). This is an average value for the majority of the truck-tractors on the market at present.[3,54] The threshold pressure, also measured at the coupling head of the semi-trailer, and which is defined as that small amount of air pressure required to initiate braking at the road wheels, is assumed to be 50 KPa. This accounts for the small amount of pressure required in the service brake chambers to bring the brake shoes into contact with the brake drum before any braking takes place, and any pressure losses in the air lines and valves of the service brake system between the coupling head and the brake chambers. In actual practice both of these components of the coupling head threshold pressure will, at any particular time, be dependent on the prevailing service line pressure and the load sensing valve ratio. However, no reliable information with regard to the cam-shaft threshold torque required for the Henred Fruehauf 420 x 160 mm foundation brake, or of the expected losses in any of the valves used, was available to the author. For this reason, and in keeping with current industry practice,[3,55] a constant threshold pressure was decided upon. Such an assumption will not significantly affect the accuracy of the compatibility calculation.

The maximum useful brake chamber pressure, is hence, 600 KPa. For this pressure, the maximum total available braking force for the full trailer is shown to be greater than 45 percent of the maximum weight borne by the wheels of the trailer when stationary. The minimum performance require-

ments of SABS SV 1051:1980[24] for the trailer service braking system are thus exceeded and an overload of approximately 3 000 kg per axle is allowed for. Such an allowance for overloading is appropriate when it is borne in mind that a large proportion of the semi-trailers on South African roads at present are overloaded to some degree. The average overload on a semi-trailer was estimated during 1984 by the Automotive Engineering Division of the South African Bureau of Standards to be in the region of 6000 kg per vehicle.[54]

4.7.3 Braking compatibility of the truck-tractor and semi-trailer combination

In order to ensure the safe braking performance, particularly on road surfaces which have reduced adhesion, and the braking compatibility between the semi-trailer and the drawing vehicle, laden and unladen compatibility curves were constructed in Section F.3 of Appendix F, in accordance with the requirements of SABS SV 1051:1980 - Part VI.[24]

The actual weight distribution for the semi-trailer (refer Figure 2.1, Chapter 2) is used in the compatibility curve calculations and in subsequent brake system calculations, although the design weight distribution (refer Figure 4.1, Chapter 4) was used during initial design stages to size brake system components. This is in accordance with current industry practice and is necessary for the accurate determination of load sensing valve settings.

Load sensing ratios of 1,2 and 2,7 were selected for the legal laden and unladen conditions, respectively. In the legal laden condition (ie. maximum legal payload), the load sensing valve ratio of greater than unity allows a factor of safety in the event of the trailer being overloaded.

The laden and unladen compatibility curves are presented in Graphs F1 and F2 of Appendix F.

4.6 Lights, retro-reflectors and electrical system

The positions of the various lights and retro-reflectors fitted to the semi-trailer are as detailed in Drawing Nos. GA-01 and EL-01. In each case the selection of the type of light or retro-reflector, in terms of its mechanical characteristics (eg. angles of directional visibility, etc.), and its positioning on the trailer chassis, was determined relative to SABS SV 1046: 1980 'Motor vehicle safety specification for lighting'[56] and the Road Traffic Ordinance and Regulations of the Transvaal.[5]

Three stop/position lights and three direction indicator lights were used on each side at the rear of the trailer for reasons of increased visibility and safety. The use of multiple lights also ensures that, in the event of the failure of one of the globes, the trailer rear indicator lights will remain fully operational. Two white reverse lights and a reverse buzzer were also fitted at the rear of the trailer to assist the driver when reversing, and to warn other road users that the vehicle is reversing or about to reverse.

Six amber combination direction indicator and side marker lights, as well as six amber retro-reflectors were fitted down either side of the semi-trailer. The purpose of the direction indicator lights is to indicate the driver's intentions to pedestrians or other road users positioned to the side of the truck/trailer combination. The amber retro-reflectors and side marker lights serve to ensure that the presence and length of the vehicle, when viewed from the side, will be readily visible at night.

Thirteen rectangular red retro-reflectors were fitted at the rear of the semi-

trailer. Eleven of these were mounted horizontally to form a chevron pattern over the full width of the chevron board, and one was mounted vertically at each end of the chevron board, to indicate the width of the trailer. A white retro-reflector was mounted on either front corner of the trailer, on the lower ends of the headboard outer uprights.

The electrical wiring diagram for the semi-trailer is detailed in Drawing No. EL-01 (refer Appendix H) together with a full list of all of the lights and electrical components used on the semi-trailer. As indicated in the drawing, all of the lights at the rear of the vehicle, the reverse buzzer, the rearmost set of side direction indicator and marker lights, as well as the two solenoid valves of the steering axle pneumatic control circuit, are powered via a seven core cable running down the centre of the trailer chassis. The remaining side marker and the direction indicator lights are powered by a two core cable running down either side of the vehicle. These three supply cables join together above the rubbing plate and are coupled to the truck-tractor electrical system via two electrical suzies.

CHAPTER 5

SEMI-TRAILER CONSTRUCTION

5.1 General

Construction work on the aluminium semi-trailer began late in January 1984 with the fabrication of components at the University's Mechanical Engineering Laboratory workshops and at Afrox Ltd in Germiston. The majority of plate components, especially thick plate, were plasma arc profile cut at Afrox, whilst thin plate (ie. less than 5 mm thick) and all aluminium extrusions, were cut to size and machined or formed as required at the Mechanical Engineering Laboratory workshops. Over the ensuing months the fabrication of the various components was scheduled to coincide with the order of construction of the trailer assemblies.

The following sections discuss the significant steps in all subsequent phases of construction of the semi-trailer. Unless otherwise stated, the order of presentation of these sub-sections follows in general the order of assembly. Liberal use of photographs is made throughout the chapter for the purpose of illustration.

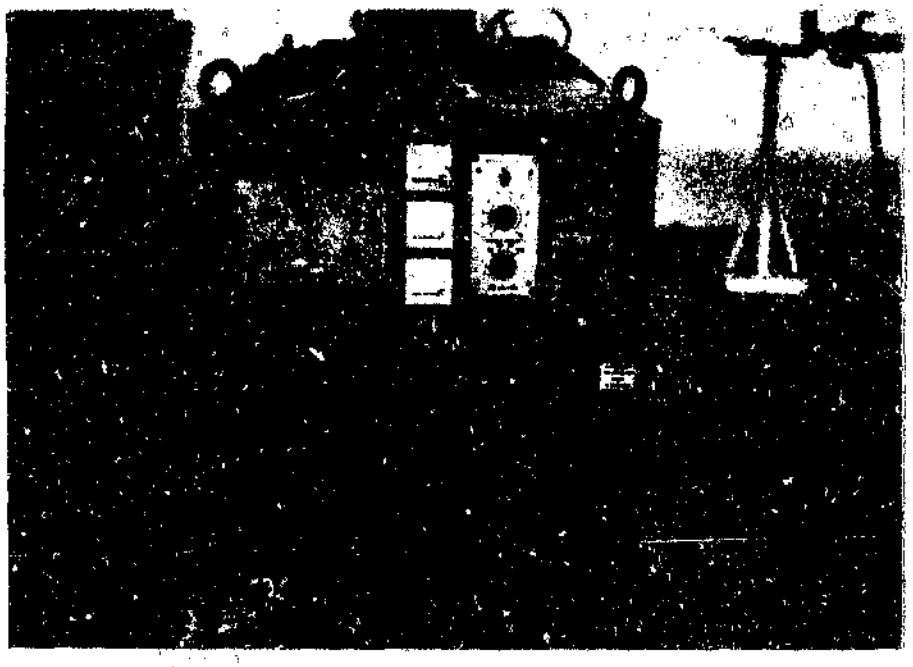
The chapter starts with a discussion of the aluminium welding process and equipment employed before going on to the construction of the semi-trailer itself.

5.2 Aluminium welding

Photographs 5.1 and 5.2 show the metal inert gas (MIG) welding equipment used in the construction of the aluminium semi-trailer chassis and substructure.

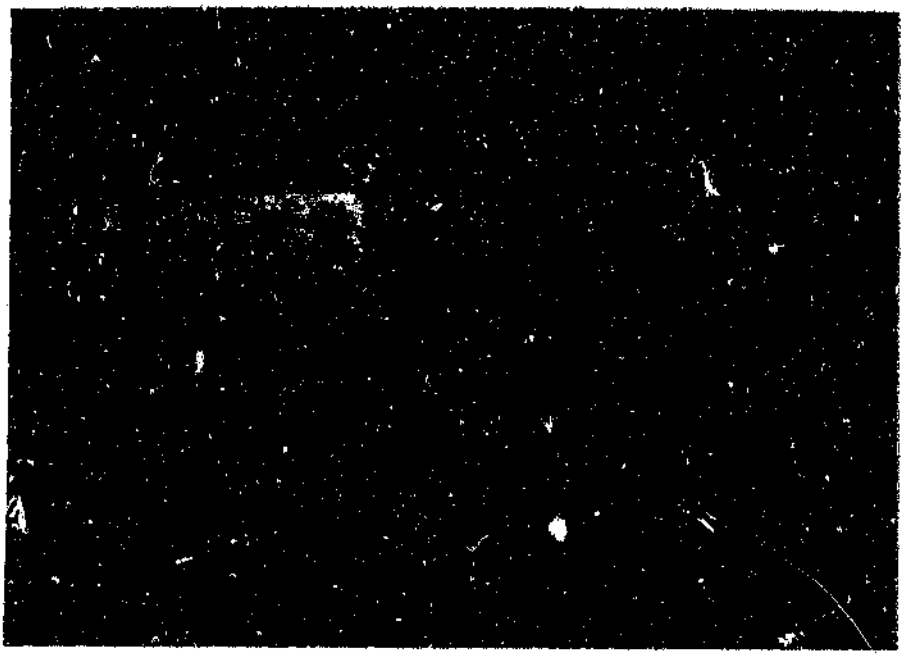
The detailed equipment specifications are as follows:

- 'Cloos' shielded arc automatic MIG welding machine (Type GLC 353 PA).
- 'Cloos' wire feeding device (Type CK 11/4).
- 'Messer Griesheim' push/pull motor hand welding torch.
- 1,2 mm filler wire diameter.
- Argon shielding gas.



Photograph 5.1 'Cloos' shielded arc automatic MIG welding machine (Type GLC 353 PA)

The MIG welding process was selected in this project mainly because of the high welding speeds attainable relative to other processes suitable for aluminium welding. This contributed to a faster rate of construction



Photograph 5.2 'Messer Griesheim' motor hand welding torch and 'Cloos' wire feeding device

and helped to keep costs to a minimum. Some further advantages of the MIG welding process that were considered are the lower overall heat input (due to the higher welding speeds) than, for example, tungsten inert gas welding (TIG), thereby minimising distortion in critical areas, and the suitability of the process to the range of material thicknesses used in the trailer construction.[57,58]

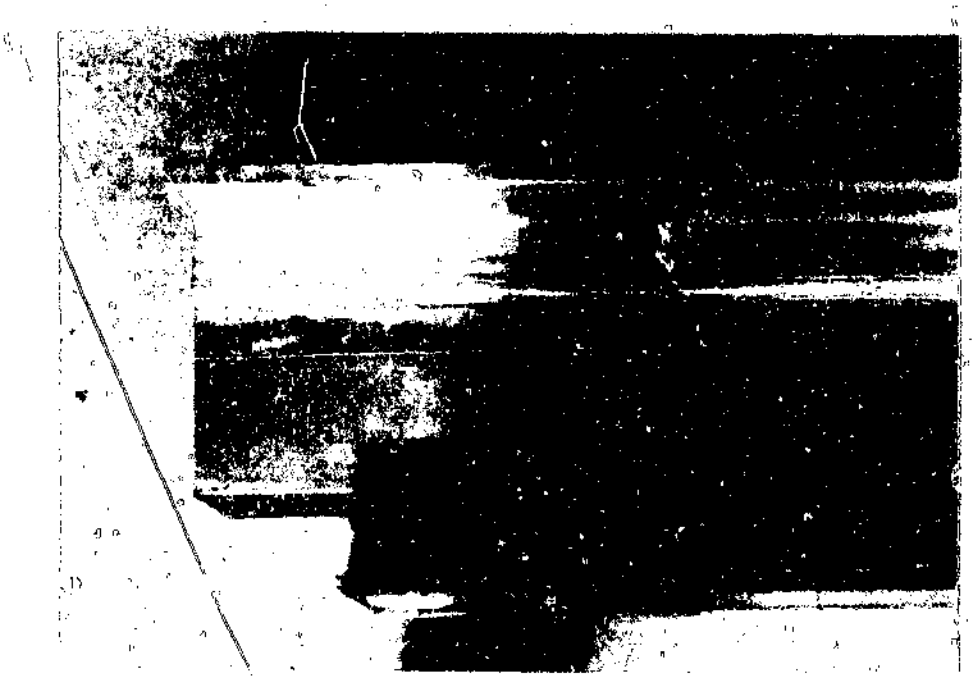
The combinations of parent alloys welded and the filler alloys used in each case are presented in Section E.2 of Appendix E.

Cleaning of the aluminium alloy material, both before and after welding, was accomplished using a stainless steel wire brush. Where it was necessary for welds to be dressed smooth these were ground using non-carborundum grinding discs.

5.3 Construction of the aluminium chassis structure and associated sub-structure

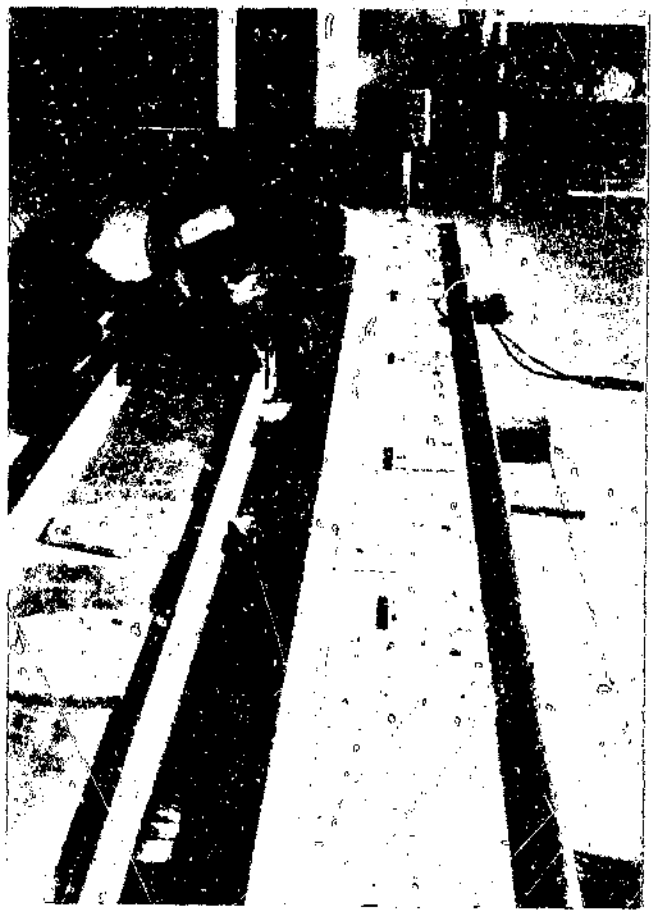
Construction of the aluminium semi-trailer chassis itself commenced at Industrial Research and Development (Pty) Ltd in Boksburg North during early April 1984.

Work began on the main chassis I-beams with the beams being chamferred at the front to receive the rubbing plate lead-in (refer Photo. 5.3). The two beams were also cut accurately to length at this stage (refer Drawing No. CH-04) since they were supplied marginally over-length by Schweizerische Aluminium AG (Alusuisse).



Photograph 5.3 Chamfer at front of chassis I-beams for rubbing plate lead-in

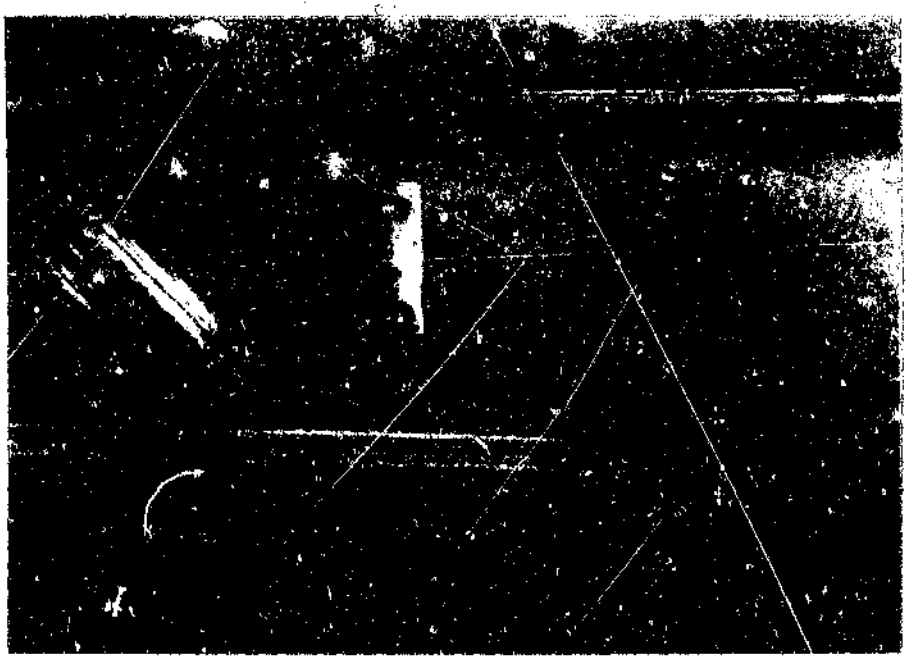
Both chassis beams were then laid on their sides and the bolt holes to receive the torsion tube and suspension mounting flange bolts were drilled (refer Photo. 5.4 and Photo. 5.5). A magnetic base pillar drill mounted on a 12 mm thick mild steel plate platform (refer Drawing No. JG-01), which was guided on and clamped to the I-beam flanges, was used for this purpose. Two diagonally opposite holes in each bolt pattern were marked out on the I-beam web and drilled first. The flanges were then bolted in place and the remaining holes drilled using the mounting flanges as templates. The landing leg mounting bracket and rearward brace bracket (refer Photo. 5.6 and Photo. 5.7) were also assembled at this time and welded, together with the rear flange extensions, onto the beams.



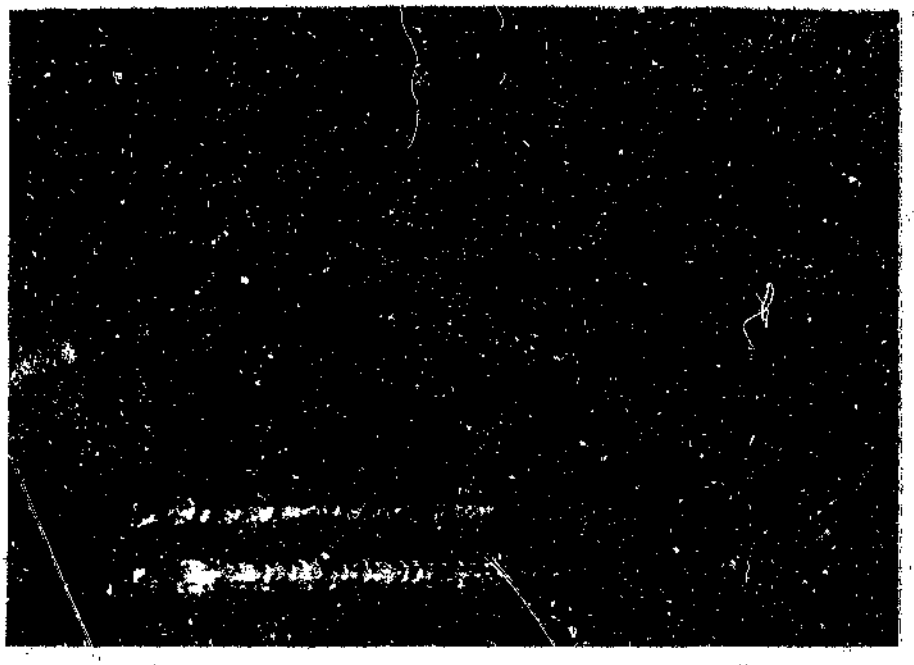
Photograph 5.4 Drilling of torsion tube and suspension mounting bolt holes



Photograph 5.5 Magnetic ¹ pillar drill on drilling platform



Photograph 5.6 Landing leg mounting bracket

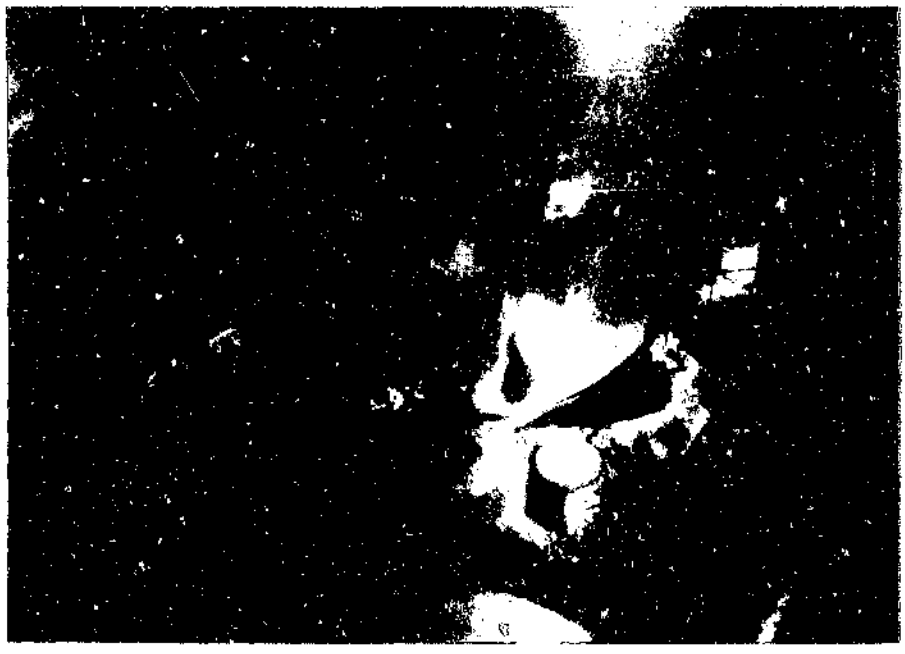


Photograph 5.7 Landing leg rearward brace bracket

The torsion tubes were then assembled onto the main I-beams to construct the basic 'ladder' frame chassis. This was accomplished by standing the 160 millimetre diameter tubes on end on their respective flanges with the first I-beam lying on its outer side (refer Photo. 5.8). The tubes were then tacked to the flanges as shown in Photo. 5.9. Perpendicularity was ensured since the tubes were cut accurately square and to length.



Photograph 5.8 Assembly of torsion tubes onto first chassis I-beam

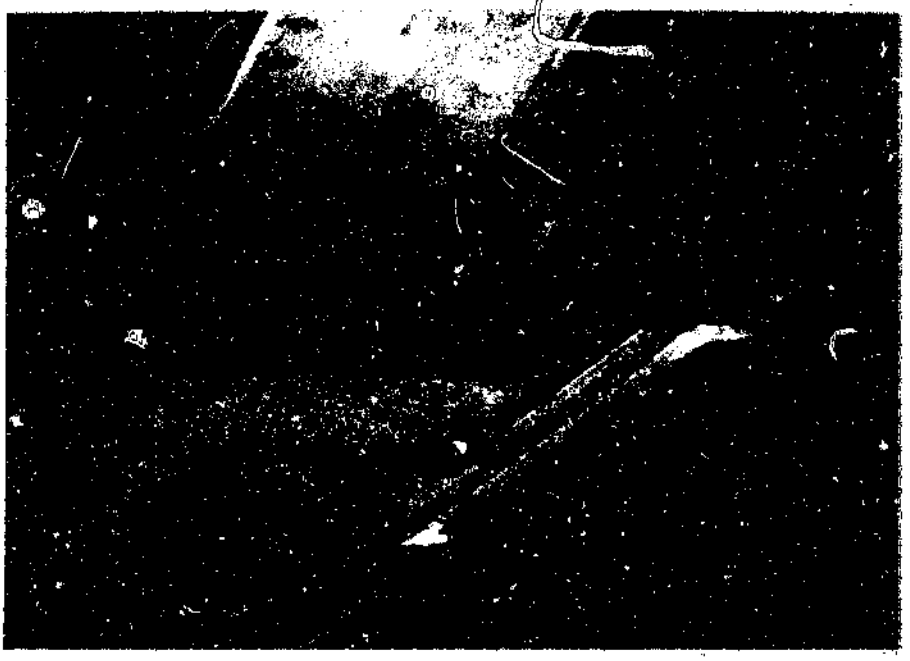


Photograph 5.9 Torsion tube tacked to flange

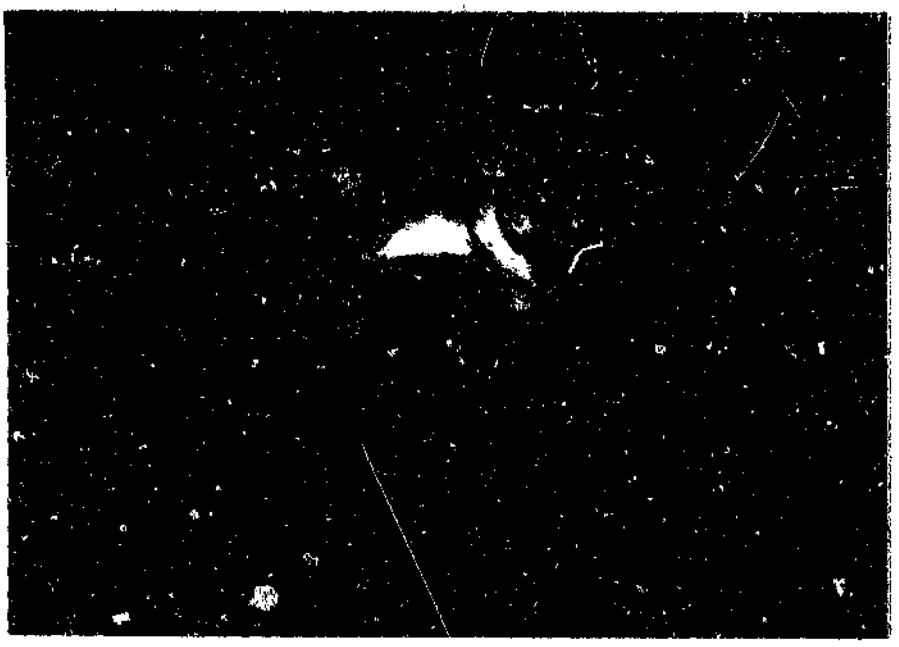
The second I-beam was then lowered into position using the overhead crane and the tubes tacked to the upper flanges. The landing leg cross-member flanges were then bolted onto the mounting brackets and the landing leg cross-member tacked in position (refer Photo. 5.10 and Photo. 5.11). The lower ends of the torsion tubes and landing leg cross-member could then be fully welded in this position after cleaning (refer Photo. 5.12). The frame was turned over onto the other beam to complete the welding.



Photograph 5.10 Second chassis I-beam assembled onto torsion tubes



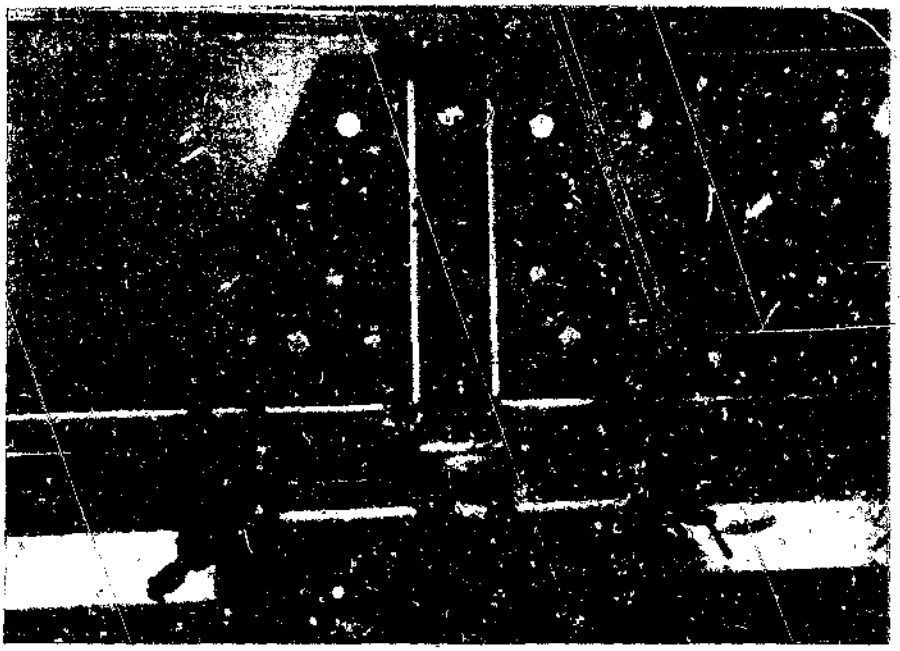
Photograph 5.11 **Landing leg cross-member tacked to flange**



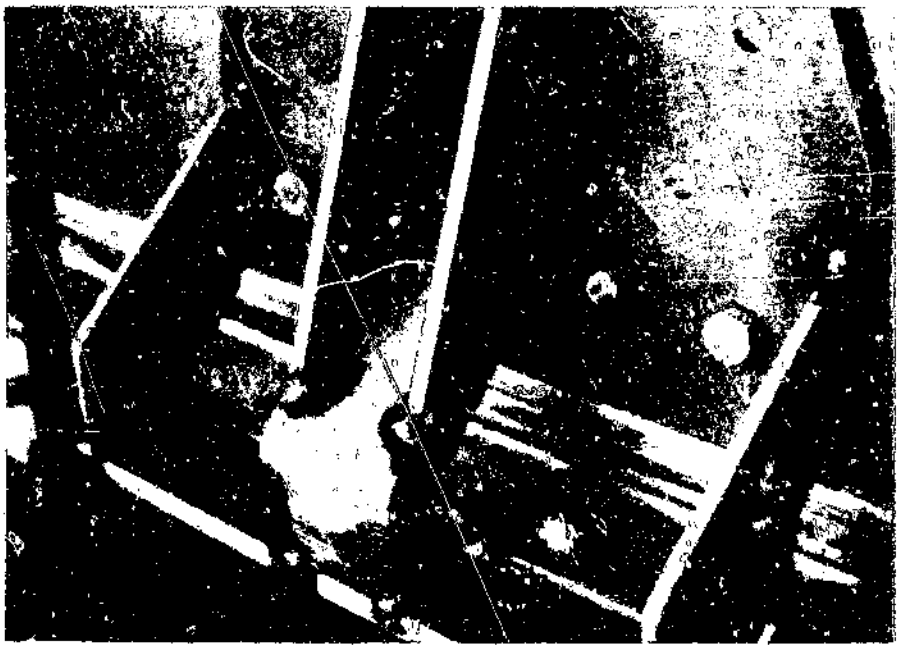
Photograph 5.12 **Torsion tube cleaned and ready for welding to flange**

This completed, the frame was lowered to stand on the underside of the two main I-beams and the centre portion of the rear end rail welded in position.

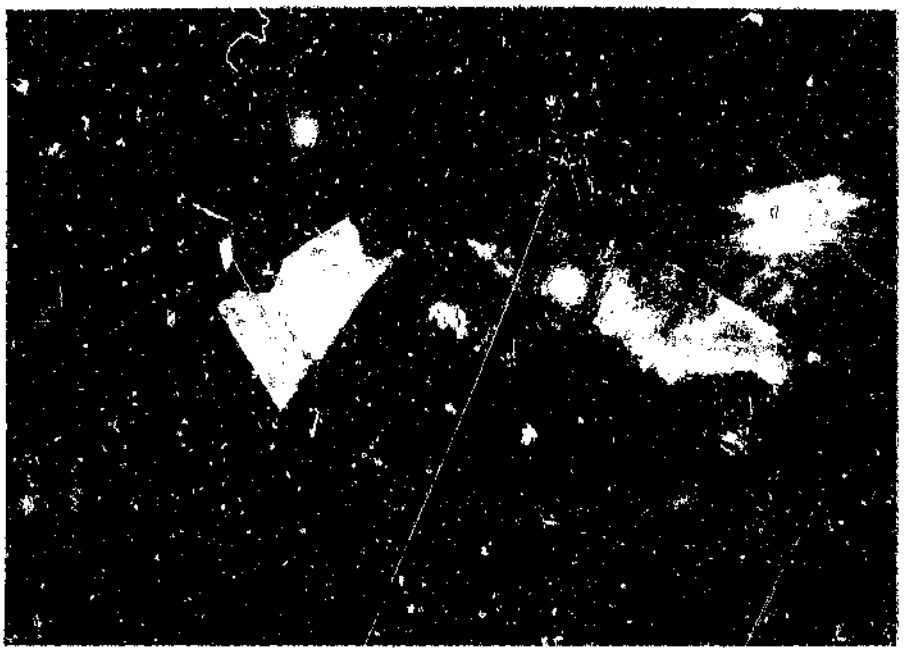
With the suspension mounting flanges bolted to the main I-beam webs, the suspension mounting jigs for both the hanger and air bag positions were clamped in place at the foremost axle position. The suspension hanger and air bag mount components and cross-member were then assembled onto the jigs and tacked in position (refer Photo. 5.13 and Photo. 5.14). Note the weld preparations which have been ground on the edges of the various components. The outer tee-gussets were fully welded, however, before being tacked in place. Both mountings were then fully welded, except for those areas where welding was required from underneath, before the jigs were removed. This was done in order to minimise welding distortion. The tee-gussets and the suspension mount assemblies were pre-heated before welding to ensure good weld penetration and to further reduce welding distortion (refer Photo. 5.15). This process was then repeated for the centre and rearmost axle mountings (refer Photo. 5.16). Finally, the jigs were removed and the welds cleaned and ground (refer Photo. 5.17 to Photo. 5.19).



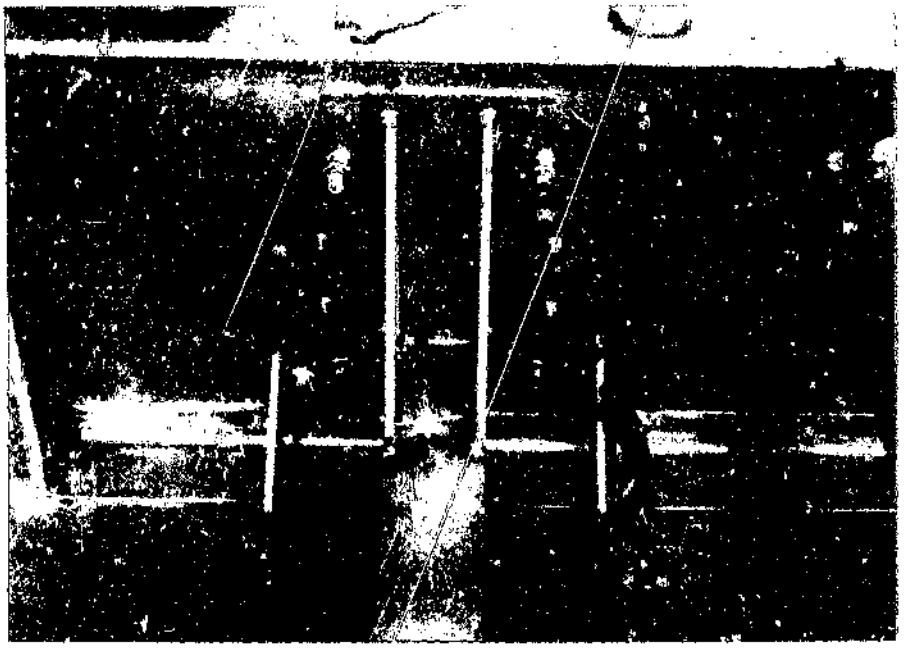
Photograph 5.13 Foremost axle suspension hanger mounting outer bracket components assembled onto welding jig



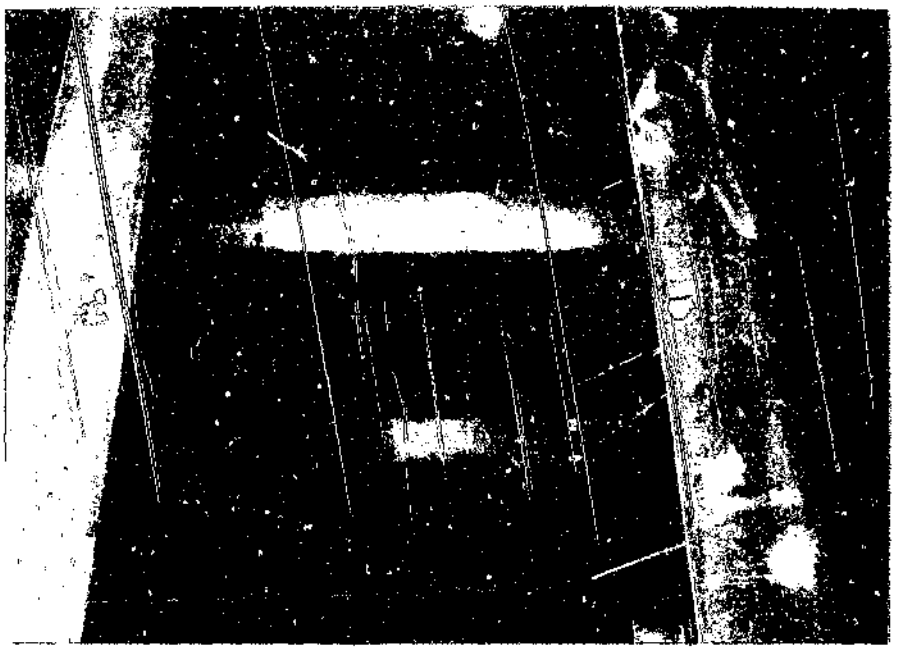
Photograph 5.14 Foremost axle suspension hanger mounting outer bracket components tacked into position



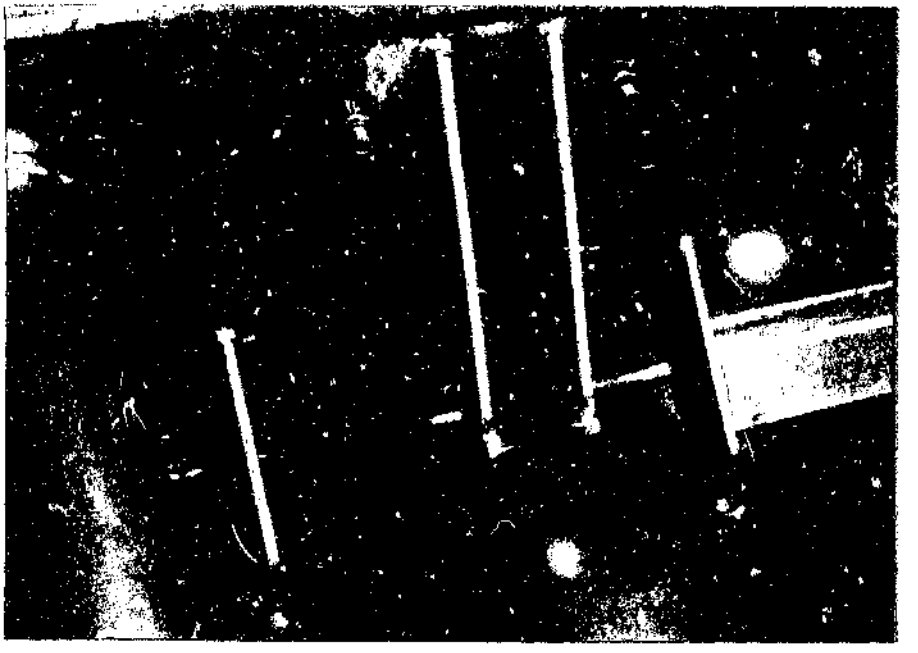
Photograph 5.15 Pre-heating of suspension mounting components before welding



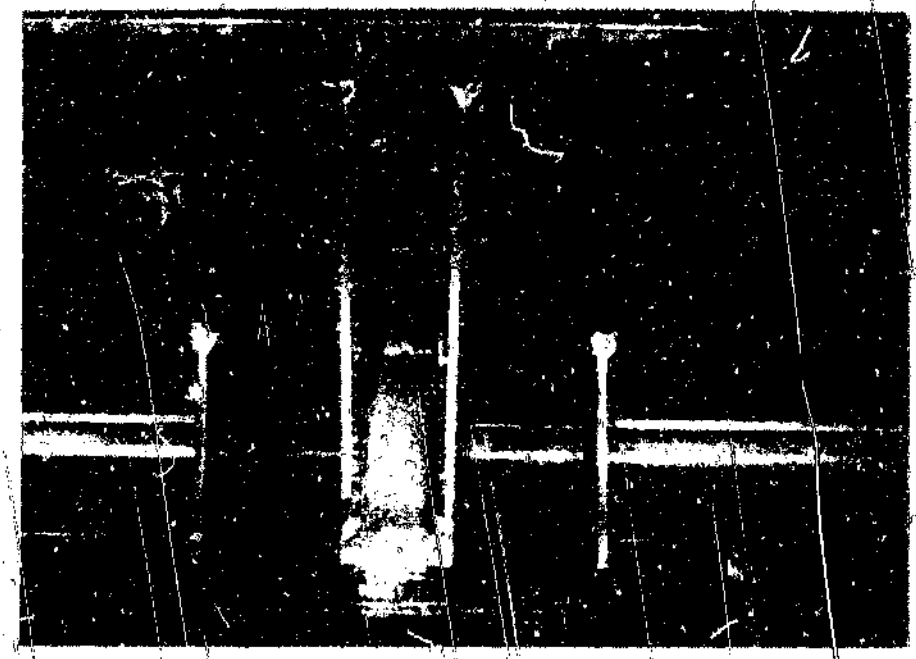
Photograph 5.16 Rearmost axle suspension air bag mounting cross-member components assembled onto welding jig



Photograph 5.17 Rearmost axle suspension hanger and air bag mounting cross-members

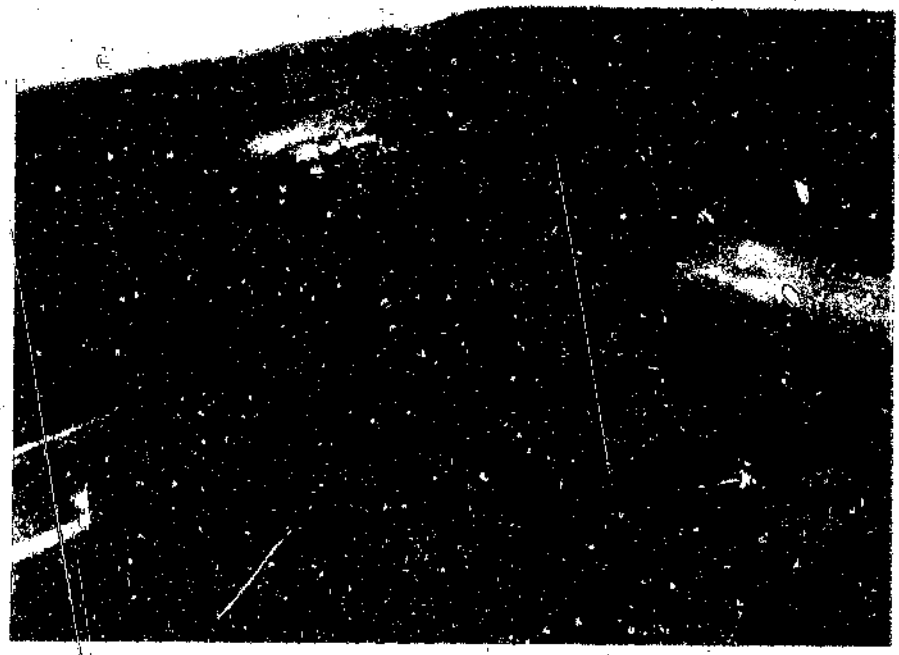


Photograph 5.18 Suspension hanger mounting cross-member assembly after cleaning and grinding of welds



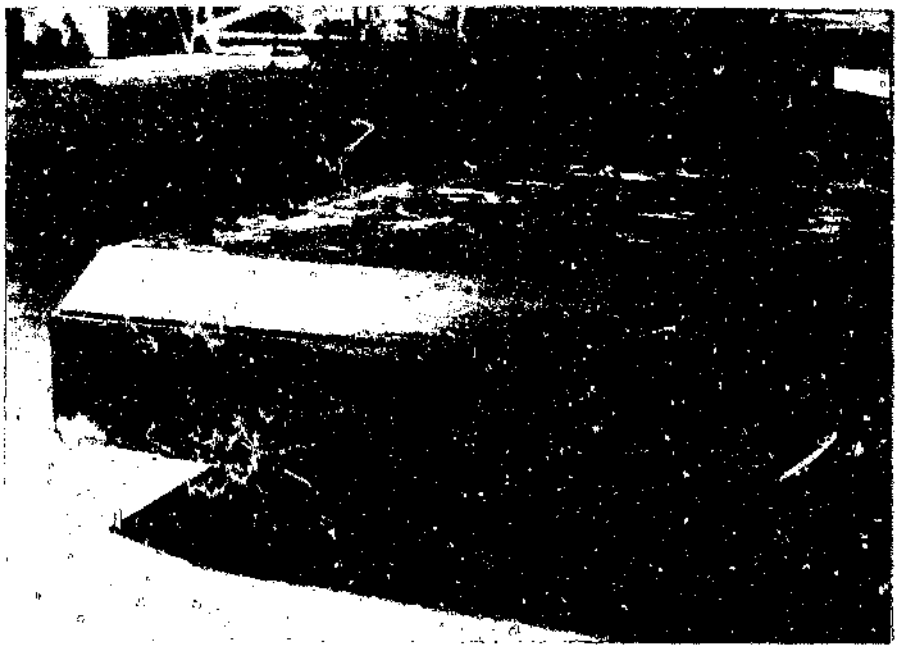
Photograph 5.19 Suspension air bag mounting outer bracket after cleaning and grinding of welds

The lower flanges of the upper coupler cross-members were now modified to step over the lower flange of the main I-beams (refer Drawing No. UC-09), and the cross-members slid into position from the front of the trailer and tacked. Thereafter, the front plate, front plate gussets and rubbing plate lead-in were assembled. These were then welded, along with the upper coupler cross-members, where possible from above (refer Photo. 5.20)



Photograph 5.20 Upper coupler cross-member welded to chassis I-beam

At this point the chassis was turned over in order to complete the welding on the underside of the suspension mounts, rear end rail and upper coupler region (ie. on the underside of the cross-members and the weld between the front plate and the rubbing plate lead-in) (refer Photo. 5.21 and Photo. 5.22).



Photograph 5.21 Chassis turned over to complete welding on underside of upper coupler assembly



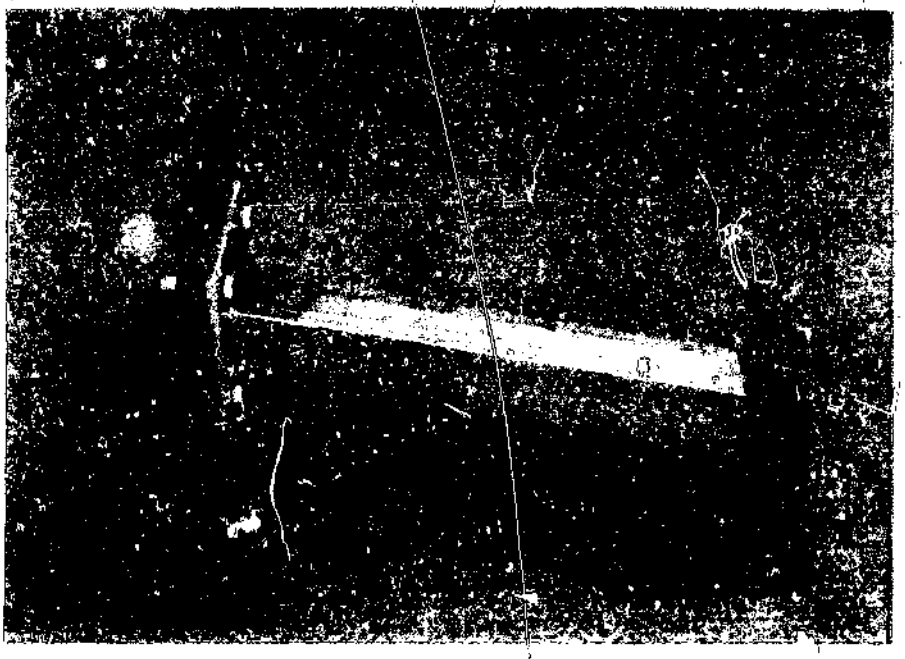
Photograph 5.22 Chassis turned over to complete welding on underside of suspension mounts, etc.

With the trailer chassis still inverted, the rubbing plate was assembled and fitted to the chassis. First of all, the rubbing plate cross braces and longitudinal braces were welded to the rubbing plate. Although care was taken to minimise distortion of the rubbing plate as a result of the welding of the longitudinal and cross-braces (ie. by pre-heating and clamping the rubbing plate flat) a certain amount of distortion did occur and the rubbing plate had to be pressed flat before being fitted. The mounting bolt holes were then drilled through the main I-beam flanges and the upper coupler cross-members. This was done by clamping the rubbing plate assembly in position and drilling through the previously drilled and countersunk holes in the rubbing plate. In this way exact location of the bolt holes was ensured. The chassis was then returned to the upright position.

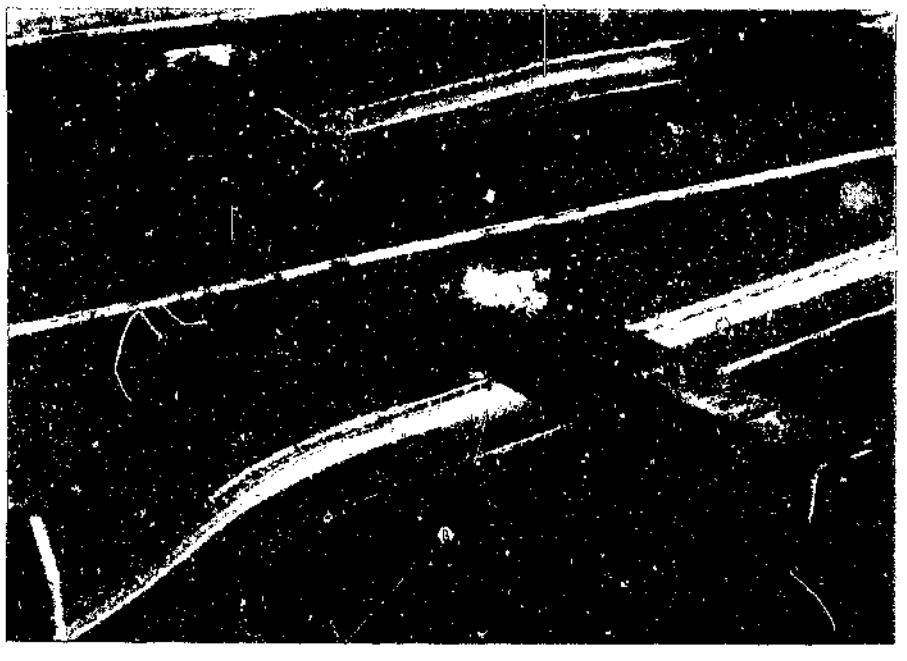
The outrigger flanges were now clamped into a jig (refer Photo. 5.23) and welded to the 100 mm square tube outriggers. Jig welding with pre-heating was employed to limit welding distortion since the angle between the tube and the flange was important to ensure the correct height location of the side rail relative to the main I-beams. The design of the jig was such that it accommodated both the deep section outriggers and the four degree tapered section outrigger. Each outrigger was then assembled onto the chassis (refer Photo. 5.24).

With the trailer chassis still inverted, the rubbing plate was assembled and fitted to the chassis. First of all, the rubbing plate cross braces and longitudinal braces were welded to the rubbing plate. Although care was taken to minimise distortion of the rubbing plate as a result of the welding of the longitudinal and cross-braces (ie. by pre-heating and clamping the rubbing plate flat) a certain amount of distortion did occur and the rubbing plate had to be pressed flat before being fitted. The mounting bolt holes were then drilled through the main I-beam flanges and the upper coupler cross-members. This was done by clamping the rubbing plate assembly in position and drilling through the previously drilled and countersunk holes in the rubbing plate. In this way exact location of the bolt holes was ensured. The chassis was then returned to the upright position.

The outrigger flanges were now clamped into a jig (refer Photo. 5.23) and welded to the 100 mm square tube outriggers. Jig welding with pre-heating was employed to limit welding distortion since the angle between the tube and the flange was important to ensure the correct height location of the side rail relative to the main I-beams. The design of the jig was such that it accommodated both the deep section outriggers and the four degree tapered section outrigger. Each outrigger was then assembled onto the chassis (refer Photo. 5.24).

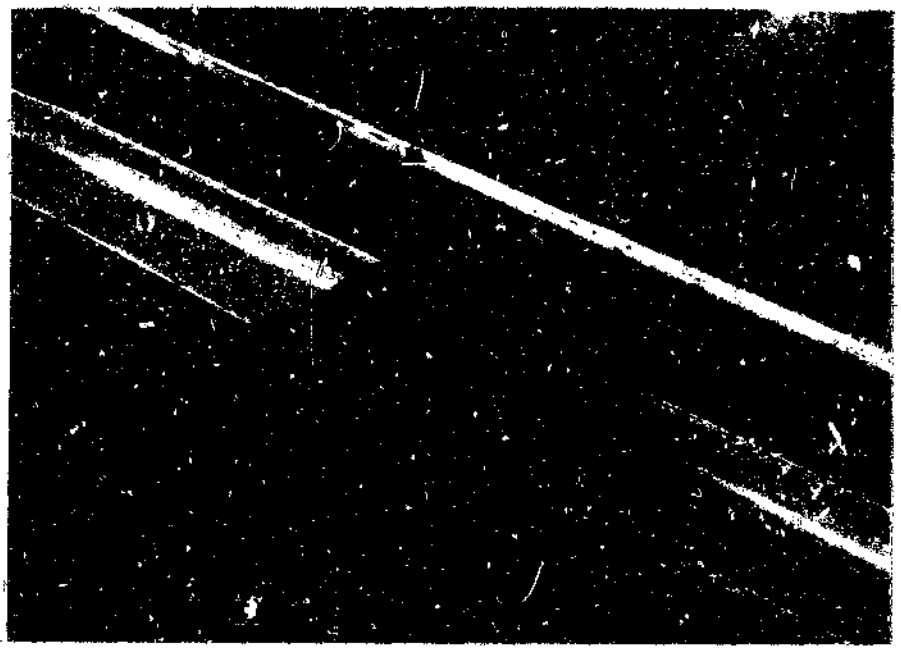


Photograph 5.23 Assembly and welding jig for outriggers

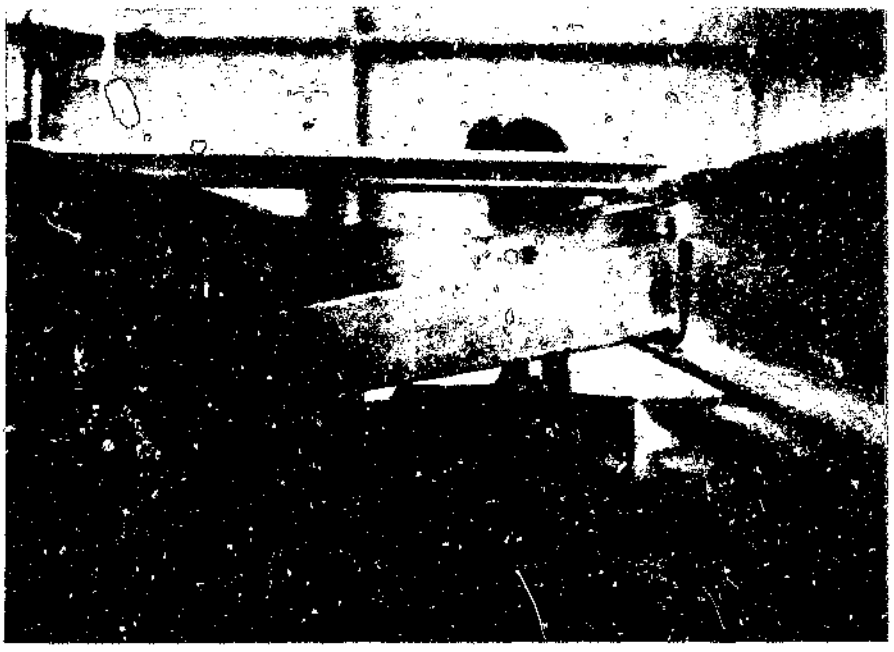


Photograph 5.24 Four degree tapered section outriggers assembled onto chassis I-beams

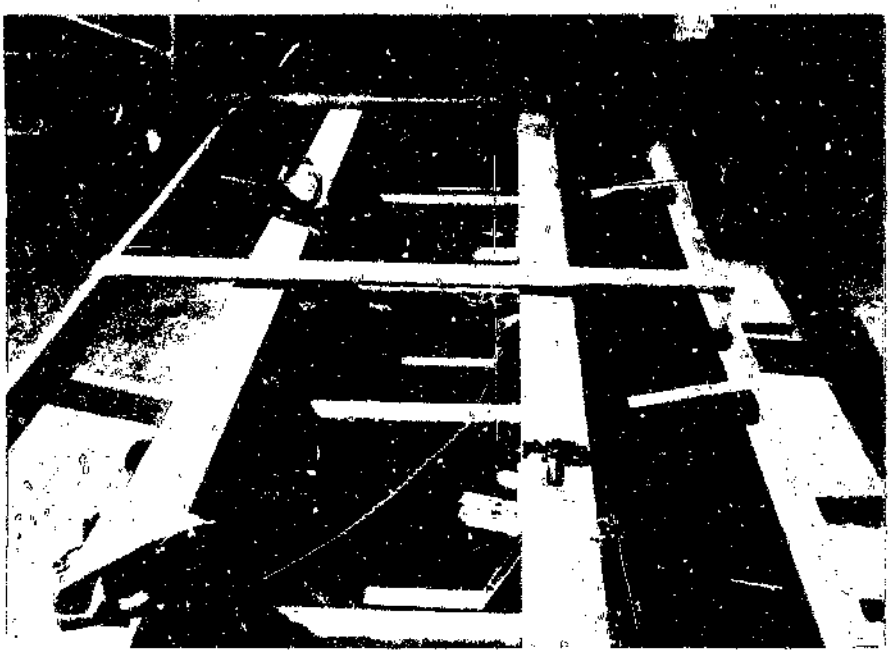
This completed, the outer portions of the front and r[illegible] rails and the upper coupler outriggers were tacked into position and the side rails tacked to the outriggers and end rails (refer Photo. 5.25 to 5.28).



Photograph 5.25 Upper coupler outrigger tacked to chassis I-beam



Photograph 5.26 Side rail being assembled onto outriggers



Photograph 5.27 Side rails positioned and tacked to outriggers



Photograph 5.28 Outer portions of rear end rails positioned and tacked to side rails

The side rail structure was then fully welded after ensuring that it was properly straight and level (refer Photo. 5.29 and 5.30).



Photograph 5.29 - A hydraulic jack used to assist with levelling of the side and end rail structure



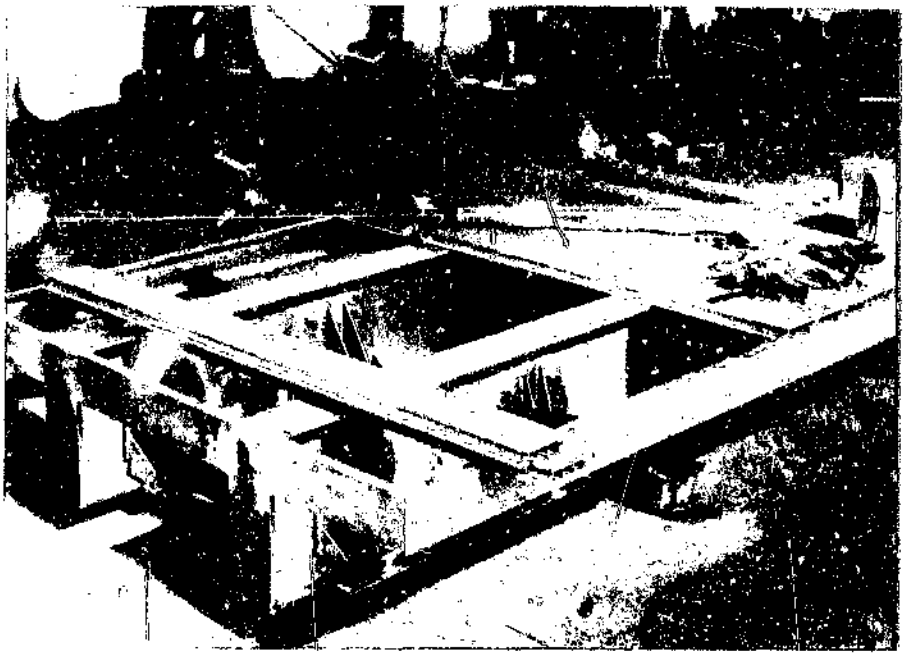
Photograph 5.30 Welding and grinding of side and end rail structure

The final stage in the construction of the semi-trailer chassis was the mounting of the ribbed plank deck. This was begun at the front of the chassis where the foremost deck plank (refer Drawing No. DE-03) was welded to the front rail and side rails. The first removable deck plank was then bolted in place immediately behind the foremost plank, and thereafter the remaining deck planks towards the rear of the trailer (refer Photo. 5.31 and 5.32). Each plank was firstly clamped to the top flanges of the main I-beams, using the deck clamp brackets (refer Drawing No. DE-11) whilst carefully ensuring that it was properly centred and square to the chassis. The bolt holes were then drilled and the plank bolted to the side rail (refer Photo. 5.33 to 5.35). The rearmost deck plank (Drawing No. DE-02) was cut to size only once all the other planks were fitted, and was welded to the side rails and rear rail. With all the deck planks mounted, the front and rear deck cover angles were

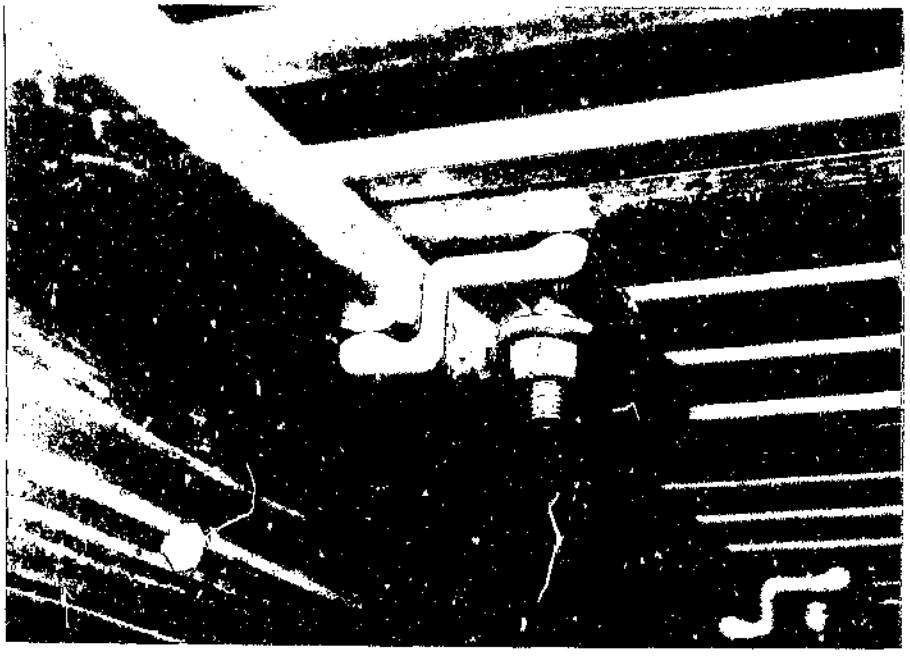
welded in place (refer Photo. 5.36). Finally, the holes for mounting the angle brackets for the wooden rubbing strake were drilled and countersunk, and the brackets mounted. The wooden rubbing strake was then fixed in position by drilling through the wood and the aluminium bracket and inserting self-tapping screws (refer Photo. 5.37).



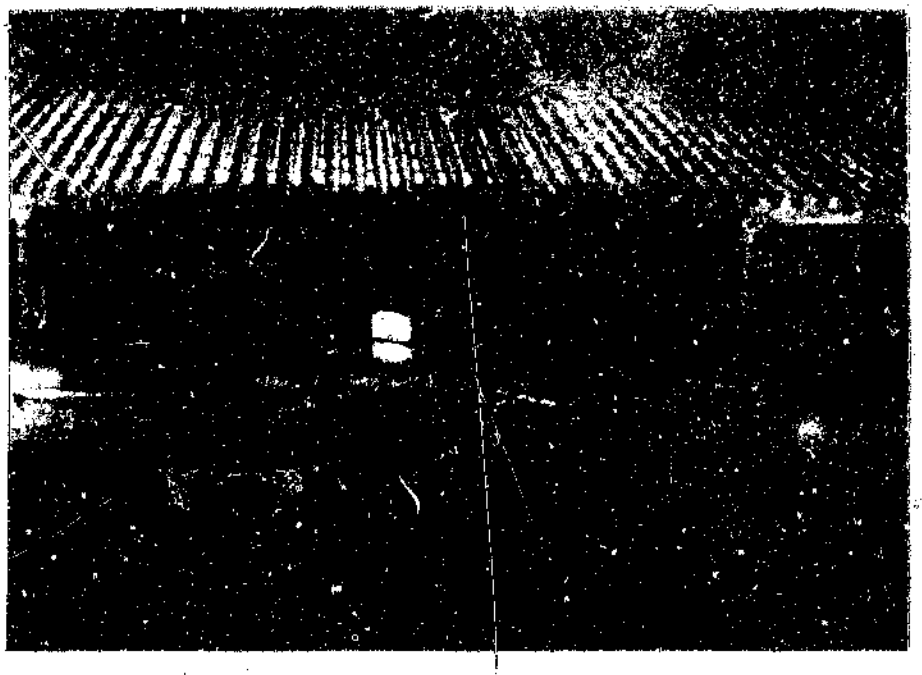
Photograph 5.31 Deck planks being mounted from the foremost deck plank rearward



Photograph 5.32 Deck planks being mounted towards the rear of the chassis



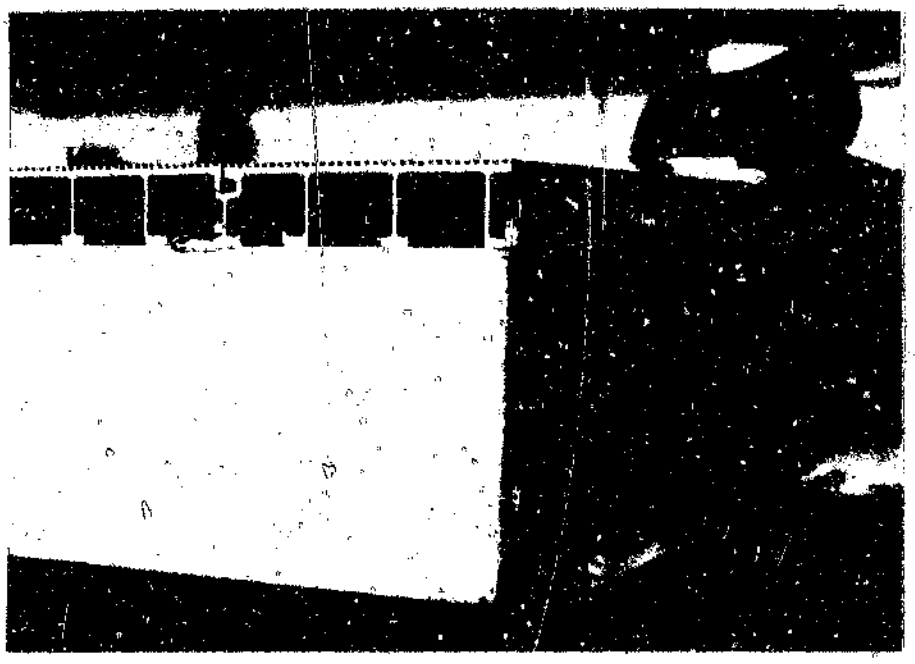
Photograph 5.33 Deck planks clamped to top flange of chassis I-beam by means of deck clamp brackets



Photograph 5.34 Deck planks bolted to side rail



Photograph 5.35 Completed deck mounting viewed from underneath



Photograph 5.36 Front deck cover angles being welded to foremost deck plank and front rail



Photograph 5.37 Mounting of wooden rubbing strake

The headboard and rear bumper were assembled and welded as detailed in Drawing Nos. HB-01 and RB-01 respectively, at times in between the various construction phases of the main chassis. Photograph 5.38 shows the rear under-ride bumper assembly almost completed, just before the outer upright web plates have been welded in place. In both cases the mounting bolt holes in the main chassis members were only drilled through on final assembly.



Photograph 5.38 Rear under-ride bumper

With the construction completed thus far the complete trailer chassis, without the headboard and bumper fitted, was loaded onto a semi-trailer and transported to the University of the Witwatersrand Technology Centre (UWtec) at Frankenwald (refer Photo. 5.39 and Photo. 5.40).



Photograph 5.39 Loading of the completed chassis onto a semi-trailer



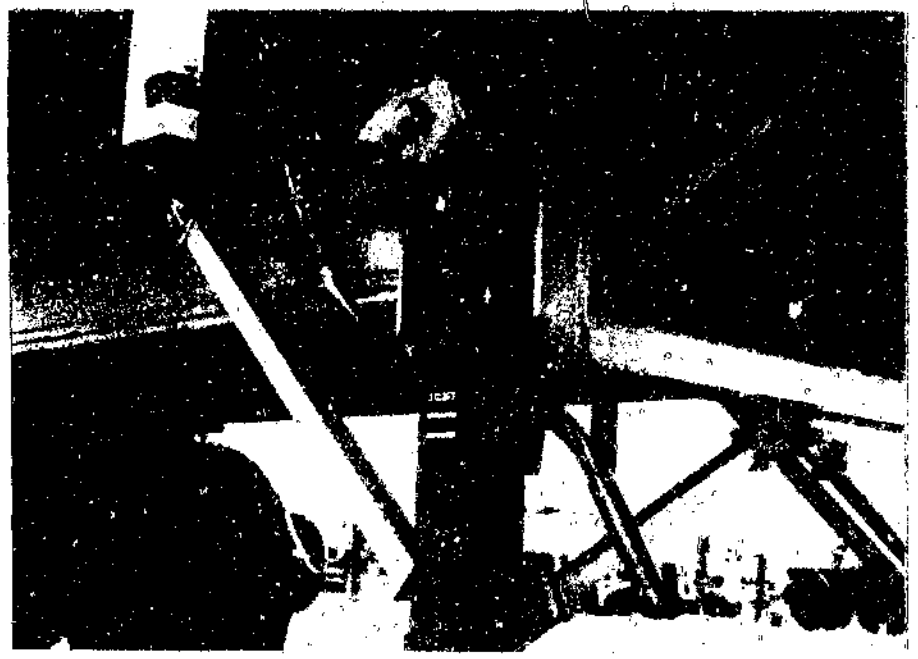
Photograph 5.40 Completed aluminium trailer chassis leaving I.R. & D. for Uwtec

5.4 Assembly of landing legs

The landing legs were mounted as shown in Photograph 5.41 below.

In order to ensure the accurate location of the bolt hole centres for the landing leg braces, the steel angle bracket at the lower end of the landing legs was tacked in position with the landing legs mounted to the chassis and with the rearward and cross-braces bolted to the angle bracket. All four braces were then removed and the bracket was fully welded.

Similarly, the bolt holes in the side rail for the landing leg crank brackets were drilled on assembly (refer Photo. 5.42).



Photograph 5.41 Landing legs mounted to chassis

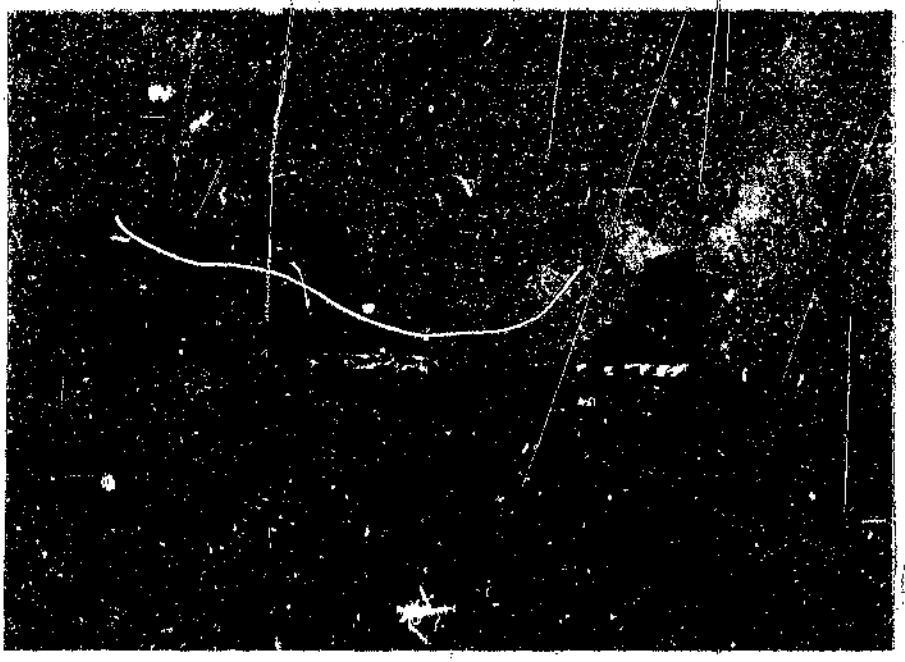


Photograph 5.42 Landing leg crank bracket

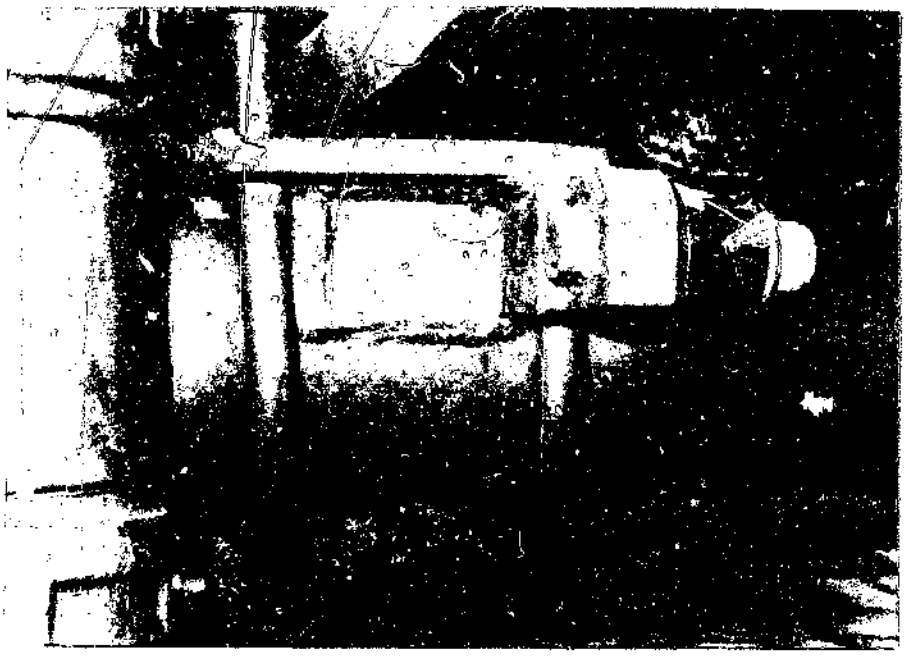
5.5 Assembly of axles and suspension

Both the steering axles and the centre fixed axle were supplied without clamp plates fitted and these, together with the lower shock absorber brackets, had to be mounted to the axles at the correct suspension trailing arm centres (ie. 950 mm). The clamp plate assemblies for the round section steering axle beam were assembled and fully welded as shown in Photograph 5.43 before being welded to the axles. Considerable care was taken to ensure that the plates were accurately positioned and square to the axles, and in the case of the steering axles, that the clamp plate surface was perpendicular to the

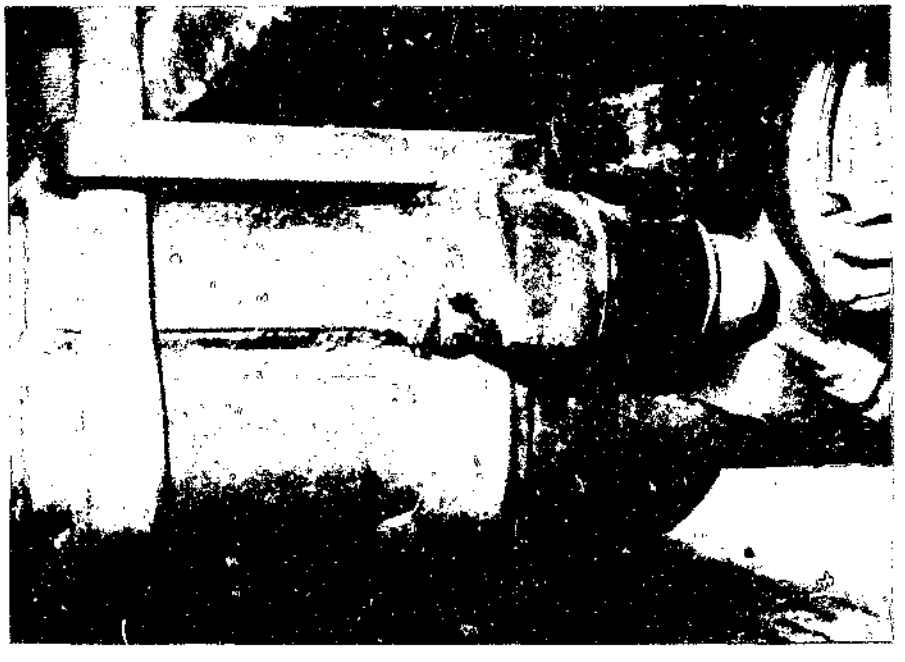
pivot axis of the steering arm pin. In both cases the clamp plate gussets were welded to the sides of the axle beams only, well away from the extreme fibres (refer Photo. 5.44 and Photo. 5.45).



Photograph 5.43 Clamp plate assembly for FIA steering axle



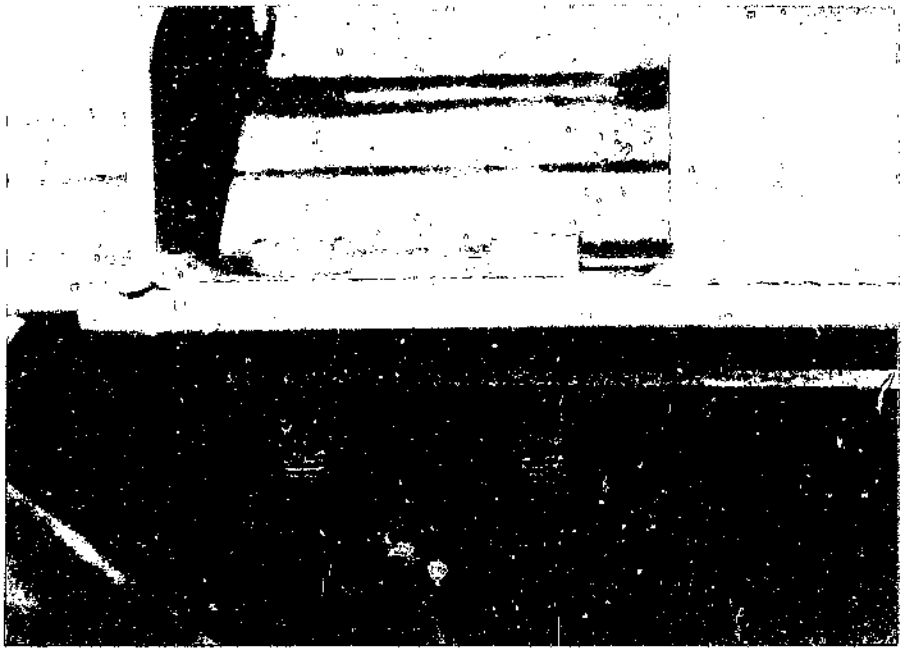
Photograph 5.44 Clamp plate assembly and shock absorber bracket welded to FIA steering axle



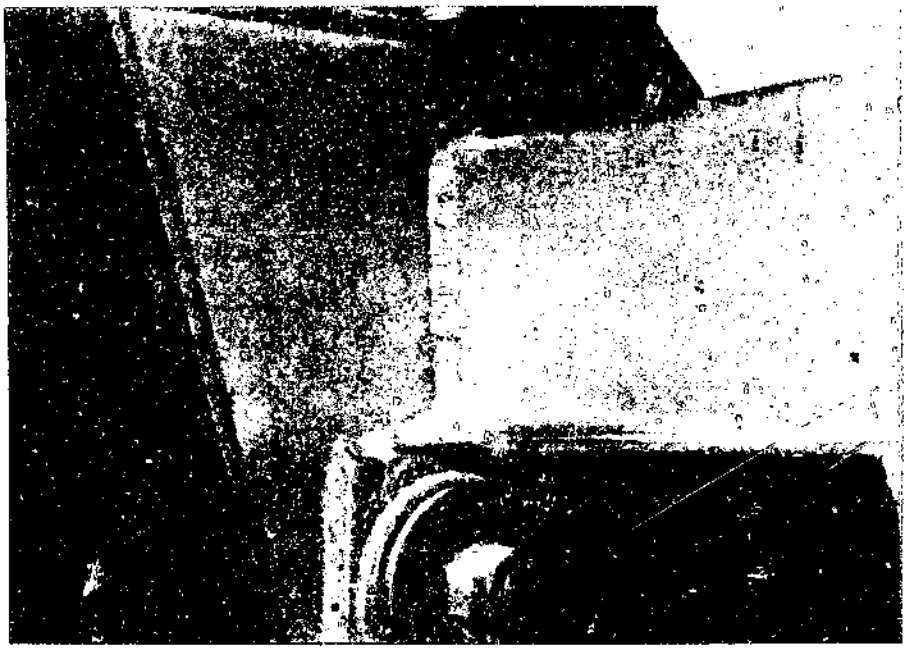
Photograph 5.45 Clamp plate assembly and shock absorber bracket welded to Propar fixed axle

Four M20 studs were welded into the four centre bolt holes on the 10 mm thick, mild steel suspension hanger mounting plates (refer Drawing No. SS-01). This was necessary since the positioning of the suspension hanger relative to its mounting plate prevented the use of bolts in these holes. The suspension hangers were then welded to their respective mounting plates. The upper shock absorber brackets were also welded to the rear of the hangers at this stage.

With the trailer supported on trestles in the upright position, the suspension hangers and the air-bag mounting plates were assembled onto the suspension mounts and the cadmium plated mounting bolts tightened to the required torque (refer Table E3 in Appendix E). A 10 mm thick rubber pad or gasket was inserted between the suspension mounts and the hanger and air-bag mounting plates to take up any out of flat on the suspension mountings (refer Photo. 5.46). The rubber gasket also serves to prevent galvanic corrosion between the aluminium chassis and the mild steel of the suspension hanger, and reduces the severity of shock loads transmitted through the suspension into the chassis. With the hangers firmly bolted in place, the Z-pressing cross-braces were welded between each pair of suspension hangers (refer Photo. 5.47).



Photograph 5.46 Rubber gasket inserted between suspension mount and hanger assembly

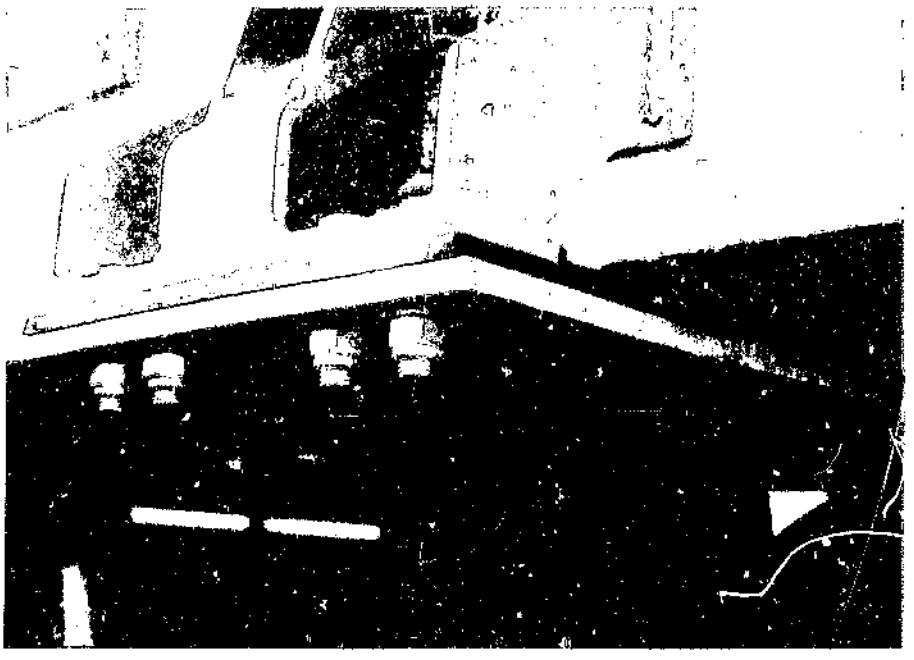


Photograph 5.47 Z-pressing cross brace welded to inner face of suspension hanger

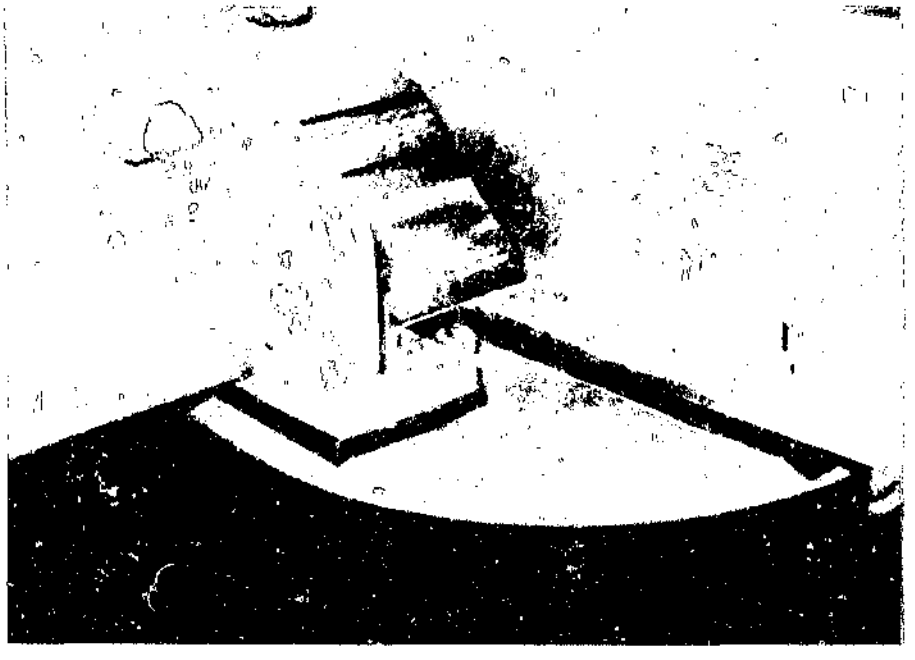
The suspension trailing arms were then assembled onto the hangers (Photo. 5.48). The rubber cone trailing arm bushings were firstly dipped in a solution of fifty percent water and fifty percent liquid soap before being assembled, to help ensure that they seated properly. The trailing arm pivot bolt was pushed through from the outside so that the nut was towards the centre of the trailer and was tightened to hold the trailing arm firmly in position. Final tightening to the correct torque was done later with the semi-trailer standing on its tyres. Whilst supporting the trailing arms in an approximately level position, the air-bag assemblies were bolted to their respective mounting plates (refer Photo. 5.49 and Photo. 5.50) and the air-bag trumpets to the trailing arms.



Photograph 5.48 View of suspension hanger showing trailing arm and pivot pin assembly



Photograph 5.49 Suspension air bag assembled onto air bag mounting plate

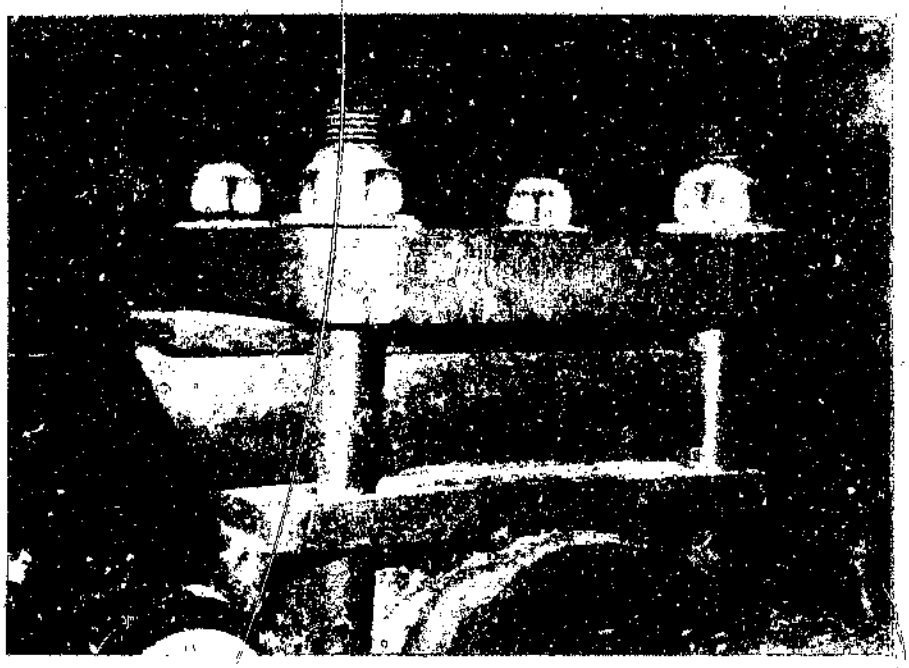


Photograph 5.50 Air bag and mounting plate bolted to suspension air bag mounting cross-member

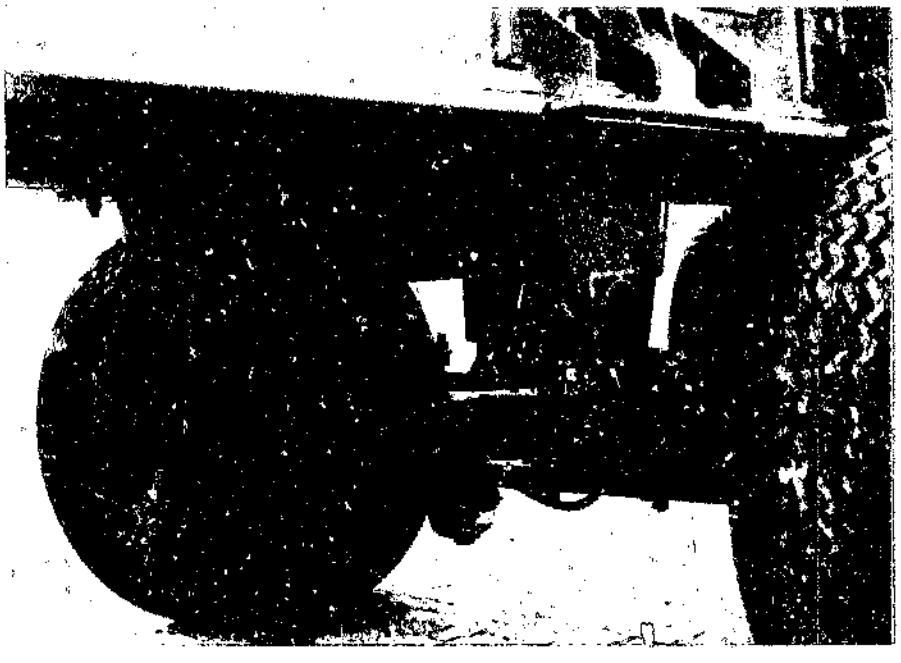
The wheels and tyres were now fitted to the axles (wheel studs tightened to a torque of 530 Nm) and the axles rolled under the chassis to their respective positions. The axle clamp plates, top clamp plates, and U-bolts were assembled into position about the axle locator plate on the trailing arm, and the U-bolts tightened until they held the axles firmly in place (refer Photo. 5.51 to Photo. 5.54). As with the trailing arm pivot bolt, final tightening to the required torque was only done with the trailer standing on its tyres and after axle alignment.



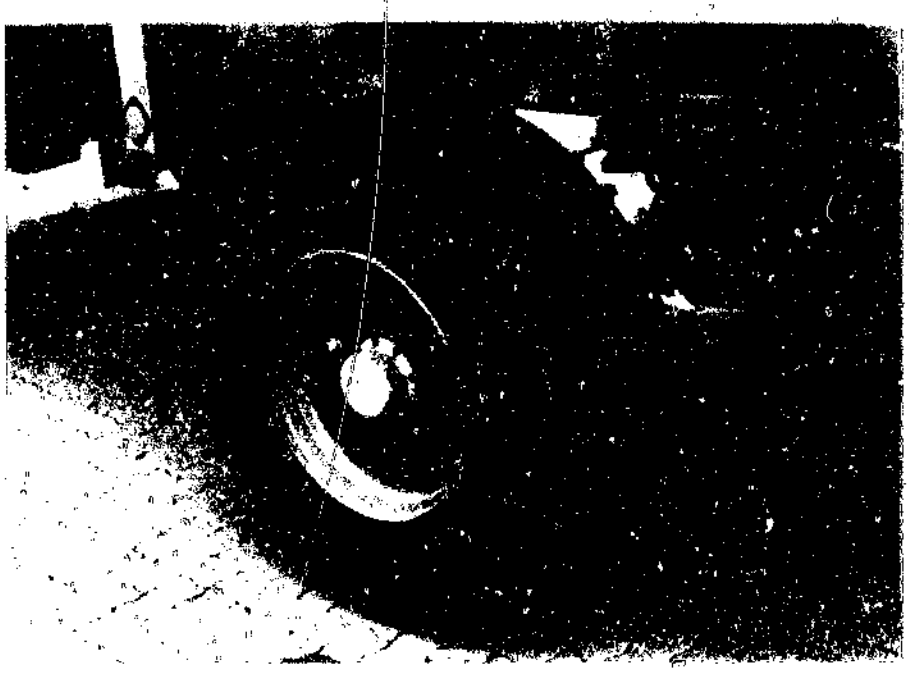
Photograph 5.51 Propar axle mounted onto suspension trailing arm



Photograph 5.52 FIA steering axle mounted onto suspension trailing arm

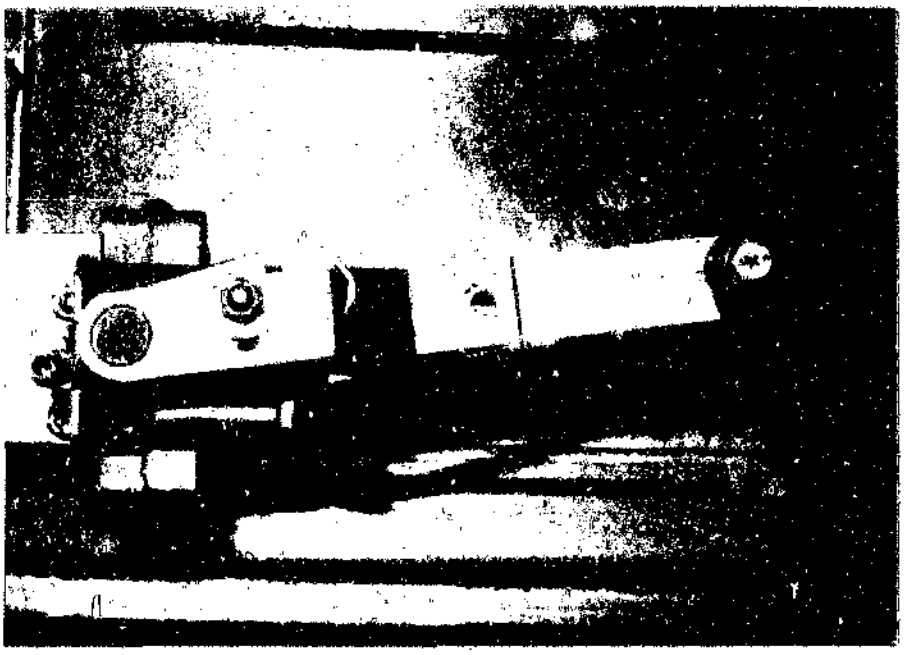


Photograph 5.53 FIA steering axle and suspension assembly



Photograph 5.54 Michelin 16.5 R 22.5 super single tyres on steel single piece rims

The supports under the chassis were then removed and the trailer lowered until the chassis was at the correct ride height relative to the centre line of the centre axle. Two correctly sized wooden chocks were inserted between the trailing arms of the centre axle and the chassis, immediately in front of the air-bags to maintain this height, and the landing legs adjusted to level the trailer. The bracket on the chassis for the suspension levelling valve (refer Photo. 5.55) and the adjustable bracket on the centre axle for the levelling valve control rod, were then fitted. The levelling valve was then provisionally set for the correct ride height, after which the wooden chocks were removed and the suspension allowed to settle onto the rubber buffers inside the air-bags.



Photograph 5.55 Suspension levelling valve mounted onto chassis

Once the piping of all the pneumatic circuits on the semi-trailer was completed (ie. brakes, suspension, etc. - refer Section 5.7), the correct ride height of the suspension was finally adjusted with the suspension circuit charged to 6 bar pressure. The trailing arm pivot bolts were then tightened to the required torque with the trailing arms in this neutral position.

With the axle locking pins engaged, the steering axles were centralised and set at a toe-in of 6 mm at maximum tyre radius (as required by the axle manufacturer FIA). All three axles were then aligned perpendicular to the longitudinal axis of the trailer. This was accomplished by loosening the axle U-bolts slightly and aligning the front axle by equalizing king-pin to axle steering pivot distance between the road and pavement side of the semi-trailer (ie. dimensions A and B in Figure 5.1 below). The second and third axles were aligned parallel to the first axle (ie. dimension C). In each case the relevant dimensions were required to correspond to within 2 mm of each

other. The U-bolts on all three axles were then tightened to the specified torque, to clamp the axles firmly in place. The top clamp plates were welded to their respective axle locator plates on each trailing arm to further ensure that the axles remained correctly positioned. While the clamp plates were being welded care was taken to protect the trailing arms and the air-bags from weld splatter.

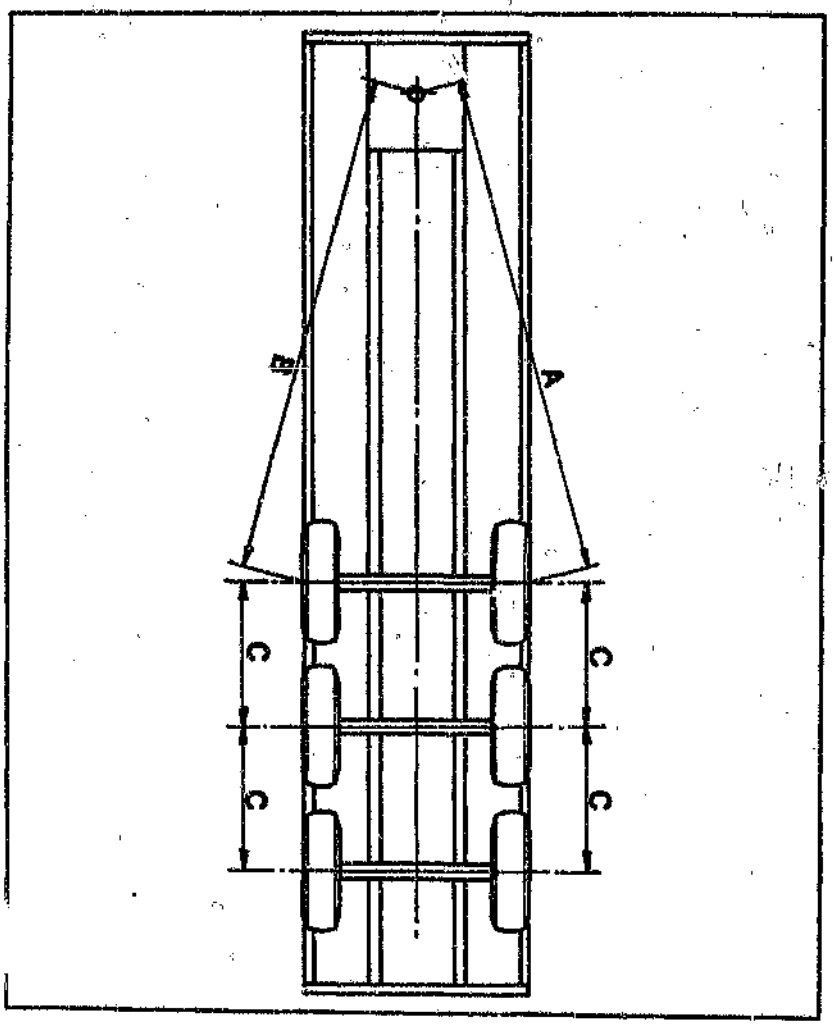


Figure 5.1 Relevant dimensions for the alignment of the semi-trailer axles

Finally, the shock absorbers were fitted (Photo. 5.56) and tightened the torque specified on Drawing No. SS-01.



Photograph 5.56 Shock absorber fitted between brackets on axle clamp plate and suspension hanger

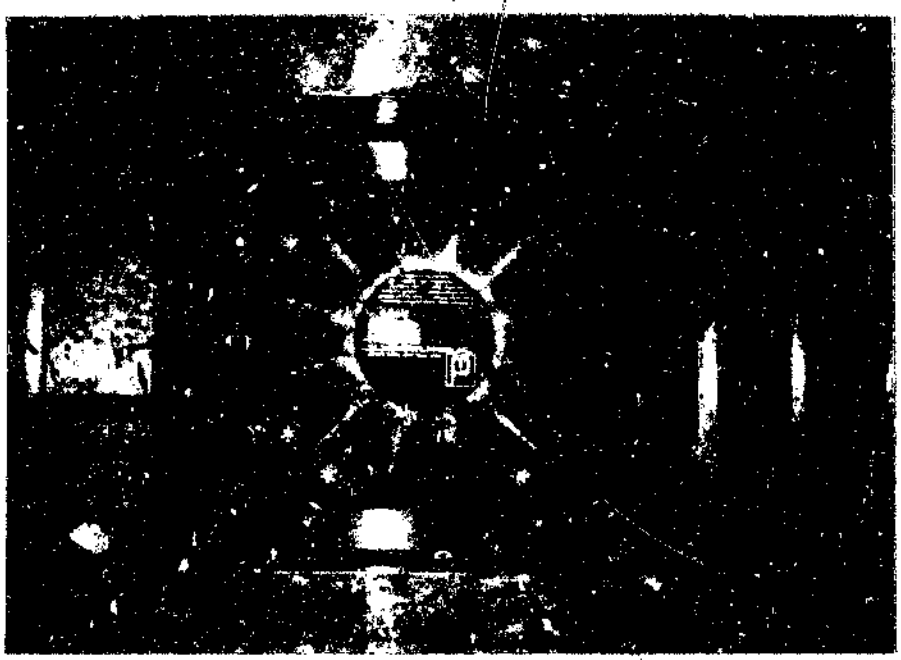
5.6 Mounting of Hope anti-jack-knife king-pin

After completing the chassis and suspension assembly, the first eight deck planks over the rubbing plate were removed (ie. from the first removable deck plank rearward) to facilitate the fitment of the Hope anti-jack-knife device (Photo. 5.57).



Photograph 5.57 First eight deck planks removed to reveal upper coupler assembly

The foundation plate was bolted in place between the two longitudinal king-pin braces (refer Photo. 5.58) and the eighteen M16 bolts tightened to the specified torque. The Hope device was then lowered into place and secured using the eight half-inch UNF mounting bolts supplied. Before these eight bolts were tightened however, the two 9,5 mm diameter dowel pins were driven home until flush with the top of the device cover. The dowels ensure that the body and cover of the device are properly located relative to the foundation plate. The eight device mounting bolts were then tightened to the required torque, and the two transit screws in the cover removed.



Photograph 5.58 Hope anti-jack-knife device bolted to rubbing plate

With the device thus installed, the following checks as required by the manufacturer[59] were undertaken:

- The king-pin arm was rotated through 180 degrees in each direction to ensure that the movement was free and smooth. A certain residual restriction from the internal components is, however, normal.
- With the aid of feeler gauges, the minimum clearance between the arm and the rubbing plate was checked. This clearance should be between 0,2 mm and 0,9 mm (refer Figure 5.2).
- Using a suitable straight edge to span the rubbing plate aperture, the minimum clearance all round between the king-pin flange and the rubbing plate surface was checked (refer Figure 5.2).

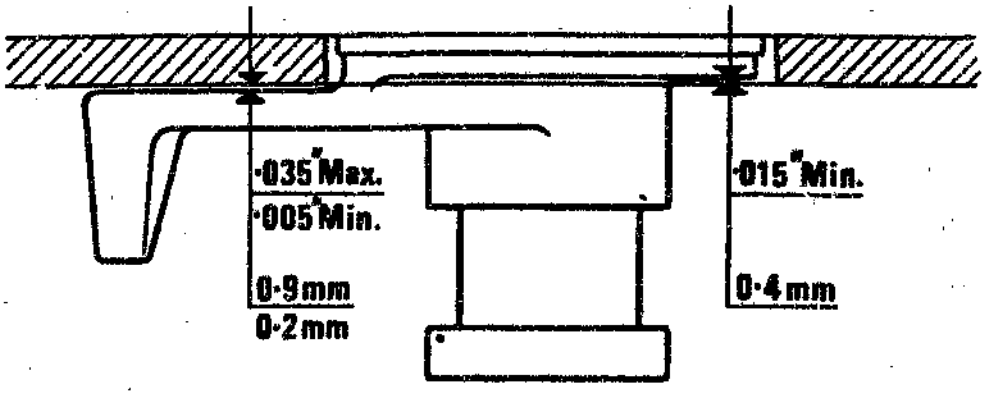
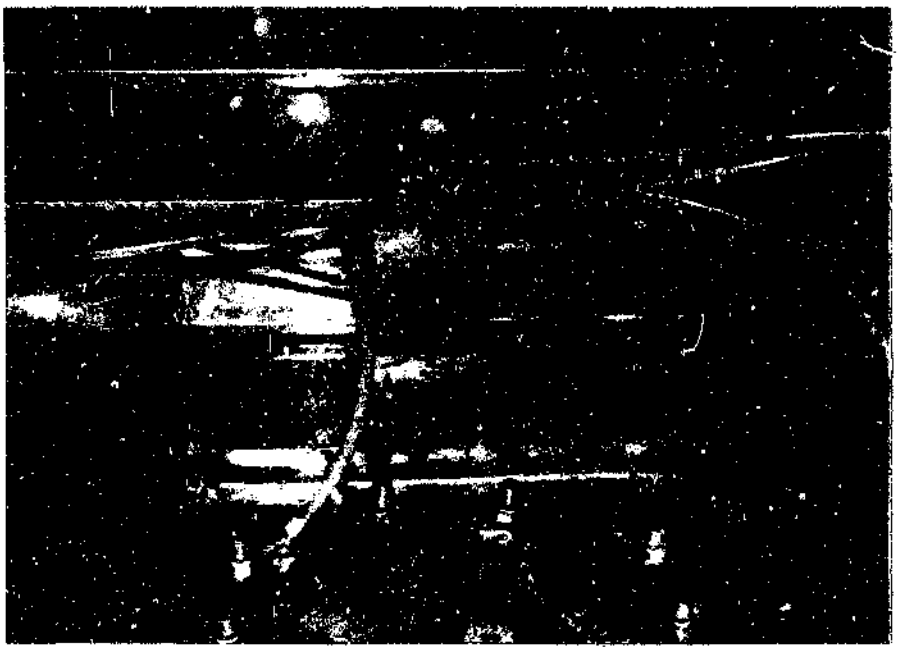


Figure 5.2 Minimum clearances for Hope anti-jack-knife installation

Finally, the device control valve was mounted, as shown in Photograph 5.59 below, and connected to the pneumatic circuitry (refer also Section 5.7).



Photograph 5.59 Hope anti-jack-knife control valve mounted in close proximity to Hope device

5.7 Assembly of brake system and pneumatic circuitry

Once the Hope anti-jack-knife device and the complete suspension were fully assembled onto the chassis, the trailer brake components and all the pneumatic circuitry (ie. [illegible]stem, Hope King-pin, suspension and auxiliary circuit for steering axle control) were fitted to the trailer.

Photographs 5.60 and 5.61 show the type 24/30 spring brake chambers used on both the fixed and steering type axles.



Photograph 5.60 Type 24/30 spring brake chamber fitted to Propar fixed axle



Photograph 5.61 Type 24/30 spring brake chamber fitted to FIA steering axle

The procedure adopted in mounting these chambers was firstly to assemble the chamber onto its respective mounting bracket with the spring brake fully caged by means of the caging bolt, and with the uncut push-rod extending past the slack adjuster arm. The loose push-rod clevis was fitted to the slack adjuster at the correct lever length (ie. 152 mm on the centre axle and 145 mm on the self-steering axles) and the slack adjuster adjusted to obtain a 90 degree angle between the push-rod and the slack adjuster arm, with the push-rod held at the same level and in line with the clevis pin. The slack adjuster was then adjusted to move the clevis approximately 28 mm back

towards the brake chamber, and the push-rod cut to suit the clevis threads in this position (refer Figure 5.3). The resultant angle between the push-rod and the slack adjuster arm for the brakes fully released, is of the order of 100 degrees. Finally, the caging bolt was removed, allowing the spring brakes to apply the brakes.

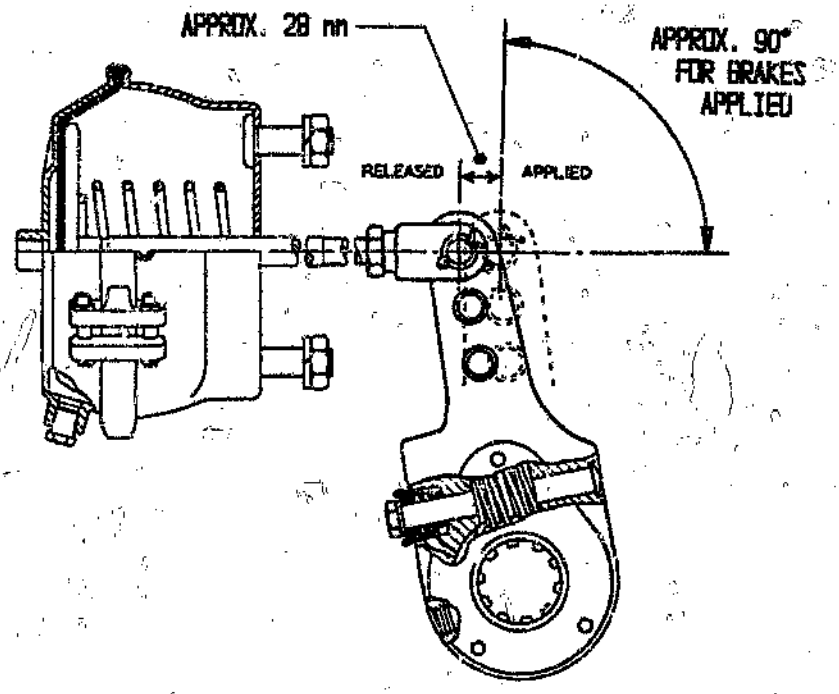
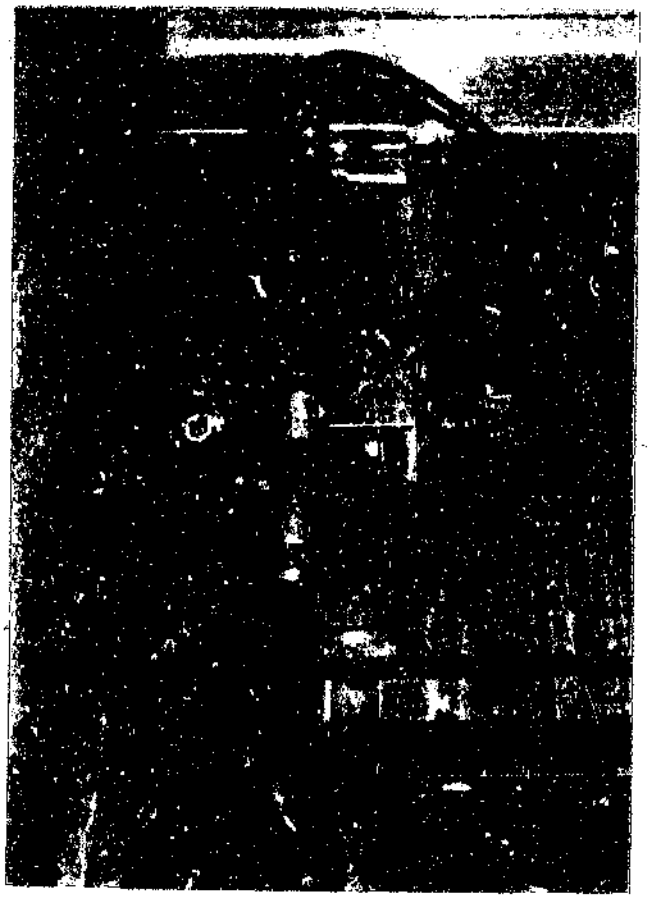


Figure 5.3 The correct brake chamber push-rod length and slack adjuster position for the brakes fully released

The various pneumatic circuits were then assembled as detailed in Drawing Nos. PM-01 to PM-03. Some of the various methods employed to mount the pneumatic valves and reservoirs are shown in Photographs 5.62 to 5.65.

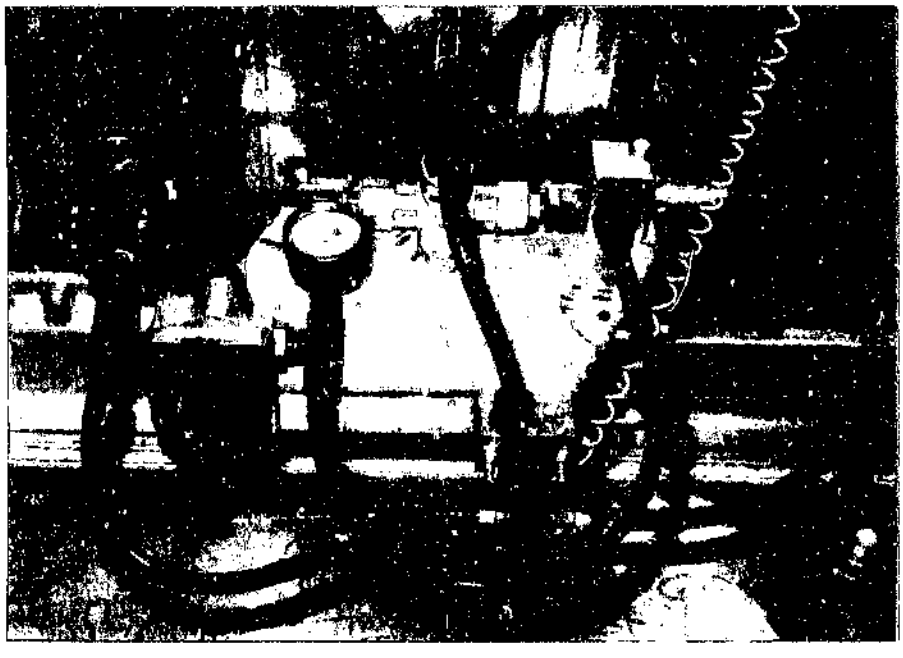
Wherever possible these have been mounted in accessible positions to the underside of the extruded plank deck, using T-bolts. This was done to allow for easy removal for maintenance and to alleviate the need to drill holes for mounting bolts in load bearing chassis members. Furthermore, with the semi-trailer being a prototype vehicle, modifications and improvements to the vaious pneumatic systems may be made at a later stage, which will require the positions of valves to be altered, or valves, etc, to be added to or removed from the system.



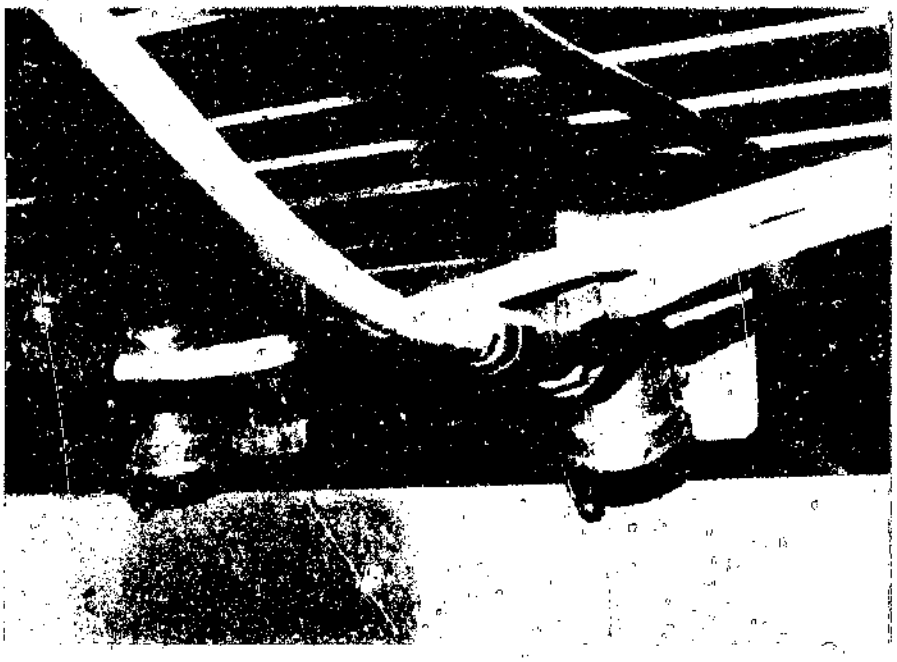
Photographs 5.62 Wabco automatic load sensing valve mounted to underside of deck



Photograph 5.63 Relay valve and brake system reservoir mounted to underside of deck



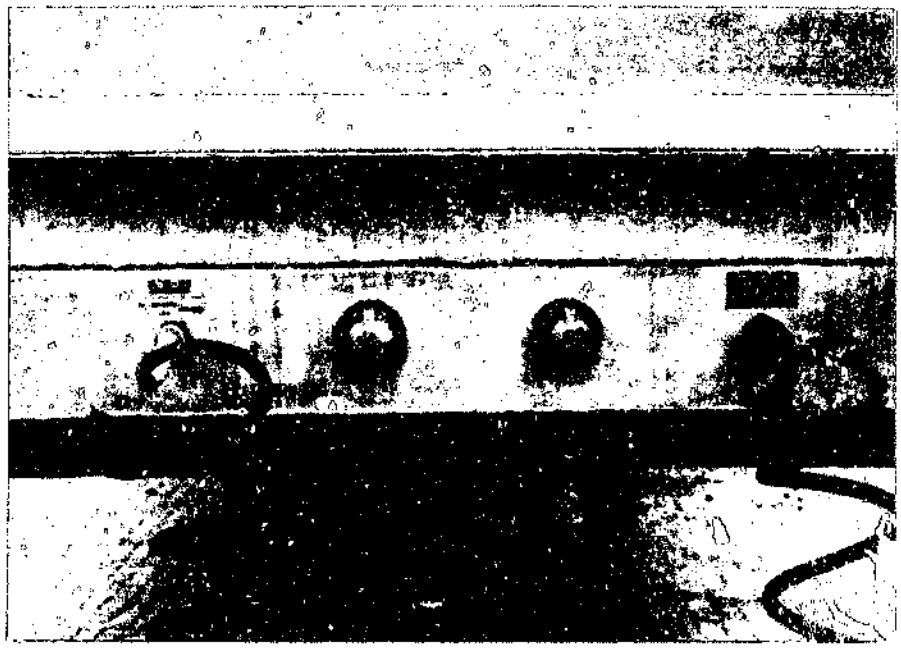
Photograph 5.64 Auxiliary pneumatic circuit pressure control valves mounted to underside of deck



Photograph 5.65 Emergency and service line filters mounted to underside of deck above rear of rubbing plate

The Hope anti-jack-knife control valve (refer Photo. 5.59) was mounted above the rubbing plate in close proximity to the device, in order to minimise the time delay between the application of the brake pedal in the truck-tractor, and the operation of the device. This is particularly important in that the device is designed to prevent the onset of jack-knifing, and thus is most effective if activated momentarily before the trailer brakes.

The emergency and service suzies were mounted through the front plate as shown in Photograph 5.66. Dummy fittings were provided on the lowest headboard cross-member (refer Photo. 5.67) to allow the suzies to be hooked up out of the way during trailer coupling and uncoupling operations.

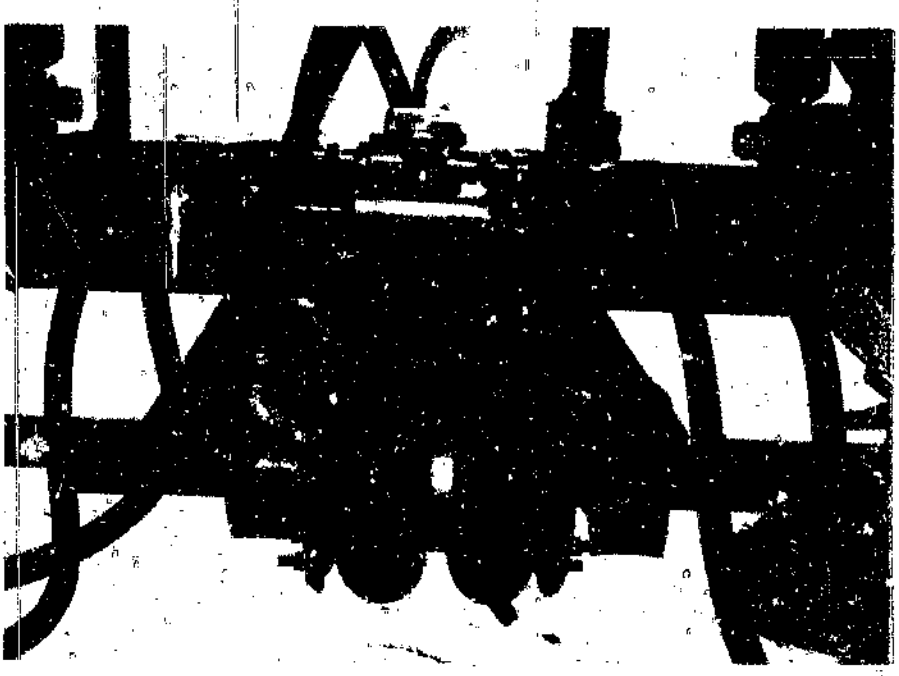


Photograph 5.66 Emergency and service line suzies mounted through front plate



Photograph 5.67 Dummy fittings on headboard for stowage of brake suzies

As already mentioned in Section 4.7.1, colour coded nylon tubing was used throughout on all of the pneumatic lines, except between the chassis and the axles and on the axles themselves where rubber hose was used because of the need for greater flexibility (refer Photo. 5.68). The nylon brake lines were, for the most part, routed along the underside of the deck planks and pop rivetted using the appropriate clips to the deck planks, as shown in Photograph 5.63. Wherever possible, Schäfer plug type fittings were used to connect all the 12 mm diameter polyamide tubing to the valves, etc. Using this system the vast majority of the brake lines could be made up on the work bench and then merely clipped into place on the trailer as the various pneumatic circuits were assembled. Other advantages of the Schäfer system over conventional type fittings, are the reliable air seal provided by the O-ring and the fact that each fitting is easily removed and reconnected when a valve has to be dismounted for servicing.



Photograph 5.68 Rubber pneumatic hoses used on axles

Once all of the pneumatic circuits were fully assembled, the full system was charged to 600 kPa pressure and checked for leaks. The pressure regulating

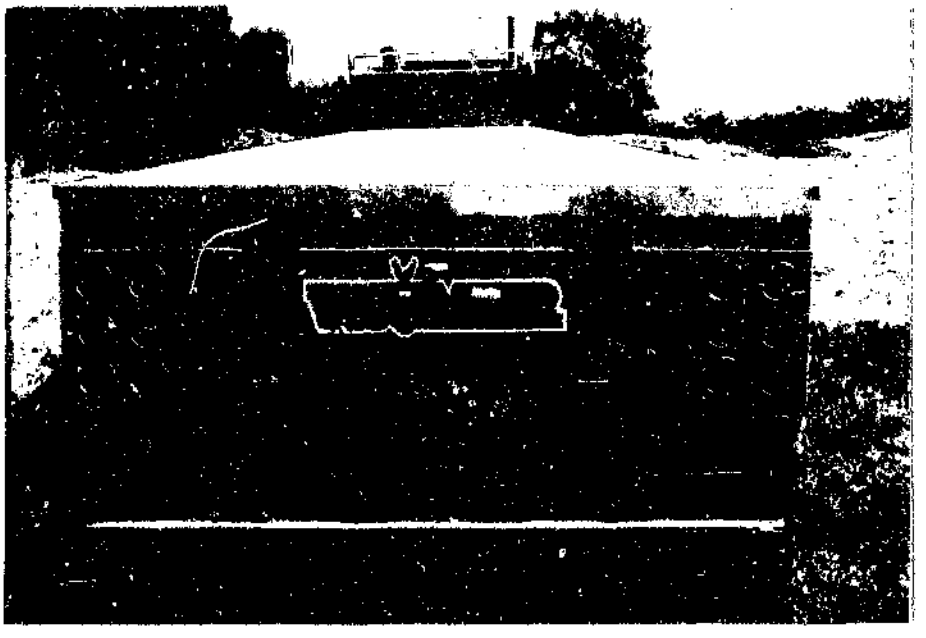
valves for the auxiliary steering axle circuit were also set to the correct upper and lower pressure settings of 345 kPa and 172 kPa, respectively, at this stage.

The 'S'-type cam brakes were then adjusted. With the brake system charged to fully release the spring brakes, and with the parking and service brake controls released, each slack adjuster was adjusted until the shoes made contact with the drum. The slack adjusters were then backed off slightly to obtain a small free-running clearance.

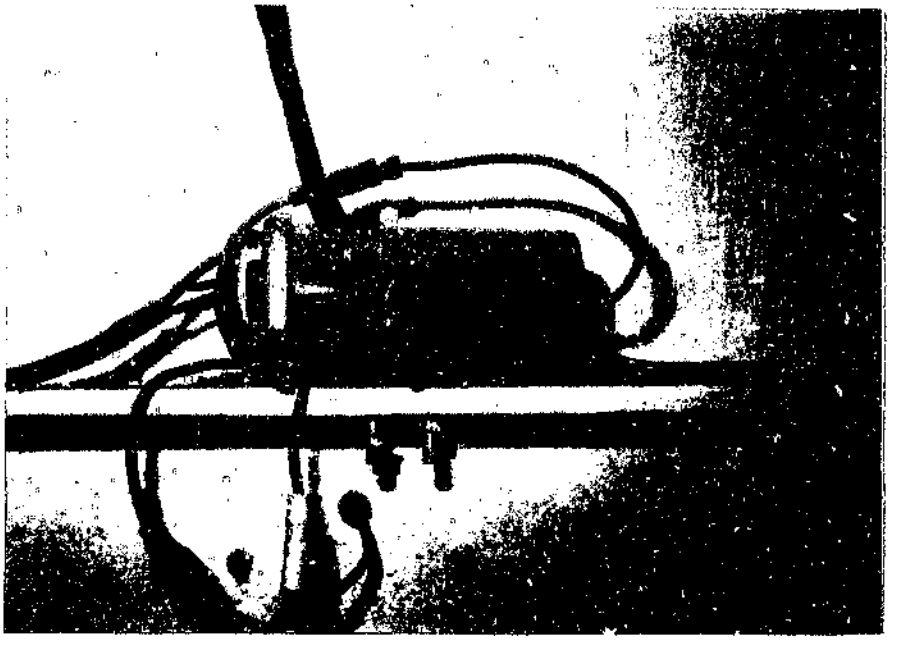
Finally, the correct adjusting screws and springs for the Wabco automatic load sensing valve were determined by the procedures set out in Section F.4 in Appendix F, and the load sensing valve adjusted accordingly.

5.8 Assembly of lights, retro-reflectors, and electrical system

The final stage in the construction of this aluminium semi-trailer was the mounting of lights and retro-reflectors and the wiring of the electrical system. Photograph 5.69 shows the direction indicator, stop and rear position lights, as well as the red retro-reflectors, mounted in their respective positions in the rear light boards at the rear of the trailer. The two reversing lights were not fitted at the time that this photograph was taken, due to certain supply problems, and their respective mounting holes are obscured by the 'WUMHR' sign. The two red retro-reflectors, as discussed in Section 4.8, which were mounted vertically at either end of the chevron board were also not fitted at the time that the photograph was taken. The reversing buzzer was mounted on the inside of the rear end rail, as shown in Photograph 5.70.

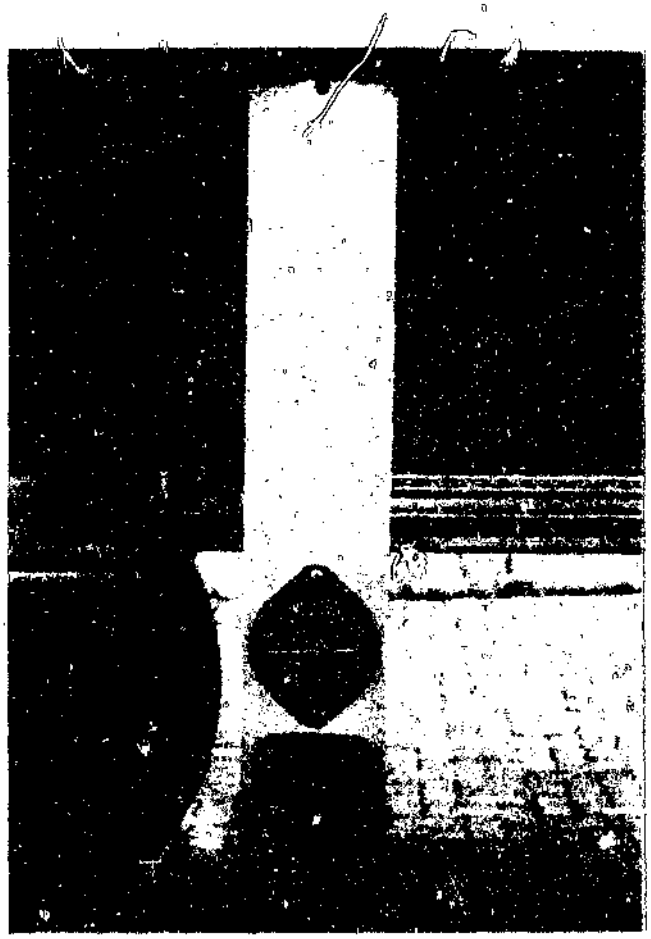


Photograph 5.69 **View of rear of semi-trailer showing lights and retro-reflectors**

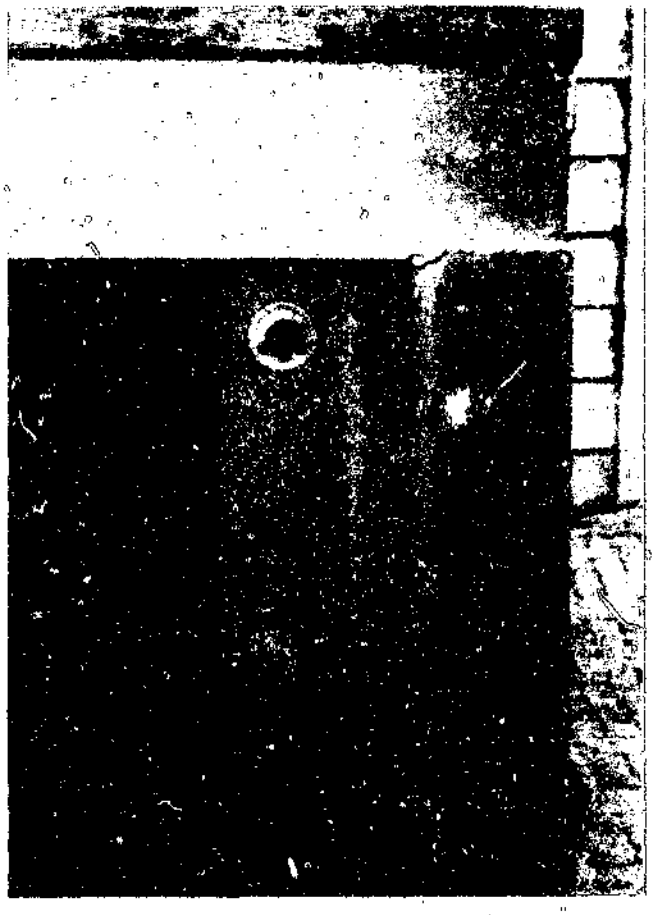


Photograph 5.70 **Reversing buzzer mounted on inside of rear end rail**

The amber retro-reflectors, side marker lights and direction indicator lights, as fitted along each side of the trailer, are shown in Photographs 5.71 and 5.72.



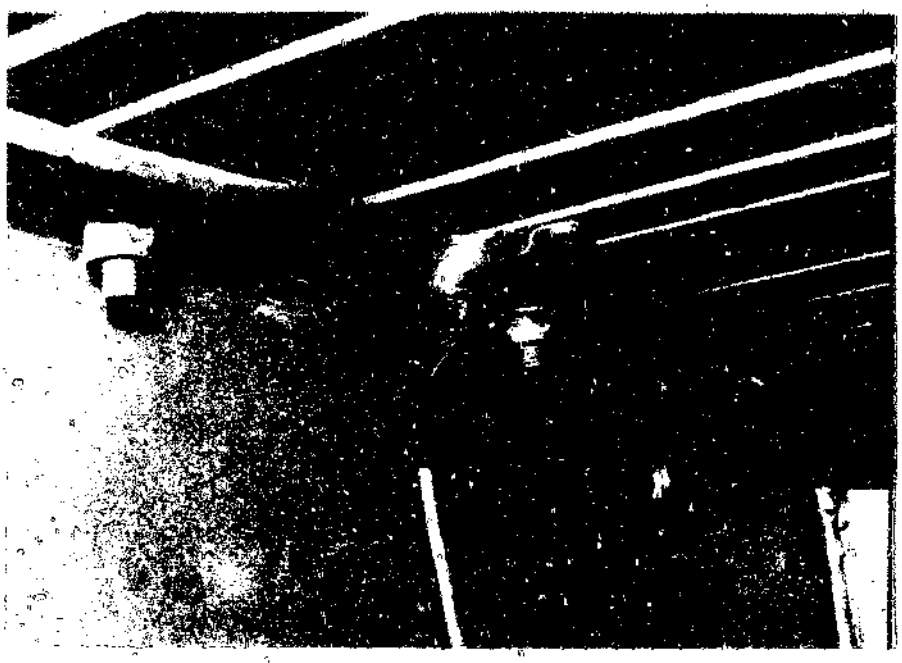
Photograph 5.71 Retro-reflector and side marker and direction indicator light mounted below side rail



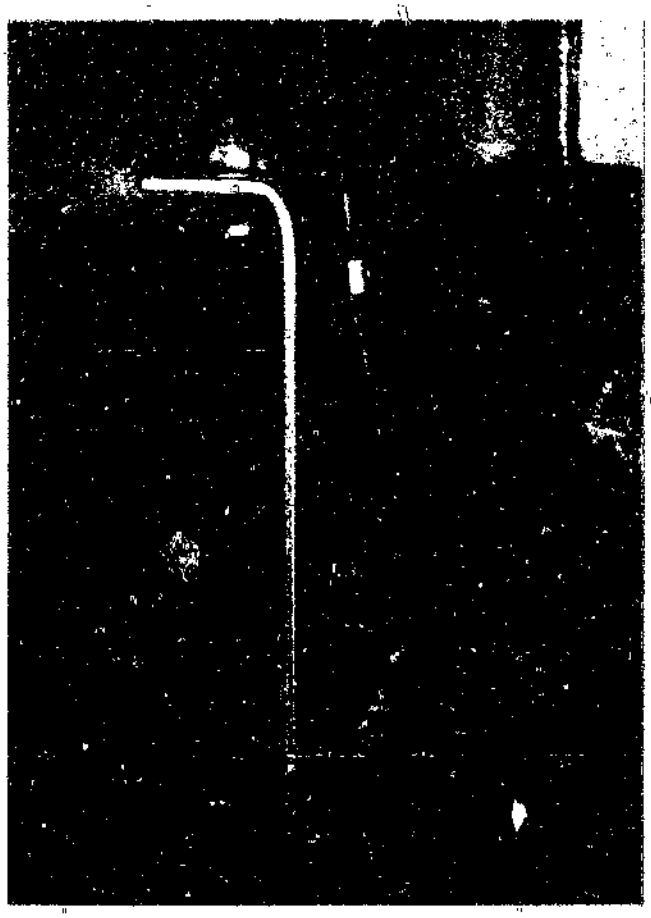
Photograph 5.72 Retro-reflector and side marker and direction indicator light mounted at rear of trailer

As indicated in the electric wiring diagram (Drawing No. EL-01 in Appendix H), all of the lights at the rear of the vehicle, including the rearmost set of side marker and direction indicator lights, as well as the two solenoid valves of the auxiliary steering axle pneumatic control circuit, are powered via a seven core cable running down the full length of the vehicle, between the two main chassis beams. This cable was clipped to the underside of the deck planks in a similar manner to the nylon air lines (refer Photo. 5.63). The remaining side marker and direction indicator lights are powered by separate

two core cables, one running down either side of the trailer on the inside of the side rail (refer Photos 5.73 and 5.74).



Photograph 5.73 Two core electrical supply cable clipped to underside of deck next to side rail



Photograph 5.74 Electrical supply cable clipped to rear of side marker light bracket

The three electrical supply cables are connected to the two electrical suzies via a junction box mounted immediately behind the front end rail above the rubbing plate. All of the lights, etc., are connected to the electrical system by means of separable connectors, to facilitate easy removal for servicing or replacement.

CHAPTER 6

CONCLUSION

6.1 Lightweight aluminium chassis

The completion of this aluminium semi-trailer project has demonstrated the practicality and suitability of aluminium, or more specifically aluminium alloys, for lightweight semi-trailer design within the context of the relevant South African road loading regulations. Despite the fact that a number of design decisions were severely limited by the availability of certain materials and of funds and production facilities, a substantial saving in tare mass has been achieved. This is illustrated by comparison to Henred Fruehauf Trailer's PET prototype (also refer Section 3.2), a steel chassied wide spaced tridem axle semi-trailer of similar overall dimensions and built around the same time as this aluminium trailer, viz.

Henred Fruehauf PET semi-trailer[1]	7 800 kg
Lightweight aluminium semi-trailer	6 680 kg
Tare mass saving	1 120 kg

Since the legal gross vehicle mass is the same in each case, this difference in tare mass can be used as additional revenue earning payload. The higher basic material cost of the aluminium chassis will result in a higher purchase price in comparison to the steel unit. However, the economic validity of the aluminium semi-trailer is borne out by the following comparison of the operation of the two trailers.

A precise determination of the aluminium price premium in this instance is difficult to arrive at since the semi-trailer was not constructed under representative production conditions. The best that can be done is to calculate a price premium based solely on the basic material cost of aluminium and steel

and on the respective chassis tare masses. The production costs are assumed to be similar in each case and thus do not have a marked effect on the price premium. Furthermore, in order to keep the comparison on an equitable basis, the additional cost of the safety equipment fitted to the aluminium trailer (for example, the 'Hope' anti-jack-knife device and the extra lights) and which was not fitted to the PET steel trailer, as well as the additional cost of the aluminium trailer's imported air suspension relative to the PET trailer's locally made steel spring suspension, were not included. In this way an aluminium price premium of R58 000-00 was calculated based on material prices at September 1990[60,61] and on 13 percent GST.

The following assumptions were made with regard to the operation of the two semi-trailers:

(i) When additional payload is carried, it amounts on average to seventy-five percent of the full possible 1 120 kg, ie. 840 kg.[62,63]

(ii) The route is Johannesburg to Durban and back; 585 km each way.

(iii) Five return trips are made each week for a total of fifty weeks per year (ie. ten trips one way).[62,63]

(iv) The additional revenue accrued from carrying additional payload is at the rate of R90-00 per one way trip (ie. R170-00 per return trip).[62,63]

(v) The additional insurance payable on the higher value of the aluminium trailer is at the rate of four percent of the aluminium price premium.[63]

Furthermore, the annual licence fees for the steel and aluminium semi-trailers at the tare masses indicated above are R2 211-00 and R1 707-00 respectively.[64]

The net additional revenue accrued per month for the aluminium semi-trailer,

and which is available to finance the price premium, is calculated thus:

10 single trips per week for (50/12) weeks per month	=	41,67 trips per month
Additional revenue per single trip (0,840 tonnes × R90-00/trip)	=	R75-60
Additional revenue per month (500 trips × R75-60)	=	R3 150-00
Plus: Saving on licence fees per month (R504-00/12)	=	R42-00
Less: Additional insurance premium per month (4% of R58 000-00/12)	=	R193-33
Net additional revenue per month available to finance price premium on aluminium semi-trailer	=	R2 998-67

The pay back period for the aluminium semi-trailer is then equal to the shortest period over which finance would have to be obtained for the amount of the price premium and on which the monthly repayment would be R2 998-67. The governing equation for compound interest on an annuity due type loan is[65] is as shown below. The interest rate has been taken to be 22 percent (ie. one percent above the prime interest rate at September 1990).[63]

$$-PV = \frac{PMT}{i}(1+i)[1-(1+i)^{-n}]$$

where

PV = present or starting value of the loan

= R58 000-00

PMT = the periodic payment

= -R2 998-67

i = periodic interest rate expressed as a decimal fraction

= 0,01833

n = the number of compounding periods (ie. months in this case)

Rearranging:

$$n = \frac{\ln\left[1 + \frac{PV.i}{PMT(1+i)}\right]^{-1}}{\ln(1+i)}$$

The pay back period for the aluminium semi-trailer is then 23,6 months.

These calculations show that, even without taking advantage of the full amount of the additional payload, it is possible to recoup the initial cost premium within a relatively short period. In addition, no account has been taken of the scrap value of the aluminium chassis at the end of the semi-trailer's life, or of the potential savings in fuel, tyre and brake wear, etc., that would arise when travelling light.

Furthermore, and as already mentioned at the beginning of this chapter, the tare mass saving achieved in this project was despite the fact that many decisions were severely limited by the availability of certain materials and funds and of production facilities. The most severely significant examples of this are the main chassis I-beams which, after a number of unsuccessful attempts to manufacture the beams in South Africa, had to be selected from Alusuisse's standard product range in Switzerland and were slightly heavier than they needed to be. If local manufacture had been possible the beams could have been sized more optimally, and thus would have been marginally

lighter. Similarly, if deck planks without anti-skid ribs and a thinner rubbing plate had been used (15,88 mm rubbing plate used to reduce the number of different plate thicknesses required - 12 mm would have been sufficient), and safety items such as the Hope anti-jack-knife device and the extra lighting and braking equipment had not been fitted, further mass savings would have been achieved.

If all of these additional or potential mass savings are taken into account, the total mass saving over the steel unit could have been as high as 1 500 kg or 19 percent, and the payback period as low as 16,3 months.

6.2 Wide spaced tridem axle concept

The wide spaced tridem axle concept incorporating self-steering axles, as introduced via this project, and Henred Fruehauf's PET semi-trailer, has proved to be highly successful. During initial trials, on both freeway and urban roads, the aluminium semi-trailer handled as well and showed itself to be no less manoeuvreable, except when reversing, than conventional 12,3 metre fixed axle semi-trailers. Moreover, because a semi-trailer of this type is intended primarily for long distance haulage, the problem of severe tyre scuff when reversing can be minimised or eliminated altogether through the proper design of end terminals and loading bays.

Further operating experience has indicated greater rates of tyre wear for the two self-steering axles of the aluminium semi-trailer than for the centre fixed axle. This was to be expected and is due to, firstly, the 14 degree maximum tracking angle limitation on the FIA self-steering axles, which results in a certain amount of tyre scuff in tight turns (refer Section 4.6.1) and, secondly, tyre scuff when reversing with all three axles fixed (ie. steering axles locked). However, as predicted in Section 4.6, the tyre wear experienced on these axles

is in general no worse than that typically experienced on the foremost and rearmost axles of a conventional tridem semi-trailer with closely spaced fixed axles. The correct wheel and axle alignment was also found to be important for the two self-steering axles in order to ensure the directional stability of the trailing arms, especially at low axle damping pressures.

An efficient and responsive load equalisation system between the axles of the tridem axle suspension, as well as a greater than normal amount of vertical suspension travel on each individual axle, has been shown to be of importance for wide spaced suspensions (refer Section 3.2 and Section 4.6.2). This is not only to properly distribute forces into the chassis and to maintain all three axles in contact with the road surface at all times, but also to ensure a uniform load distribution at the road surface, thereby minimising pavement damage. During the initial trials of this aluminium semi-trailer, the Fruehauf-T suspension has proved to be well suited in this regard. Further testing is, however, required to determine the respective axle loads under varying conditions, in order to quantify the efficiency of the inter-axle load equalisation. This should be done both statically and dynamically and for various payloads and road surface conditions. Should it be necessary to improve the responsiveness of the suspension, larger air lines than the standard 6,35 mm ($\frac{1}{4}$ inch) nominal bore polyamide plastic tubing can be substituted between the suspension air bags along each side of the trailer chassis to improve the air flow. Increased vertical suspension travel can be achieved, if necessary, by moving the axle locator plates and, hence, the axle mounting position, further along the suspension trailing arm towards the air bags.

6.3 Pseudo-dynamic acceleration based design model

A methodology for platform semi-trailer design has been presented in the form of the design of a lightweight aluminium platform semi-trailer. The dynamic acceleration based design methodology adopted for the chassis design in this project (refer Chapter 4 and Appendices A and B) is considered superior to the more commonly used approach of applying a load factor to the stresses calculated from the static load distribution. The reasons for this are, firstly, because it is a more realistic approximation to the actual situation, in that it takes into account such occurrences as load transfer (eg. during braking) and high dynamic loads resulting from travelling over potholes and other road surface irregularities. Secondly, it gives a direct indication of the expected factor of safety over and above the maximum dynamic design stresses, whereas in the load factor approach the factor of safety and the dynamic load factor are combined, and the relative proportions of each remain unknown. Lastly, the dynamic accelerations applied in the design stages may be compared directly to accelerations measured during later prototype testing and conclusions drawn. In the design of this aluminium trailer chassis (refer Section 4.2.3) the dynamic acceleration factors applied were based on published figures for highway vehicles.

The fatigue-life calculations for the main chassis members have been based on a stress-life approach in conjunction with the Palmgren-Miner Linear Damage Rule. The Palmgren-Miner hypothesis was adopted since it is still the most widely used approach because of its simplicity and ease of application, and the experimental fact that other much more complex cumulative damage theories do not yield a significant improvement in failure prediction reliability. An assumed loading spectrum based on the initial vibration frequency tests described in Section 3.2, and a Gaussian frequency distribution had to be used to approximate the fatigue stress history over the projected service life

of the trailer, since no valid in-service loading data was available for this type of vehicle in South African conditions.

In order to ensure that the peak stresses correlate sufficiently well with design values, and to obtain more accurate data with regard to the projected fatigue stress history, simulated in-service testing of the semi-trailer chassis needs to be undertaken. The methodology for endurance testing of heavy duty vehicles, as discussed in Section 3.4, should be used for this purpose in conjunction with the data logging system described in Section 3.3. In some instances laboratory testing of specific components may be useful.

For the most part, the design calculations relating to the chassis sub-structure (refer Section 4.4 and Appendix C) and to the ancillary structure (refer Section 4.5 and Appendix D) have been undertaken for specific maximum load situations relating to the operating conditions of that area of the trailer. In the case of the side rails and deck, the upper coupler structure and the rear under-ride bumper, the maximum load conditions are related to applicable design specifications.

In all aspects of this design, safety has been maintained as an important criterion and, wherever possible, appropriate safety equipment has been incorporated in the design (eg. 'Hope' anti-jack-knife device and extra lights). In the design of safety related systems and components, such as the braking system and the upper coupler structure, relatively large factors of safety are used to allow for overloading.

6.4 Final conclusions and recommendations

The completion of this aluminium semi-trailer project contributed at the time to the establishment of a valid road transport research program at UWtec. Furthermore, as evidenced by reaction to the trailer from the transport industry, it has helped to promote the use of alternative materials for road vehicle design.

The trailer, together with the infrastructure developed during the project, will serve as a useful semi-trailer test platform for the future testing of such items as structural components, brake systems, running gear, etc, and for the collection of road loading data. It is thus recommended that the remainder of Phase 2 of the project, as discussed in Chapter 1, be completed.

THE DESIGN AND DEVELOPMENT OF A LIGHT-WEIGHT ALUMINIUM SEMI-TRAILER

Malcolm John Mac Gregor Elston

VOLUME II

APPENDIX A

STRESS ANALYSIS OF MAIN CHASSIS I-BEAMS

A.1 Introduction

This appendix details the design calculations relating to the various load and support cases for the semi-trailer, as well as the stress and buckling analyses and the fatigue analysis for the two main chassis I-beams. The actual loading analysis of each load case is undertaken in Appendix B.

A.2 Loading analysis of main chassis I-beams.

A.2.1 General

In an attempt to cover all possible loading conditions, various load analyses (denoted case 1 – case 7 loading) are detailed in this section for both static and dynamic loading of the semi-trailer, and for various support conditions. In all cases the load is assumed to be distributed over the full length of the trailer. Further, it is assumed that all the load is carried by the two main chassis I-beams, since the contribution of the deck and side rails to the longitudinal bending stiffness of the trailer is negligible. Transverse loads are neglected and torsional loading is dealt with separately. A design payload of 30 000 kg, a chassis mass of 2 900 kg and a running gear mass of 2 820 kg are used, with the chassis I-beam length (ie. deck length) being 13 729 mm (refer Section 4.2.2). The auxiliary equipment tare (ie. landing legs, Hope king-pin, braking equipment, etc.) of 250 kg is neglected.

Values of shear force, bending moment and deflection at 31 nodes along the length of the chassis I-beams are calculated for the loads and support cases discussed below, using the "Genesys Frame-analysis/2" structural analysis

sub-program (refer Case 1 to Case 7 loading – Appendix B). The resultant shear force, bending moment and deflection diagrams are presented in Graphs 4.1 to 4.3 and Graphs 4.5 to 4.22 in Chapter 4. Longitudinal loading is analysed separately and these results are presented in Table A1 and Graph 4.4.

It should be noted here that, since the sub-program is used to analyse a single chassis I-beam coupled to a two-dimensional model of one side of the suspension system, the loading figures calculated in this section are halved in order to yield the loading per beam. Similarly, the support reactions calculated by the sub-program are for a single chassis beam and, hence, are half the reactions for the full trailer. The reactions at the suspension hanger and air-bag mounts are obtained from the compressive forces in the links of the suspension model at those respective nodes.

A.2.2 Pseudo dynamic fully distributed load analysis (Case 1)

This load analysis simulates the combination of dynamic vertical loads imposed on the structure with longitudinal forces due to, for example, braking decelerations. The approach adopted is to firstly calculate the load transfer from the semi-trailer tri-axle bogie to the king pin, due to an assumed distribution of retarding forces between the king pin and bogie, as well as load transfer within the suspension itself, and thereby to obtain pseudo-dynamic reactions at the king pin and at suspension hanger and air-bag mounts. Then, working backwards, a skewed load distribution (Figure A4), of total magnitude equal to the design payload plus chassis mass multiplied by the vertical acceleration, is calculated to produce these pseudo-dynamic reactions. In this analysis it is assumed that a maximum downward deceleration of 2-g and a maximum forward braking deceleration of 1-g acts upon the fully laden vehicle. Further, the brake retarding forces are assumed to be distributed such

that 40 percent of the braking deceleration is due to retarding forces at the tyres of the semi-trailer and 60 percent due to retarding forces at the king-pin (refer Section 4.3.1). The height of the centre of gravity of the fully distributed payload and semi-trailer (including axles and suspension) combined is estimated to be 800 millimetres above the deck (ie. approximately 2 470 millimetres above ground level).

Static reactions

Referring to Figure A1, the static reactions at the king-pin and at the suspension mounting are calculated in the following manner.

Summing vertical forces

$$R_1 + R_2{}' = P_t{}' = (9,81)(32900)(10^{-1})$$
$$= 322,7 \text{ kN}$$

where $P_t{}'$ is the combined weight of the chassis and payload and $R_2{}'$ is the total static reaction at the suspension mountings.

Taking moments about the centre of the tri-axle bogie:

$$R_1(8924) = (6864,5 - 3450)(322,7)$$

that is

$$R_1 = 123,5 \text{ kN}$$

and substituting

$$R_2{}' = 199,3 \text{ kN}$$

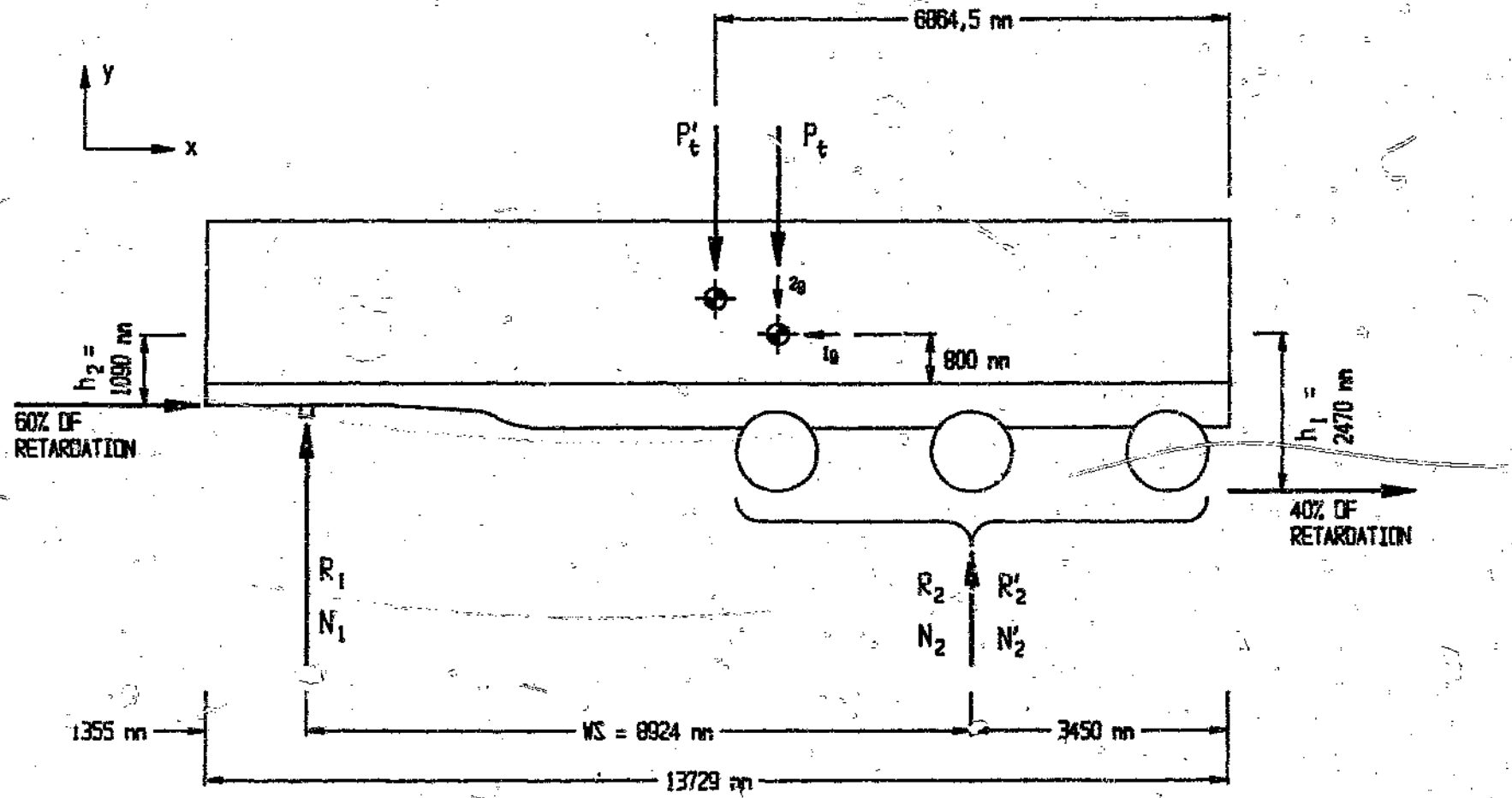


Figure A1 Free body diagram for pseudo-dynamic fully distributed load analysis

Adding the running gear mass (ie. axles, tyres, suspension, etc.) to $R_2{}'$:

$$R_2 = R_2{}' + (9,81)(2820)(10^{-3})$$
$$= 226,9 \text{ kN}$$

Load transfer between the suspension and the king-pin

For a downward deceleration of 2-g and a forward deceleration of 1-g, and for 60 percent of the braking of the trailer via the king-pin and 40 percent at the trailer tyres, the dynamic reactions are as follows:

$$N_1 = (2)R_1 + (0,4)(1)\frac{h_1}{WS}(2)P_t + (0,6)(1)\frac{h_3}{WS}(2)P_t$$

$$N_2 = (2)R_2 - (0,4)(1)\frac{h_1}{WS}(2)P_t - (0,6)(1)\frac{h_3}{WS}(2)P_t$$

$$N_2{}' = (2)R_2{}' - (0,4)(1)\frac{h_1}{WS}(2)P_t - (0,6)(1)\frac{h_2}{WS}(2)P_t$$

where $N_2{}'$ is the total dynamic reaction at the suspension mountings.

Now:

$$P_t = (9,81)(35720)(10^{-3})$$
$$= 350,4 \text{ kN}$$

Hence, substituting into the above equations:

$$N_1 = 375,9 \text{ kN}$$

$$N_2 = 324,9 \text{ kN}$$

$$N_2{}' = 269,6 \text{ kN}$$

Load transfer within the suspension

The air suspension fitted to the semi-trailer distributes the load equally between each of the three axles of the tri-axle bogie. Hence, the static load on each of the axles under fully laden conditions is:

$$R_{AX} = \frac{R_2}{3}$$

$$= 75,64 \text{ kN}$$

Similarly, the load at the suspension mountings for each of the axles is:

$$R_{AX}{}' = \frac{R_2{}'}{3}$$

$$= 66,43 \text{ kN}$$

Referring to Figure A2, the static reactions at the suspension hanger and air-bag mountings are:

$$R_H = \frac{(381)R_{AX}{}'}{(865)}$$

$$= 29,26 \text{ kN}$$

$$R_A = \frac{(484)R_{AX}{}'}{(865)}$$

$$= 37,17 \text{ kN}$$

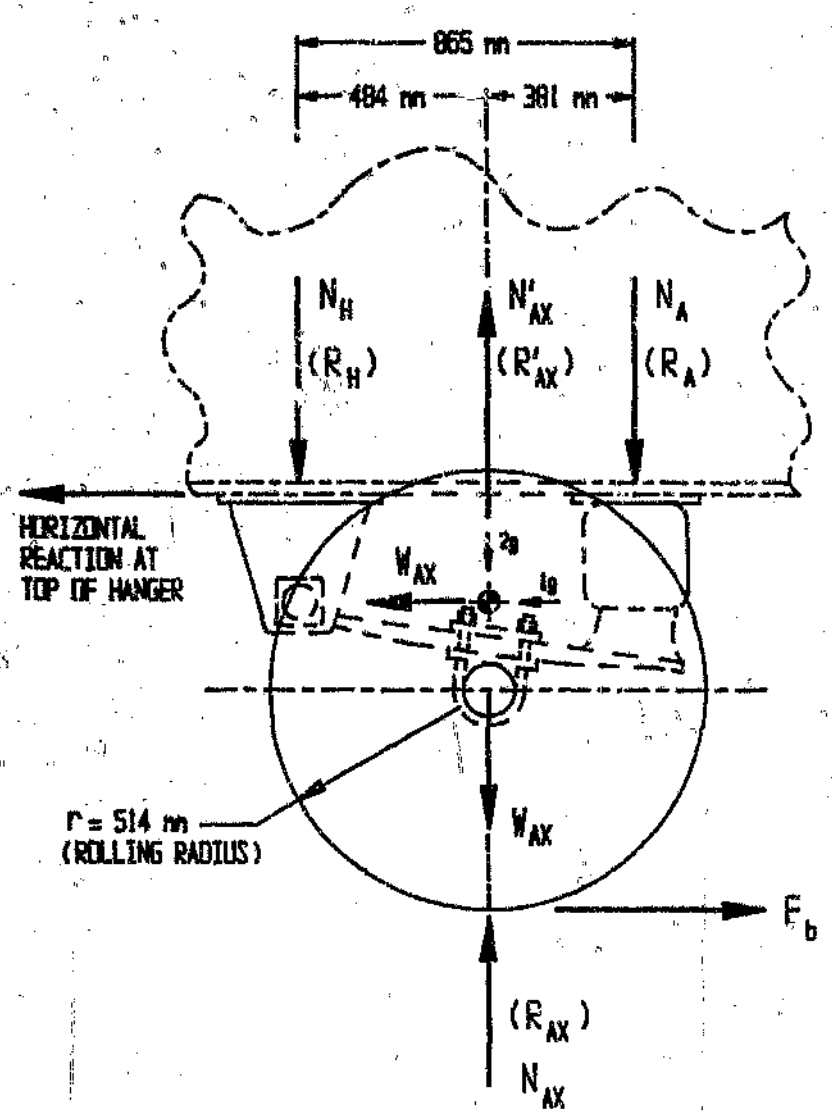


Figure A2 Load transfer within the suspension during braking

Similarly, under dynamic fully laden conditions:

$$N_{AX} = \frac{N_2}{3}$$

$$= \frac{324,9}{3}$$

$$= 108,3 \text{ kN}$$

$$N_{AX}{}' = \frac{N_2{}'}{3}$$

$$= \frac{269,6}{3}$$

$$= 89,86 \text{ kN}$$

As a result of the equalising effect of the air suspension, the braking force (F_b) is assumed to be equal for each of the trailer axles. As above, the trailer axles are assumed to account for 40 percent of the braking action on the vehicle. Then, referring to Figure A2, the braking force at the tyres on one axle is:

$$F_b = \frac{(35\,720)(0,4)(1,0)(9,81)(10^{-3})}{(3)}$$

$$= 46,72 \text{ kN}$$

Hence, the braking torque on each of the axles is:

$$T_b = F_b \times r$$

$$= (46,72)(514)(10^{-3})$$

$$= 24,01 \text{ kNm}$$

Taking moments about the suspension hanger pivot:

$$N_A(865) = T_b + N_{AX}{}'(484)$$

that is

$$N_A = 78,04 \text{ kN}$$

Similarly

$$N_H = 11,82 \text{ kN}$$

Note that since the centre of gravity of the running gear mass is close to the same height as the suspension trailing arm pivot pin, the horizontal inertial force W_{AX} in Figure A2 is assumed to act through the pivot pin centre.

Suspension hanger moments

During braking, the braking force at the tyre/road surface interface is transferred to the chassis via the suspension hanger. This results in a moment about the neutral axis of the main chassis I-beams. The braking force at the suspension hanger pivots for each axle is given by:

$$F_b' = F_b - \left(\frac{1}{3}\right)(9,81)(2820)\,(10^{-3})$$

$$= 37,50 \text{ kN}$$

Then, referring to Figure A3, the suspension hanger moment for each of the axles is:

$$M_H = (594)\,(10^{-3})\,F_b'$$

$$= 22,28 \text{ kNm}$$

Skewed loading distribution

The maximum (ω_m) and minimum (ω_n) values of the skewed load distribution used in this analysis are now determined from the support reactions calculated above. Summing vertical forces as indicated in Figure A4:

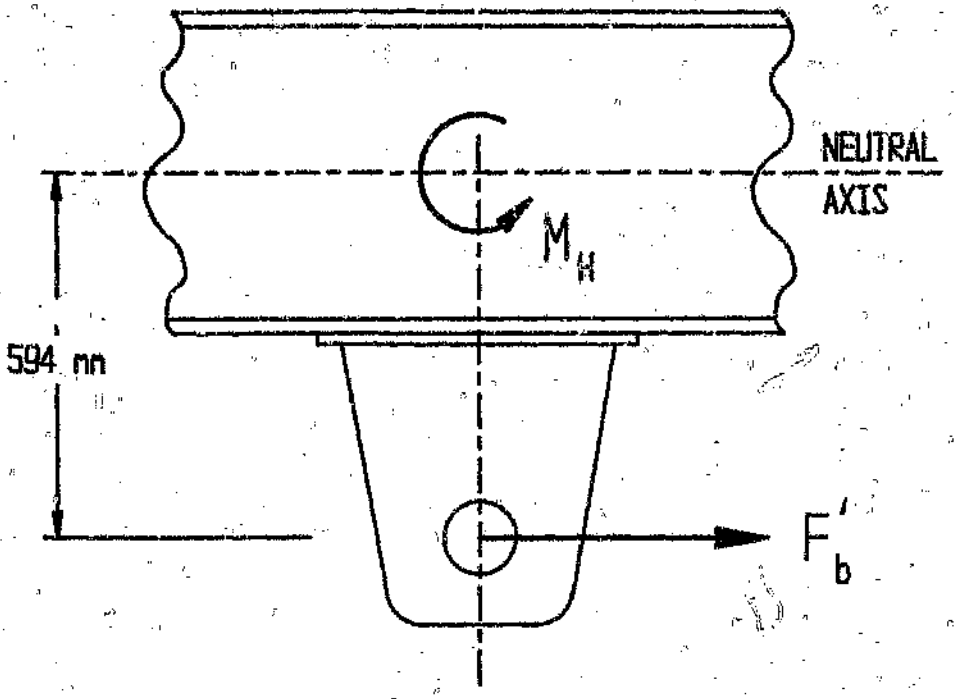


Figure A3 Suspension hanger moments

$$\frac{1}{2}(\omega_m + \omega_n)(13,729) = N_1 + 3N_H + 3N_A$$

$$= 645,5 \text{ kN}$$

that is

$$\omega_m = (94,03) - \omega_n \quad [\text{kN/m}]$$

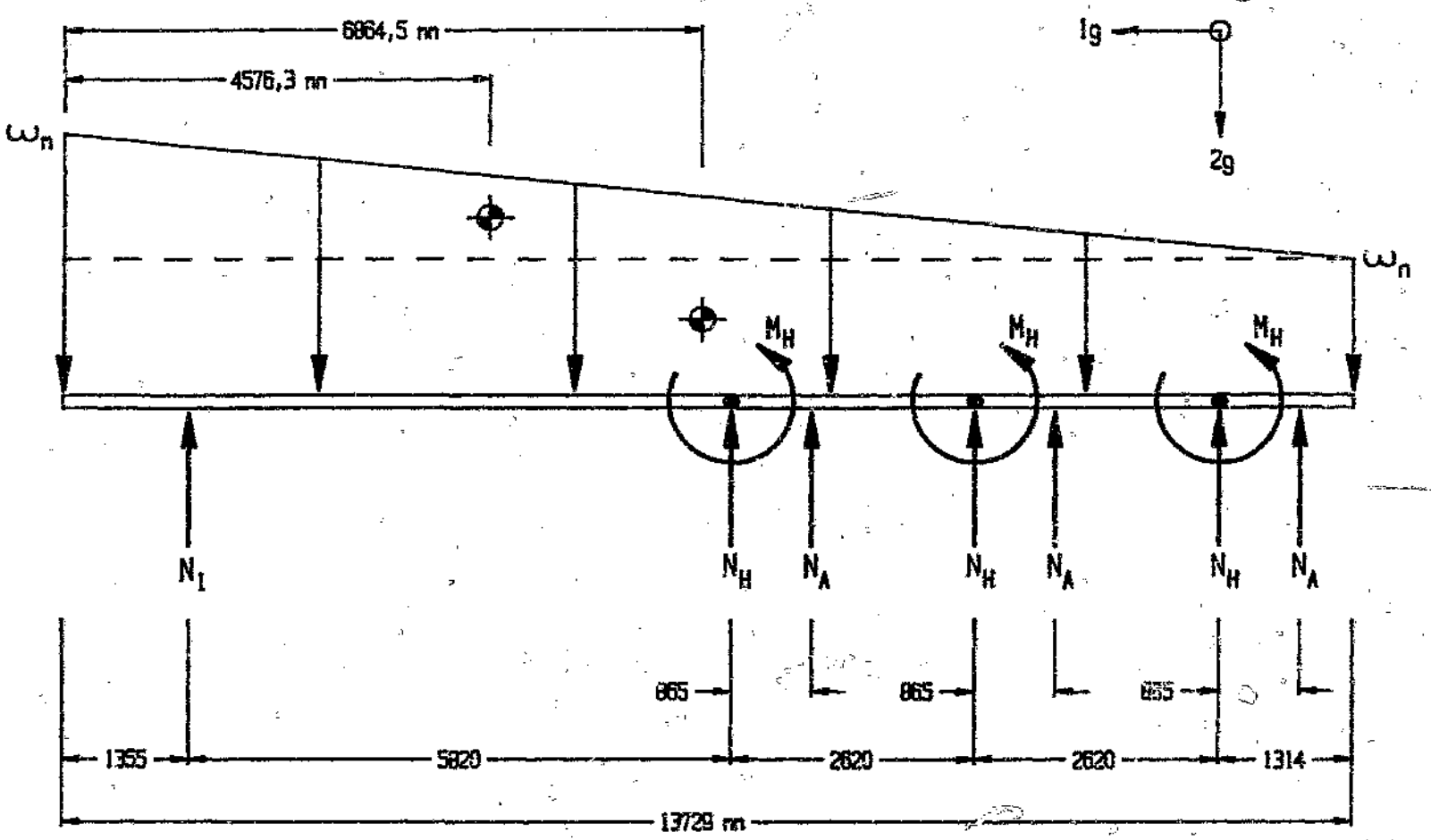


Figure A4 Skewed load distribution

Taking moments about the very front of the trailer:

$$\frac{1}{2}(\omega_m - \omega_n)\frac{(13,729)^2}{3} + \omega_n\frac{(13,729)^2}{2} - 3M_H - N_1(1,355)$$
$$- N_H(7,175 + 9,795 + 12,415) - N_A(8,04 + 10,66 + 13,28) = 0$$

that is

$$\omega_m = (108,84) - 2\omega_n \quad [\text{kN/m}]$$

Thus:

$$\omega_n = 108,84 - 94,03$$
$$= 14,81 \text{ kN/m}$$

and

$$\omega_m = 79,23 \text{ kN/m}$$

Shear force, bending moment and deflection diagrams

Shear force, bending moment and deflection diagrams for the above skewed load distribution from results tabulated in Appendix B, are presented in Graphs 4.1 to 4.3 in Section 4.3.1.

A.2.3 Static fully distributed load analyses (Case 2 and Case 3)

Static load distributions are analysed in this section for the trailer at rest or parked. Two different situations are considered. Firstly, for support at the king-pin (ie. truck-tractor coupled - Case 2 loading) and secondly for support at the landing legs (ie. truck-tractor uncoupled - Case 2 loading).

All three trailer axles are assumed to be firmly in contact with the ground. No longitudinal or transverse loads are considered in either case.

The value of the static distributed load on the semi-trailer is:

$$\omega_s = \frac{(9,81)(32\,900)(10^{-3})}{(13,729)}$$

$$= 23,51 \text{ kN/m}$$

Support at the king-pin and three trailer axles (Case 2 loading)

The support reactions for the whole trailer are (refer Appendix B):

$R_1 = 123,5$ kN

$R_2{}' = 199,3$ kN

$R_H = 28,9$ kN

$R_A = 37,4$ kN

Support at the landing legs and three trailer axles (Case 3 loading)

The static reactions at supports for the whole trailer, in this case, are as follows (refer Appendix B):

$R_L = 181,5$ kN

$R_2{}' = 141,3$ kN

$R_H = 20,74$ kN

$R_A = 26,37$ kN

Shear force, bending moment and deflection diagrams

Shear force, bending moment, and deflection diagrams from the results tabulated in Appendix B, are presented in Graphs 4.5 to 4.10 in Section 4.3.1.

A.2.4 Static load analyses for various axles lifted (Case 4 to Case 7)

When negotiating large humps and dips in the road surface, situations can arise where the tyres on one or more of the axles of the trailer are lifted completely off the road surface. This is due to the load equalisation system of the suspension not having sufficient travel to maintain all three sets of tyres firmly on the ground, thereby equalising axle loads, and is accentuated to a large extent by the wide spacing of the axles of the semi-trailer tri-axle bogie. Due to the extreme nature of the road surface required to produce these conditions, they are considered to occur at low speed and, hence, at low dynamic acceleration. For example, when entering and exiting driveways, over storm water gulleys, or when turning sharp corners where there is a large difference in slope between the two intersecting roads. For this reason all of the following analyses are undertaken for a 1-g (vertical) load distribution (ie. static loading).

The value of the 1-g uniformly distributed load for the whole trailer is:

$$\omega_g = \frac{(32900)(9,81)(10^{-3})}{(13,729)}$$

$$= 23,51 \text{ kN/m}$$

Support at the king-pin and foremost axle (Case 4 loading)

In this case the tyres of the centre and rearmost axles are lifted clear of the ground. The support reactions for the whole trailer are as follows (refer Appendix B):

$$R_1 = 40,70 \text{ kN}$$

$$R_{AX}{}' = 282,0 \text{ kN}$$

$$R_H = 124,1 \text{ kN}$$

$$R_A = 157,9 \text{ kN}$$

Support at the king-pin and centre axle (Case 5 loading)

This case covers the situation for the tyres of the foremost and rearmost axles lifted clear of the ground. The reactions at the supports for the whole trailer are (refer Appendix B):

$$R_1 = 123,5 \text{ kN}$$

$$R_{AX}{}' = 199,3 \text{ kN}$$

$$R_H = 87,88 \text{ kN}$$

$$R_A = 111,5 \text{ kN}$$

Support at the king-pin and rearmost axle (Case 6 loading)

Here the tyres of the foremost and centre axle are lifted off the ground. Support reactions are (refer Appendix B):

$$R_1 = 163,7 \text{ kN}$$

$$R_{AX}{}' = 154,1 \text{ kN}$$

$$R_H = 67,75 \text{ kN}$$

$$R_A = 86,00 \text{ kN}$$

Support at the king-pin and front and centre axle (Case 7 loading)

In this case the tyres of only the rearmost axle are lifted clear of the ground. The reactions at the supports for the whole trailer are as follows (refer Appendix B):

$$R_1 = 89,21 \text{ kN}$$

$$R_2{}' = 233,5 \text{ kN}$$

$$R_{AX}{}' = 116,8 \text{ kN}$$

$$R_H = 51,46 \text{ kN}$$

$$R_A = 65,31 \text{ kN}$$

Shear force, bending moment and deflection diagrams

Shear force, bending moment, and deflection diagrams for the above four load cases, from the results tabulated in Appendix B, are presented in Graphs 4.11 to 4.22 in Section 4.3.1.

A.2.5 Longitudinal loading analysis

Longitudinal loads are imposed on the chassis I-beams during braking. In this analysis a forward braking deceleration of 1-g is assumed to act upon the payload and the trailer mass. The payload mass is distributed over the full length of the semi-trailer and it is assumed that the retarding forces

between the deck of the trailer and the payload are evenly distributed along the full length of the deck. As in previous analyses it is assumed that 40 percent of the braking deceleration is due to retarding forces at the tyres of the semi-trailer and 60 percent due to retarding forces at the king-pin.

Referring to Figure A5, the longitudinal load induced in a chassis I-beam at a distance, x, from the front of the beam, for span A, is given by:

$$F_l = \frac{z}{2}\left[(0,6)P_t + (3)F_b{}' - \left(\frac{\ell_b - x}{\ell_b}\right)P_t{}'\right]$$

where z is the braking ratio (ie. 1) and ℓ_b is the length of the beam.

Similarly, for spans B, C, D and E:

$$\text{Span B}: \quad F_l = \frac{z}{2}\left[(3)F_b{}' - \left(\frac{\ell_b - x}{\ell_b}\right)P_t{}'\right]$$

$$\text{Span C}: \quad F_l = \frac{z}{2}\left[(2)F_b{}' - \left(\frac{\ell_b - x}{\ell_b}\right)P_t{}'\right]$$

$$\text{Span D}: \quad F_l = \frac{z}{2}\left[F_b{}' - \left(\frac{\ell_b - x}{\ell_b}\right)P_t{}'\right]$$

$$\text{Span E}: \quad F_l = \frac{P_t{}'}{2}\left(\frac{\ell_b - x}{\ell_b}\right)$$

The distribution of longitudinal loads per chassis I-beam for the 31 nodes along the length of the I-beams (refer Appendix B) are presented in Table A1 overleaf and in Graph 4.4 in Section 4.3.1.

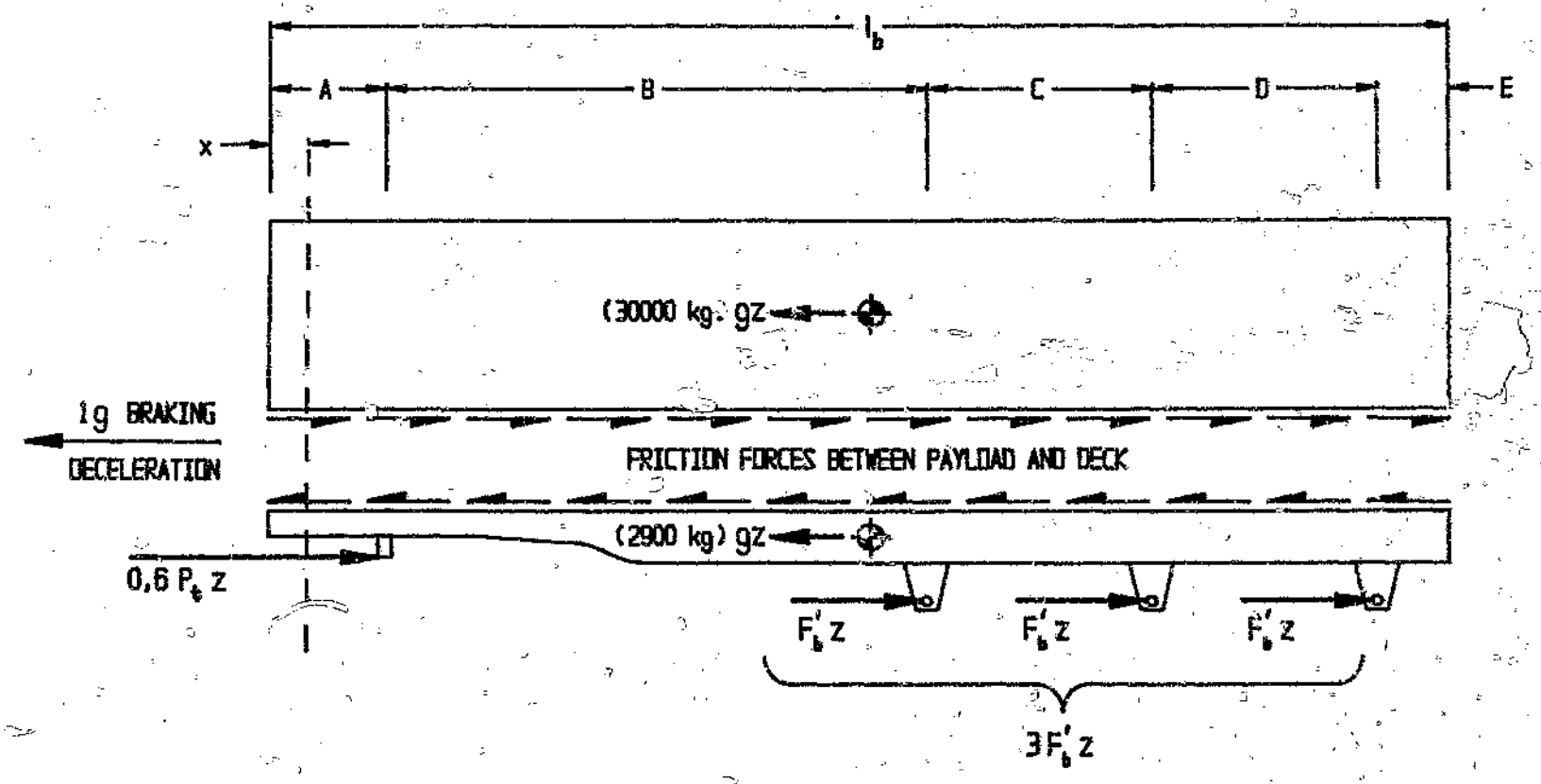


Figure A.5 Longitudinal loading on chassis I-beams during braking

Table A.1 Longitudinal loading distribution for main chassis I-beams

Node	Distance from front of I-Beam (mm)	Longitudinal load per I-Beam – F_l (kN)
1	0,0	0,0
2	677,5	7,96
3	1355,0	15,93/ – 89,20
4	1905,0	–82,73
5	2455,0	–76,27
6	2730,0	–73,04
7	3005,0	–69,80
8	3280,0	–66,57
9	3555,0	–63,34
10	3771,67	–60,79
11	3988,33	–58,24
12	4205,0	–55,70
13	4354,0	–53,95
14	4918,2	–47,31
15	5482,4	–40,68
16	6046,6	–34,05
17	6610,8	–27,42
18	7175,0	–20,79/ – 39,54
19	7607,5	–34,45
20	8040,0	–29,37
21	8625,0	–22,49
22	9210,0	–15,62
23	9795,0	–8,74/ – 27,49
24	10227,5	–22,1
25	10660,0	–17,32
26	11245,0	–10,45
27	11830,0	–3,57
28	12415,0	3,30/ – 15,45
29	12847,5	–10,36
30	13280,0	–5,28
31	13729,0	0,0

A.3 Stress analysis of main chassis I-beams

A.3.1 Stress distributions

The following distributions of stress over the full length of the chassis I-beams were calculated for the pseudo-dynamic (Case 1) loading conditions and are presented here in tabular form (Tables A2 to A7). Each of these stress distributions is also discussed in Section 4.3.2 and the results presented in graphical form in Graphs 4.23 to 4.34.

- Longitudinal direct stress.
- Maximum transverse shear stress (neutral axis).
- Extreme fibre bending stress (upper flange).
- Principal stresses at the extreme fibres (upper flange).
- Principal shear stress at extreme fibres (upper flange).
- Von Mises stress at extreme fibres (upper flange).
- Principal stresses at the web/flange joint (above the neutral axis).
- Principal shear stress at the web/flange joint (above the neutral axis).
- Von Mises stress at the web/flange joint (above the neutral axis).
- Principal stresses in the main I-beam welds (above the neutral axis).
- Principal shear stress in the main I-beam welds (above the neutral axis).
- Von Mises stress in the main I-beam welds (above the neutral axis).

The positions of the nodes quoted in the tables are as defined in Figure B1 and Section B.. of Appendix B.

Table A2 Longitudinal direct stress distribution (Case 1 loading)

Node	I-beam depth (mm)	Longitudinal stress (MPa)
1	290,0	0,00
2	290,0	0,76
3	290,0	1,52
		−8,50
4	290,0	−7,88
5	290,0	−7,26
6	309,2	−6,83
7	328,5	−6,41
8	347,7	−6,01
9	366,9	−5,62
10	418,8	−5,16
11	530,8	−4,51
12	588,8	−4,13
13	600,0	−3,97
14	600,0	−3,48
15	600,0	−2,99
16	600,0	−2,50
17	600,0	−2,02
18	600,0	−1,53
		−2,91
19	600,0	−2,53
20	600,0	−2,16
21	600,0	−1,65
22	600,0	−1,15
23	600,0	−0,64
		−2,02
24	600,0	−1,65
25	600,0	−1,27
26	600,0	−0,77
27	600,0	−0,26
28	600,0	0,24
		−1,14
29	600,0	−0,76
30	600,0	−0,39
31	600,0	0,00

Table A3 Maximum transverse shear stress distribution (Neutral axis - Case 1 loading)

Node	I-beam depth (mm)	Shear Force (kN)	Trans. shear stress (MPa)
1	290,0	0,00	0,00
2	290,0	−26,30	−10,22
3	290,0	−51,52	−20,02
		136,27	52,95
4	290,0	116,59	45,30
5	290,0	97,61	37,93
6	309,2	88,44	32,19
7	328,5	79,34	27,16
8	347,7	70,48	22,79
9	366,9	61,80	18,93
10	418,8	54,72	14,70
11	530,8	46,95	10,01
12	588,8	41,63	8,03
13	600,0	37,59	7,12
14	600,0	21,40	4,05
15	600,0	5,94	1,13
16	600,0	−8,84	− 1,67
17	600,0	−22,76	− 4,31
18	600,0	−36,03	− 6,82
		−30,03	− 5,69
19	600,0	−39,66	− 7,51
20	600,0	−48,91	− 9,26
		− 9,91	− 1,88
21	600,0	−21,64	− 4,10
22	600,0	−32,51	− 6,16
23	600,0	−42,64	− 8,08
		−36,55	− 6,92
24	600,0	−43,53	− 8,24
25	600,0	−50,13	− 9,49
		−11,21	− 2,12
26	600,0	−19,35	− 3,66
27	600,0	−26,68	− 5,05
28	600,0	−33,20	− 6,29
		−27,15	− 5,14
29	600,0	−31,46	− 5,96
30	600,0	−35,39	− 6,70
		3,58	0,68
31	600,0	0,00	0,00

Table A4 Extreme fibre bending stress distribution

(Upper flange - Case 1 loading)

Node	I-beam depth (mm)	Bending Moment (kNm)	Bending stress (MPa)
1	290,0	0,00	0,00
2	290,0	8,91	8,12
3	290,0	35,27	32,15
4	290,0	−34,30	−31,26
5	290,0	−93,23	−84,97
6	309,2	−118,83	−99,95
7	328,5	−141,90	−110,66
8	347,7	−162,53	−118,07
9	366,9	−180,73	−122,77
10	418,8	−193,44	−111,39
11	530,8	−204,68	−87,53
12	588,8	−214,55	−80,46
13	600,0	−220,43	−80,70
14	600,0	−237,07	−86,80
15	600,0	−244,76	−89,61
16	600,0	−243,95	−89,31
17	600,0	−235,04	−86,05
18	600,0	−218,45	−79,98
		−207,31	−75,90
19	600,0	−192,25	−70,39
20	600,0	−173,13	−63,39
21	600,0	−163,92	−60,01
22	600,0	−148,09	−54,22
23	600,0	−126,11	−46,17
		−114,97	−42,09
24	600,0	−97,62	−35,74
25	600,0	−77,36	−28,32
26	600,0	−68,43	−25,05
27	600,0	−54,98	−20,13
28	600,0	−37,47	−13,72
		−26,33	−9,64
29	600,0	−13,63	−4,99
30	600,0	0,84	0,31
31	600,0	0,00	0,00

Table A5 Distributions of principal stresses, principal shear stress and Von Mises stress at the extreme fibres of the upper flange (Case 1 loading)

Node	Max. prin. stress (MPa)	Min. prin. stress (MPa)	Prin. shear stress (MPa)	Von Mises stress (MPa)
1	0,00	0,00	0,00	0,00
2	8,88	0,00	4,44	8,88
3	33,66	0,00	16,83	33,66
	23,65	0,00	11,83	23,65
4	0,00	− 39,14	19,57	39,14
5	0,00	− 92,24	46,12	92,24
6	0,00	06,78	53,39	106,78
7	0,00	17,07	58,54	117,07
8	0,00	−124,08	62,04	124,08
9	0,00	−128,39	64,20	128,39
10	0,00	−116,55	58,27	116,55
11	0,00	− 92,04	46,02	92,04
12	0,00	− 84,59	42,29	84,59
13	0,00	− 84,67	42,33	84,67
14	0,00	− 90,27	45,14	90,27
15	0,00	− 92,60	46,30	92,60
16	0,00	− 91,82	45,91	91,82
17	0,00	− 88,07	44,03	88,07
18	0,00	− 81,51	40,75	81,51
	0,00	− 78,81	39,40	78,81
19	0,00	− 72,92	36,46	72,92
20	0,00	− 65,55	32,77	65,55
21	0,00	− 61,67	30,83	61,67
22	0,00	− 55,37	27,68	55,37
23	0,00	− 46,81	23,41	46,81
	0,00	− 44,11	22,06	44,11
24	0,00	− 37,39	18,69	37,39
25	0,00	− 29,60	14,80	29,60
26	0,00	− 25,82	12,91	25,82
27	0,00	− 20,39	10,20	20,39
28	0,00	− 13,48	6,74	13,48
	0,00	− 10,78	5,39	10,78
29	0,00	− 5,75	2,88	5,75
30	0,00	− 0,08	0,04	0,08
31	0,00	0,00	0,00	0,00

Table A6 Distributions of principal stresses, principal shear stress and Von Mises stress at the web/flange joint above the neutral axis (Case 1 loading)

Node	Max. prin. stress (MPa)	Min. prin. stress (MPa)	Prin. shear stress (MPa)	Von Mises stress (MPa)
1	0,00	0,00	0,00	0,00
2	13,61	−5,85	9,73	17,30
3	37,41	−8,18	22,79	42,09
	56,85	−37,63	47,24	82,39
4	25,82	−60,65	43,24	76,89
5	11,88	−92,40	52,14	98,88
6	7,63	−101,49	54,56	105,51
7	4,98	−108,57	56,77	111,14
8	3,27	−113,77	58,52	115,44
9	2,15	−117,16	59,65	118,25
10	1,34	−107,25	54,30	107,93
11	0,69	−86,14	43,42	86,49
12	0,46	−79,58	40,02	79,81
13	0,36	−79,65	40,00	79,82
14	0,11	−84,60	42,35	84,65
15	0,01	−86,64	43,32	86,64
16	0,02	−85,88	42,95	85,89
17	0,13	−82,46	41,29	82,52
18	0,34	−76,51	38,43	76,69
	0,24	−73,99	37,12	74,11
19	0,46	−68,69	34,57	68,92
20	0,77	−62,09	31,43	62,48
	0,03	−61,35	30,69	61,37
21	0,16	−57,83	29,00	57,91
22	0,41	−52,16	26,28	52,36
23	0,82	−44,55	22,69	44,97
	0,64	−41,95	21,29	42,27
24	1,05	−36,06	18,56	36,60
25	1,71	−29,42	15,57	30,31
	0,09	−27,80	13,94	27,84
26	0,31	−24,46	12,38	24,61
27	0,72	−19,77	10,25	20,14
28	1,56	−14,13	7,84	14,97
	1,29	−11,43	6,36	12,12
29	2,50	−7,92	5,21	9,43
30	4,96	−5,06	5,01	8,68
	0,46	−0,56	0,51	0,88
31	0,00	0,00	0,00	0,00

Table A6 Distributions of principal stresses, principal shear stress and Von Mises stress at the web/flange joint above the neutral axis (Case 1 loading)

Node	Max. prin. stress (MPa)	Min. prin. stress (MPa)	Prin. shear stress (MPa)	Von Mises stress (MPa)
1	0,00	0,00	0,00	0,00
2	13,61	− 5,85	9,73	17,30
3	37,41	− 8,18	22,79	42,09
	56,85	− 37,63	47,24	82,39
4	25,82	− 60,65	43,24	76,89
5	11,88	− 92,40	52,14	98,88
6	7,63	−101,49	54,56	105,51
7	4,98	−108,57	56,77	111,14
8	3,27	−113,77	58,52	115,44
9	2,15	−117,16	59,65	118,25
10	1,34	−107,25	54,30	107,93
11	0,69	− 86,14	43,42	86,49
12	0,46	− 79,58	40,02	79,81
13	0,36	− 79,65	40,00	79,82
14	0,11	− 84,60	42,35	84,65
15	0,01	− 86,64	43,32	86,64
16	0,02	− 85,88	42,95	85,89
17	0,13	− 82,46	41,29	82,52
18	0,34	− 76,51	38,43	76,69
	0,24	− 73,99	37,12	74,11
19	0,46	− 68,69	34,57	68,92
20	0,77	− 62,09	31,43	62,48
	0,03	− 61,35	30,69	61,37
21	0,16	− 57,83	29,00	57,91
22	0,41	− 52,16	26,28	52,36
23	0,82	− 44,55	22,69	44,97
	0,64	− 41,95	21,29	42,27
24	1,05	− 36,06	18,56	36,60
25	1,71	− 29,42	15,57	30,31
	0,09	− 27,80	13,94	27,84
26	0,31	− 24,46	12,38	24,61
27	0,72	− 19,77	10,25	20,14
28	1,56	− 14,13	7,84	14,97
	1,29	− 11,43	6,36	12,12
29	2,50	− 7,92	5,21	9,43
30	4,96	− 5,06	5,01	8,68
	0,46	− 0,56	0,51	0,88
31	0,00	0,00	0,00	0,00

Table A7 Distributions of principal stresses, principal shear stress and Von Mises stress at the main I-beam welds above the neutral axis (Case 1 loading)

Node	Max. prin. stress (MPa)	Min. prin. stress (MPa)	Prin. shear stress (MPa)	Von Mises stress (MPa)
1	0,00	0,00	0,00	0,00
2	14,24	−9,28	11,76	20,52
3	33,35	−15,21	24,28	43,02
	63,77	−55,64	59,71	103,50
4	40,34	−64,39	52,36	91,49
5	24,16	−75,37	49,76	89,92
6	16,52	−78,05	47,29	87,49
7	11,14	−81,05	46,09	87,15
8	7,44	−83,97	45,70	87,93
9	4,90	−86,44	45,67	89,00
10	2,96	−82,27	42,62	83,79
11	1,45	−70,40	35,92	71,14
12	0,94	−66,39	33,67	66,87
13	0,73	−66,57	33,65	66,93
14	0,22	−70,25	35,23	70,36
15	0,02	−71,71	35,86	71,72
16	0,04	−71,02	35,53	71,03
17	0,26	−68,25	34,25	68,38
18	0,70	−63,56	32,12	63,90
	0,50	−61,60	31,05	61,85
19	0,94	−57,43	29,19	57,91
20	1,57	−52,32	26,95	53,12
	0,07	−50,82	25,44	50,85
21	0,33	−48,00	24,17	48,17
22	0,83	−43,55	22,19	43,97
23	1,65	−37,69	19,67	38,55
	1,29	−35,58	18,43	36,24
24	2,09	−31,14	16,61	32,23
25	3,28	−26,27	14,78	28,05
	0,19	−23,17	11,68	23,27
26	0,62	−20,60	10,61	20,92
27	1,43	−17,12	9,27	17,88
28	2,88	−13,15	8,01	14,80
	2,33	−10,86	6,59	12,19
29	3,97	− 8,56	6,26	11,09
30	6,48	− 6,63	6,55	11,35
	0,59	− 0,74	0,67	1,16
31	0,00	0,00	0,00	0,00

A.3.2 Failure critical stress areas

In this section eleven areas along the length of the main chassis I-beams are identified as being possible failure sites. The first four positions are apparent from the stress distributions of Section A.3.1 and are as follows:

- Stress at extreme fibres of the top flange at maximum bending moment ($\sigma_m = 92,60$ MPa).
- Stress in upper main I-beam welds at maximum bending moment ($\sigma_m = 71,72$ MPa).
- Stress at extreme fibres of the top flange at maximum bending stress ($\sigma_m = 128,4$ MPa).
- Stress in upper main I-beam welds at maximum bending stress ($\sigma_m = 89,00$ MPa).

The remaining seven areas are analysed in the following pages. All eleven positions are discussed in general in Section 4.3.3 in Chapter 4.

As in Section A.3.1, all of the analyses that follow are undertaken for pseudo-dynamic (Case 1) loading since the maximum loads in each case occur under these loading conditions.

Stress at torsion tube bolt hole nearest to maximum bending moment

For Case 1 loading, node 16 is close to a pair of torsion tube bolt holes, each of which causes a concentration of stress which can be related to the principal stress field at the hole position.

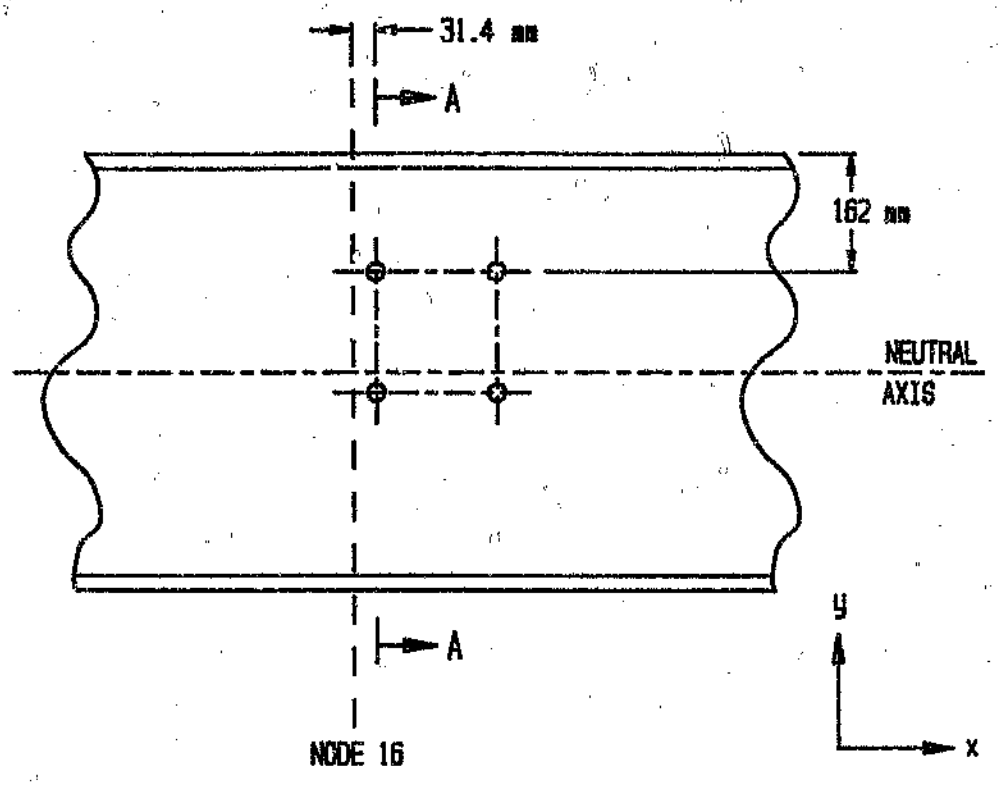


Figure A6 Bolt holes nearest to position of maximum bending moment

Interpolating linearity between the bending stresses at nodes 16 and 17 in Table A4, the extreme fibre bending stress at Section A-A in Figure A6 is:

$\sigma_b = \pm 89,13$ MPa

The principal stress of largest magnitude will occur at the upper of the two bolt holes since, firstly, it is further from the neutral axis and hence bending stress is greater, and secondly, since the longitudinal direct stress is of the same sign above the neutral axis (ie. compressive).

Calculating stresses at the centre of the upper bolt hole:

$$\sigma_b = \left(\frac{300 - 162}{300}\right)(-89,13)$$

$$= -41,00 \text{ MPa}$$

From Table A2, the longitudinal stress at Section A-A by linear interpolation is:

$$\sigma_l = -2,47 \text{ MPa}$$

Summing stresses in the x-direction:

$$\sigma_x = -43,47 \text{ MPa}$$

The shear force at section A-A by linear interpolation from the results of Appendix B is:

$$V = -9,61 \text{ kN}$$

Hence, the shear stress at the upper bolt hole is given by:

$$\tau = \frac{VA\bar{y}}{t_2 I}$$

where

$$A = 5420 \text{ mm}^2$$

$$\bar{y} = 268,8 \text{ mm}$$

$$t_2 = 10 \text{ mm}$$

$$I = 8,1941 \times 10^8 \text{ mm}^4 \qquad \text{(refer Appendix B)}$$

Thus

$\tau = 1,709$ MPa

The principal stresses at the upper bolt hole position are then:

$$\sigma_{1,2} = \left(\frac{\sigma_x}{2}\right) \pm \sqrt{\left(\frac{\sigma_x}{2}\right)^2 + \tau^2}$$

that is

$\sigma_1 = 0,067$ MPa

$\sigma_2 = -43,54$ MPa

Multiplying both of these principal stresses by a stress concentration factor of 3 (refer Section 4.3.3) and applying the Von Mises failure criterion for σ_3 zero:

$$(\sigma_1 - \sigma_2)^2 + {\sigma_1}^2 + {\sigma_2}^2 \leq 2{\sigma_{yt}}^2$$

$$(0,201 + 130,62)^2 + (0,201)^2 + (-130,62)^2 \leq 2{\sigma_{yt}}^2$$

that is

$\sigma_m = 130,7$ MPa $< \sigma_{yt}$

where $\sigma_{yt} = \sigma_{0,2} = 260$ MPa for the Anticorodal -112 alloy (refer Section E.1.1).

Thus

$\tau = 1,709$ MPa

The principal stresses at the upper bolt hole position are then:

$$\sigma_{1,2} = \left(\frac{\sigma_x}{2}\right) \pm \sqrt{\left(\frac{\sigma_x}{2}\right)^2 + \tau^2}$$

that is

$\sigma_1 = 0,067$ MPa

$\sigma_2 = -43,54$ MPa

Multiplying both of these principal stresses by a stress concentration factor of 3 (refer Section 4.3.3) and applying the Von Mises failure criterion for σ_3 zero:

$$(\sigma_1 - \sigma_2)^2 + {\sigma_1}^2 + {\sigma_2}^2 \leq 2{\sigma_{yt}}^2$$

$$(0,201 + 130,62)^2 + (0,201)^2 + (-130,62)^2 \leq 2{\sigma_{yt}}^2$$

that is

$\sigma_{vm} = 130,7$ MPa $< \sigma_{yt}$

where $\sigma_{yt} = \sigma_{0,2} = 260$ MPa for the Anticorodal -112 alloy (refer Section E.1.1).

Stress at the position of maximum transverse shear stress

Maximum transverse shear stress occurs at the neutral axis at the king-pin (node 3) under dynamic loading conditions (ie. Case 1 loading).

From Table A3:

$\tau_{max} = 52,95$ MPa

The total stress along the neutral axis of the beam at node 3 (ie. σ_x) is equal to the longitudinal direct stress ($\sigma_b = 0$ at the neutral axis).

From Table A2:

$\sigma_l = -8,50$ MPa

$= \sigma_x$

The principal stresses and the principal shear stress are thus:

$$\sigma_{1,2} = \left(\frac{\sigma_x}{2}\right) \pm \sqrt{\left(\frac{\sigma_x}{2}\right)^2 + \tau^2}$$

that is

$\sigma_1 = 48,87$ MPa

$\sigma_2 = -57,37$ MPa

and

$$\tau_p = \sqrt{\left(\frac{\sigma_x}{2}\right)^2 + \tau^2}$$

$= 53,12$ MPa

Applying the Von Mises failure criterion for $\sigma_3 = 0$:

$$(\sigma_1 - \sigma_2)^2 + \sigma_1^2 + \sigma_2^2 \leq 2\sigma_{yt}{}^2$$

that is

$$\sigma_m = 92,10 \text{ MPa} < \sigma_{yt}$$

where $\sigma_{yt} = \sigma_{0,2} = 260$ MPa for the Anticorodal -112 aluminium alloy (refer Section E.1.1).

Stress in lower main I-beam welds at maximum shear force

Under dynamic loading conditions the maximum shear force occurs at the king pin. Maximum stress in the main I-beam welds at this section will be below the neutral axis where the bending stress is of the same sign as the longitudinal direct stress. From Table A3, the shear force at the king pin is:

$$V = 136,27 \text{ kN}$$

The shear stress in the web/flange welds is given by:

$$\tau = \frac{VA\bar{y}}{t_2 I}$$

where, referring to Figure A7 and approximating the shape of the flange extrusion to that of a simple T-shape, ie:

$A = 4\,500 \text{ mm}^2$

$\bar{y} = 131,1 \text{ mm}$

$b = (2)(0,707)(6)$

$= 8,484 \text{ mm}$

$I = 1,5909 \times 10^6 \text{ mm}^4$ (refer Appendix B)

Thus:

$\tau = 59,56 \text{ MPa}$

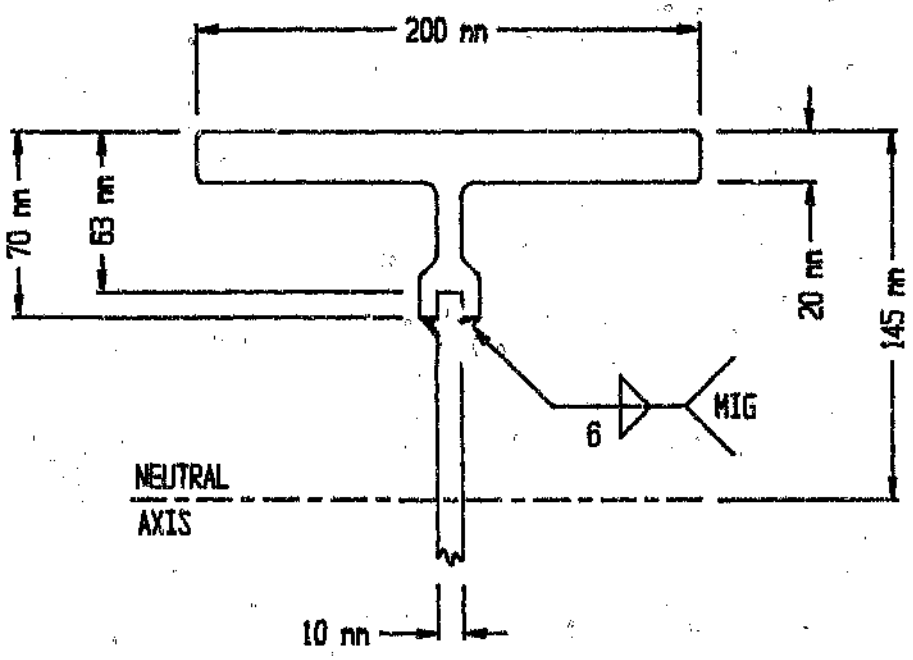


Figure A7 Main chassis I-beam cross-section at the king pin

From Table A4, the extreme fibre bending stress at the king-pin is:

$$\sigma_b = \pm 32,15 \text{ MPa}$$

The bending stress at the web/flange welds are then given by (refer Figure A7)

$$\sigma_b = \pm \left(\frac{145-70}{145}\right)(32,15)$$

$$= \pm 16,63 \text{ MPa}$$

The longitudinal stress at the king-pin from Table A2 is:

$$\sigma_l = -8,50 \text{ MPa}$$

The maximum direct stress in the direction of the longitudinal axis of the beams is thus:

$$\sigma_x = \sigma_b + \sigma_l$$

$$= (-16,63) + (-8,50)$$

$$= -25,13 \text{ MPa}$$

Whence, the principal stresses and the principal shear stress in the lower I-beam welds at the king-pin are:

$$\sigma_{1,2} = \left(\frac{\sigma_x}{2}\right) \pm \sqrt{\left(\frac{\sigma_x}{2}\right)^2 + \tau^2}$$

and

$$\tau_p = \sqrt{\left(\frac{\sigma_x}{2}\right)^2 + \tau^2}$$

that is

$\sigma_1 = 48,31$ MPa

$\sigma_2 = -73,44$ MPa

$\tau_p = 60,87$ MPa

Applying the Von Mises failure criterion for $\sigma_3 = 0$:

$(\sigma_1 - \sigma_2)^2 + \sigma_1^2 + \sigma_2^2 \leq 2{\sigma_{yt}}^2$

that is

$\sigma_m = 106,18$ MPa $< \sigma_{yt}$

where $\sigma_{yt} = \sigma_{0,2} = 110$ MPa for the Anticorodal -112 aluminium alloy in the welded condition (refer Section E.1.1). Note also that the principal shear stress in the welds at this position is less than the allowable weld shear yield stress of 65 MPa (refer Section E.1.1).

Stress at torsion tube bolt holes 2 000 mm rearward of the king pin

The forward and rearward pairs of bolt holes at the torsion tube/outrigger position 2 000 mm from the king pin are within 309 mm and 91 mm respectively the maximum bending stress for dynamic loading (ie. node 9 for Case 1 loading). Each of these bolt holes causes a stress concentration which is related to the principal stress field in the I-beam web at that point (refer Section 4.3.3). Maximum stress will occur at one of the upper two bolt holes (Figure A8) since these two holes are marginally further from the neutral axis, and since the compressive longitudinal direct stress over this section of the I-beams adds to the compressive bending stress above the neutral axis

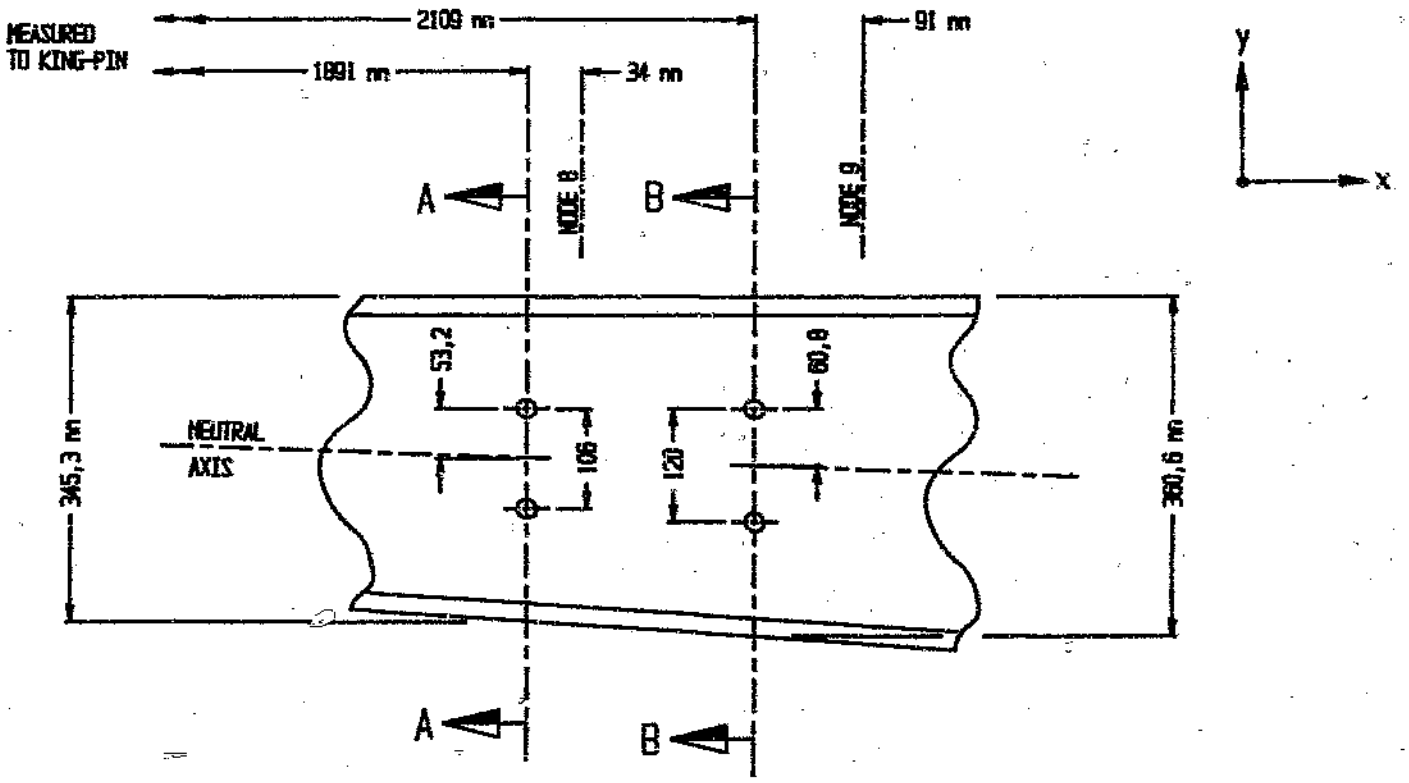


Figure A8 Torsion tube bolt pattern at 2 000 mm from the king pin

Interpolating linearly between node 7 and node 8 for section A-A and between node 8 and node 9 for section B-B, the extreme fibre bending stresses from Table A4 are:

Section A-A : $\sigma_b = \pm 117,15$ MPa

Section B-B : $\sigma_b = \pm 121,21$ MPa

Hence, with reference to Figure A8, the bending stresses at the centres of the upper bolt holes are:

Section A-A : $\sigma_b = -36,10$ MPa

Section B-B : $\sigma_b = -40,87$ MPa

The longitudinal direct stresses at the two sections from Table A2 are:

Section A-A : $\sigma_l = -5,96$ MPa

Section B-B : $\sigma_l = -5,75$ MPa

Adding stresses in the x-direction:

Section A-A : $\sigma_x = -42,06$ MPa

Section B-B : $\sigma_x = -46,62$ MPa

The shear forces at the two cross-sections by interpolation from Table A3:

Section A-A : $V = 71,58$ kN

Section B-B : $V = 64,67$ kN

These result in shear stresses at the upper bolt holes of:

Section A-A : $\tau = 28,87$ MPa

Section B-B : $\tau = 19,77$ MPa

The principal stresses at the upper bolt holes are then:

Section A-A : $\sigma_1 = +10,04$ MPa

$\sigma_2 = -52,10$ MPa

Section B-B : $\sigma_1 = +7,25$ MPa

$\sigma_2 = -53,87$ MPa

Multiplying each of these principal stresses by a stress concentration factor of 3 (refer Section 4.3.3):

Section A-A : $\sigma_1 = +30,12$ MPa

$\sigma_2 = -156,30$ MPa

Section B-B : $\sigma_1 = +21,75$ MPa

$\sigma_2 = -161,61$ MPa

Applying the Von Mises failure criterion for σ_3 zero, ie:

$$(\sigma_1 - \sigma_2)^2 + \sigma_1^2 + \sigma_2^2 \leq 2{\sigma_{yt}}^2$$

Section A-A : $\sigma_m = 173,33$ MPa $< \sigma_{yt}$

Section B-B : $\sigma_m = 173,51$ MPa $< \sigma_{yt}$

where $\sigma_{yt} = \sigma_{0,2} = 260$ MPa for the Anticorodal -112 aluminium alloy (refer Section E.1.1).

Stress in main I-beam w b at landing leg mounting bracket welds

The welds between the landing leg mounting bracket and the main chassis I-beams result in reduced material strength in the I-beam webs in the heat affected zone adjacent to the welds.

In this section the state of stress in the I-beam webs, at the position of the landing leg mounting bracket welds is analysed for the pseudo-dynamic (Case 1) loading conditions. In this situation the landing legs are raised. The case of loading via the landing legs, under static conditions and when uncoupling, is discussed in Section D.4.

The highest stress occurs at the lower end of the foremost weld, ie. 65 mm forward of node 12 (refer Drawings CH-04 and LL-01 in Appendix H). Interpolating linearly in Table A4, the extreme fibre bending stress at this section is:

$$\sigma_b = 82,58 \text{ MPa}$$

Referring to Figure A9 below, the bending stress at the lower end of the weld is:

$$\sigma_b = \left(\frac{285,7 - 92,4}{285,7}\right)(82,58)$$

$$= 55,87 \text{ MPa}$$

The longitudinal direct stress at this section, by interpolation from Table A2, is:

$$\sigma_l = -4,24 \text{ MPa}$$

Summing stresses in the direction of the longitudinal axis of the I-beam:

$$\sigma_x = \sigma_b + \sigma_l$$
$$= 51,63 \text{ MPa}$$

Here it appears that, since the longitudinal stress subtracts from the bending stress when x-direction stresses are summed at this section, greater stresses would result if an accelerating 1-g longitudinal load was used in this analysis instead of a decelerating load. However, an accelerating longitudinal load would skew the dynamic loading distribution in the opposite direction to that shown in Figure A4 and would result in substantially lower bending stresses at this section. The resulting x-direction stress and the principal stresses can be shown to be less than the stresses calculated for a longitudinal deceleration.

From Table A3, the shear force at this section is:

$$V = 43,23 \text{ kN}$$

The shear stress at the lower end of the weld is then given by:

$$\tau = \frac{VA\bar{y}}{t_2 I}$$

where

$$A = 4\,724 \text{ mm}^2$$
$$\bar{y} = 268,6 \text{ mm}$$
$$t_2 = 10 \text{ mm}$$
$$I = 7,334 \times 10^6 \text{ mm}^4$$

that is

$\tau = 7,48$ MPa

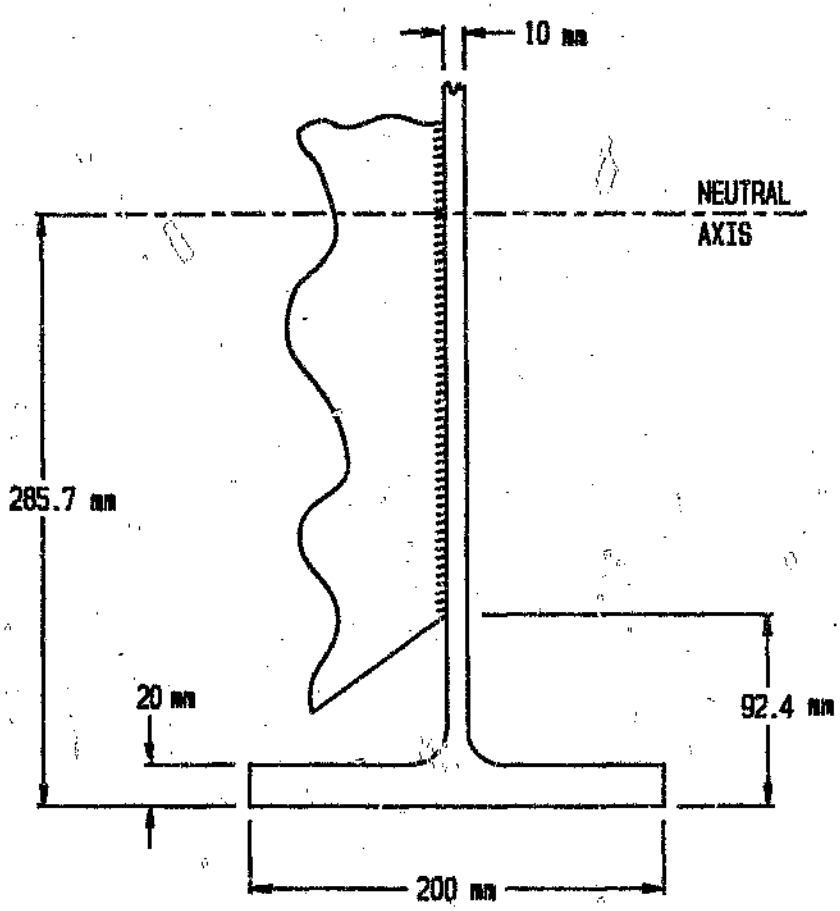


Figure A9 Chassis I-beam cross-section at foremost landing leg mounting bracket weld

Hence, the principal stresses and the principal shear stress at the lower end of the weld for $\sigma_y = 0$ are:

$\sigma_1 = 52,69$ MPa

$\sigma_2 = -1,06$ MPa

and

$\tau_y = 26,88$ MPa

Applying the Von Misces failure criterion (for $\sigma_3 = 0$):

$$(\sigma_1 - \sigma_2)^2 + \sigma_1^2 + \sigma_2^2 \leq 2{\sigma_{yt}}^2$$

that is

$\sigma_m = 53,23$ MPa $< \sigma_{yt}$

Here it is assumed that the allowable stresses for the Anticorodal -112 aluminium alloy in a heat affected zone are the same as for the alloy in the welded condition, ie. $\sigma_{yt} = 110$ MPa (refer Section E.1.1).

Similarly, the principal shear stress is significantly lower than the allowable shear yield stresses for the welded condition of 65 MPa (refer Section E.1.1).

Stress at rubbing plate bolt holes in I-beam flanges

Maximum stress at the rubbing-plate attachment bolt holes occurs during dynamic loading at the bolt hole directly in line with the king-pin, ie. at node 3 during Case 1 loading.

From Tables A4 and A2 respectively, the extreme fibre bending stress in the lower flange and the longitudinal direct stress at node 3 are:

$\sigma_b = -32,15$ MPa

$\sigma_l = -8,50$ MPa

Hence, total x-direction stress is:

$$\sigma_x = (-32,15) + (-8,50)$$
$$= -40,65 \text{ MPa}$$

Since shear stress is zero at the extreme fibres:

$$\sigma_2 = \sigma_x = -40,65 \text{ MPa}$$

and

$$\sigma_1 = \sigma_3 = 0$$

The hole will cause a concentration of stress in the area adjacent to the hole. Multiplying the principal stress by a stress concentration factor of 3 (refer Section 4.3.3):

$$\sigma_2 = -121,95 \text{ MPa}$$

Whence, the Von Mises stress is:

$$\sigma_m = 121,95 \text{ MPa} < \sigma_{yt}$$

where $\sigma_{yt} = 260$ MPa for the Anticorodal -112 aluminium alloy (refer Section E.1.1).

Stress in main I-beam web at upper coupler cross-member welds

In this section, the state of stress in the heat affected zone of the chassis I-beam webs, at the position of the upper coupler cross-member welds, is analysed for pseudo-dynamic (Case 1) loading. The stress analysis of the upper coupler cross-members themselves and associated coupler components,